DETERMINATION OF A CONSISTENT VISCOSITY DISTRIBUTION IN THE EARTH'S MANTLE BENEATH NORTHERN AND CENTRAL EUROPE

vorgelegt von
Holger Steffen

DISSERTATION
zur Erlangung des Doktorgrades
im Fachbereich Geowissenschaften
am Institut für Geologische Wissenschaften
der Freien Universität Berlin
Berlin, 2006

Tag der mündlichen Prüfung: 5. Dezember 2006
1. Gutachter: Prof. Dr. Georg Kaufmann
2. Gutachter: Prof. Dr. Serge A. Shapiro

Zusammenfassung

Während der letzten Eiszeit bedeckten große Eisschilde Nordamerika, Grönland, Nordeuropa, Teile Asiens und die Antarktis. Das Wachstum der Eisschilde begann nach dem letzten Interglazial vor etwa 125.000 Jahren. Ihre größte Ausdehnung erreichten die Eisschilde zum Letzten Glazialen Maximum (LGM) vor ca. 22.000 Jahren v. h. und durch ihr Gewicht drückten sie die darunterliegende Erdoberfläche nach unten. Im Anschluss an das LGM verschwanden die Eisschilde relativ schnell, aber die deformierte Erde stellt sich immer noch aufgrund der zeitabhängigen viskoelastischen Eigenschaft des Erdmantels auf ein neues isostatisches Gleichgewicht ein. Diese Ausgleichsbewegung wird heute noch beobachtet. Dabei stellen u.a. alte Küstenlinien (Meeresspiegeldaten) und die derzeitigen Krustenbewegungen wichtige Beobachtungen dar.

Diese Arbeit bedient sich einer Vielzahl von Meeresspiegeldaten aus Nord- und Mitteleuropa und den durch das skandinavische BIFROST-Projekt mittels GPS beobachteten Krustengeschwindigkeiten. Die Daten werden genutzt, um unterhalb dieses Gebietes die Viskositätsstruktur im Erdmantel mit Hilfe eines realistischen Eismodells und verschiedener Rechentechniken, wie einer Inversionsmethode und der Finite-Element-(FE)-Modellierung, zu untersuchen. Dabei wird auf die folgenden Regionen und Strukturen eingegangen: (i) der Erdaufbau unter Skandinavien, insbesondere mit Augenmerk auf einen niedrigviskosen Kanal im obersten Mantel, der in diversen Veröffentlichungen diskutiert wird, (ii) das post-glaziale Verhalten der Nordsee anhand neuer, erst kürzlich veröffentlichter Meeresspiegeldaten, und (iii) die dreidimensionale Struktur des Mantels, die aus einem Scherwellen-Tomographiemodell und unterschiedlichen thermodynamischen Annahmen berechnet wurde. Des Weiteren wird eine Sensitivitätsanalyse mit einem FE-Modell und dem BIFROST-Datensatz durchgeführt, und die Wasserlast des Hohenwarte-Stausees in Thüringen genutzt, um den Mantelaufbau zu untersuchen. Dabei werden vorher erzielte Ergebnisse in das FE-Modell einbezogen.

Die Ergebnisse der Inversionsmethoden deuten auf eine niedrigviskose Schicht unter der Barentssee hin. Sie befindet sich zwischen 120 und 200 km Tiefe und ist durch Viskositäten von 10^{19} - 10^{20} Pa s gekennzeichnet. Unter Skandinavien kann eine solche Zone nicht nachgewiesen werden, während für Nordwesteuropa keine zweifelsfreie Aussage dafür oder dagegen möglich ist. Die Mächtigkeit der Lithosphäre nimmt von etwa 60 - 70 km unterhalb von Nordwesteuropa und der Barentssee in Richtung Skandinavien zu. Unter der Nordsee ist sie ca. 90 km mächtig, in Skandinavien 120 km. Zusätzlich wird das relativ stabile Verhalten des London-Brabanter Massives, das sich am Rand des Gebietes mit anhaltender Ausgleichsbewegung befindet, während und nach der Eiszeit bestätigt. Dagegen zeigt die südliche Nordsee von den Niederlanden bis nach Norddeutschland eine deutliche Beeinflussung durch die isostatische Ausgleichsbewegung.

Mit den FE-Modellierungen können Unterschiede von bis zu 7 mm/a zwischen den berechneten vertikalen Krustenbewegungen der ein- und dreidimensionalen Erdmodelle ermittelt werden. Die Horizontalkomponenten werden noch stärker beeinflusst: Mit dem besten dreidimensionalen Erdmodell findet man zusätzlich zu der bekannten divergenten Ausgleichsbewegung ein regionales Geschwindigkeitsfeld von der norwegischen Küste zum Baltischen Schild hin. Durch eine Sensitivitätsanalyse zeigt sich, dass dieses in der Übergangszone zwischen 450 und 670 km Tiefe entsteht. Weitere spezielle Sensitivitätsanalysen zum oberen Mantel mit dem realistischen Eismodell zeigen, dass die Vertikalgeschwindigkeiten generell an Viskositätsvariationen zwischen 220 und 540 km Tiefe gekoppelt sind, die Horizontalgeschwindigkeiten dagegen an die Übergangszone. Die durch die Wasserlast des Hohenwarte-Stausees induzierten Deformationseffekte können auf eine instantane elastische Krustendeformation zurückgeführt werden. Die Wasserlast des Stausees ist damit zu gering, um Aussagen über die Beschaffenheit des Erdmantels in diesem Gebiet machen zu können.

Die Ergebnisse dieser Arbeit zeigen, dass die beobachtete Ausgleichsbewegung in Nord- und Mitteleuropa keine Rückschlüsse auf die Viskosität im unteren Erdmantel zulässt. Für eine genauere Bestimmung der dreidimensionalen Struktur der Erde in diesem Gebiet bedarf es weiterer Beobachtungsdaten wie Meerespiegeldaten und Krustengeschwindigkeiten, aber auch hochauflösender seismischer Profile.

Abstract

During the last ice age, large ice sheets covered North America, Northern Eurasia, Greenland and Antarctica. The ice sheets expanded slowly between 125,000 years BP and the last glacial maximum around 22,000 years BP to their maximum size, and depressed the solid Earth underneath. Subsequent to the last glacial maximum, the ice sheets disappeared rapidly and the solid Earth is readjusting towards a new isostatic equilibrium. Due to the time-dependent viscoelastic behaviour of the Earth's mantle this process, called glacial isostatic adjustment (GIA), is still observable today. It is documented in numerous observations, such as palaeo-shorelines and ongoing crustal movements.

In this work, palaeo-shoreline data from Northern and Central Europe, as well as crustal velocities from the BIFROST GPS campaign, are used to infer the viscosity structure of the Earth's mantle underneath this area. The following regions or structures are investigated with the help of a realistic ice model and different techniques such as a global inverse procedure and Finite Element (FE) modelling: (i) the Earth's structure beneath Scandinavia, including the search for a low-viscosity zone in the upper mantle, which has been proposed in the literature, (ii) the post-glacial behaviour of the North Sea area with new, recently published sea-level data, and (iii) the three-dimensional (3D) structure of the mantle derived from a seismic shear-wave tomography model and different thermodynamic considerations. Furthermore, a sensitivity analysis of the BIFROST data to variations of the mantle viscosity is made, and in a regional study the mantle structure in Thuringia, Germany, based on former results, is investigated with a FE model and the water load of the Hohenwarte reservoir.

The results from inverse procedures indicate a low-viscosity zone underneath the Barents Sea, with viscosities between 10^{19} - 10^{20} Pa s in a depth interval of 120 - 200 km. No such low-viscosity zone is found underneath Scandinavia, and there is no clear indication for such a zone underneath northwestern Europe. The thickness of the rheological lithosphere increases from 60 - 70 km underneath northwestern Europe and the Barents Sea towards 90 km underneath the North Sea area and finally to values exceeding 120 km underneath Scandinavia. In addition, it is confirmed that the Belgian crust (London-Brabant massif), which is in the periphery of the GIA area, was fairly stable during and after the last ice age and insensitive to GIA. The southern North Sea region including the Netherlands and northwestern Germany, however, has a strong GIA-induced signal.

The FE modellings reveal that between 3D and one-dimensional earth models the vertical crustal velocities have differences of up to 7 mm/yr, and that horizontal crustal velocities are affected even stronger. The horizontal motions of the best 3D earth model indicate a regional velocity field with movements away from the Norwegian coast towards the old Baltic Shield. A sensitivity analysis shows that the dramatic change in the horizontal flow pattern has its origin in the deeper upper mantle, between 450 and 670 km depth. The detailed sensitivity analysis of the upper mantle with the realistic ice-sheet model reveals that the present-day uplift velocity is mostly sensitive to viscosity variations in upper-mantle layers between 220 and 540 km depth. For the present-day horizontal velocity, the sensitivity is strongly influenced by lateral viscosity variations in the transition zone of the mantle. The FE modelling concerning deformation effects caused by the water load of the Hohenwarte reservoir, shows that effects are mainly induced by instantaneous elastic deformation, which indicates the insensitivity of the water

load of the reservoir to the time-dependent relaxation of a realistic mantle model.

All methods and investigations confirm that the observed GIA process in Northern and Central Europe is not sensitive to the viscosity structure in the lower mantle. The determination and understanding of the Earth's 3D structure needs more observational data, from geological records to seismic profiles, for a clearer view.

Contents

1. Introduction

The Earth's climate responds to long-term (10^4 to 10^5 years) variations in the Earth's orbital parameters, commonly summarised in the *Milankovitch theory* [e.g. Hays et al., 1976; Berger, 1978], and these variations result in warm and cold periods on that time scale. Periods with a long-term decrease in the surface temperature on the Earth and a drop by more than 10°C result in an expansion of the continental ice sheets, polar ice sheets and mountain glaciers. These colder phases with advancing ice sheets are called *glacials*. Warmer phases with retreating ice sheets are termed *interglacials*. The entire period is commonly referred to as *ice age cycle*, and the *ice age* comprises several cycles. Today, we live in an interglacial of an ice age.

Since the beginning of the Quaternary 2.59 million years ago, the Earth has experienced several cycles of glaciation (cyclicity of about 120,000 years) with ice sheets advancing and retreating in North America, Northern Eurasia, Greenland and Antarctica. In Northern Germany, the cold periods were known as the Elster glacial, the Saale glacial and the Weichsel glacial. The last time the Earth was covered by large ice sheets ca. 22,000 years ago, an era referred to as the *Last Glacial Maximum* (LGM). The last remnants of the Late Pleistocene ice sheets vanished around 6000 years ago.

Fig. 1.1 shows the additional ice covering the Northern Hemisphere during the last glacial cycle. North America experienced the largest ice-sheet growth with up to 3400 m thickness during the LGM. The Greenland Ice Sheet was around 500 m thicker than today (3000 m) and in Fennoscandia the ice height reached around 1700 m in the centre. Furthermore, smaller ice sheets covered the British Isles and the Barents Sea. In contrast to the retreat shown in Fig. 1.1, most of the ice masses of the Greenland Ice Sheet and the Antarctic Ice Sheet on the Southern Hemisphere have survived until the interglacial period, today representing the two major ice sheets. The former major ice sheets occupied $\sim$30% of the land area at the LGM, compared to $\sim$10% today.

The spatial and temporal distribution of the ice sheets is constrained by glacial moraines, glacigenic sediments, and glacial striations. From field evidence such as moraines and glacial erratics the extent of the ice sheets at a certain time is reconstructed, and the glacial striations show the direction of the ice flow. Finally, the δ^{18}O record and numerical models are needed to get the information about the timing, the height and the flow of the ice sheets, which are necessary for the construction of a time-dependent and three-dimensional (3D) ice model. In this work, the global ice model **RSES** for the Late Pleistocene glacial history will be used, compiled by Kurt Lambeck at the **R**esearch **S**chool of **E**arth **S**ciences, Canberra, Australia.

During the LGM, 5.5% of the world's water was bound in ice, as opposed to 1.7% today [Williams et al., 1998]. The transfer of water from the oceans to the expanding ice sheets resulted in a global sea level fall by an average of up to 130 m [Fairbanks, 1989; Fleming et al., 1998; Yokoyama et al., 2000]. Fig. 1.2 summarises the contributions of the major glaciated regions to the total amount of the sea-level fall as calculated with the ice model RSES. It can be seen that more than a half of the transferred water was bound in the ice sheet of North America, around one third in the enlarged Antarctic Ice Sheet, and "only" one seventh in the Fennoscandian region.

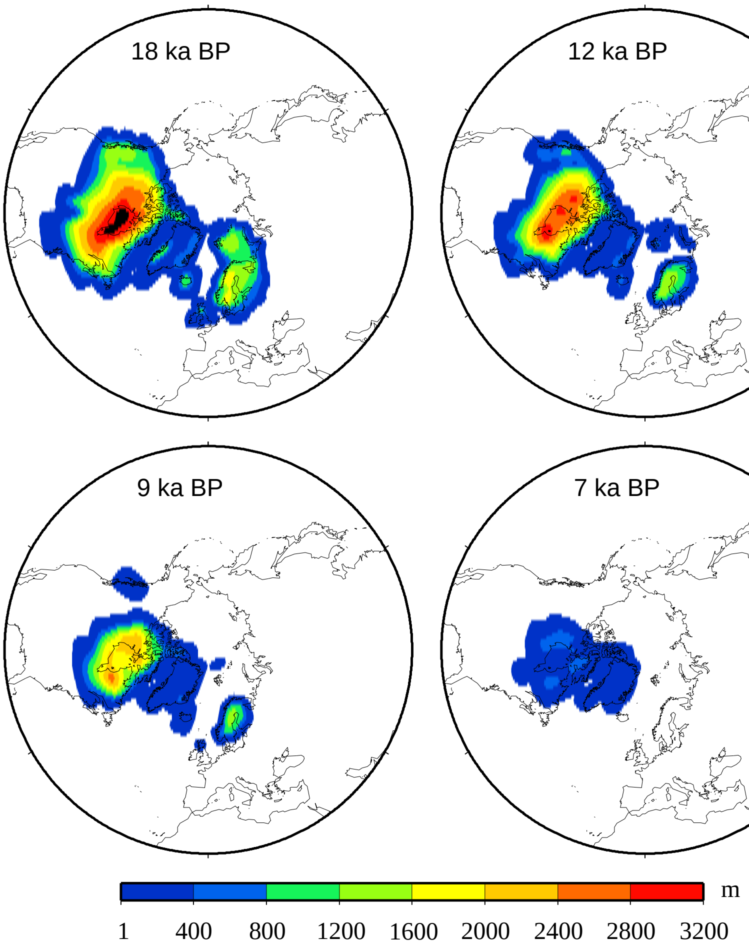

Figure 1.1: The additional ice on the Northern Hemisphere at four times during the last ice age.

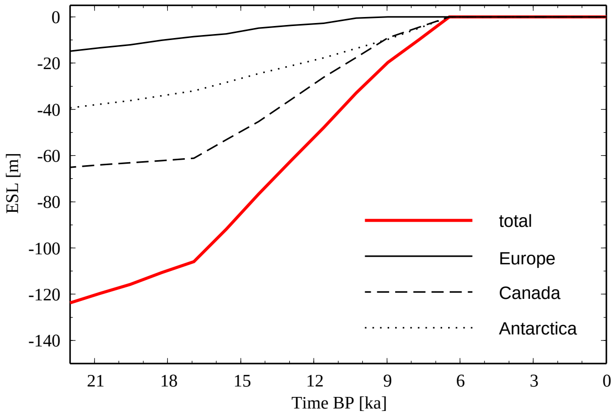

Figure 1.2: Estimated sea-level change induced by the ice sheets of the last ice age, calculated with the global ice model RSES [from Kaufmann, 2004].

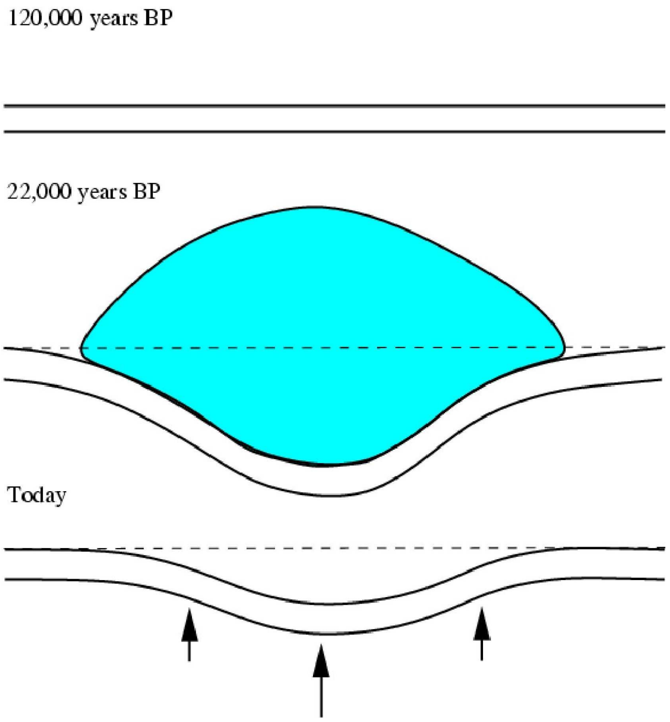

Figure 1.3: Sketch of the rebound principle [modified from Kaufmann, 2004].

Due to the water-mass transfer between the ice sheets and the ocean, the Earth's crust and mantle were deformed by the changing weight of the ice sheets on land and the water load in the oceans. This process, termed *glacial isostatic adjustment* (GIA), is sketched in Fig. 1.3: 125,000 years ago, during the Last Interglacial, the Earth's surface was free of additional ice and the crust and the mantle have (almost) relaxed after the former glaciation. No deformation is observed. During the build-up of the ice sheets until the LGM at 22,000 years BP, the surface was depressed by several hundreds of metres. The enormous weight of this ice caused the crust to sink into the fluid mantle. During the melting phase, the surface rebounded due to the buoyancy of the displaced material relative to the mantle, but not to its initial state. This lag is due to the time-dependent viscoelastic relaxation of the Earth's mantle with its fairly high viscosity. The GIA is still going on and thus observable today. It is documented by numerous observations all around the world. In Fennoscandia and northwestern (NW) Europe, where the large Weichselian Ice Sheet complex was located during the last glacial cycle, the GIA process was early recognised in numerous field observations [see Ekman, 1991, for a review]. Here, the scientific record of the crustal response is documented in various observations such as (i) palaeo-strandlines (relative sea levels, RSL), (ii) tide gauges, (iii) shoreline tilting, (iv) present-day crustal deformations monitored by GPS observations, and (v) present-day changes in the gravity field seen by satellite missions and field campaigns. Together with the knowledge of the ice-sheet retreat since the LGM, this large set of different observations, both in space and time, provides a detailed picture of the past and ongoing deformation. The database allows, amongst other things, to construct a detailed model of sea-level change induced by the mass redistribution between ice sheets and the ocean.

From the five observation types mentioned above, the last three methods (tilt, GPS, gravity) comprise short time periods in the decadal range, which is very short compared to the relaxation time. With these

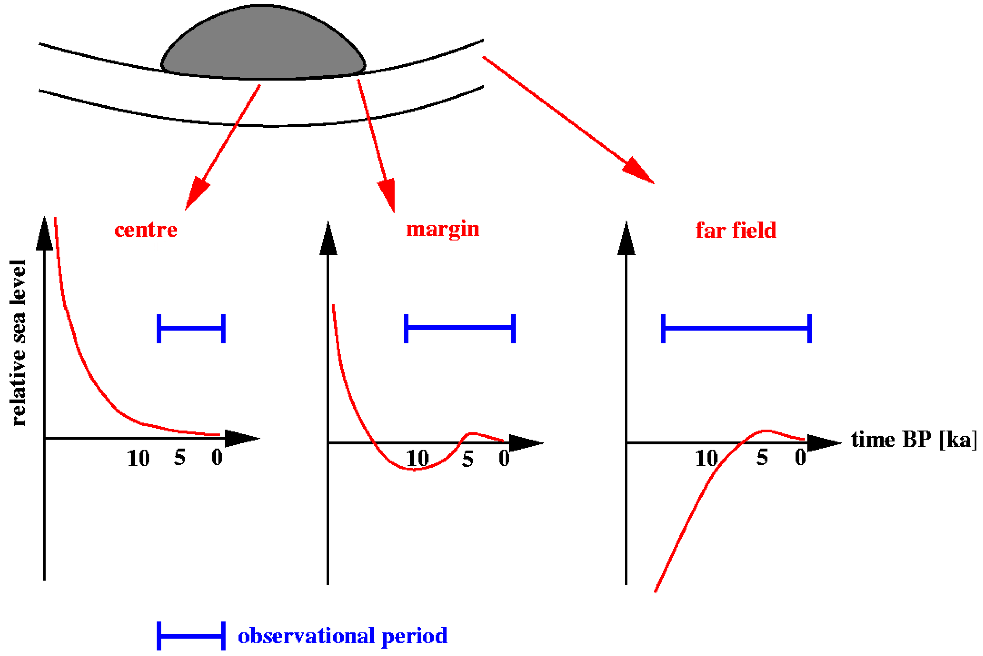

Figure 1.4: Anatomy of sea-level records in distance to the ice sheet [modified from Kaufmann, 2004].

methods the present-day GIA is observed. The tide gauge records are available from some selected stations since ca. 300 years, comprising a longer time period than the three other methods, but still short compared to the relaxation time. The longest time period is covered by RSL data, where two main parts contribute to: (i) the isostatic contribution resulting from the deformation of the solid surface by ice loading/unloading, (ii) the eustatic contribution due to the change in the sea level as a consequence of mass conservation. Hence, the RSL curve at a particular location varies with distance to the former ice sheet. Fig. 1.4 summarises these effects: In the centre of the ice sheet, the isostatic component is largest and the uplift has taken place in two distinct stages: The initial uplift was rapid and took place as the ice was being unloaded. Once the deglaciation was complete, the uplift was slower and decreased exponentially after that. The observational period starts when the last ice is melted. At the margin of the ice sheet the isostatic contribution is smaller than in the centre and the eustatic contribution becomes more important. Thus, until 10,000 years BP a sea-level fall is observed to a point below the present-day sea level. Then the eustatic contribution dominates until today. As the ice vanishes earlier at the margin, the observational period also starts earlier. In the far field only the eustatic part contributes to the RSL, which allows an observational period over the whole deglaciation. It is possible that the sea level rises to points higher the sea level today (Holocene highstand). Due to the increasing water load, the surface of the ocean basin and/or the continental shelf is depressed again (5000 years BP). Today, typical uplift rates in the centre of formerly glaciated areas are in the order of 10 mm/yr [see Johansson et al., 2002] and typical rates of sea-level rise are in the order of 1.5 mm/yr [see Töppe, 1992, 1995].

Fennoscandia and NW Europe turned out to be key regions of investigations to GIA, due to a large number of available observation data. Some examples for sea-level data in these regions are presented in Fig. 1.5. Ångermanaelven is located in the centre of the former Fennoscandian Ice Sheet and thus experiences a monotonic land uplift. The earliest data have an age of ca. 10,000 years BP, indicating the time when this location became ice free. In contrast to Ångermanaelven, Zeeland shows the typical

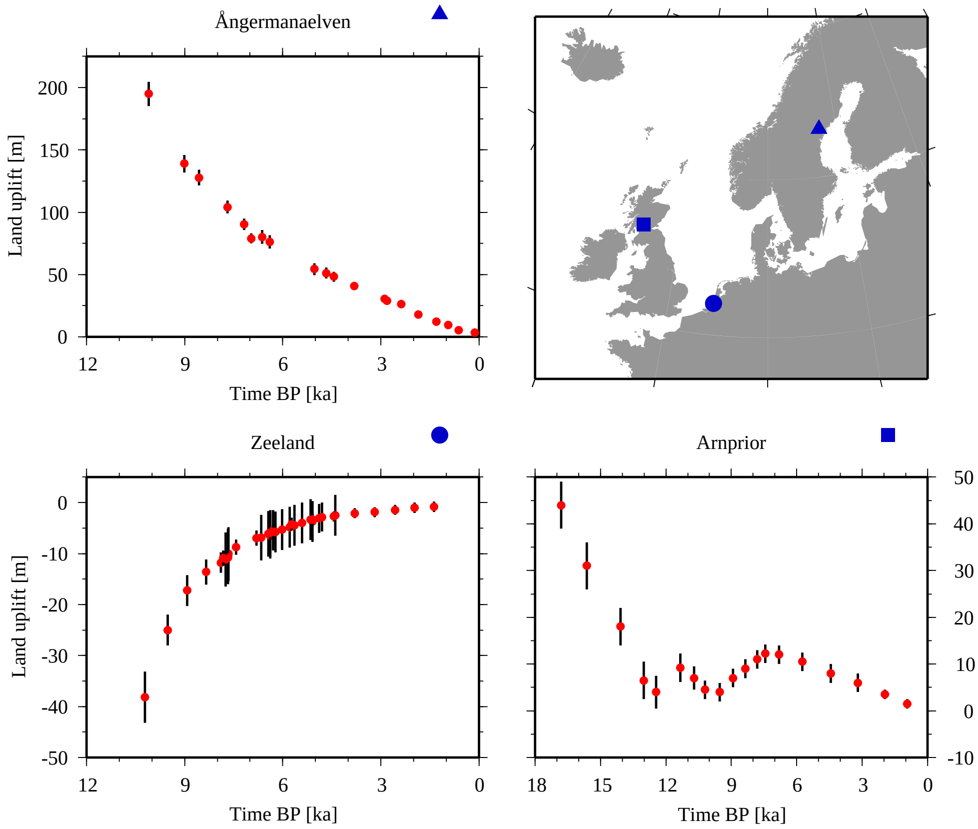

Figure 1.5: Examples of sea-level data (red dots with error bars) in Europe showing the different types of RSL curves.

eustatic sea-level curve. Here, the data record also begins around 10,000 years BP. This is due to the fact that the North Sea was above sea level during the last ice age. The first observation mark holds the time when the first water left a trace in near distance to the present-day coastline and the sea level rose steadily due to the melt-water impact. The last example from the location of Arnprior includes both the isostatic and the eustatic component. Furthermore, this data set envelopes a long time period, starting at 17,000 years BP. The first part until 11,000 years BP includes the uplift phase after the melting of the British Isles Ice Sheet and the eustatic contribution. After 11,000 years BP, one can see again a short dominating isostatic part for around 2000 years, which is induced by a short readvance (Loch Lomond readvance) of the British Ice Sheet. Then the eustatic part dominates.

In addition to the RSL data set, the GPS observations from the BIFROST project [Johansson et al., 2002, Fig. 1.6] are often used in investigations of the rebound in Fennoscandia. These 44 stations monitor the ongoing crustal deformation of the Netherlands and the United Kingdom in the Southwest to Sweden and Finland in the Northeast, and thus provide the present-day vertical and horizontal crustal motion in that region. The data show a broad ellipsoidal uplift dome with a major axis oriented roughly southwest to northeast. The maximum uplift rate of more than 10 mm/yr is observed in the Gulf of Bothnia. The horizontal velocities are relatively low where the radial uplift rates are largest, and they are directed outward from this location on all sides, indicating a divergent motion of the crust. These rates increase with distance away from the uplift centre, and reach up to 2 mm/yr at sites far outside.

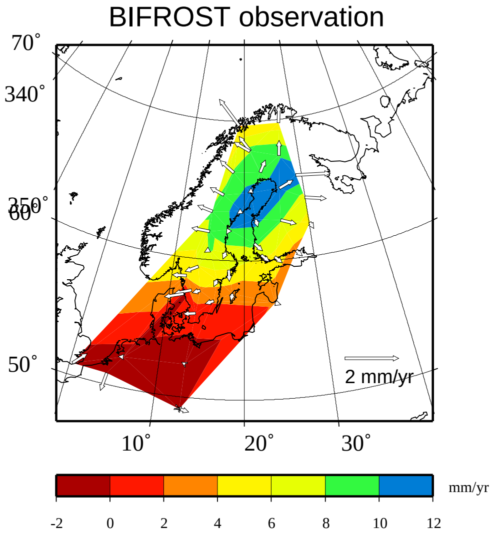

Figure 1.6: GPS observation of the crustal velocities (contours: vertical; arrows: horizontal) in Fennoscandia at BIFROST stations.

In this thesis both the RSL data [based on several studies and summarised in Lambeck, 1993a,b; Kaufmann and Wolf, 1996; Lambeck et al., 1998a; Vink et al., 2006] and the BIFROST results [Johansson et al., 2002] will be used.

1.1 Concept of the thesis

A number of factors, such as the ice-sheet geometry, the ocean load, the lithospheric thickness and the mantle viscosity affect the ongoing GIA. The most interesting factor is the mantle viscosity, as the time dependence of the GIA process is a characteristic of the viscosity. Thus, compared to the other factors only the mantle material produces significant GIA effects on the timescales of 10^4 to 10^5 years.

In general, the viscosity is a measure of the resistance of a fluid to deform under shear stress. It describes a fluid's internal resistance to flow and may be thought of as a measure of fluid friction. A typical example to visualise “What is viscosity?” is the comparison of water and oil: water is so-called "thin", having a lower viscosity, while oil is so-called "thick", having a higher viscosity.

The mantle viscosity was firstly introduced by Haskell [1935] in a hydrodynamic theory of postglacial rebound. He was able to determine a viscosity $\eta = 10^{21}$ Pa s of the upper mantle beneath Fennoscandia. In contrast, van Bemmelen and Berlage [1935] confined all mantle flow to a 100 km thick asthenosphere with a viscosity of $\eta = 1.3 \times 10^{19}$ Pa s, which should be the reason for the glacial rebound. Haskell instead found that by thickening their 100 km thick asthenosphere four times, the viscosity would agree with his one [Ekman, 1991]. This example demonstrates the difficulty in determining the mantle viscosity right from the start, and since then a large number of publications are dedicated to the GIA and the determination of the mantle viscosity, which will be extensively discussed in the following chapters.

The traditional theory of the GIA has been developed for a one-dimensional (1D) earth model [Peltier, 1974; Farrell and Clark, 1976; Milne and Mitrovica, 1998]. Several techniques can be used for the calculation, such as forward modelling using an iterative procedure in the spectral domain for predefined earth

Table 1.1: Summary of the numerical approaches used in the following chapters. The dimension of the investigated Earth structure is listed together with the source of the applied load and the number of the calculated models. The ice model FBKS8 is the Fennoscandian part of the global ice model RSES.

chapter	approach	dimension	load	model	model numbers
2	pseudo-spectral method	1D	ice/water	RSES	1089
	neighbourhood algorithm	1D	ice/water	RSES	1500
3	pseudo spectral method	1D	ice/water	RSES	1089
4	Finite-element method	3D	ice	FBKS8	10
5	Finite-element method	3D	ice	FBKS8	153
6	Finite-element method	1D	water	reservoir	3

models [pseudo-spectral approach after Mitrovica et al., 1994; Milne and Mitrovica, 1998], or inverse inferences [Tarantola and Valette, 1982; Mitrovica and Peltier, 1991]. The results of these modellings are compared to observational data such as the RSL data and the crustal velocities mentioned above. The numerical models of the GIA based on the Scandinavian and NW European observational data have converged towards a radial (1D) viscosity structure, with viscosities increasing by one to two orders of magnitude with depth. However, the mantle viscosity can vary in all three dimensions. Thus, in the GIA investigations the Finite-element (FE) technique is increasingly used in the last years. This method allows including lateral heterogeneities in the lithospheric thickness and in the mantle viscosity. Here, the application envelopes mixed spectral-FE codes [Martinec, 2000; Zhong et al., 2003], a finite volume formulation [Latychev et al., 2005b], and the use of commercial program packages [Wu, 2004; Spada et al., 2006].

In this thesis, we search for a consistent 3D viscosity structure of the Earth's mantle beneath Fennoscandia and NW Europe using both the forward and inverse modelling for 1D earth models and the FE method for 3D models. The forward and inverse techniques are used, as they are fast and efficient. The 1D-viscosity profiles found are used as input for the 3D investigations, which focus on different 3D viscosity structures and the sensitivity of the observational data to viscosity variations. Finally, the 3D modelling is used for a special investigation regarding the regional influence of a reservoir, again under the view of the Earth structure beneath and additionally in view of an influence on the instrument‘s registration in an observatory nearby. The 3D modellings are carried out with the commercial program package ABAQUS [Hibbitt et al., 2005].

Tab. 1.1 summarises all the numerical approaches used in this thesis, and lists the number of the calculated models and the sources of the applied load in each of the following chapters.

1.2 Outline of the thesis

This thesis consists of seven chapters. After this introduction five articles follow, with chapters 2, 4 and 6 already published in peer-reviewed journals and written by myself as first author. Chapter 3 is under revision at the moment and here I am a co-author. At the beginning of this chapter is stated for which sections I'm responsible. Chapter 5 is submitted to a peer-reviewed journal.

Chapter 2 discusses the topic of a weak asthenosphere underneath Fennoscandia and NW Europe. Therefore the pseudo-spectral approach and the Neighbourhood Algorithm (NA) are used. Earth models with a special 1D structure are defined for the calculation. Then, the NA randomly creates additional earth models in a predefined range of lithospheric thickness and mantle viscosity. This allows us to explore the hypothesis of a low-viscosity zone in the upper mantle, which has been proposed in the literature. At first, a simple (three-layer) radial earth model is calculated for the subregions Scandinavia, NW Europe, and the Barents Sea, which best fits the sea-level data of those regions, then the global inverse procedure based on the NA is employed to further refine the viscosity profile in the upper mantle under the view of a possible asthenosphere. The global ice model RSES is used to predict the GIA of these earth models and the predictions are compared to the observed sea-level data from these regions and the BIFROST data. The results have been published in Steffen and Kaufmann [2005].

In chapter 3, the pseudo-spectral approach is used again to infer the radial Earth structure underneath the southern North Sea area. For this region, a comprehensive observational database of Holocene RSL index points from the NW European coast was recently compiled by the Bundesanstalt für Geowissenschaften und Rohstoffe (BGR). The data were collected from different countries / regions and by different workers. They were compared and reassessed by the BGR colleagues on a common time-depth scale. The database revealed a non-linear, glacio- and / or hydro-isostatic subsidence component, which is negligible on the Belgian coastal plain but increases significantly along the NW German coast. It was also found, that the subsidence is at least partly related to the post-glacial collapse of the so-called peripheral forebulge [see Kiden et al., 2002], which developed around the Fennoscandian ice-load centre during the last glacial maximum. Hence, special subsets of the new RSL data are compared to three-layer radial earth models as it is done in chapter 2. The aim is to infer the structure of the Earth mantle underneath the southern North Sea area, and conversely to predict RSL in regions of this area where no observational data are available. The results contribute to the investigations of Vink et al. [2006, submitted in July].

However, the former investigations only focus on a 1D Earth structure. The investigations in chapter 4 include the consideration of more complex earth models with lateral heterogeneities in the mantle viscosity. Here, a set of so-called flat 1D and 3D FE earth models with viscoelastic material properties is developed to study the GIA response induced by the ice-load model RSES. The emphasis is on a comparison of one 1D and three 3D viscosity models. The 1D viscosity model is a laterally homogeneous model based on the results of chapter 2, the 3D viscosity models are based on results of a shear-wave tomography. For the 3D structure, different rheological reference models were used. One aim is to investigate how the thermodynamic properties of the mantle affect the background radial viscosity profile and also the inferred lateral viscosity variations. Another aim is to study the different contribution of the lateral viscosity variations in various layers in the upper mantle and that from the lower mantle. In addition to the model comparison, a simple sensitivity analysis for different upper-mantle layers is performed to localise regions, which influence the rebound pattern. The GIA predictions of RSL change and crustal velocities are compared to observed sea-level data and the BIFROST project. The results of this chapter are published in Steffen et al. [2006a].

The results of chapter 4 put forward the question of the sensitivity of the present-day crustal velocities in Fennoscandia to radial and lateral viscosity changes in the upper mantle. Wu [2006] has recently shown such an analysis for the Laurentide Ice Sheet using an axially symmetric earth model with a simple symmetric ice model. His statistical approach is followed in chapter 5, but, (i) a *realistic* ice-load history of the Fennoscandian ice sheet (RSES ice model) is applied, and (ii) the *flat* 3D FE model from chapter 4 is employed. The model is subdivided into blocks of variable size, which results in a large number of sensitivity kernels to interpret. Thus, a simple approach is introduced to calculate the kernel of a block by averaging the perturbed predictions of all surface nodes of this block to one value for this block. The main emphasis is to show how sensitive BIFROST stations are to special mantle layers and regions and to suggest locations for new GPS stations with higher sensitivity. The results of this chapter will be published in Steffen et al. [2006b, submitted in October].

In the chapters 4 and 5 the load is caused by ice. However, also water can be applied as load, as it is done in the first two chapters, where the sea-level equation is used and thus the mass imbalance of ice and water is calculated. In chapter 6, the load of the Hohenwarte reservoir in Thuringia, Germany, is used for the FE calculation. The calculated viscosity of chapter 2 is assigned in a FE model to investigate (i) if the reservoir load is large enough to deform the upper mantle, and (ii) the influence of lake-level fluctuations on regional deformation changes, which could possibly be observed with sensitive instruments in the nearby Geodynamic Observatory Moxa. It is focused on short-term elastic and long-term viscoelastic deformations resulting in tilt and strain. The results of this chapter are published in Steffen and Kaufmann [2006a,b].

Finally, chapter 7 concludes this thesis with a discussion of the results.

2. Glacial isostatic adjustment of Scandinavia and northwestern Europe and the radial viscosity structure of the Earth’s mantle

Abstract[a]

During the last glacial maximum, large ice sheets covered Scandinavia, the Barents Sea, and the Northern British Isles. Subsequent to the last glacial maximum, the ice sheets disappeared and the solid Earth readjusts towards a new isostatic equilibrium. The glacial isostatic adjustment process is documented in numerous observations, e. g. palaeo-shorelines covering the last deglaciation phase, and ongoing crustal deformations monitored by GPS stations, e. g. the BIFROST project. In this study, we use palaeo-shoreline data from Scandinavia, the Barents Sea, and northwestern Europe as well as radial crustal velocities from the BIFROST campaign to infer the radial viscosity structure of the Earth’s mantle underneath Scandinavia and northwestern Europe. A global inverse procedure based on the Neighbourhood Algorithm allows us to explore the hypothesis of a low-viscosity zone in the upper mantle, which has been proposed in the literature. Our results indicate a low-viscosity zone underneath the Barents Sea, with viscosities between 10^{19} - 10^{20} Pa s in a depth interval of 160 - 200 km. No such low-viscosity zone is found underneath Scandinavia, and no clear indication for such a zone underneath northwestern Europe. The thickness of the rheological lithosphere increases from 60 - 70 km underneath the northwestern Europe and the Barents Sea towards values exceeding 120 km underneath Scandinavia.

---

[a] Steffen and Kaufmann (2006). Glacial isostatic adjustment of Scandinavia and northwestern Europe and the radial viscosity structure of the Earth’s mantle, Geophys. J. Int. 163/2, 801-812.

2.1 Introduction

During the Quaternary period, surface temperatures on the Earth have repeatedly dropped by more than 10°C. These palaeo-climatic variations have induced the growth of large ice sheets over North America and Europe. The interior of the Earth has responded to the additional weight of these palaeo-ice sheets by adjusting its shape: During the build-up of ice sheets the surface was depressed by several hundreds of metres, during the melting phase the surface rebounded to its initial state. The viscoelastic nature of this process, termed *glacial isostatic adjustment* (GIA), causes a time delay between the removal of the last palaeo-ice sheets and the deformation of the solid surface.

In Scandinavia and northwestern (NW) Europe, where the large Weichselian Ice Sheet complex was located during the last glacial cycle, the GIA process was recognised early as being responsible for numerous field observations [see Ekman, 1991, for a review]. The good geological record of the crustal response in Scandinavia, documented in various observations such as palaeo-shorelines (relative sea levels, RSL), shoreline tilting, and the present-day crustal motion, together with a reasonable knowledge of the ice-sheet retreat since the *last glacial maximum* (LGM), allow to construct a detailed model of sea-level change induced by the mass redistribution between ice sheets and the ocean.

In the past decade, numerical models of the GIA based on Scandinavian and NW European observational data have converged towards a radial viscosity structure, with viscosities increasing by one to two orders of magnitude with depth. The use of linear rheological laws for the Earth's mantle has been shown to be both an adequate and consistent description for deformations on the time scale of 10^2 to 10^7 years. Some representative examples for the interpretation of observational data for the Scandinavian and NW European regions will be discussed below.

Palaeo-shoreline data: Based on palaeo-shoreline data from the British Isles, Lambeck [1993a,b] has derived a simple radial viscosity profile, with viscosities increasing from $(4 - 5) \times 10^{20}$ Pa s in the upper mantle to 10^{22} Pa s in the lower mantle. Lambeck et al. [1996] have extended the interpretation of the British Isles data and concluded that the upper-mantle viscosity can be refined further, with viscosities ranging from 10^{20} Pa s for the low-velocity zone beneath the lithosphere to 10^{21} Pa s in the transition zone. In these studies, the lithospheric thickness best fitting the observations was around 70 km.

Using observational data from Northern Europe, Lambeck et al. [1998a] found a similar best-fitting viscosity structure, with lithospheric thickness values around 70 - 80 km, an upper-mantle viscosity around $(3 - 4) \times 10^{20}$ Pa s, and lower-mantle viscosity at least one order of magnitude larger.

Kaufmann and Lambeck [2002] improved mantle viscosity inferences for this region through the application of a formal inverse procedure to data sets of palaeo-shorelines, present-day sea level and crustal response, and rotational data. The mantle viscosity profiles found are characterised by a two order of magnitude variation with depth. Upper-mantle viscosity increases from 2×10^{20} below the lithosphere to around 10^{21} Pa s towards the 660-km seismic discontinuity. The rebound-related observations cannot distinguish between a sharp increase of viscosity between the upper and lower mantle, or a more gradual variation. The viscosity in the lower mantle is generally one order of magnitude larger, with peak values close to 10^{23} Pa s in around 1000 km depth.

Relaxation-time spectra: If high-quality palaeo-shoreline data exist – as in Scandinavia – spatially continuous palaeo-shoreline profiles may be constructed and an inverse relaxation-time spectrum (IRTS) be derived. The IRTS is based on the assumption of a free relaxation of the surface after the deglaciation event was completed. Using such a dataset, Wieczerkowski et al. [1999] inferred an average viscosity of the upper mantle beneath central Scandinavia of 5×10^{20} Pa s (between 95 and 515 km depth). The permitted lithospheric thickness values range between 70 and 120 km. Fleming et al. [2003] extended this interpretation by allowing the lithosphere to be viscoelastic, but they obtained similar viscosities for the upper mantle. Klemann and Wolf [2005] added two new shoreline diagrams to the dataset and obtained an upper-mantle viscosity of 5×10^{20} Pa s and a – poorly resolved – lower-mantle viscosity of 2.4×10^{21} Pa s.

Present-day crustal motions: The ongoing improvement of space-geodetic observations such as the global positioning system (GPS) allows a fairly accurate measurement of present-day crustal motions. The BIFROST project [Johansson et al., 2002] has recorded the three-dimensional crustal motion of Scandinavia over a period of seven years. Based on this dataset, Milne et al. [2001, 2004] have derived a radial viscosity profile with permitted lithospheric thickness values between 90 and 170 km, upper-mantle viscosities in the range of $(5 - 10) \times 10^{20}$ Pa s, and lower-mantle viscosities in the range of $(0.5 - 5) \times 10^{22}$ Pa s.

Low-viscosity asthenosphere: In all of the examples quoted above, no particular attempt was made to resolve a *low-viscosity asthenosphere* underneath the elastic lithosphere. While the simple three-layer viscosity models [e.g. Lambeck, 1993a,b; Lambeck et al., 1998a; Wieczerkowski et al., 1999; Fleming et al., 2003] did not account for such a possibility, the more detailed viscosity profiles resulting from formal inverse procedures [e.g. Kaufmann and Lambeck, 2002; Milne et al., 2004] also found no evidence for a low-viscosity asthenosphere. There are, however, a number of publications, which have modelled the GIA of Scandinavia (mostly with flat geometries), and which favour a viscosity profile including a low-viscosity asthenosphere. Early results on the *asthenosphere problem* include a 100 km thick asthenosphere with 1.3×10^{19} Pa s [van Bemmelen and Berlage, 1935], a 200 km thick asthenosphere with 10^{20} Pa s [McConnell, 1968], a 75 km thick asthenosphere with 4×10^{19} Pa s [Cathles, 1975], and a 100 km thick asthenosphere with 1.2×10^{19} Pa s [Wolf, 1987]. Later on, Fjeldskaar [1994, 1997] used both present-day crustal motion data and palaeo-shoreline data from the Scandinavian region to infer the rheological layering of the Earth's mantle, using a GIA model. He strongly advocated the presence of a low-viscosity asthenosphere, at most 150 km thick and with a viscosity around 7×10^{19} Pa s.

Further evidence of a weak asthenospheric layer offshore Western Europe comes from seismic tomographical imaging [e.g. Su and Dziewonski, 1991; Li and Romanowicz, 1996; Romanowicz, 1998; Ekström and Dziewonski, 1998]. Here, the shear-wave velocity anomalies underneath the Atlantic and western Scandinavia indicate lower than average velocities underneath the ocean, while central Scandinavia is characterised by higher than average shear-wave velocities [Ekström and Dziewonski, 1998]. Relating the shear-wave velocity perturbations to density variations, which in turn are (at least partially) related to temperature variations [e.g. Ivins and Sammis, 1995], the seismic velocities down to 400 km depth clearly reveal the cold, more viscous mantle material of the Baltic Shield, and a warmer, less viscous region offshore the Scandinavian West Coast, possibly correlated to the Mid-Atlantic Ridge.

The effect of such a three-dimensional viscosity structure on models of GIA has been discussed in the literature [e.g. Kaufmann and Lambeck, 2000; Kaufmann and Wu, 2002]. It has been shown that lateral variations in lithospheric thickness and in asthenospheric viscosity do influence model predictions of palaeo-shorelines and crustal motions. However, Martinec and Wolf [2005] have shown that a two-dimensional earth model for Scandinavia with a central 200 km thick lithosphere underneath the Gulf of Bothnia and a peripheral 80 km thick lithosphere underlain by a 100 km thick asthenosphere with 8×10^{18} Pa s essentially results in the same IRTS for central Scandinavia as a one-dimensional viscosity profile with a 100 km thick lithosphere and no asthenosphere. Hence, they found no strong evidence for a weak asthenosphere.

In this paper we return to the question of a weak asthenosphere underneath Scandinavia and NW Europe. Therefore sea-level data from Scandinavia, the Barents Sea, the North Sea, the British Isles and the Atlantic and English Channel coasts were collected. The global ice model RSES (developed by Kurt Lambeck from the Research School of Earth Sciences, Canberra, Australia) was used to predict GIA and then predictions are compared to the observed data. For the subregions Scandinavia, NW Europe, and the Barents Sea, we determine the best simple (three-layer) viscosity profile for each region, then a global inverse procedure is employed to further refine the viscosity profile in the upper mantle.

2.2 Theory

The results presented in this paper are based on model predictions for a spherically symmetric, compressible, Maxwell-viscoelastic earth model. The elastic structure is derived from PREM [Dziewonski and Anderson, 1981], and lithospheric thickness is a free parameter. Mantle viscosity is parameterised in several sub-lithospheric layers with constant viscosity within each layer. The Earth's core is assumed to be inviscid, and incorporated as lower boundary condition.

We solve the sea-level equation [Farrell and Clark, 1976] for a rotating Earth given by

$$W(\theta,\varphi,t) = C(\theta,\varphi,t)\,[G(\theta,\varphi,t) - R(\theta,\varphi,t)]\,. \tag{2.1}$$

In (2.1), θ and φ are co-latitude and eastern longitude, t is time, $W(\theta,\varphi,t)$ is the ocean load thickness, $G(\theta,\varphi,t)$ and $R(\theta,\varphi,t)$ are response functions of the geoidal and the radial surface displacements [for details see Kaufmann and Lambeck, 2002], and $C(\theta,\varphi,t)$ is the time-dependent ocean function [Munk and MacDonald, 1960], equalling one over oceanic areas and zero elsewhere. The sea-level equation can be rewritten as an integral equation, which we solve iteratively. Once we have determined the ocean load thickness W, we derive several quantities of interest, such as relative sea-level change, present-day surface motions, time-dependent perturbations of the gravitational field, and rotational contributions from the ice-ocean imbalance. We follow the pseudo-spectral approach outlined in Mitrovica et al. [1994] and Mitrovica and Milne [1998], using an iterative procedure in the spectral domain, and a spherical harmonic expansion truncated at degree 192. The calculated quantities are then compared to observational data.

2.3 Ice and ocean models

The surface load comprises two contributions: The Late Pleistocene ice sheet thickness, $I(\theta,\varphi,t)$, and the corresponding ocean load thickness, $W(\theta,\varphi,t)$. Introducing the densities of ice and water, ρ_I and ρ_W, we find the surface load density:

$$L(\theta,\varphi,t) = \rho_I I(\theta,\varphi,t) + \rho_W W(\theta,\varphi,t). \tag{2.2}$$

For the Late Pleistocene glacial history, the ice model RSES is used. RSES is a global ice model comprising Late Pleistocene ice sheets over North America, North Europe, Greenland, the British Isles, and Antarctica. The extent and the melting history follow model ICE-1 [Peltier and Andrews, 1976] for the Laurentide Ice Sheet and Greenland, model FBKS8 [Lambeck et al., 1998a] for the Scandinavian and Barents Sea Ice Sheets, model BK4 [Lambeck, 1993b] for the British Ice Sheet, and model ANT3 [Nakada and Lambeck, 1988] for the Antarctic Ice Sheet. All reconstructions are based on glaciological and geomorphological evidence and thus reflect the approximate extent of the Late Pleistocene Ice Sheets throughout the last glacial cycle. Of these ice sheets only the Scandinavian, Barents Sea and British Isles ice sheets are high spatial and temporal resolution models that are consistent with the majority of the field evidence for ice-margin retreat and with the rebound data. The Antarctic and Laurentide ice sheets are both of a coarser resolution, which, however, is of secondary importance for our regional study. All ice sheet models have been converted from the radiocarbon timescale to the U/Th timescale, using the CALIB-4 program [Stuiver and Reimer, 1993; Stuiver et al., 1998]. The ice volume at the LGM approximately 21,400 years BP corresponds to 124 m of eustatic sea-level change, and the extent for four different times is shown in Fig. 2.1. We simulate the time-dependence of the ice sheets throughout the Late Pleistocene glacial cycles by modelling the last two cycles with linear changes in ice load thickness

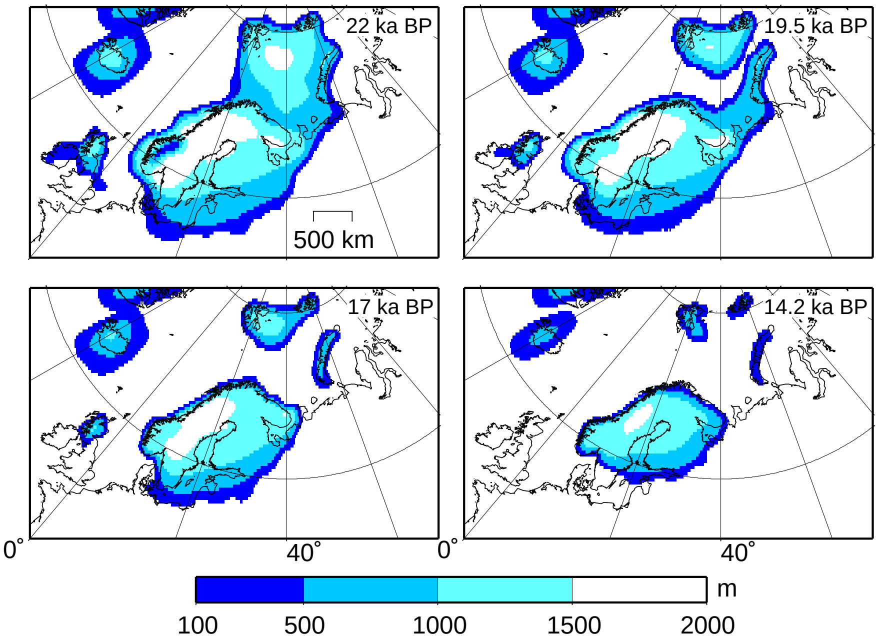

Figure 2.1: Map of ice model RSES over Europe for four different time epochs. Contours are drawn every 500 m.

approximating the oxygen isotope data record [Chappell and Shackleton, 1986] and by assuming a time-averaged ice load before that time. This parameterisation of the last glacial cycles has been shown to be sufficient to correctly predict changes in the Earth's gravitational field and rotation, as well as surface displacements [Johnston and Lambeck, 1999]. For the deglaciation following the LGM, the more detailed ice load thickness maps are used.

2.4 Observational data

For our analysis, we have chosen observed sea-level indicators from Scandinavia (569), the Barents Sea (264), and NW Europe (487) sampling the near field of the Weichselian Ice Sheet fairly evenly (Fig. 2.2). The Barents Sea data (circles) are based on several studies and were summarised in Kaufmann and Wolf [1996]. NW Europe data (squares) are taken from Lambeck [1993a,b]. The Scandinavian observations (triangles for central locations and inverse triangles for peripheral locations) are summarised in Lambeck et al. [1998a]. The data are based on faunal assemblages and preservation status of sediments. Radiocarbon dating was used and converted to U/Th-times.

The RSL data reflect the complicated three-dimensional response of the solid Earth to changes in the ice and ocean load and thus are reliable constraints for mantle viscosity models. The spatial and temporal distribution of the RSL data can be seen in Fig. 2.3: The Scandinavian RSL data cover a broad range from present-day sea level to more than 250 m height, while reaching back to around 15,000 years, with isolated data even marking the LGM. The deformation process of the solid Earth is therefore documented over a wide spatio-temporal range. The NW Europe RSL data are much smaller in amplitude, reaching only heights around 60 m. A significant part of the data is submerged down to 50 m depth, documenting a significant contribution from sea-level rise. The temporal distribution covers the last 18,000 years. The

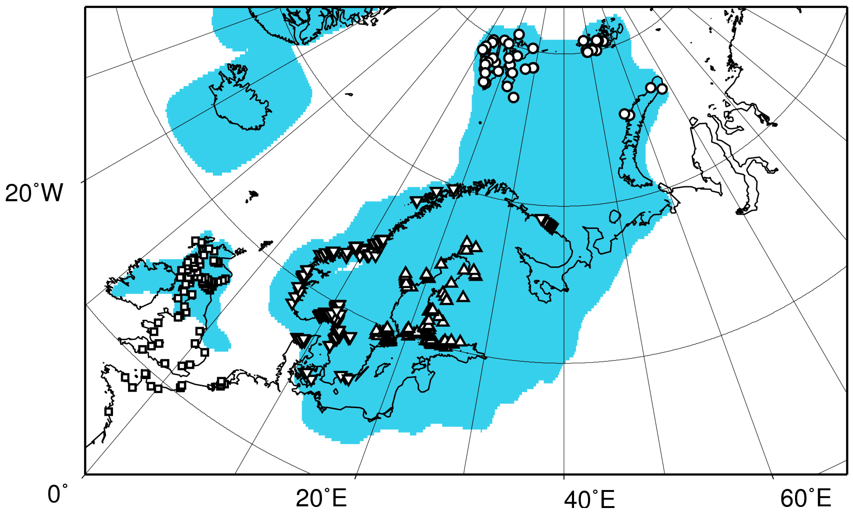

Figure 2.2: Map of Europe, with ice margins at last glacial maximum superimposed in blue. Locations for RSL data are shown as symbols for Scandinavia (569 triangles, triangles for central, inverted triangles for peripheral regions), the Barents Sea (264 circles), and the NW Europe (487 squares).

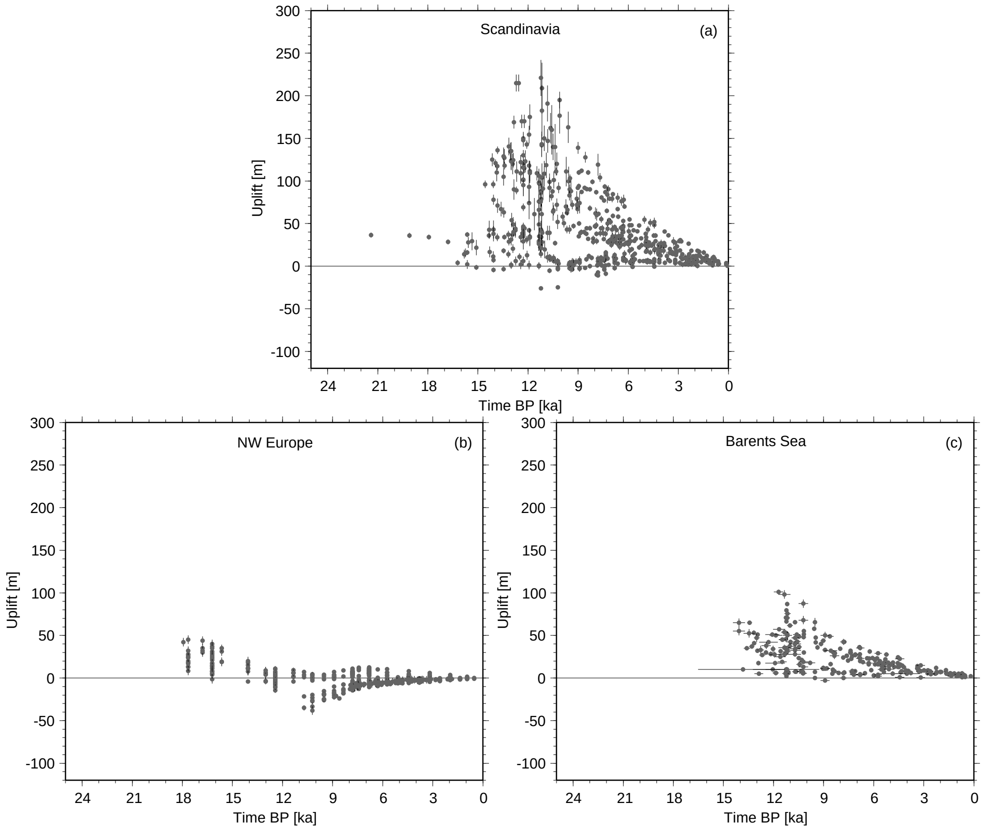

Figure 2.3: Summary of RSL datasets. Dots are observations, bars the uncertainties of the data. (a) Scandinavian RSL data, (b) NW European RSL data, (c) Barents Sea RSL data.

Barents Sea RSL data are restricted to land uplift, with amplitudes up to 120 m. However, the temporal distribution is more limited, reaching 14,000 years back in time.

In addition to the sea-level indicators we use the vertical velocities determined by the BIFROST project [Johansson et al., 2002].

2.5 Results

In this section, we present model predictions of RSL changes and we compare the predictions to the three subsets of RSL data from Scandinavia, NW Europe, and the Barents Sea. The comparison of model predictions and data is based on a least-squares misfit, defined as

$$\chi = \sqrt{\frac{1}{n}\sum_{i=1}^{n}\left(\frac{o_i - p_i(a_j)}{\Delta o_i}\right)^2}, \tag{2.3}$$

with n the number of observations considered, o_i the observed RSL or BIFROST data, $p_i(a_j)$ the predicted RSL for a specific earth model a_j, and Δo_i the data uncertainties. We search for the minimum value of χ within the parameter range, which gives us an earth model a_b, fitting the observational dataset best. If the model is complete and the observational uncertainties are normally distributed with known standard deviations and uncorrelated, the expected best fit would be $\chi = 1$. To bracket all earth models, which fit the observational data equally well as the best-fitting earth model a_b within the observational uncertainties, a confidence parameter is calculated:

$$\Psi = \sqrt{\frac{1}{n}\sum_{i=1}^{n}\left(\frac{p_i(a_b) - p_i(a_j)}{\Delta o_i}\right)^2}. \tag{2.4}$$

For all confidence parameters $\Psi \leq 1$, the prediction $p_i(a_j)$ fits the data as well as the best-fitting model $p_i(a_b)$ within the 1σ-uncertainty.

2.5.1 Three-layer models

We start discussing our results with a parameter search through the three-dimensional parameter space lithospheric thickness H_l, upper-mantle viscosity η_{UM}, lower-mantle viscosity η_{LM} for the three-layer earth models. Elastic parameters are assigned from PREM [Dziewonski and Anderson, 1981], and the parameter space of the free parameters is listed in Tab. 2.1. The total number of earth models calculated is 1089.

Scandinavia: In Fig. 2.4a and b, the misfit values based on the Scandinavian RSL data are shown as misfit maps of the parameter space. The best-fitting three-layer earth model found has a fairly thick lithosphere of $H_l = 120$ km, an upper-mantle viscosity of $\eta_{UM} = 4 \times 10^{20}$ Pa s, and a lower-mantle viscosity of $\eta_{LM} = 10^{23}$ Pa s. The misfit for this model is $\chi = 2.71$. While the upper-mantle viscosity is well constrained ($\eta_{UM} \in [3,5] \times 10^{20}$ Pa s), the predictions are largely insensitive to the lithospheric thickness over a large range of parameter values ($H_l \in [100,140]$ km), as it can be seen by the large confidence regions in Fig. 2.4a. Similarly, the RSL data from Scandinavia are not very sensitive to lower-mantle viscosity, as the confidence region in Fig. 2.4b covers a range from $\eta_{LM} \in [3 \times 10^{22}, 10^{23}]$ Pa s. The estimate of the upper-mantle viscosity found agrees with previous studies, e.g. the inference from Lambeck et al. [1998a,b] of $\eta_{UM} = 4 \times 10^{20}$ Pa s based on Scandinavian RSL data, the $\eta_{UM} = 5 \times$

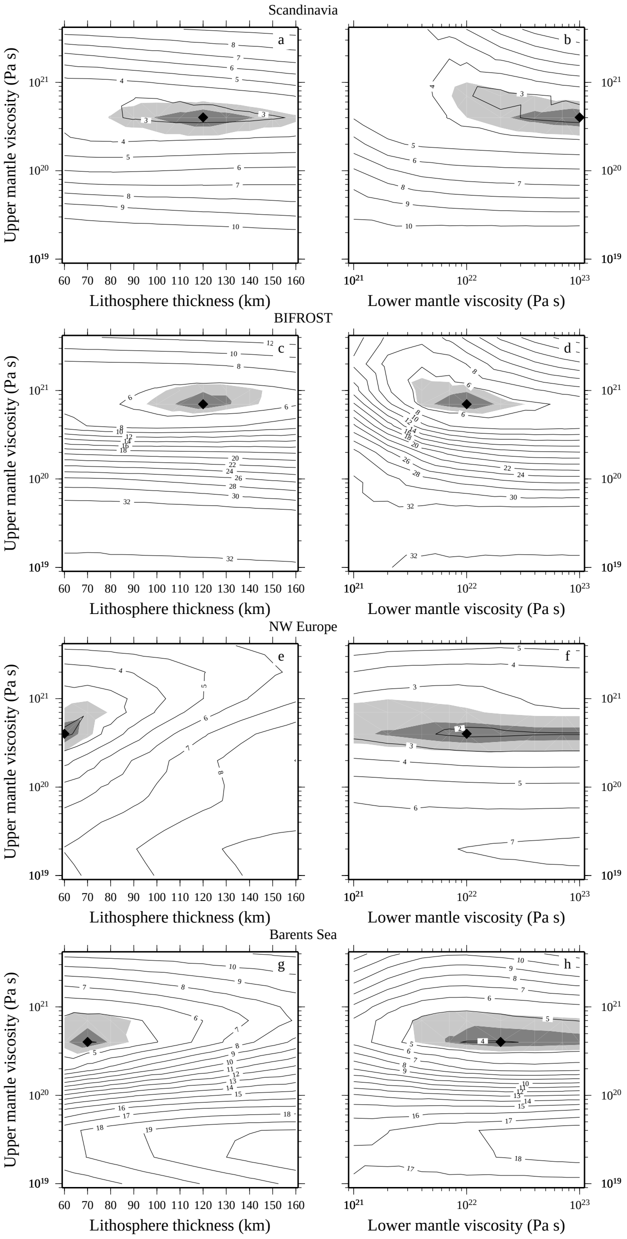

Figure 2.4: Misfit for ice model RSES, three-layer earth model and different data sets: (a) Misfit map for Scandinavian RSL data as a function of lithospheric thickness and upper-mantle viscosity for a fixed lower-mantle viscosity of 10^{23} Pa s. (b) Misfit map for Scandinavian RSL data as a function of upper and lower-mantle viscosities for a fixed lithospheric thickness of 120 km. (c) Misfit map for the BIFROST data as a function of lithospheric thickness and upper-mantle viscosity for a fixed lower-mantle viscosity of 10^{22} Pa s. (d) Misfit map for the BIFROST data as a function of upper and lower-mantle viscosities for a fixed lithospheric thickness of 120 km. (e) Misfit map for the NW European RSL data as a function of lithospheric thickness and upper-mantle viscosity for a fixed lower-mantle viscosity of 10^{22} Pa s. (f) Misfit map for the NW European RSL data as a function of upper and lower-mantle viscosities for a fixed lithospheric thickness of 60 km. (g) Misfit map for the Barents Sea RSL data as a function of lithospheric thickness and upper-mantle viscosity for a fixed lower-mantle viscosity of 2×10^{22} Pa s. (h) Misfit map for the Barents Sea RSL data as a function of upper and lower-mantle viscosities for a fixed lithospheric thickness of 70 km. The best 3-layer earth model is marked with a diamond, the light and dark shadings indicate the confidence regions $\Psi \leq 1$ and $1 < \Psi \leq 2$, respectively.

10^{20} Pa s estimate from Wieczerkowski et al. [1999] and Klemann and Wolf [2005] based on the IRTS of Scandinavia, the value of $\eta_{UM} \in [5 \times 10^{20}, 10^{21}]$ Pa s from Milne et al. [2004], based on the BIFROST crustal motion data, and the results from Martinec and Wolf [2005] in the range of $(4$ - $6) \times 10^{20}$ Pa s based on the IRTS including a lithospheric root. The estimate for the lithospheric thickness is at the upper limit of previous estimates, but viewed in the light of the larger permitted range of lithospheric thickness values, the best model is satisfactory. The low resolving power for lower-mantle viscosity also agrees well with the estimated depth resolution of the Scandinavian RSL data, which according to Mitrovica [1996] is limited to the upper 1000 - 1400 km of the Earth's mantle.

We have subdivided the Scandinavian RSL dataset further into *central* locations close to the former ice sheet centre (triangles in Fig. 2.2), and *peripheral* locations around the coastal areas (inverted triangles in Fig. 2.2). With this subdivision we have tested for different best lithospheric thickness estimates in these different regions. As it can be seen in Tab. 2.1, the RSL data from the central region prefer a thick lithosphere ($H_l = 160$ km), while the peripheral RSL data result in a thinner lithosphere ($H_l = 100$ km). The different lithospheric thickness estimates correlate with the seismic observation of a thick cratonic root underneath central Scandinavia [e.g. Panza et al., 1980; Calcagnile, 1982; Goes and Govers, 2000]. The permitted ranges for the lithospheric thickness values, $H_l \in [140, 160]$ km for the central and $H_l \in [80, 120]$ km for the peripheral regions, indicate that the distinction of different lithospheric thickness estimates is significant.

In Fig. 2.4c and d, the misfit values based on the data of vertical crustal motion of Scandinavia (BIFROST project) are shown. The best-fitting three-layer earth model found has a lithospheric thickness of $H_l = 120$ km, and upper- and lower-mantle viscosities of $\eta_{UM} = 7 \times 10^{20}$ Pa s and $\eta_{LM} = 1 \times 10^{22}$ Pa s, respectively. The misfit for this model is $\chi = 4.59$. The upper mantle is well constrained ($\eta_{UM} \in [6, 9] \times 10^{20}$ Pa s), while the lithosphere in Fig. 2.4c can be predicted within a tight range of parameter values ($H_l \in [110, 130]$ km). The lower mantle confidence region in Fig. 2.4d covers a range from $\eta_{LM} \in [5 \times 10^{21}, 2 \times 10^{22}]$ Pa s. These values agree well with the earlier results of Milne et al. [2001, 2004]. We have not subdivided the BIFROST data into central and peripheral locations, as the are practically no data along the periphery (Norwegian Coast).

NW Europe: In Fig. 2.4e and f, the misfit values based on the British Isles and Central European RSL data are shown. The best-fitting three-layer earth model for this data subset is characterised by a lithospheric thickness of $H_l = 60$ km, and upper- and lower-mantle viscosities of $\eta_{UM} = 4 \times 10^{20}$ and $\eta_{LM} = 10^{22}$ Pa s, respectively. The misfit for this model is $\chi = 1.81$. All values agree well with the earlier inference of the British Isles RSL data from Lambeck [1993a,b]. While the large confidence range for the lower-mantle viscosity ($\eta_{LM} \in [2 \times 10^{21}, 10^{23}]$ Pa s) again confirms the poor resolving power of the NW European RSL data for larger mantle depths, the lithospheric thickness is better constrained, with permissible ranges limited to $H_l \in [60, 70]$ km.

Barents Sea: In Fig. 2.4g and h, the misfit values based on the Barents Sea palaeo-shoreline data are shown. The best-fitting three-layer earth model for this data subset is characterised by a lithospheric thickness of $H_l = 70$ km, and upper- and lower-mantle viscosities of $\eta_{UM} = 4 \times 10^{20}$ and $\eta_{LM} = 2 \times 10^{22}$ Pa s, respectively. However, the misfit for this model is $\chi = 3.96$, which is significantly worse than for the previous datasets for Scandinavia and the British Isles. This might be a result of the less reliable ice-sheet reconstruction over this region, or of an inadequate earth model. Again, lower-mantle viscosity is almost unconstrained, while the range of permitted lithospheric thickness values is $H_l \in [65, 75]$ km.

Tab. 2.1 summarises the results discussed above. Here, upper-mantle viscosities for all regions are around 4×10^{20} Pa s, and cover a range between $\eta_{UM} \in [3 \times 10^{20}, 5 \times 10^{20}]$ Pa s. Compared to the results of Kaufmann & Amelung [2000] with upper-mantle viscosities of $(2$ - $5) \times 10^{20}$ Pa s, we find a good

Table 2.1: Three-layer earth models. Free parameters are lithospheric thickness H_l, upper-mantle viscosity η_{UM}, lower-mantle viscosity η_{LM}. χ_{three} is the misfit for the best 3-layer earth model. Results for the three-layer earth models fitting the data within the 1σ-uncertainty range are shown for the different data sets, with the best-fitting earth model in brackets.

	H_l km	η_{UM} 10^{20} Pa s	η_{LM} 10^{22} Pa s	χ_{three}
Search range	60-160	0.1-40	0.1-10	
Dataset		RSES		
Scandinavia	100-140 (120)	3-5 (4)	3-10 (10)	2.71
central	140-160 (160)	3-5 (4)	2-10 (10)	1.94
peripheral	80-120 (100)	5-10 (7)	2-10 (7)	2.60
NW Europe	60-70 (60)	3-6 (4)	0.2-10 (1)	1.81
Barents Sea	65-75 (70)	3-6 (4)	0.7-10 (2)	3.96
BIFROST	110-130 (120)	6-9 (7)	0.5-2 (1)	4.59

agreement. The lower-mantle viscosity is almost unconstrained, confirming the low resolving power for lower-mantle viscosity of the Scandinavian RSL data [see Mitrovica, 1996, for more information]. The thickness of the lithosphere indicates a lithospheric root (160 km thick) under the Archean crust of Scandinavia, decreasing towards the Mid Ocean Ridges in the Atlantic and Arctic Ocean. Here, the lithosphere has a thickness of 60 km under the British Isles and 70 km under the Barents Sea.

2.5.2 Multi-layer models

Next, we try to assess the potential of the datasets to resolve more structure in the Earth's mantle. Our aim is to search for a possible low-viscosity zone in the uppermost mantle, as proposed, for example, by Fjeldskaar [1994, 1997] for the Scandinavian region. Therefore, we refine our radial viscosity structure in the upper mantle as follows: We first assign a thickness of 60 km for the first layer, representing the elastic lithosphere, which is in agreement with the results for the NW European and Barents Sea RSL data. The rest of the upper mantle is subdivided into five layers with viscosities $\eta_{UMi}, i = 1,5$. The thickness values of these layers are: $H_{UM1} = 60$ km, $H_{UM2} = 40$ km, $H_{UM3} = 40$ km, $H_{UM4} = 230$ km, $H_{UM5} = 230$ km. The lower mantle remains uniform, stretching from the 660 km seismic discontinuity to the core-mantle boundary, with a viscosity fixed to the best-fitting result from the three-layer model for each data set. This choice of refinement is guided by the three-layer earth models, which have shown the poor resolving power of the RSL data for lower-mantle structure.

Simple forward search in the parameter space, as done in the three-layer earth model cases, is no longer suitable for the proposed multi-layer earth models. In the past, more detailed radial viscosity structures derived from GIA-related observations have been performed by formal inverse procedures, such as Tarantola-Valette inverse procedures [e. g. Kaufmann and Lambeck, 2002] or Bayesian inverse procedures [e. g. Forte and Mitrovica, 1996; Mitrovica and Forte, 1997; Peltier, 1998; Milne et al., 2004]. These methods are all based on a linearisation of the non-linear inverse problem of mantle viscosity, and thus depend on an a-priori viscosity profile as a starting model. Usually, such an a-priori profile was based on a simpler three-layer earth model. However, the resulting inverse inference of the more detailed viscosity profile, though having a more detailed depth resolution, critically depends on the a priori starting model [see Kaufmann and Lambeck, 2002, for a detailed investigation of this dependence].

In this paper, we have chosen a different approach, using a global-search inverse procedure based on the Neighbourhood Algorithm (NA). The Neighbourhood algorithm introduced by Sambridge [1999a,b] is a direct search method for non-linear inverse problems. The NA method is applicable to a wide range of inversion problems, particularly those with rather complex dependencies between data and model. During the search stage of the NA method, a multidimensional parameter space is sampled for combinations of model parameters, which provide a satisfactory fit to the observed data. The search is guided by randomised decisions similar to techniques used for genetic algorithms (GA) and simulated annealing (SA), but the NA method needs only two control parameters. A misfit between model prediction and observation is calculated, and the search is driven towards the minimum misfit within the parameter space. The NA method is based on the geometrical concept of Voronoi cells. These Voronoi cells are nearest-neighbour regions around each sampling point. The Voronoi cells are used to guide the sampling. Further details can be found in Sambridge [1998, 2001].

The NA method is run in several steps:

1. We initialise the NA search for one RSL dataset o_i with an initial set of $n_{si} = 1000$ models, generated randomly within the 5D parameter space of upper-mantle viscosities. The search range for all upper-mantle viscosity layers is η_{UM1} - $\eta_{UM5} \in [10^{19}, 10^{22}]$ Pa s. For each of these n_{si} forward models, the misfit function (2.3) is then calculated.

2. We then use the $n_r = 10$ best-fitting models of the initial ensemble, define Voronoi cells around each of the n_r samples, and place $n_s = 20$ new models within these n_r cells (that is n_s/n_r new models in each cell).

3. For the n_s new models, the misfit function is evaluated, and the algorithm returns to step 2. Steps 2 and 3 are repeated $N = 25$ times, resulting in a total of $n_{si} + N \times n_s = 1500$ model predictions for each data set.

An example of the misfit reduction is shown in Fig. 2.5. Here, the $n_{si} = 1000$ initial samples result in a misfit around $\chi \sim 8$. Then, the NA method starts refining the regions of lowest misfit, and misfit values drop significantly over the next N iterations. The rough misfit curve indicates the resampling of the $n_r = 10$ best cells at a given iteration step, hence in between misfits might increase, but then the NA method leaves this local minimum in misfit, and continues to trace the best global minimum within the parameter range.

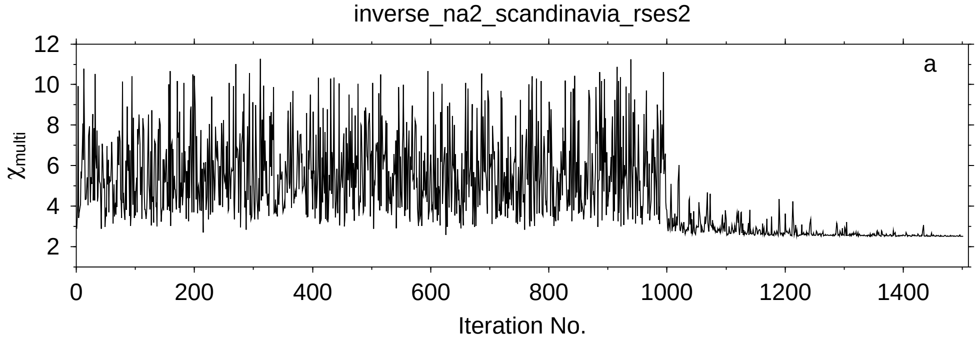

Figure 2.5: Misfit χ_{multi} as a function of the iteration counter.

In Fig. 2.6a, the best-fitting multi-layer viscosity profile based on the Scandinavian RSL dataset is shown as black line. Also shown as grey lines are all multi-layer viscosity profiles, which fit the RSL data equally well within the 1σ-uncertainty, based on the confidence parameter (2.4). Misfit values have dropped from an initial value of $\chi_{three} = 2.71$ to a final value of $\chi_{multi} = 2.51$, an improvement of only 8 percent. Two points are obvious: Firstly, the relatively high viscosity in the first layer ($\eta_{UM1} \in [2 \times 10^{21}, 10^{22}]$ Pa s) tries to rebuild the lower part of the elastic lithosphere, which was found previously by the three-layer model. Secondly, viscosities in the other four layers are only determined to within half to one order of magnitude. For the second and third layer, the possible asthenosphere, valid viscosities are $\eta_{UM2} \in [1 \times 10^{20}, 4 \times 10^{21}]$ Pa s and $\eta_{UM3} \in [8 \times 10^{19}, 2 \times 10^{21}]$ Pa s. Thus, no indication for a low-viscosity asthenosphere is found. For the two lowermost layers, permitted viscosities are $\eta_{UM4} \in [5 \times 10^{19}, 2 \times 10^{20}]$ Pa s and $\eta_{UM5} \in [2 \times 10^{21}, 1 \times 10^{22}]$ Pa s. Hence, only the fourth layer, below a depth of 200 km, is characterised by a viscosity around 10^{20} Pa s.

We also performed a NA inversion for the BIFROST uplift data. In Fig. 2.6b, the best-fitting multi-layer viscosity profile based on the BIFROST dataset is shown as black line. Here, the misfit is reduced by 12 percent from $\chi_{three} = 4.59$ to $\chi_{multi} = 4.06$. Both viscosities in the first and second layer are acceptable to within one order of magnitude: $\eta_{UM1} \in [2 \times 10^{19}, 4 \times 10^{20}]$ Pa s and $\eta_{UM2} \in [2 \times 10^{19}, 2 \times 10^{20}]$ Pa s. Interestingly, the best-fitting viscosity profile from the BIFROST data indicates a fairly low-viscosity of 2×10^{19} Pa s in the region between 160 and 200 km depth. However, acceptable viscosities for this depth range spread over a large range: $\eta_{UM3} \in [1 \times 10^{19}, 1 \times 10^{22}]$ Pa s. A similar feature has also been found by Milne et al. [2004] in their Bayesian inversion, and the authors also claim that their thin low-viscosity zone is also not resolvable by the BIFROST data. In the remaining upper mantle, the viscosity profile is not too different from the one found from the Scandinavian RSL data (Fig. 2.6a).

In Fig. 2.6c, the best-fitting multi-layer viscosity profile based on the NW European RSL dataset is shown as black line. Misfit values have dropped from an initial value of $\chi_{three} = 1.81$ to a final value of $\chi_{multi} = 1.60$, an improvement of around 12 percent. However, the permitted viscosity profiles vary over a large range throughout the entire upper mantle (see Tab. 2.2), indicating the poor resolving power of the NW European RSL data for more structure in the upper mantle. In a further test, we have excluded most of the submerged RSL data points from the NW European dataset, as they are dominated by the signal of sea-level rise. However, searching the 5D-parameter space of upper-mantle viscosities for the reduced dataset results in an almost identical set of viscosity profiles as shown in Fig. 2.6c. Thus we argue that the small spatial amplitudes of the NW European RSL data as shown in Fig. 2.3b do not provide more detailed information of the upper mantle viscosity structure.

In Fig. 2.6e, the best-fitting multi-layer viscosity profile based on the Barents Sea RSL dataset is shown as black line. Misfit values have dropped from an initial value of $\chi_{three} = 3.96$ to a final value of $\chi_{multi} = 2.68$, an improvement of more than 32 percent. Here, viscosities between 120 and 200 km depth indicate a low-viscosity asthenosphere, with viscosities of $\eta_{UM2} \in [1 \times 10^{19}, 1 \times 10^{20}]$ Pa s and $\eta_{UM3} \in [1 \times 10^{19}, 1 \times 10^{20}]$ Pa s. However, the inversion provides an alternative viscosity profile with a low viscosity of $\eta_{UM1} = 3 \times 10^{19}$ Pa s directly beneath the 60 km thick lithosphere and a high viscosity of $\eta_{UM2} = 6 \times 10^{21}$ Pa s in the layer below. Thus, the location of the low-viscosity asthenosphere is not well determined. Below a depth of 200 km, viscosities are again similar to the inference based on the Scandiavian RSL data.

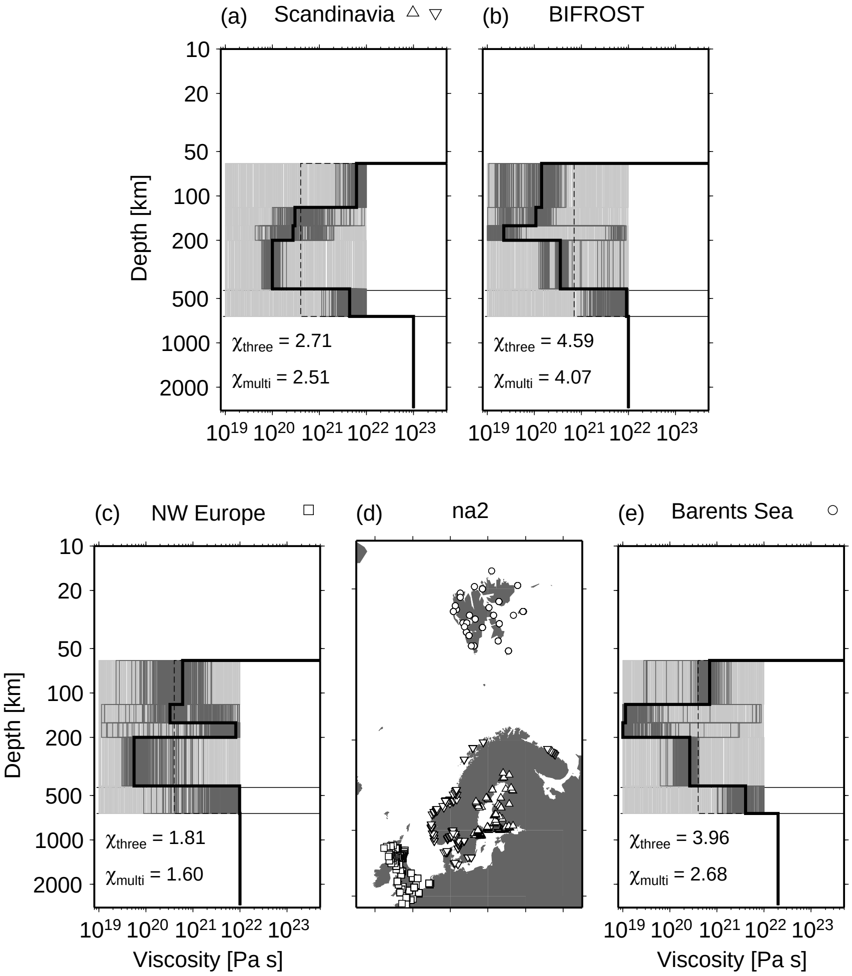

Figure 2.6: Best earth models from NA inversion for (a) the Scandinavian RSL data, (b) the BIFROST uplift data, (c) the NW European RSL data, and (e) the Barents Sea RSL data. RSL locations are marked by symbols and shown in the map (d). Shown are the best 3-layer viscosity profile (dashed line), the search range for all multi-layer viscosity profiles (light grey area), all multi-layer viscosity profiles acceptable within the 1σ-uncertainty range (dark grey lines), and the best multi-layer viscosity profile (solid line).

Table 2.2: Multi-layer earth models. Fixed parameters are lithospheric thickness ($H_l = 60$ km) and lower-mantle viscosity (η_{LM}, fixed to best three-layer inference). Free parameters are the upper-mantle viscosities $\eta_{UMi}, i = 1,5$. χ_{multi} is the misfit for the best multi-layer earth model. Results for the multi-layer earth models fitting the data within the 1σ-uncertainty range are shown for the different data sets, with the best-fitting earth model in brackets.

	η_{UM1} 10^{20} Pa s	η_{UM2} 10^{20} Pa s	η_{UM3} 10^{20} Pa s	η_{UM4} 10^{20} Pa s	η_{UM5} 10^{20} Pa s	χ_{multi}
Search range	0.1-100	0.1-100	0.1-100	0.1-100	0.1-100	
Dataset			RSES			
Scandinavia	20-100 (60)	1-40 (3)	0.8-20 (3)	0.5-2 (1)	20-100 (40)	2.51
NW Europe	0.8-20 (6)	1-100 (3)	1-100 (80)	0.3-10 (1)	2-100 (100)	1.60
Barents Sea	3-20 (7)	0.1-1 (0.1)	0.1-1 (0.1)	1-4 (3)	10-100 (40)	2.68
BIFROST	0.2-4 (1)	0.2-2 (1)	0.1-100 (0.2)	1-10 (4)	10-100 (90)	4.06

2.5.3 Comparison with sea-level observations

In Fig. 2.7, selected sea-level observations are visually compared to predictions of the best multi-layer model for the Barents Sea, the NW European and the Scandinavian region, respectively. The red points indicate observations, the blue line the predictions for the best Barents Sea region model, the green line the predictions for the best model of the NW European region and the grey line the results for the Scandinavian region with its best model. The best multi-layer prediction for the Barents Sea model acceptably fit the observations of the three locations on Svalbard in the Barents Sea (blue circle, triangle and square). On the other hand, differences up to 15 m can be found between predictions and observations for the best multi-layer NW European region model, resulting from differences in the upper-mantle structure. Differences of up to 40 m 11,000 years ago can be found for the best multi-layer Scandinavian region model, caused by a different mantle structure with no indication of a low-viscosity zone.

The observations of the two locations on the British Isles (green circle and triangle) are acceptably fitted with the predictions of the best multi-layer NW European region model. For observations of the location Aberystwyth an good agreement is obtained for the two other best region models, caused by its

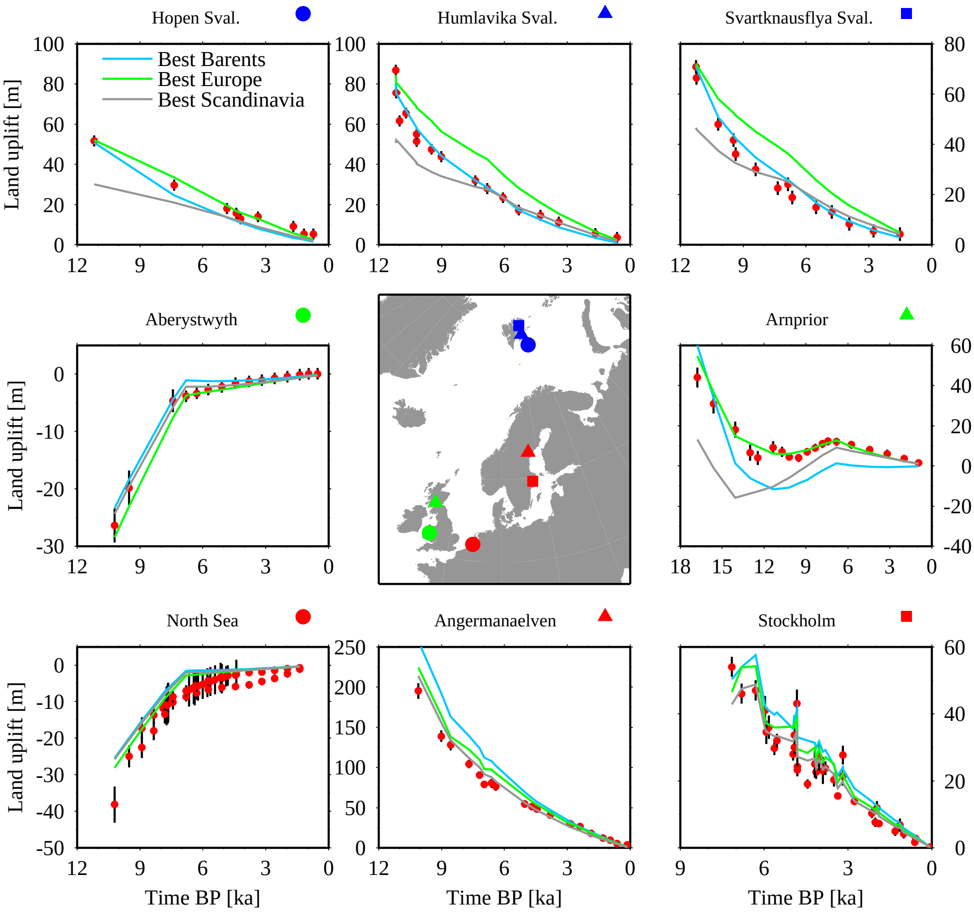

Figure 2.7: RSL observations (red dots with error bars) at selected locations on Europe compared with the predicted sea-level results from the best multi-layer model of the Barents Sea (blue lines), the NW European (green lines) and the Scandinavian region (grey lines). Symbols indicate the locations on the map.

distance to the former ice sheet. Here the eustatic sea-level change dominates the signal. In contrast, the observations of the location Arnprior show greater differences up to 60 m 17,000 years ago, a result of the different viscosity estimates.

The best multi-layer Scandinavian region model acceptably fits the observations of the two Swedish locations (red triangle and square). The two other best multi-layer models cause differences up to 50 m 10,000 years ago (see Ångermanaelven). Here, the best NW European model with no low-viscosity zone fits better than the best Barents Sea model including a low-viscosity zone.

No difference between the best region models can be found by comparison of observations of the North Sea location (red circle) with the results of the models. This is caused by the distance of this location to the former ice sheet, the eustatic sea-level change again controls the signal.

In Fig. 2.8, the radial component of the BIFROST GPS data [Johansson et al., 2002] are shown, together with a model prediction for the best NA solution, based on the viscosity profile shown in Fig. 2.6b. The predictions capture the uplift pattern well, both in amplitude and in shape. In general, differences between observations and predictions are below 1 mm/yr, with the two exceptions in Northern Finland and between Denmark and South Sweden.

2.6 Discussion

In this paper we have used two sets of observational data related to GIA: On the one hand, palaeo-shoreline data from Scandinavia, the Barents Sea, and NW Europe, covering the last deglaciation interval (21,400 years BP to present), and indicating a viscoelastic readjustment of the solid Earth after the disappearance of the Late Pleistocene ice sheets. On the other hand, crustal uplift data from Scandinavia collected by the BIFROST project, indicating an ongoing rebound of central Scandinavia.

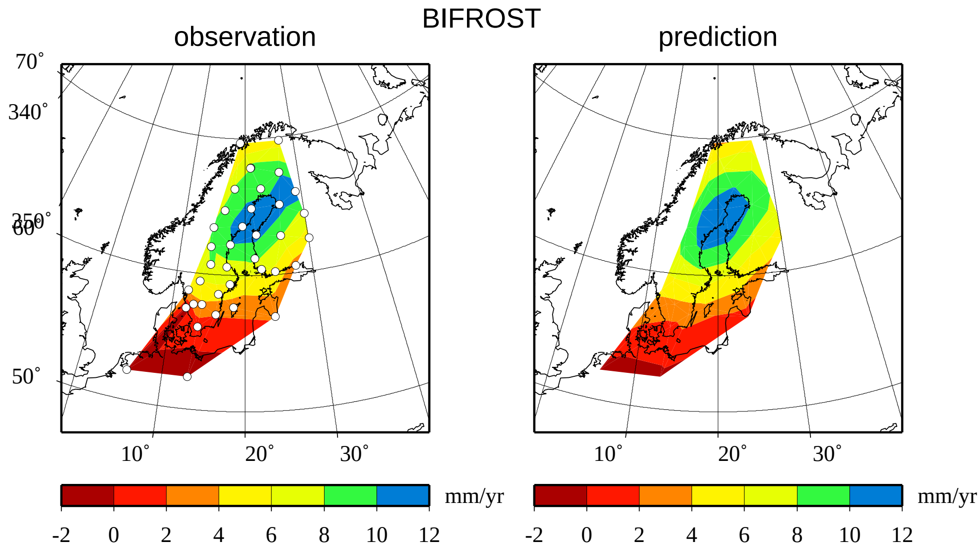

Figure 2.8: BIFROST uplift data (left) and model prediction from the best NA model (right). The BIFROST GPS stations are shown as circles. The difference between observations and predictions is smaller than 1 mm/yr almost everywhere.

We have used both data sets in an attempt to determine the radial viscosity variation in the Earth's mantle. In a first step, subregions of the shoreline data (Scandinavia, Europe, Barents Sea) are used to infer optimum values for lithospheric thickness and bulk upper- and lower-mantle viscosities. While lower-mantle viscosity is poorly constrained ($\eta_{LM} > 10^{22}$ Pa s), values for bulk upper-mantle viscosities are similar for all three subsets ($\eta_{UM} \sim 4 \times 10^{20}$ Pa s). Differences arise for the thickness of the lithosphere, with thicker values underneath Scandinavia ($H_l \sim 120$ km), and thinner values underneath the British Isles and the Barents Sea ($H_l \sim 60$ - 70 km). This lateral variability correlates with the thickening of the crust and lithosphere from the North Atlantic Mid-Ocean Ridge towards the Baltic Shield.

In a second step, we have refined the radial viscosity profiles with the Neighbourhood Algorithm, a global inverse procedure developed by Sambridge [1999a,b]. We therefore subdivided the upper mantle into five layers, in which viscosity can vary independently. This approach allows us to search for a low-viscosity asthenosphere, which has been proposed on the basis of RSL data from Scandinavia. The results from the NA inversion indicate a low-viscosity zone underneath the Barents Sea between 120 and 200 km depth, which is characterised by viscosities around 10^{19} - 10^{20} Pa s. The lower part of the upper mantle in these two regions becomes more viscous, with viscosities up to 10^{22} Pa s. However, underneath Scandinavia and NW Europe no evidence for a low-viscosity zone was found from the inversion of palaeo-shoreline data. Interestingly, the NA inversion of the BIFROST uplift data favours a thin low-viscosity layer between 160 - 200 km depth, which is in agreement with an earlier inference by Milne et al. [2004], but which is actually not resolved by the data.

Acknowledgements

We are grateful for numerous comments and suggestions by Detlef Wolf and an anonymous referee. Many thanks to Kurt Lambeck for providing the RSES ice model. We would also like to thank Malcolm Sambridge for permission to use the NA inversion package [Sambridge, 1999a,b, 1998, 2001]. The figures in this paper are drawn using the GMT graphics package [Wessel and Smith, 1991, 1998]. This research was funded by the DFG (research grant KA1723-1).

3. Holocene relative sea-level change, isostatic subsidence and the radial viscosity structure of the mantle of north-western Europe (Belgium, the Netherlands, Germany, southern North Sea)

Abstract[a]

A comprehensive observational database of Holocene relative sea-level index points from the NW European coast (Belgium, the Netherlands, north-western Germany, southern North Sea) has been compiled in order to compare and reassess the data collected from the different countries/regions and by different workers on a common time-depth scale. Relative sea-level (RSL) rise varies both in magnitude and form between these regions, revealing a complex pattern of differential crustal movement which cannot be solely attributed to tectonic activity. It clearly contains a non-linear, glacio- and/or hydro-isostatic subsidence component, which is negligible on the Belgian coastal plain but increases significantly to a value of ca. 7.5 m (since 8 cal. kyr BP) along the north-western German coast. The subsidence is at least in part related to the post-glacial collapse of the so-called peripheral forebulge which developed around the Fennoscandian centre of ice loading during the last glacial maximum. The RSL data have been compared to geodynamic earth models in order to infer the radial viscosity structure of the Earth's mantle underneath NW Europe (lithosphere thickness, upper and lower mantle viscosity), and conversely to predict RSL in regions where we have no observational data (e. g. in the southern North Sea). A broad range of Earth parameters fit the Belgian RSL data, confirming the stable behaviour and insensitivity to glacial isostatic adjustment (GIA) of the Belgian crust (London-Brabant massif) during and after the last ice age. In contrast, a narrow range of Earth parameters define the southern North Sea region, reflecting the greater influence of GIA on these deeper/older samples. Identification of the effects of local-scale factors such as compaction or past changes in tidal range on the spatial and temporal variations of sea-level index points based on model-data comparisons is possible but is still complicated by the relatively large range of earth model parameters fitting each RSL curve, emphasising the need for more observational data.

---

[a] Vink, Steffen, Reinhardt and Kaufmann (2006). Holocene relative sea-level change, isostatic subsidence and the radial viscosity structure of the mantle of north-western Europe (Belgium, the Netherlands, Germany, southern North Sea), Quat. Sci. Rev., under revision (Sections 3.1 to 3.3 by Vink, 3.4 to 3.6.2 by Steffen, 3.6.3 and 3.7 both).

3.1 Introduction

The nature and magnitude of relative sea-level movement (i. e. rise or fall or a sequence of events involving both) in any particular coastal or estuarine area since the last glacial maximum is determined mainly by three regional-scale factors which interact with each other: (i) the climatically-induced global / eustatic increase in ocean water volume, (ii) tectonic subsidence or uplift, and (iii) glacio- and / or hydro-isostatic adjustment of the lithosphere in reaction to spatially and temporally changing ice, water and sediment volumes. Local-scale processes such as past modifications in the tidal regime / range, changing relationships between the local water table and sea level, and / or adaptation in sample elevation due to sediment consolidation can additionally influence the registration of relative sea-level changes in the sedimentary record [we refer to Shennan et al., 2000a, for a detailed account of these processes]. Focussing on the three main controlling factors, it has often been suggested that the sea-level changes which are recorded in tectonically stable and formerly ice-free areas such as north-western Europe should mainly reflect global ocean volume and climate change. However, the comparison of detailed, published composite Holocene sea-level curves obtained mainly through the analysis of basal and intercalated fen and wood peats in estuaries and the coastal lowlands of Belgium [Denys and Baeteman, 1995], Zeeland [Kiden, 1995], the western Netherlands [van de Plassche, 1982], the central Netherlands [van de Plassche et al., 2005], north-western Germany [Behre, 2003] and the southern North Sea [Jelgersma et al., 1979; Ludwig et al., 1979; Behre, 2003] reveals that the time-depth positions of the German and southern North Sea data lie considerably lower than those of the Netherlands and Belgium. The differences could in part be due to the fact that calibration methods for converting radiocarbon to calendar years have undergone significant change since the acquisition of data began in the nineteen sixties, and so calibrated ^{14}C dates over the decades and from different laboratories cannot necessarily be compared with each other. The same applies to the depth reference, which varies between the Belgian TAW, the Dutch NAP and the German NN ordnance datum. Thus, the first aim of this paper was to critically reassess and compare valid sea-level index points of all the above-mentioned sea-level curves on a common time-depth scale and with standardised vertical error margins so that relative sea-level rise in north-western Europe can be directly compared and interpreted, and to approximate the dimension and rate of tectonic and / or isostatic subsidence of north-western Germany and the southern North Sea relative to the Netherlands and Belgium after Kiden et al. [2002] for the interval between ca. 9 and 3 cal. kyr BP, which is the period in which most of the basal peats were formed.

In response to the melting of the ice sheets, isostatic relaxation of the Earth's surface occurs at a rate that is governed by the mechanical properties of the Earth, in particular mantle viscosity and lithosphere thickness. Sea-level indicators from the geological record indicate that large regional and even local differences in isostatic rebound and relative sea-level rise occurred, which are used as input in order to successfully model sea-level change using a variety of Earth and ice parameters (i. e. incorporating ice sheet reconstructions, Earth rheology, and glacio- and hydro-isostasy). Results of geophysical modelling of Holocene glacio- and hydro-isostatic crustal movements in the Dutch North Sea sector and in the Belgian-Netherlands coastal plain [Kiden et al., 2002] show that post-glacial isostatic lowering of the crust has occurred in this area and that it increases significantly from the southwest to the northeast, although only eight North Sea index points were used in the analysis. Indeed, these regions are sufficiently close to the Fennoscandian ice-sheet that they may be differentially affected by it, yet the glacio-isostatic effects from other ice sheets such as the British ice sheet can be assumed to be identical in both countries because of the large distances and / or smaller volumes of ice involved. However, both Kiden et al. [2002] and van de Plassche et al. [2005] state that new suites of data, preferably older than 8 cal. kyr BP, should be collected in the northern part of the Netherlands in order to test model predictions of stronger isostatic subsidence. In this paper, we attempt to do so without disposing of more northern Netherlands data but rather by extending the dataset to include many more samples from the north-western German and southern North Sea sectors in geophysical modelling analyses. Definitive models for isostatic subsidence and the viscosity of the mantle beneath north-western Germany do not yet exist, mainly due to the fact that until recently, German sea-level observational data were scattered and relatively inaccessible as they were chiefly published in local German journals. The extremely detailed synthesis of reliable German sea-level index points as published by Behre [2003] has opened the door for comparisons with sea-level data from neighbouring countries such as Belgium and the Netherlands, and will be used as the main input for comparison and geophysical modelling in this paper.

3.2 Sea-level observational data: an overview

3.2.1 Nature and constraints of the applied sea-level observational data

The database of sea-level observational data used for this study includes 144 basal peat dates (base, top or whole layer; transgressive overlaps), 12 dates from intercalated peat beds (transgressive or regressive overlaps), 8 tidal-flat / salt marsh dates (transgressive overlaps), 20 dates based on sea-level related sedimentary structures (e. g. dune soils; transgressive overlaps) and 64 archaeological / historical dates (settlement levels indicating transgressive or regressive phases). Basal peats are especially important for the determination of former local water and tide levels, and form the backbone of all sea-level curves discussed here. They were formed during the early and middle Holocene, when the sandy, gently inclined Pleistocene palaeosurface was gradually submerged by the transgressive North Sea. The sea-level rise raised the regional groundwater level, thus initiating the development of basal peat in a narrow belt in front of the tidal area. The growth of this peat ["basis peat" following Lange and Menke, 1967] did not however last very long: the rising sea level quickly drowned the peat and a lagoonal environment with clayey deposition followed. The base of a basal / basis fen peat layer is generally assumed to represent the local mean high water tide (MHW) in a tidally influenced area such as along the coast of north-western Germany. In contrast, it will approximate the upper limit of local mean sea level (MSL) when, for example, sand dunes and coastal barrier systems lead to extinction of the tidal wave, as is the case in broad coastal systems of the Netherlands. The positions of these index points thus tend to converge to MSL, but may still lie well above this level. The uncertainty in their exact indicative meaning means that these index points can only be considered as being limiting, whereas MHW index points are exact. For detailed information on the relationship between basal peat formation and water or tide levels, see van de Plassche [1982]. Additional complications in the indicative meaning of peat layers may arise due to (i) the floodbasin effect or tidal dampening [Zonneveld, 1960], which causes a decrease in tidal amplitude (and hence of the MHW) in an upstream direction in an estuary or tidal channel due to the frictional dissipation of tidal energy in large intertidal storage basins; (ii) the estuary effect [Fairbridge, 1961], which causes an increase in tidal amplitude due to confinement of the tidal wave in a funnel-shaped embayment, or (iii) the river gradient effect [Louwe Kooijmans, 1974], which refers to a gently sloping groundwater surface in river areas and leads to a relative increase in MHW altitude in a longitudinal upstream direction along the estuary. Groundwater-influenced peat growth above contemporaneous sea level may also occur in sheltered sand dunes (e. g. due to convex water tables). Thus, the nature and geographical location of each peat layer has to be analysed carefully in order to determine its indicative meaning before it can be used as a valid sea-level index point. The top of the basal / basis peat is assumed to indicate the marine flooding contact / lowest limit of the highest local mean high water spring tide

(MHW-MHWS) when continuous sedimentation to the following lagoonal / brackish water clays can be assured and the presence of an erosional contact can be completely dismissed. Dune soils and habitation levels are likewise considered not to have formed below MHWS. Such index points may have been influenced by compaction and care must be taken during their interpretation. Intercalated peats are found in open coastal areas in between marine clayey sediments, the base indicating a regressive overlap (MHW) and the top a transgressive overlap (MHW-MHWS). Their depths of formation are difficult to determine as compaction effects may have been considerable, but their indicative meaning for the determination of sea-level stagnation or regressive phases is of great importance.

The depths of the samples from the analysed regions were converted to the German NN ordnance datum (Normalnull) in order to allow comparison with each other. NN is an approximate value for MSL. The Dutch NAP ordnance datum (Nieuw Amsterdams Peil) is equivalent to NN; the Belgian TAW (Tweede Algemene Waterpassing) however lies 2.33 m below NAP / NN and sample depths were thus adjusted accordingly. Altitude accuracy of samples deriving from land boreholes or open pits / outcrops was, save several exceptions, generally good at ca. $\pm$0.10 m; this value being comprised mainly of errors associated with levelling and sampling. For the North Sea samples, altitude accuracy greatly decreased due to the still problematic instrumental determination of exact water depth from the ship, possible compression or extension of core material during the vibrocoring process and the conversion of time-/tidally-dependent water depth to depth below NN, which is based on comparison with tide gauge measurements which often lie far away from the sample positions. For these samples, an accuracy of no less than $\pm$1.0 m had to be assumed.

The compaction of peat and / or of silty and clayey layers underlying the peat or a particular habitation level is a problem which under certain circumstances can greatly alter the depth of a sea-level index point, rendering it useless for sea-level studies. Whether compaction occurs depends on several factors, including initial water content of the material, its composition, age, and the thickness and nature of the overburden. As these factors vary in their dimensions from sample to sample even within a small local area, compaction is practically impossible to correct for and thus samples possibly influenced by compaction have not been depth-corrected but are marked by an upward arrow in the sea-level curves (i. e. when the thickness of the compaction-sensitive peat or clay layer below the sample exceeds 0.2 m). Samples in which compaction effects were assumed to have been large (i. e. $>$ 0.5 m) were not considered in this study.

All original ^{14}C dates were calibrated to calendar years BP using the CALIB 4.4 conversion routine [Stuiver and Reimer, 1993; Stuiver et al., 1998, http://calib.qub.ac.uk/calib/]. The 1σ confidence interval (68%) in the calendar age ranges was determined and used in the construction of sea-level curves. Pre-1962 radiocarbon dates from Groningen, as derived from Bennema [1954] and Jelgersma [1961] and used in the Zeeland and western Netherlands curves, have not been corrected for isotopic fractionation effects (^{13}C correction). In the publication of van de Plassche [1982], a correction of -40 radiocarbon years has been used, based on the assumed average composition of freshwater peat. However, as highlighted by Kiden [1995], isotopic fractionation effects not only depend on the nature of the dated material but also on laboratory procedures, and so a correction was not carried out in this analysis but was considered as a possible extension of the age range of the samples under consideration in the respective sea-level curves (Figs. 3.2 and 3.3). Another problem in comparing radiocarbon peat data is that ^{14}C dates can readily be affected by sample contamination, which occurs due to admixture of small amounts of younger or older plant material [e. g. roots or humid acids; Streif, 1972]. Such dating problems can be avoided somewhat by macroscopical analysis and dating of specific botanical components (e. g. leaf remains, bud scales, seeds, pollen) rather than bulk peat analysis. However, van de Plassche et al. [2005] did show that the age differences between three fractions (organics < 200 μm, botanical macro-remains, roots) of four basal peat samples from the central Netherlands were relatively small, and the ages of the macro-remains tended to support the ages derived from bulk analysis even though the potentially rejuvenating root fraction had not been removed. Root rejuvenation thus seemed to have been compensated for by one or more aging effects.

Perhaps the greatest problem in comparing sea-level data from the different regions is that MHW- and MSL-envelopes cannot be directly compared with one another, as MHW is a function of the tidal range of the studied area and varies greatly from region to region (e. g. present-day tidal range decreases considerably in a north-easterly direction along the Belgian-Netherlands coast, being ca. 3.8 m close to the Belgian border but only 2.3 m at the mouth of the River Meuse and 1.4 m in Den Helder), whereas the index points constraining the MSL-envelope generally reflect local and relatively arbitrary depths of formation anywhere between MSL and MHW. In order to attempt a comparison of all the sea-level curves with each other in spite of these differences, extreme lower limits of MSL were derived (i) from the MHW data by subtracting the approximate present-day difference between coastal mean tide level (MTL) and MHW (i. e. the tidal amplitude) at each sample position (or a value slightly smaller where the building of dikes has probably increased present-day tidal range), and (ii) from the MSL data by subtracting half of the present-day tidal amplitude following the method described in Shennan et al. [2000a] for data from the east coast of England. The altitude accuracy greatly decreases as errors in the determination of indicative meaning and in the approximation of tidal range have to be taken into account. In the case of the MSL limiting data, the altitude error bars of sea-level index points can increase to as much as ±1.1 m. The resulting extreme lower limit of MSL values are biased mainly by the underlying assumption that tidal ranges have not changed significantly during the last 10 kyr, although there is no direct evidence that this is the case. In fact, palaeotidal models for the southern North Sea indicate lower tidal ranges during the early Holocene [Austin, 1991; Shennan et al., 2000b] and only minor changes since 6 cal. kyr BP, consistent with the changing palaeogeographies and coastline configurations at that time. Nevertheless, Roep and Beets [1988] did reconstruct a slightly higher tidal range along the western coast of the Netherlands before ca. 5 cal. kyr BP. Another problem with the conversion to extreme lower limit of MSL is that present-day coastal tidal ranges are taken as basis, thus neglecting the possibility of tidal dampening due to the floodbasin effect or tidal amplification due to the estuary effect for the more sheltered, inland samples. In regions such as Belgium and Zeeland where tidal ranges are high, tidal dampening can have a significant effect on the indicative meaning and thus the MSL-altitude of sea-level index points. As such, we consider that the calculation of extreme lower limits of MSL using present-day coastal tidal ranges is not faultless or precise, but represents the most acceptable method for the direct comparison and modelling of sea-level data from different regions until more information on past tidal ranges becomes available.

3.2.2 The database

A list of the samples used in this paper, together with all the relevant information concerning these samples, is provided in Tab. A.1. Only those samples which were considered as valid sea-level index points were selected from their original publications; geographic positions are shown in Fig. 3.1. For better comparison and clarity, sample numbers / codes in Tab. A.1 and in the individual sea-level curves (Figs. 3.2 - 3.4) always refer to those provided by the original authors.

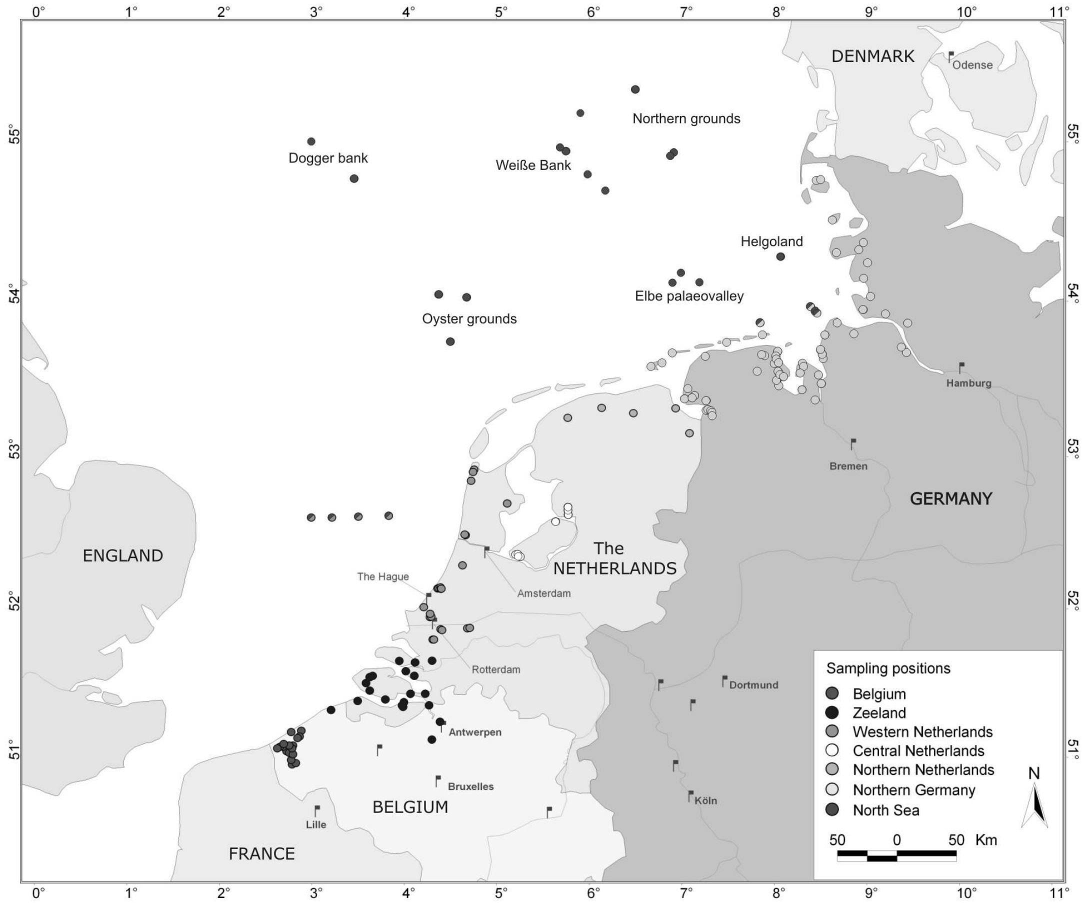

Figure 3.1: Locations of samples used for the determination of Holocene relative sea-level rise in Belgium, the Netherlands, north-western Germany and the southern North Sea. More than one index point can derive from each sample site where several samples were taken from the same core / outcrop or where samples lie very close to each other.

3.2.2.1 Belgium

Basal peat data deriving from the Belgian coastal plain have been reassessed in terms of local and tide levels in Denys and Baeteman [1995] and were used as the basis for the Belgian dataset in this paper. Many of the samples in the original dataset were found to be unreliable by the authors, and so only the 21 most reliable samples covering the time span from 9.5 to 3 cal. kyr BP were selected here (Tab. A.1; Fig. 3.2). Generally the bases of peat layers were sampled; tops were taken only when no visible signs of erosion were found (e. g. through diatom analysis). Error envelopes for local MHW and for the upper limit of local MSL were drawn, depending on the indicative meaning of the dated peat layers as determined by the original authors. The area under consideration is crossed by only one small river, the Ijzer, and edaphic dryness during the early Holocene explains why the effects of local seepage and river gradient effects on the altitude of peat formation were found to be limited or even absent on the Belgian coastal plain. However, several samples deriving from the tops of thicker peat layers (0.2 - 0.4 m) may have experienced some compaction. The resulting MHW- and MSL-error bands encompassing the Belgian sea-level data are relatively narrow (1 - 1.5 m) and focussed (Fig. 3.2).

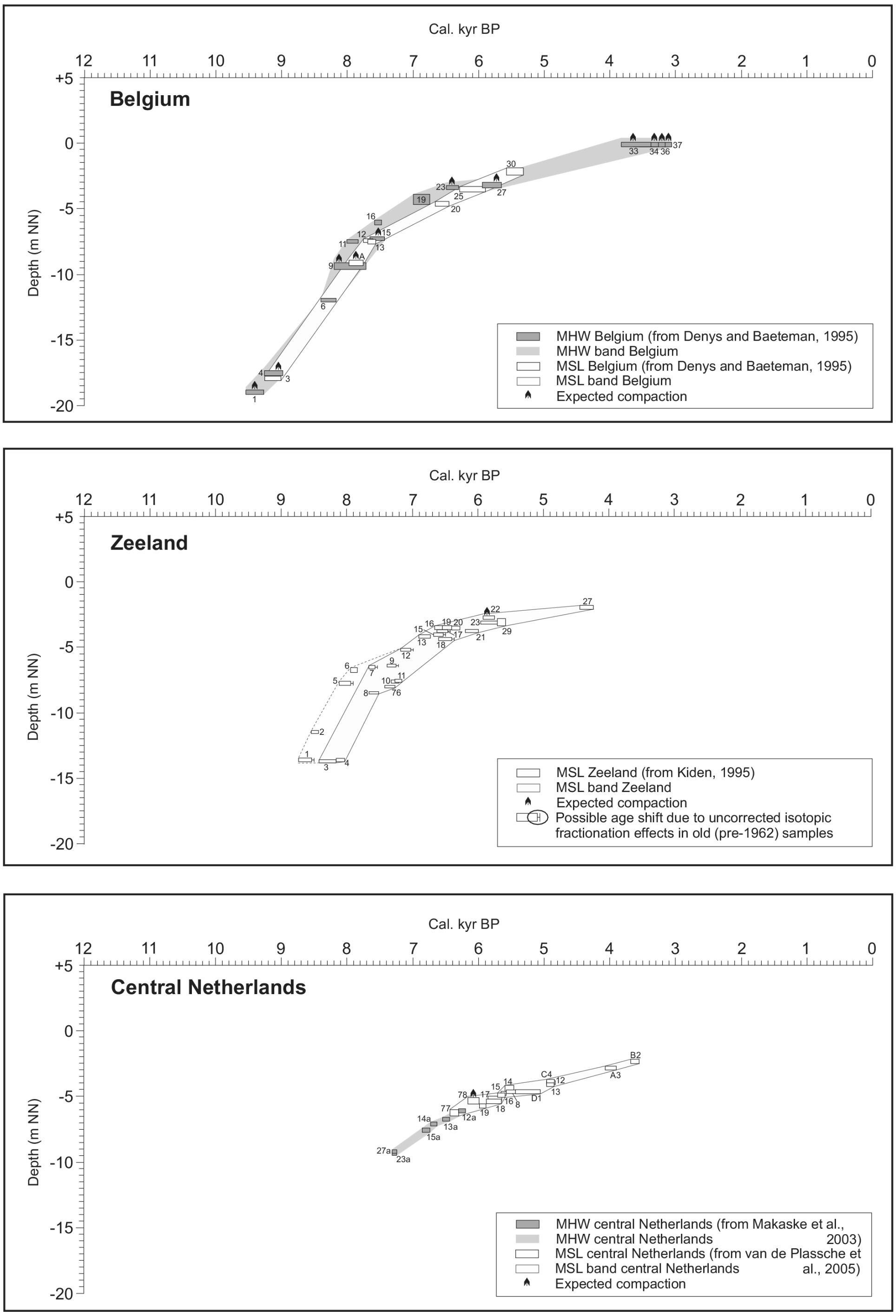

Figure 3.2: Age-depth distribution of sea-level index points obtained mainly from basal peat data from Belgium [after Denys and Baeteman, 1995], Zeeland [after Kiden, 1995] and the central Netherlands [after Makaske et al., 2003; van de Plassche et al., 2005]. The widths of the error boxes represent the 1σ-calibrated age range of the conventional radiocarbon age; the height corresponds to twice the total vertical error. Depending on the indicative meaning of the basal peats under consideration, error bands / envelopes have been drawn for local mean high water (MHW) and / or the upper limit of local mean sea level (MSL). Samples in which some compaction may be expected are marked by an upward arrow.

3.2.2.2 The Netherlands

3.2.2.2.1 Zeeland Sea-level index points (mostly bases of basal peats) deriving from Zeeland and the adjacent estuarine flood plain of the River Schelde in northern Belgium have been obtained from Kiden [1995] and the publications therein, and were used to produce an error envelope for the upper limit of MSL for Zeeland covering the time period of approximately 9 - 4 cal. kyr BP (Fig. 3.2). Compaction effects were considered to be negligible, as the peat samples were generally thin (2 - 5 cm) and came from the base of the basal peat which directly rests on the sandy Pleistocene subsoil. However, a number of the sea-level index points listed by Kiden [1995] have to be considered unreliable due to early peat growth in closed depressions independent of sea level, poor drainage and / or high local groundwater tables. Thus, only the 25 more reliable sea-level index points, as described by the author in the original article, have been selected for this study (Tab. A.1; Fig. 3.2). Despite this critical selection, the MSL error band of the Zeeland data remains relatively wide in comparison to the Belgian and other Dutch data, varying from 1.5 to at least 2.5 m between 8 and 6 cal. kyr BP (Fig. 3.2). Kiden [1995] in part attributes the relatively high but variable positions of most of the Zeeland index points in comparison to the western Netherlands MSL-envelope to the interaction between the pronounced local Pleistocene morphology and topography, differential palaeo-groundwater levels and the variable influence of floodbasin and river gradient effects on the altitude of peat growth. This complexity does not allow a clear definition of the indicative meaning of the basal peats, and this is reflected in the broad MSL-envelope. However, samples deriving directly from the Schelde palaeovalley exhibit a relatively low time-depth position and appear to have been influenced far less by local and regional groundwater effects [Kiden, 1995]. Thus, although the Zeeland MSL-envelope is broad and its indicative meaning complex, it does apparently constrain values of lowest possible MSL for the area (e. g. samples 4, 10, 11, 27).

3.2.2.2.2 Western and northern Netherlands A relative (upper limit of) MSL curve for the western and northern Netherlands, deriving mainly from basal peat data, was presented and its characteristics discussed in detail by van de Plassche [1982]. The curve encompasses the time interval from ca. 8 to 2 cal. kyr BP and was obtained from a comparative analysis of old data with the inclusion of new data from the Rhine region. We have reanalysed the work of van de Plassche [1982] and the resulting MHW and MSL curves used in this study are constrained by 49 reliable sea-level index points from mainly the Rhine-Meuse river dune and beach-plain area, although 3 index points were retrieved from West Vriesland, 3 from Velsen and 4 from offshore western Netherlands (see Tab. A.1; Fig. 3.1). In the light of growing evidence that differential post-glacial isostatic crustal adjustment and / or tectonic movement did occur in the Netherlands [Kiden et al., 2002; Kooi et al., 1998, respectively], we decided not to actively integrate the 8 index points from the northern Netherlands into the western Netherlands MSL error band, although their positions have been superimposed onto the western Netherlands curve for comparative reasons (Fig. 3.3). Unfortunately, the number of reliable northern Netherlands sea-level index points is still too low to create a separate MSL curve for that region. The index points deriving from the Rhine-Meuse River sand dunes (mainly bases of basal peats) are especially difficult to interpret in terms of their indicative meaning in relation to rising sea level, as the chances of independent peat growth due to higher local (ground)water tables caused by the river gradient effect, seepage and / or hampered drainage are relatively high in this former deltaic area. In contrast, compaction effects can be cancelled out for most of these samples due to their imminent position in the very base of the basal peats, directly on the dune sands. Samples from the Rhine-Meuse beach-plain appeared to be easier to quantify in terms of MHW levels. Details of reliable as well as unreliable index points and all the problems involved in the stringent selection of rational data are provided in van de Plassche [1982].

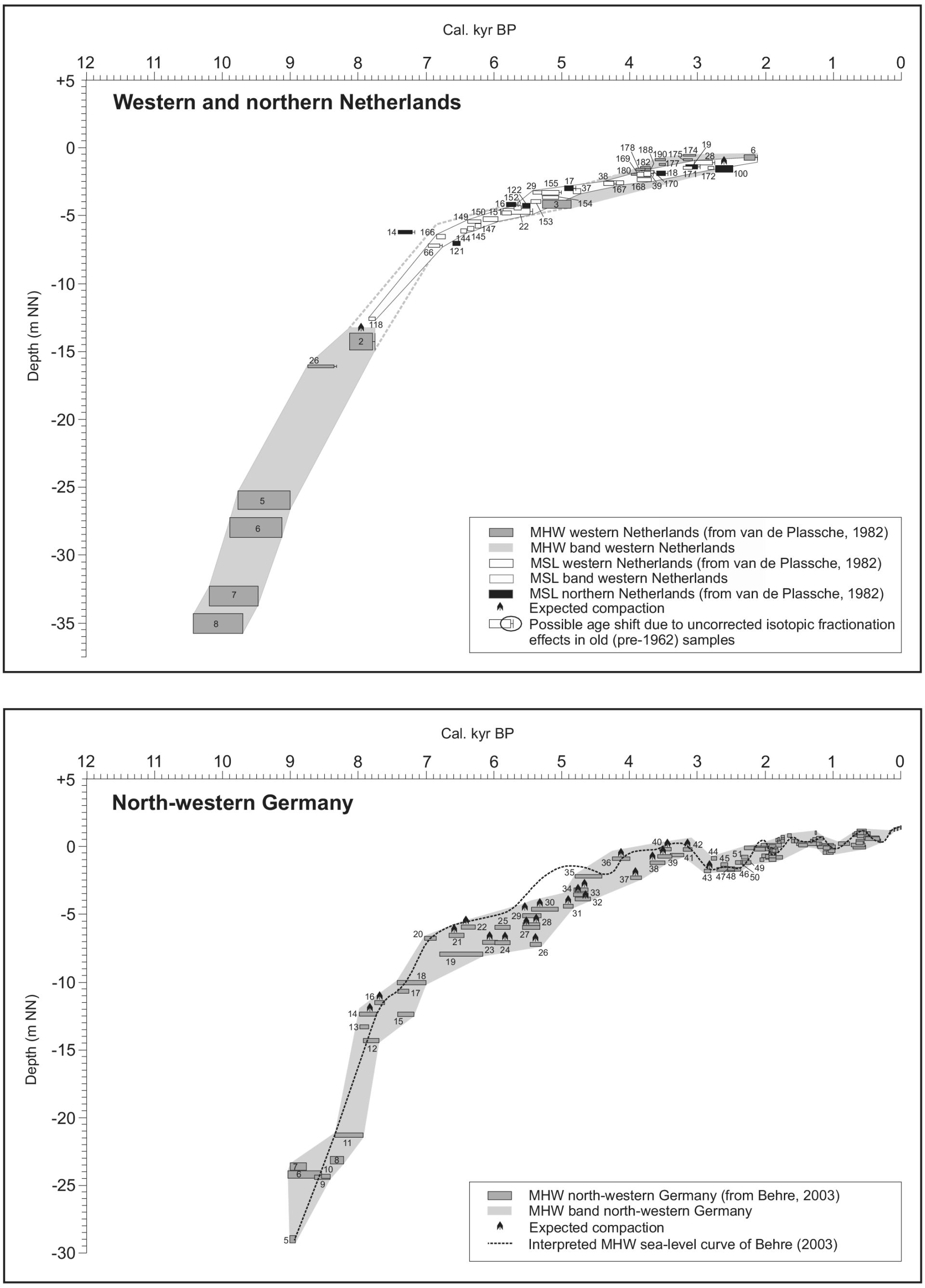

Figure 3.3: Age-depth distribution of sea-level index points obtained from basal and intercalated peat data as well as archaeological data from the western and northern Netherlands [after van de Plassche, 1982] and north-western Germany [after Behre, 2003]. The widths of the error boxes represent the 1σ-calibrated age range of the conventional radiocarbon age; the height corresponds to twice the total vertical error. Depending on the indicative meaning of the index points under consideration, error bands / envelopes have been drawn for local mean high water (MHW) and / or the upper limit of local mean sea level (MSL). Samples in which some compaction may be expected are marked by an upward arrow.

3.2.2.2.3 Central Netherlands Roeleveld and Gotjé [1993] reconstructed the mid-Holocene water-level rise in the area of Schokland (central Netherlands) using two suites of (near-)basal peat samples from the slopes of two river dunes. The resulting MSL curve was found to consistently lie somewhat below that of the western Netherlands, leading to slight confusion and consequently to the retrieval of new data and a critical reassessment of the central Netherlands curve by van de Plassche et al. [2005]. 19 reliable basal peat sea-level index points resulting from that comparative analysis, and 2 from the original western Netherlands curve [van de Plassche, 1982], were used to form the central Netherlands dataset of this study (Tab. A.1). The data cover the time interval from 7.5 to 3.5 cal. kyr BP and were used to produce a relatively narrow (< 1 m) error envelope for the upper limit of MSL for the area (Fig. 3.2). Samples were taken near or from the base of peat layers and so compaction effects are considered to be negligible [van de Plassche et al., 2005, did calculate a compaction factor of 2 for samples deriving from slightly above the surface of the dune sand, but this leads to a compaction correction of 0.07 m at the most]. The effects of local (ground)water gradients on the development of peat in the area have not been quantified, but may well have been small considering the generally low age-depth positions of the index points compared to the western Netherlands curve.

3.2.2.3 North-western Germany

A detailed relative MHW curve for north-western Germany has recently been published by Behre [2003], based on the collection and synthesis of all reliable sea-level index points which had been collected from the coastal regions of the German Bight throughout the last few decades. The samples derive from a relatively large geographical area (see Fig. 3.1), including the Ems, Weser, Elbe and Eider river mouths / estuaries and ranging from Emden in the southwest (East Frisia; Lower Saxony) to Föhr in the northeast (Schleswig-Holstein). The curve is based on an extensive dataset containing 112 sea-level index points, of which 47 cover the time interval from ca. 9 to 2 cal. kyr BP, the rest being younger (Tab. A.1; Fig. 3.3). Most of these younger dates derive from archaeological, historical or hydrological data; the older dates are based mainly on the analysis of basal and intercalated peats or tidal flat / salt marsh systems. In contrast to many of the peat layers in Belgium and the Netherlands which formed in (river-influenced) dune / barrier systems and for which the relationship to MSL is often difficult to reconstruct, the continuous past existence of an open coast along the German Bight favours a more precise definition of the indicative meaning of the basal / intercalated peats; generally in terms of MHW. However, many of the samples derive from the tops of basal peats and / or from intercalated peats, in which compaction effects may have been considerable (see Tab. A.1). Intercalated peats are especially vulnerable to compaction of the peat as well as the intermediary clay, and a depth reduction exceeding half a metre may be expected for a few index points of the dataset (e. g. samples 29, 32, 42). As such, intercalated peats can strictly speaking only be used as limiting data, although they are important for the indication of sea-level stagnation or regressive phases. Partly due to the compaction problem, the MHW-envelope for north-western Germany is relatively wide, varying between 1.5 and 3 m from 9 to 3 cal. kyr BP (Fig. 3.3).

Contrary to the sea-level curves of Belgium and the Netherlands, the German curve shows a fluctuating sea-level rise and Behre [2003] reconstructed seven regressional phases after ca. 5 cal. kyr BP based on both the age-depth positions and sedimentological and archaeological characteristics of the analysed sections / samples (Fig. 3.3). Similar stagnancies or regressions have been identified in studies from the Netherlands and Belgium [e. g. Louwe Kooijmans, 1974; Roeleveld, 1974; Ervynck et al., 1999], and they support the notion of an oscillating eustatic sea level such as that described for north-western Europe by Mörner [1984]. However, when the relatively wide MHW-error band for north-western Germany as shown in Fig. 3.3 is considered, only two clear regressions are still visible at approximately 3 and 1 cal. kyr BP. It is beyond the scope of this paper to determine or describe the possible causes, effects and consequences of the differences in form between the analysed curves. Insufficient sample density, the infrequent application of "indicative" intercalated peat and / or archaeological data in the Belgian and Netherlands datasets, the large geographical regions covered by the German data rather than focussing on local basins, and the world-wide differing scientific opinions concerning the interaction between post-glacial climate change and a smooth vs. fluctuating sea-level rise could be some of the main causes of these observed differences.

3.2.2.4 The southern North Sea

The basal peats which are required to improve our still very fragmentary knowledge of the earliest Holocene transgressional history of the North Sea Basin (i. e. sea-level rise before ca. 8 cal. kyr BP) formed relatively far offshore from the present-day coastline and can thus only be obtained during time-consuming and costly ship cruises. Furthermore, the chances of encountering basal peats offshore are extremely small and the recovery method still follows a trial and error principle, because (i) the basal peats are generally extremely thin (often < 5 cm) due to the rapid rate of relative sea-level rise which did not encourage extensive peat growth at that time, and so they do not show up diagnostically on seismic or echosound profiles, (ii) large tidal channels have probably eroded the basal peat and the underlying deposits in many places, and (iii) the sampling process is greatly hampered by the fact that the overlying marine cover sands are generally very coarse, which at the moment means that fairly economical cores can only be taken using a vibrocorer which has a maximum penetration depth of 6 m. Nevertheless, several reliable index points have been obtained from the southern North Sea region during the last few decades, and these are summarised in Tab. A.1 and Fig. 3.4. Ten of these index points were used by Behre [2003] to constrain the older / lower part of his German MHW curve (sample sites 1-4 and 6-11), of which 5 derive from the early work of Ludwig et al. [1979] in the North Sea Basin (sites 172, 235, A10). In fact, Ludwig et al. [1979] and Streif et al. [1983] documented and palynologically dated several more basal peat layers deriving from the western rim of the Elbe palaeovalley, and 4 of these have been included in this analysis (sites 234, 240, 245, 280). The problem with these basal peats is that (i) their exact altitude could not be determined properly on board due to deficient measuring instruments, meaning that sample depth below NN could only be estimated afterwards using available bathymetric data of the area, and (ii) unambiguous palynological dating was not always possible due to large quantities of reworked components and / or bad preservation [Streif et al., 1983]. Due to the present lack of other / better data, these index points were considered for the MHW age-depth graph in Fig. 3.4, but have not been used as input in the modelling analyses. 6 sites from the Dutch North Sea sector originally derive from Jelgersma [1961] and Jelgersma et al. [1979] and are summarised in Kiden et al. [2002]. Last but not least, three new (bulk) basal peat data obtained by the BGR during North Sea cruises in 2004/2005 [e. g. Kudraß et al., 2004] have been included.

As the available sea-level index points derive from a geographically extensive area in which significant variations in isostatic and / or tectonic subsidence may be expected, it is theoretically impossible to compare the sample points directly with one another, and trying to draw a sea-level curve through these points would be foolish. Even within a more restricted area such as Weiße Bank / northern grounds (ca. 55^{o}N; $6 - 7^{o}$E), age-depth values of the index points vary greatly and the error band reaches a width of 2.5 to 5 m (in part due to the large error bars involved in measuring sample altitude). Compaction effects can generally be ruled out as these thin peats lie directly on the sandy Pleistocene palaeosurface. Furthermore, the interpretation of the peat in terms of indicating MHW is favoured by the relatively open

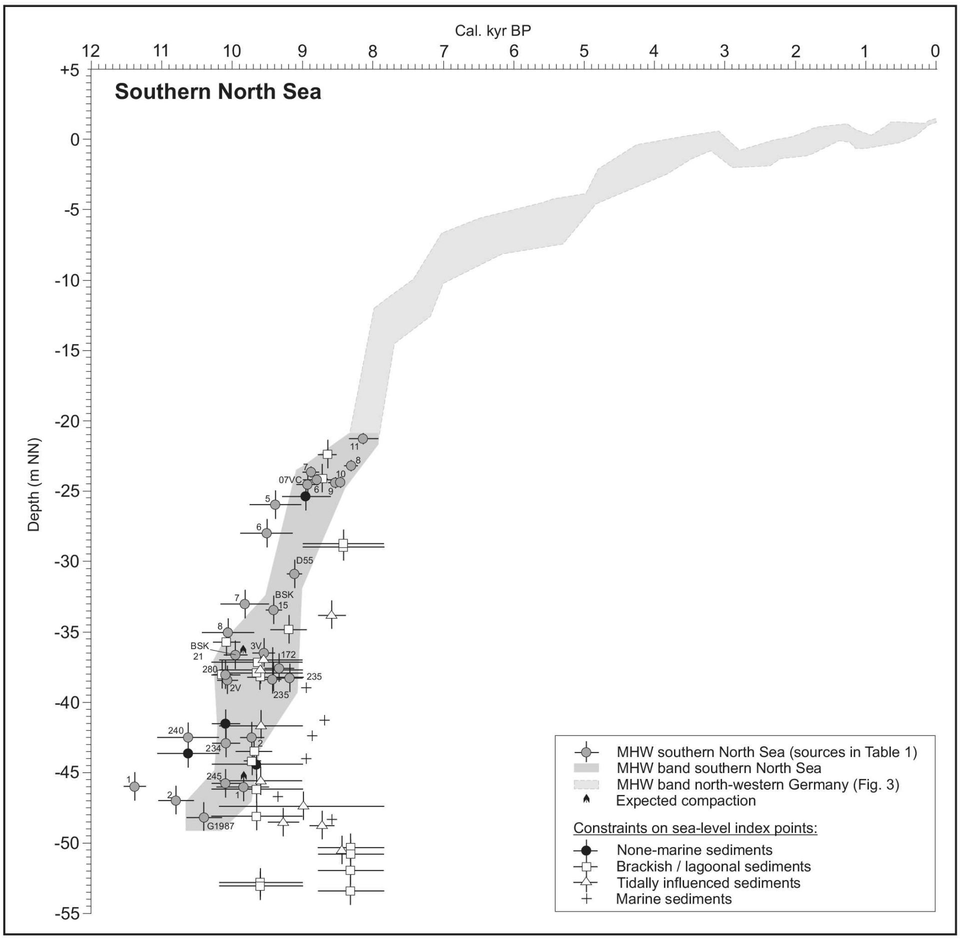

Figure 3.4: Age-depth distribution and local mean high water (MHW) error band of sea-level index points obtained from basal peat data from the southern North Sea (data compiled from different sources; see Tab. A.1). The horizontal error bars represent the 1σ-calibrated age range of the conventional radiocarbon age; the vertical error bars correspond to twice the total vertical error. Samples in which some compaction may be expected are marked by an upward arrow. The error envelope is purely theoretical and must be considered with caution, its significance being limited by the fact that samples are scattered over too large a geographical area (see Fig. 3.1) and probably experienced differential rates of post-glacial isostatic and / or tectonic subsidence. Constraints on the possible width of the error envelope were provided by dated none-marine, brackish, tidally influenced and fully marine sediments deriving from Ludwig et al. [1979], Streif et al. [1983] and from unpublished new data of the BGR..

coastal setting of the fossil peat. Thus, the large differences observed must be attributed to inadequate shipboard / bathymetrical depth measurements, age over- or underestimation due to reworking of older material or selective root rejuvenation of peat, respectively, or to sea-level independent peat growth in local landscape depressions. In spite of these problems and inconsistencies, older (North Sea) sea-level index data are extremely important for our understanding of early post-glacial ice sheet dynamics and the rates of initial sea-level rise, and they help to adjust and fine-tune geophysical models which aim at reconstructing past palaeogeographies and tidal ranges [e. g. Shennan et al., 2000b] as well as resolving the viscosity structure of the Earth's mantle [e. g. Lambeck et al., 1998a; Steffen and Kaufmann, 2005, this study].

3.3 Comparison of north-western European sea-level curves: relative isostatic subsidence

The reference MHW- and MSL-envelopes in the different north-western European areas (Figs. 3.2 - 3.4) are relatively well-constrained and we assume that they approximate the general trend of sea-level rise along their respective coast lines with a considerable degree of accuracy. Fig. 3.5 summarises the direct relationships between the extreme lower limit of MSL-envelopes of these regions. The conversion of original MHW or upper limit of MSL to the extreme lower limit of MSL (hereafter simply called MSL) introduces new vertical errors in altitude due to the underlying uncertainties in the indicative meaning and past tidal range, and so the error envelopes as depicted in Fig. 3.5 are somewhat wider than those drawn from the raw data (Figs. 3.2 - 3.4) only.

The MSL-envelope of north-western Germany lies significantly below those of the Netherlands and Belgium between ca. 10 and 4 cal. kyr BP, the MSL-envelopes generally diverging progressively back in time. This pattern of divergence becomes even clearer when hypothetical MSL curves are drawn through the lowest / youngest index points (Fig. 3.5 inset). The Belgian MSL-envelope shows the best fit with

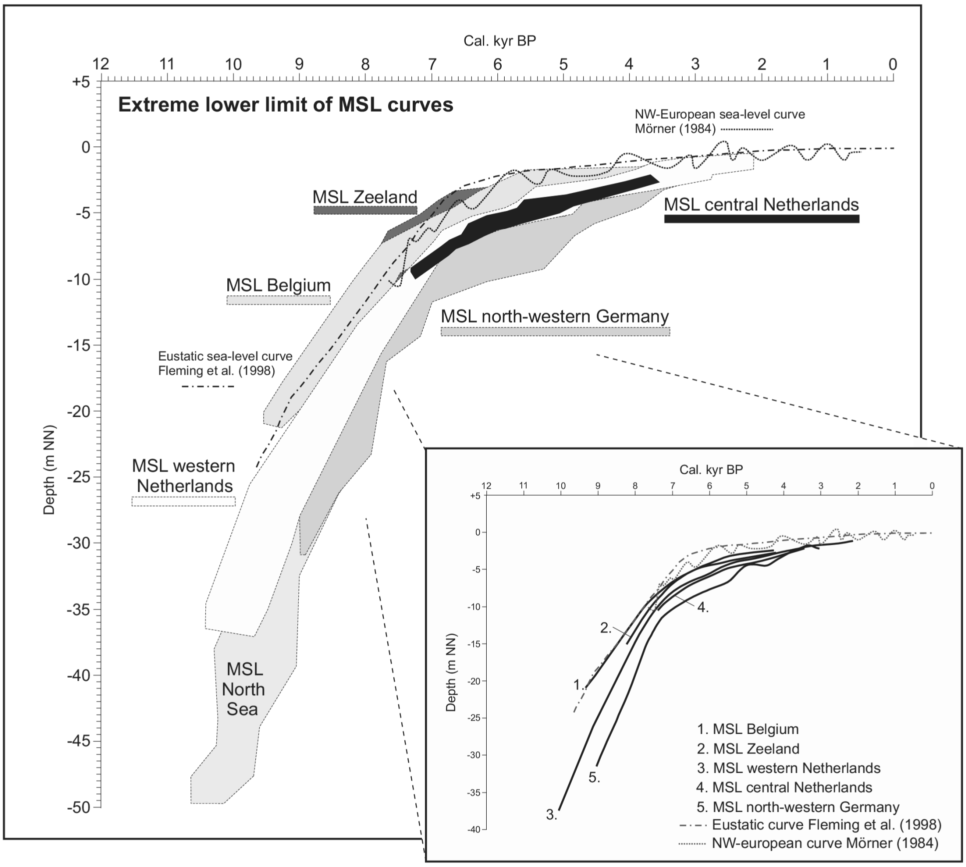

Figure 3.5: Relationships between the extreme lower limit of MSL curves and error bands (calculated from the raw MHW/MSL data: see section 3.2.1) of Belgium, the Netherlands, Germany and the southern North Sea in comparison with the eustatic sea-level curve of Fleming et al. [1998] and the north-western European sea-level curve of Mörner [1984].

the general trend of the northwest European sea-level curve of Mörner [1984] and the composite eustatic curve of Fleming et al. [1998], suggesting that tectonic and / or isostatic crustal movements have only had a small to negligible effect on the altitude and position of the Belgian coastal plain during the Holocene. This crustal stability of the Belgian coastal region is most likely associated with its geographical position on the margin of the Precambrian Brabant-London Massif/High. However, the Netherlands, north-western Germany and the southern North Sea have clearly subsided relative to Belgium between 10 and 4 cal. kyr BP. This relative subsidence will have been caused either by ongoing regional / local tectonic subsidence or by isostatic crustal movements, or indeed a combination of both, and it is extremely difficult, if not impossible, to completely separate the effects of these two processes. As a first observation, the vertical difference between the three sea-level curves from the Netherlands, which do not converge or diverge greatly with time, could theoretically be explained solely by differential local tectonic movements, which are considered linear for the time frame under consideration. The small altitude difference between the central and western Netherlands MSL curves is consistently so small (ca. 200-300 ^{14}C years) that van de Plassche et al. [2005] even suggest an aging effect due to the presence of older carbon in the extreme bases of the western Netherlands basal peats rather than a geophysical process to elucidate the difference. However, the divergence of the Belgian, Dutch and German curves clearly indicates that a non-linear glacio- and / or hydro-isostatic component, most likely related to the postglacial rebound of Fennoscandia and / or water and sediment loading of the North Sea Basin, must also be involved.

In a particularly illustrative study, Kiden et al. [2002] used the difference in altitude between submerged sea-level data from the last interglacial (Eemian) sea-level highstand in Belgium and the Netherlands as a measure of the Late Quaternary long-term tectonic subsidence component between these regions, and subtracted this approximate tectonic component from the differential total crustal movement (i. e. the altitudinal difference between the two MSL error bands) in order to obtain a slowly decaying isostatic subsidence component of the western Netherlands relative to Belgium [Fig. 3.6; for methodical details see Kiden et al., 2002]. Of course, such tectonic subsidence rates represent rough estimations only, and are based on the assumptions that (i) the Eemian highstand sediments in the different regions are isochronous with an age of exactly 125 kyr, and (ii) selected Eemian sea-level highstand data are representative of the entire region, thus neglecting possible local-scale tectonic differences. Both assumptions could be problematic [e. g. Schellmann and Radtke, 2004], although the error introduced over the time scale under consideration remains relatively small. After subtraction of the maximal tectonic component, the error bands of both areas are still discrete and only converge at ca. 3.5 cal. kyr BP (Fig. 3.6B), leading to the conclusion that the western Netherlands has undergone considerable isostatic subsidence relative to Belgium during the early and middle Holocene. However, one potential pitfall of the Kiden et al. [2002] analysis is that both the Belgian and the western Netherlands curves were considered to represent MSL, although each sample point rather reflects the upper limit of MSL (i. e. any altitude between MSL and MHW) in its local area. Taking the large present-day differences in local tidal range into consideration they can, strictly speaking, thus only be qualitatively compared with one other. The extreme lower limit of MSL data exhibit significantly larger error bars due to the limited indicative meaning of the sea-level index points and the need to incorporate all depths for possible MSL into the error band. When these data are treated in the same manner, we find that the upper range of the western Netherlands MSL band consistently plots within the lower range of the Belgian MSL band (Fig. 3.7B), showing that the isostatic subsidence of the western Netherlands relative to Belgium may have been a lot smaller than that predicted by Kiden et al. [2002] in the theoretical situation in which, for example, Belgian index points actually represent values close to MHW whereas Dutch ones represent values close to MSL. In reality, it is clear that the extreme lower limit of MSL data are probably also biased by an overcorrection

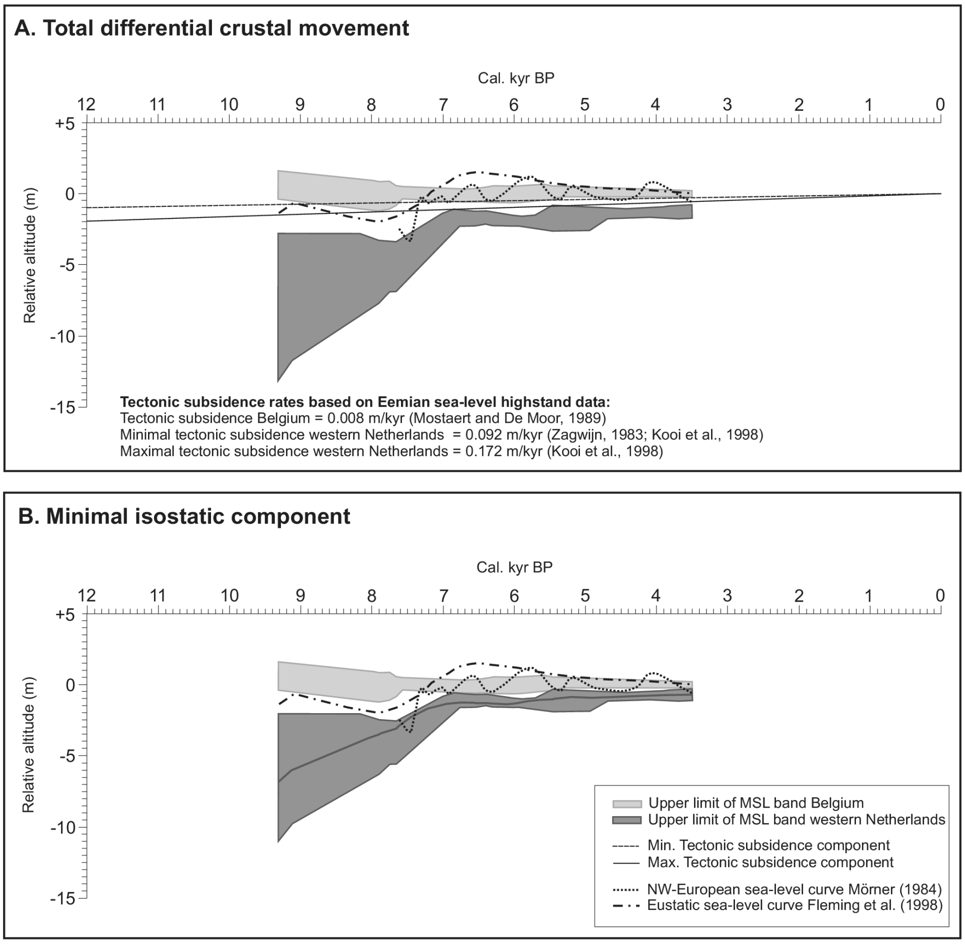

Figure 3.6: Differential crustal movements between Belgium and the western Netherlands following the methods of Kiden et al. [2002] but with the standardised data used in this paper. Note that the error bands for the upper limits of local MSL (i. e. the raw data) are compared. (A) Total differential crustal movement; (B) Minimal isostatic component (i. e. the maximal long-term tectonic subsidence component has been subtracted from the total differential movement).

resulting from the use of present-day large tidal ranges, and so the actual isostatic component is likely to lie between the values indicated in Figs. 3.6B and 3.7B.

Interestingly, the extreme lower limit of MSL error bands of Belgium and north-western Germany show no overlap until ca. 4.8 cal. kyr BP when they finally converge, even after subtraction of the maximal tectonic component between the two areas (Fig. 3.7). This means that even when the sea-level index points from the Belgian coastal plain should represent MHW, and when the exceedingly large present-day tidal range is used for correction to MSL (both situations being highly unlikely), there is still no overlap between the MSL error bands of the two areas from 9 to 5 cal. kyr BP. Thus, contrary to the general belief that the German North Sea coast has remained isostatically stable during the Holocene [e. g. Behre, 2003], these comparisons show that the north-western German coast has indisputably undergone considerable isostatic subsidence during the last 10 cal. kyr BP. Assuming that the tectonic activity has been adequately corrected for (i. e. neglecting the possibility of small-scale, local differential crustal

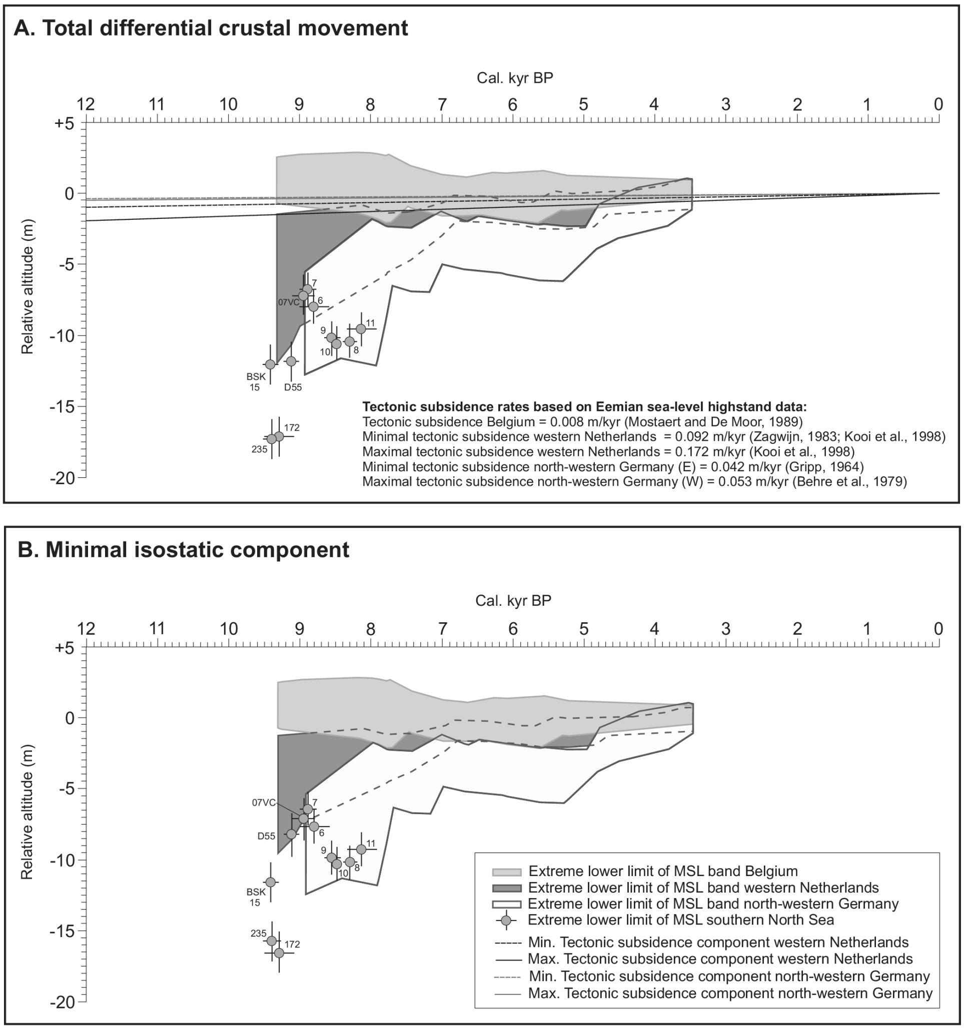

Figure 3.7: Differential crustal movements between Belgium, the western Netherlands, north-western Germany and several positions in the southern North Sea based on the error bands for the extreme lower limits of MSL. (A) Total differential crustal movement; (B) Minimal isostatic components (i. e. the maximal long-term tectonic subsidence components between the regions have been subtracted from the total differential movements). Note that conversion to extreme lower limit of MSL leads to significant overlap between the Belgian and western Netherlands MSL error bands, whereas north-western Germany shows a discrete isostatic subsidence component relative to Belgium before 4.8 cal. kyr BP. The isostatic subsidence components of the southern North Sea samples are based on the subtraction of estimated Quaternary tectonic subsidence rates only (see text), and should thus be interpreted with caution.

movement within the studied areas themselves) and using MSL curves which are drawn through the lowest / youngest index points, we can tentatively provide a rate of isostatic subsidence relative to Belgium of ca. 7.5 m over the last 8 cal. kyr BP for north-western Germany and ca. 2.5 m over the same time interval for the western Netherlands. These values can even be considered to approximate absolute isostatic subsidence rates as the Belgian sea-level curve compares well to the eustatic and north-western European sea-level curves, so that the area has probably been minimally affected by isostatic crustal adjustment processes.

The heights of several sea-level index points from the southern North Sea are also illustrated in relation to the Belgian curve in Fig. 3.7A. Unfortunately, the absence of Belgian sea-level data before 9.4 cal. kyr BP means that relationships with older North Sea samples cannot be analysed. Nevertheless, the sea-level index points around 9 cal. kyr BP illustrate how variable the crustal movements in the North Sea may have been: sample 07VC from Helgoland shows a total differential crustal movement of only 7.2 m with respect to Belgium, sample D55 from the Dogger Bank, however, shows a difference of 11.85 m and samples 235 and 172 from the Weiße Bank and northern grounds (near the border with the Danish North Sea sector) provide huge altitude differences of 17.35 m and 17.15 m, respectively. We cannot differentiate clearly between tectonic and isostatic components in this case, as most short-term tectonic subsidence rates are unknown for the North Sea region. When, in the absence of other data, average Quaternary sedimentation rates [Caston, 1979] are taken as an approximate measure of long-term tectonic subsidence, the hypothetical isostatic component of the total differential crustal movement in the North Sea almost doubles from the approximate Dogger Bank – Helgoland – north-western German coast 7.5-m-isobase to the locations of the Weiße Bank and the northern grounds (Fig. 3.7B). We must however bear in mind that these values are rough predictions only and not based on suitably young tectonic subsidence data, which may well deviate from those taken to represent the Quaternary as a whole [e. g. Kiden et al., 2002, section 3.6.3 of this paper].

Despite the uncertainties involved we believe that the relationships described above provide additional evidence for the original hypothesis of Kiden et al. [2002], which states that the amount of isostatic subsidence decreases strongly in a south-westerly direction through north-western Europe and with time. The data do not contradict the idea of Holocene subsidence of a so-called peripheral glacial forebulge around the Fennoscandian ice zone or zone of glacio-isostatic rebound, which was previously reconstructed from both model and observational data and is assumed to have been centred in the North Sea between Norway and Great Britain, extending through north-western Netherlands and northern Germany [Fjeldskaar, 1994; Lambeck, 1995]. In fact, the postulated strong increase in the relative isostatic subsidence component around the Weiße Bank and the northern grounds may indicate that this region lies close to the centre of the bulge.

3.4 Geodynamic modelling

In addition to allowing visual comparisons between northwest German sea-level index points and sea-level data from the Netherlands and Belgium, the newly acquired standardised dataset of relative sea-level rise in NW Europe as summarised in Tab. A.1 can be used for geodynamic modelling of the Earth's internal structure. Precise model predictions of the Earth's structure beneath north-western Germany and the southern North Sea area do not exist yet, mainly due to the fact that such sea-level data were relatively inaccessible until now. Nevertheless, although even with the present dataset only a few deep / old North Sea and German coast sea-level index points exist, such data are essential for improving the resolution of the Earth's structure modelling in general. As glacial isostatic adjustment (GIA), which we have shown to definitely influence the areas under consideration, is mainly controlled by the Earth's mantle and the thickness of the lithosphere, it is possible to investigate and determine the regional radial Earth's structure with the help of an earth model, a global ice and ocean model, and the observational data mentioned above. The applied models and the calculation method have been extensively described in Steffen and Kaufmann [2005]. Hence, the methodology is summarised only briefly here and we refer to the above-mentioned article for more detailed information.

3.4.1 Earth model

Model predictions are carried out using a spherically symmetric, compressible, Maxwell-viscoelastic earth model. The elastic parameters derive from PREM [Preliminary Reference Earth Model: Dziewonski and Anderson, 1981], and lithospheric thickness is a free parameter. The mantle viscosity is parameterised into several sub-lithospheric layers with constant viscosity within each layer. The lower boundary condition is the Earth's core, which is assumed to be inviscid. In this paper, two sub-lithospheric viscosity layers have been assigned to an upper and lower mantle with constant viscosity, respectively. Thus, together with the free parameter lithospheric thickness, the sea-level predictions are calculated for a three-layer earth model. Recently, modelling investigation for GIA has changed from 1D and 2D inversion methods [e. g. Lambeck, 1993a,b; Lambeck et al., 1996, 1998a,b; Steffen and Kaufmann, 2005] to 3D flat [e. g. Wu and Johnston, 1998; Kaufmann and Wu, 1998a,b; Kaufmann et al., 2000; Kaufmann and Wu, 2002; Kaufmann et al., 2005; Wu, 2005; Steffen et al., 2006a] and spherical Finite Element models [e. g. Wu, 2002; Zhong et al., 2003; Wu and van der Wal, 2003; Wu et al., 2005; Latychev et al., 2005a,b]. However, we have chosen the 1D inversion method here as it is simple, efficient and, in comparison to former 1D investigations, the small distance between the different regional datasets might provide more precise information concerning the Earth's 3D structure in NW Europe. The search range has been set between 60 and 160 km for the lithospheric thickness H_l, from 10^{19} to 4×10^{21} Pa s for the upper-mantle viscosity η_{UM}, and from 10^{21} to 10^{23} Pa s for the lower-mantle viscosity η_{LM}. The total number of possible earth models which can explain our observational data is thus restricted to 1089.

Surface deformation is calculated by loading each earth model with predetermined ice loads. Using the sea-level equation of Farrell and Clark [1976] for a rotating Earth, which can be rewritten as an integral equation which we solve iteratively, we then derive the relative sea-level change. This is compared to the observational data and the best-fit earth model is chosen.

3.4.2 Ice model

For the Late Pleistocene glacial ice load history, the global ice model RSES (Research School of Earth Sciences, Canberra) is used. RSES comprises Late Pleistocene ice sheets over North America, Northern Europe, Greenland, the British Isles, and Antarctica. The reconstructions are based on glaciological and geomorphological evidence and thus reflect the approximate extent of the Late Pleistocene ice sheets throughout the last glacial cycle. The model has been converted from the radiocarbon timescale to the U/Th timescale, using the CALIB-4 conversion program [Stuiver and Reimer, 1993; Stuiver et al., 1998]. The ice volume at the Last Glacial Maximum (LGM), approximately 21,400 years BP, corresponds to 124 m of eustatic sea-level change. The ice extent for four different epochs, starting at the LGM, can be found in Fig. 3.8. It shows the retreat of the large Weichselian Ice Sheet from a multi-dome complex covering Scandinavia and the Barents Sea to land-based ice-sheets over Svalbard, Franz-Joseph-Land, and Scandinavia. The ice disappeared in that model around 9000 years ago.

3.5 Observational data

The sea-level observational data presented in section 3.2 and Tab. A.1 from NW Europe have been grouped into three main regions for geophysical modelling calculations (Belgium, the Netherlands and Germany), although two additional datasets including only offshore data and including all locations were used as well. Several of the index points have been used in more than one dataset, depending on their

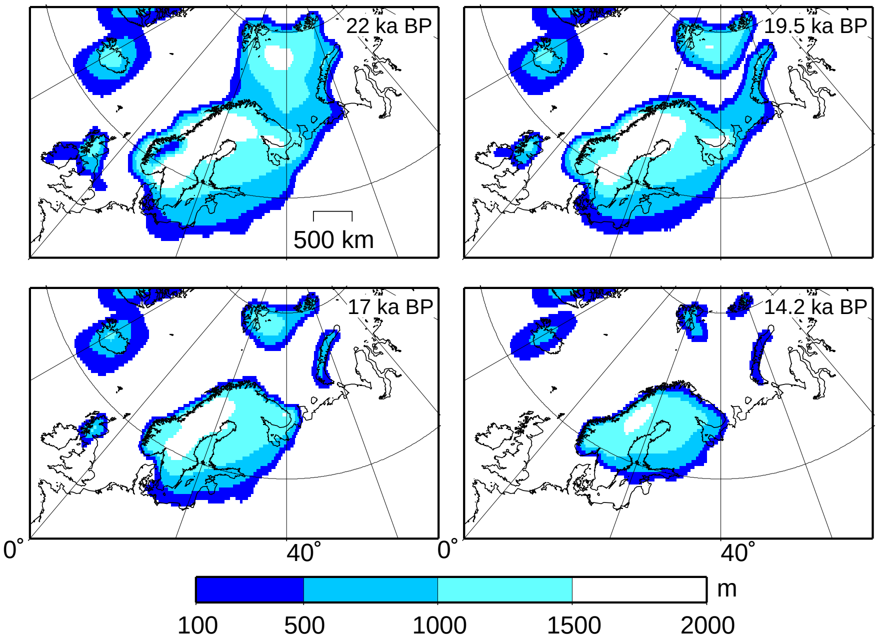

Figure 3.8: Map of ice model RSES over Europe for four different time epochs. Contours represent 500 m height intervals.

locality. Thus, five datasets were arranged as follows (total number of index points in brackets):

- Belgium (46), consisting of 21 Belgian and 25 Zeeland sea-level index points;
- The Netherlands (70), encompassing 61 Netherlands index points, the 7 Dutch North Sea points and the 2 points from the Dogger Bank;
- Germany (124), comprising the north-western German dataset with 112 index points, 5 points from Winschoten (Northern Netherlands) and 7 German North Sea index points;
- North Sea (22), including 7 German North Sea locations, 7 Dutch North Sea locations, 2 index points from the Dogger Bank and 6 German Coast index points; and
- European coast (240), a dataset of all index points.

6 of the southern North Sea index points which were originally obtained by Streif et al. [1983] have been added to Tab. A.1 and Fig. 3.4, but have not been used for geophysical modelling purposes due to poor data quality (see section 3.2.2.4 for more information). The allocation of index points to particular regional subsets was carried out in such a way that each subset comprises data points which lie within a characteristic part of the “banana” shape of the Fennoscandian forebulge as shown in Fig. 2 of Kiden et al. [2002].

As compaction might have a significant influence on our model predictions (especially in the north-western German dataset where several of the index points derive from intercalated peats), we decided to produce an additional “test” dataset in which compaction has been tentatively corrected for by simply assuming 50% compaction of original peat beds [i. e. a compaction factor of 2 following van de Plassche et al., 2005]. Index points which have likely been affected by compaction are indicated in Tab. A.1 in the last but one column and by arrows in Figs. 3.2 - 3.4. Compaction corrections were carried out for 12 index points for the Belgian dataset (26% of the total data points), 4 index points from the Netherlands (6%), 24 points from north-western Germany (19%), 2 points from the southern North Sea (9%), and thus for a total of 40 index points from the entire European Coast dataset (17%).

3.6 Results

In this section, predicted RSL changes are compared to the subsets of sea-level observational data in order to determine the best-fit earth models for the different regions under consideration. This comparison is based on a least-squares misfit, defined as

$$\chi = \sqrt{\frac{1}{n}\sum_{i=1}^{n}\left(\frac{o_i - p_i(a_j)}{\Delta o_i}\right)^2}, \tag{3.1}$$

where n represents the number of observations considered, o_i the observed RSL data, $p_i(a_j)$ the predicted RSL for a specific earth model a_j, and Δo_i the data uncertainty. The search for a minimum value of χ within the parameter range produces an earth model a_b, which fits the observational dataset best. In the ideal situation that the model is complete and the observational uncertainties are normally distributed with known standard deviations and uncorrelated, the expected best fit would be $\chi = 1$. To bracket all earth models that fit the observational data equally well as the best-fit earth model a_b within the observational uncertainties, a confidence parameter is calculated as follows:

$$\Psi = \sqrt{\frac{1}{n}\sum_{i=1}^{n}\left(\frac{p_i(a_b) - p_i(a_j)}{\Delta o_i}\right)^2}. \tag{3.2}$$

For all confidence parameters $\Psi \leq 1$, the predicted RSL for a specific earth model $p_i(a_j)$ fits the observational data as well as that of the best-fit earth model $p_i(a_b)$ within the 1σ-uncertainty.

3.6.1 Model results without compaction corrections in the observational dataset

When a parameter search of datasets without correction for possible compaction effects is carried out, the following patterns become evident (Fig. 3.9):

Belgium: In Fig. 3.9A and B, the 1σ range based on the Belgian RSL dataset is shown in the parameter space with a light-grey shading. The best-fit earth model (triangle) has a lithospheric thickness of $H_l =$ 90 km, a fairly low upper-mantle viscosity of $\eta_{UM} = 2 \times 10^{19}$ Pa s, and a lower-mantle viscosity of $\eta_{LM} = 10^{23}$ Pa s. The misfit for this model is $\chi = 1.60$. However, all three parameters are not well constrained. Notably, the lithospheric thickness varies over nearly the total range of parameter values ($H_l \in [60, 150]$ km). Taking only the 1σ range into account, the upper-mantle viscosity seems to be well constrained ($\eta_{UM} \in [1.5, 2] \times 10^{19}$ Pa s), but a closer look with the help of the 2σ range (not shown) shows a totally different second minimum area $> 4 \times 10^{20}$ Pa s with a $\chi < 2$ region in the range of $H_l \in [60, 100]$ km and $\eta_{UM} \in [8 \times 10^{20}, 2 \times 10^{21}]$ Pa s. The best-fit model for the second minima is $H_l = 60$ km, $\eta_{UM} = 2 \times 10^{21}$ Pa s, and $\eta_{LM} = 2 \times 10^{22}$ Pa s with $\chi = 1.68$ (inverted triangle in Fig. 3.9A and B). The large confidence areas and the good fit of several different earth models to the dataset are a consequence of the spatial and temporal distribution of the Belgian RSL data (Fig. 3.5), which compare well with eustatic and NW-European sea level and thus apparently simply trace our ocean model. This

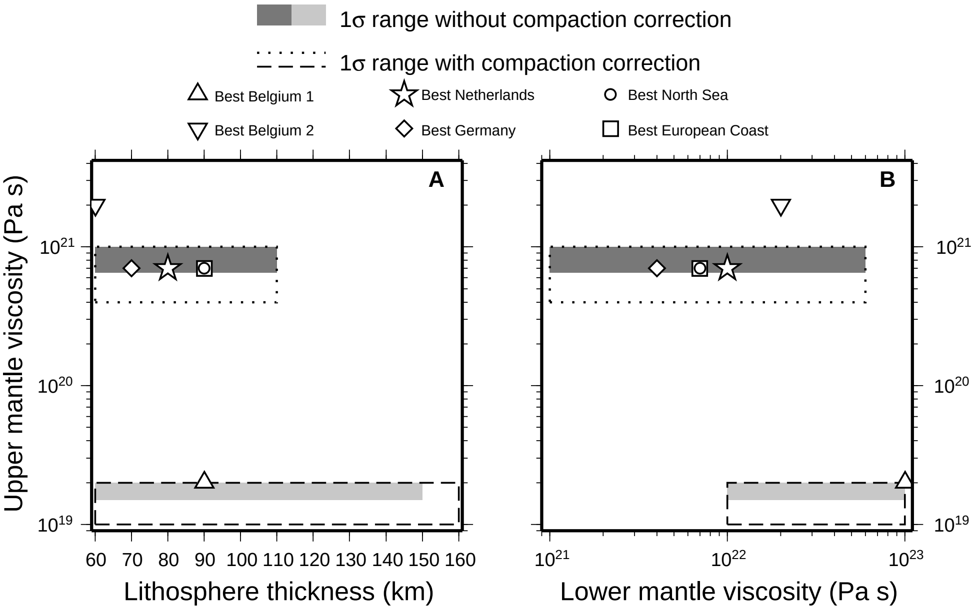

Figure 3.9: Best regional 3-layer earth models (marked with a symbol) and the confidence regions $\Psi \leq 1$ for NW Europe RSL datasets without compaction correction (shaded) and with compaction correction (framed) and ice model RSES. Belgium: light-grey shading and dashed line; other NW European regions: dark-grey shading and dotted line; (A) RSL data as a function of lithospheric thickness and upper-mantle viscosity for a fixed lower-mantle viscosity of 10^{23} Pa s for Belgium, of 10^{22} Pa s for the Netherlands, of 4×10^{21} Pa s for Germany, of 10^{22} Pa s for the North Sea, and of 7×10^{21} Pa s for Europe. (B) RSL data as a function of upper and lower-mantle viscosities for a fixed lithospheric thickness of 90 km for Belgium, of 80 km for the Netherlands, of 70 km for Germany, of 90 km for the North Sea, and of 90 km for Europe.

confirms the stable behaviour of the Belgian crust during and after the last ice age [Kiden et al., 2002]. Hence, the data are not very sensitive to the Earth's interior structure and additionally too far away from former ice sheets (British Isles and Scandinavia) to allow a better determination of the Earth's structure beneath Belgium with this method.

The Netherlands: The best-fit earth model for this data-subset (star in Fig. 3.9A and B) is characterised by a lithospheric thickness of $H_l = 80$ km, and upper- and lower-mantle viscosities of $\eta_{UM} = 7 \times 10^{20}$ and $\eta_{LM} = 10^{22}$ Pa s, respectively. The misfit for this model is $\chi = 1.36$. While the large confidence range (Tab. 3.1) for the lower-mantle viscosity ($\eta_{LM} \in [10^{21}, 6 \times 10^{22}]$ Pa s) again confirms the poor resolving power of the NW European RSL data for larger mantle depths, the lithospheric thickness as well as the upper-mantle viscosity are better constrained than for Belgium, with permissible ranges limited to $H_l \in [60, 100]$ km and $\eta_{UM} \in [7 \times 10^{20}, 10^{21}]$ Pa s, respectively. No second minimum area was found.

Germany: The best-fit earth model for the German data-subset (diamond in 3.9A and B) is characterised by a lithospheric thickness of $H_l = 70$ km, and upper- and lower-mantle viscosities of $\eta_{UM} = 7 \times 10^{20}$ and $\eta_{LM} = 4 \times 10^{21}$ Pa s, respectively. The misfit for this model is $\chi = 1.75$, which is slightly higher than those for the previous datasets of Belgium and the Netherlands. This might be a result of (i) the total number of index points (124 compared to 46 and 70, respectively), (ii) the spatial and temporal distribution of the dataset, the index points deriving from a relatively large geographical area, including several offshore points, and covering a large time interval compared to other subsets (see Figs. 3.1 and 3.3), and / or (iii) variable compaction effects, which are likely to be large for the intercalated peats of this subset. Again,

Table 3.1: Three-layer earth models. Free parameters are lithospheric thickness H_l, upper-mantle viscosity η_{UM}, and lower-mantle viscosity η_{LM}. χ is the misfit for the best 3-layer earth model. Results for the three-layer Earth models fitting the NW European RSL data within the 1σ-uncertainty range are shown for different datasets, with the best-fit earth models indicated between brackets. For Belgium, the best-fit earth model of the second minima is also shown (see section 3.6.1 for details.)

	H_l km	η_{UM} 10^{20} Pa s	η_{LM} 10^{22} Pa s	χ
Search range	60-160	0.1-40	0.1-10	
Dataset		RSES		
Belgium				
no compaction	60 - 150 (90)	0.15 - 0.2 (0.2)	1 - 10 (10)	1.60
2nd minima	60	20	2	1.68
with compaction	60 - 160 (90)	0.1 - 0.2 (0.2)	1 - 10 (10)	1.42
2nd minima	60	20	2	1.54
Netherlands				
no compaction	60 - 100 (80)	7 - 10 (7)	0.1 - 6 (1)	1.36
with compaction	60 - 100 (80)	7 - 10 (7)	0.1 - 6 (1)	1.30
Germany				
no compaction	60 - 90 (70)	6.5 - 10 (7)	0.2 - 0.8 (0.4)	1.75
with compaction	60 - 95 (70)	6.5 - 10 (7)	0.2 - 0.9 (0.4)	1.60
North Sea				
no compaction	75 - 95 (90)	6.5 - 10 (7)	0.2 - 1.5 (0.7)	2.50
with compaction	75 - 100 (90)	4 - 10 (7)	0.1 - 2 (0.7)	2.31
Europe Coast				
no compaction	60 - 110 (90)	6.5 - 10 (7)	0.2 - 1.5 (0.7)	1.76
with compaction	60 - 110 (90)	6.5 - 10 (7)	0.2 - 1.5 (0.7)	1.62

the lower-mantle viscosity is almost unconstrained (Tab. 3.1), while the range of permitted lithospheric thickness values is $H_l \in [60, 90]$ km and for upper-mantle viscosities is $\eta_{UM} \in [6.5 \times 10^{20}, 10^{21}]$. The thickness of the lithosphere (70 km) is the lowest of all analysed datasets.

North Sea: The best-fit earth model (circle in 3.9A and B) has a lithospheric thickness of $H_l = 90$ km, an upper-mantle viscosity of $\eta_{UM} = 7 \times 10^{20}$ Pa s, and a lower-mantle viscosity of $\eta_{LM} = 7 \times 10^{21}$ Pa s. The misfit for this model is $\chi = 2.50$, the highest misfit of all regions, which is not surprising considering the scattered locations of the relatively few index points in a basin which has undoubtedly been influenced by variable crustal movements associated with both tectonic and isostatic activity (see section 3.3). Nevertheless, focussing on the 1σ range (Tab. 3.1), the lithospheric thickness and the upper-mantle viscosity are well constrained ($H_l \in [75, 95]$ km, $\eta_{UM} \in [6.5 \times 10^{20}, 10^{21}]$ Pa s). Hence, the North Sea RSL dataset is more sensitive to the mantle structure than the other RSL datasets. Additionally, the index points are (i) closer to the former ice sheets (British Isles and Scandinavia), and (ii) derive from deeper parts / older deposits than most of the indicators from the other datasets. This allows a better determination of the Earth's structure beneath the southern North Sea region.

European Coast: The best-fit earth model for all data (square in 3.9A and B) is characterised by a lithospheric thickness of $H_l = 90$ km, and upper- and lower-mantle viscosities of $\eta_{UM} = 7 \times 10^{20}$ and $\eta_{LM} = 7 \times 10^{21}$ Pa s, respectively. The misfit for this model is $\chi = 1.76$, the same as that of the German

RSL dataset. It is lower than that of the North Sea, although the best-fit earth model is the same for both regions. Thus, the North Sea index points dominate the selection of the best-fit Earth model, but a better misfit is achieved by using a large amount of coastal data. The values for the entire region agree well with an earlier inference of the reduced set of NW European coastal RSL data from Steffen and Kaufmann [2005].

As summarised in Tab. 3.1, upper-mantle viscosities for all regions except Belgium are around 7×10^{20} Pa s, and cover a range between $\eta_{UM} \in [6.5 \times 10^{20}, 10 \times 10^{20}]$ Pa s. Compared to the results of Steffen and Kaufmann [2005], who reported upper-mantle viscosities of $(3-6) \times 10^{20}$ Pa s for this region, our values are slightly higher, maybe due to the fact that (i) the results of Steffen and Kaufmann [2005] are based on data from the British Isles as well as from NW Europe, and (ii) the NW European data used by these authors was revised and only a few selected for this study (see section 3.2). The lower-mantle viscosity is almost unconstrained, confirming the low resolving power for lower-mantle viscosity of RSL data with a small spatial distribution. Focussing only on the three main regions Belgium, the Netherlands and Germany, the thickness of the lithosphere is determined to be around 90 km under Belgium (the London-Brabant massif region), and then decreases towards the southern North Sea to a thickness of ca. 70 km. However, it is important to emphasise that the 1σ range of possible lithosphere thicknesses is larger ($H_l \in [60, 110]$ km, although similar trends in decreasing thickness may be postulated (Tab.3.1).

3.6.2 Model results with compaction corrections in the observational dataset

In this section, our results from the parameter search of datasets in which compaction has been taken into account are discussed:

Belgium: The 1σ range based on the Belgian RSL dataset with correction of compaction is shown in Fig. 3.9A and B with a dotted line. The resulting best-fit earth model (triangle) is the same as for the dataset without compaction and has a lithospheric thickness of $H_l = 90$ km, an upper-mantle viscosity of $\eta_{UM} = 2 \times 10^{19}$ Pa s, and a lower-mantle viscosity of $\eta_{LM} = 10^{23}$ Pa s. The misfit for this model is $\chi = 1.42$, an improvement of 11% compared to the model without compaction. However, the 1σ ranges for the parameters are slightly larger (e. g. $H_l \in [60, 160]$ km) than those for the dataset without compaction. Taking the 2σ range (not shown) into account, the second minimum area also appears (Tab. 3.1). The best-fit model for the second minima (inverted triangle) is with $H_l = 60$ km, $\eta_{UM} = 2 \times 10^{21}$ Pa s, and $\eta_{LM} = 2 \times 10^{22}$ Pa s, which is the same as that of the uncorrected Belgian dataset, although the misfit with $\chi = 1.54$ has improved by 8% (Tab. 3.1). This improvement of the misfit data after correction for compaction probably occurs due to an even better general fit with the ocean model. Despite the improved misfit, the correction for compaction of between 20 and 35 cm in selected samples is obviously too small to allow a clearer determination of a reliable earth model for this region.

The Netherlands: The best-fit earth model (star in 3.9A and B) also remains the same. The misfit for this model is $\chi = 1.30$, an improvement of 4%. This small improvement is probably due to the fact that only a small number of samples (4 out of 70 locations) were corrected for compaction. Surprisingly, the maximum χ-values around an upper-mantle viscosity of 10^{20} are higher. Here, we think a slight influence of the 4 compaction-corrected data points on model predictions of GIA is possible.

Germany: Fig. 3.9A and B, shows the same best-fit earth model (diamond) as that for the data subset without compaction. The misfit for this model is $\chi = 1.60$, which is an improvement of 8.5% compared to the dataset without compaction. This improvement is comparable with the one from Belgium (11%). Again, a general decrease in the misfit of all models is observed, which is due to the better fit with the ocean model.

North Sea: The best-fit earth model (circle in Fig. 3.9A and B) is the same as that without correction for compaction in the RSL data. The misfit for this model is $\chi = 2.31$, a difference of 8%, which is interesting as only 2 out of 22 index points have possibly been affected by compaction at all. As a general decrease in the misfit of all models is observed again, we assume that the improved misfit is due to the better fit of these 2 locations with the ocean model.

European coast: The best-fit earth model (square in Fig. 3.9A and B) is characterised by the same lithospheric thickness, upper- and lower-mantle viscosities as the model without compaction in the RSL dataset. The improvement in the misfit for this model ($\chi = 1.62$) is 8%.

Tab. 3.1 summarises the results for RSL data with compaction corrections as discussed above. It can be seen that the best-fit earth models are identical. Thus, the consideration of compaction did not help to better isolate specific earth models, despite the decrease in the misfit. Hence, a general lithospheric thickness of around 90 km and an upper-mantle viscosity of around 7×10^{20} Pa s is obtained. The lower-mantle viscosity remains almost unconstrained, confirming the low resolving power for lower-mantle viscosity of RSL data with a small spatial distribution.

3.6.3 Comparison between observational and modelled sea-level curves: some examples

The ice and earth models described in the previous section produce predicted RSL curves for NW Europe which correlate very well with the sea-level observational data (i. e. misfit values are low), thus implying that the models are good enough to predict RSL change for any arbitrary location within the analysed region (e. g. in areas where we have no observational data) as long as we are constantly aware of the assumptions and limitations on which they are based. Fig. 3.10 summarises predicted RSL for 21 selected locations across the region. For each location the best-fit regional Earth model was used to calculate the RSL curve over the last 10 kyr. A clear distinction is made between 1σ RSL in the Belgian and Zeeland areas (nrs. 1 - 5), which approach eustatic values, and those of the remaining regions, which show a quasi-continuous drop in relative altitude from the southwest to the northeast of the analysed area and reflect the increasing net effect of post-glacial isostatic adjustment / subsidence towards the Fennoscandian landmass. The relatively large predicted difference in RSL between the extreme locations of the German dataset (Hatzum [nr. 12] and Föhr [nr. 20], summing up to approximately 3 m at 10 cal. kyr BP) denotes that the data of the German sea-level curve of Behre [2003] cover a geographic area too large to be summarised into a single curve, and that more local sea-level curves are required in order to reinterpret the nature and extent of the regressional phases which Behre [2003] describes for the entire length of the German North Sea coast.

In addition, comparisons between observational and modelled RSL data within a local area allow the identification of "outlier" sea-level index points, which in turn can provide important information on local effects such as tectonic subsidence / uplift, compaction and / or possible past changes in tidal range [e. g. Shennan et al., 2000a]. In most cases, the analysed observational index points lie on or slightly below the predicted RSL curve for a particular region (Fig. 3.11), although some index points also plot too high (e. g. the Winschoten samples, Fig. 3.11E). Determining the relative importance of each of the above-mentioned local factors on these altitude discrepancies is difficult, especially considering the fact that they may have acted simultaneously. Additionally, all MSL index points deriving from limiting raw data (i. e. basal peats reflecting the upper limit of MSL rather than MHW) carry uncertainties in their indicative meaning which can be substantial in areas where present tidal ranges are large. Nevertheless, careful examination of the residuals (= difference between predicted and observed RSL values) can help to elucidate potentially important factors, and we would like to briefly discuss some examples, including

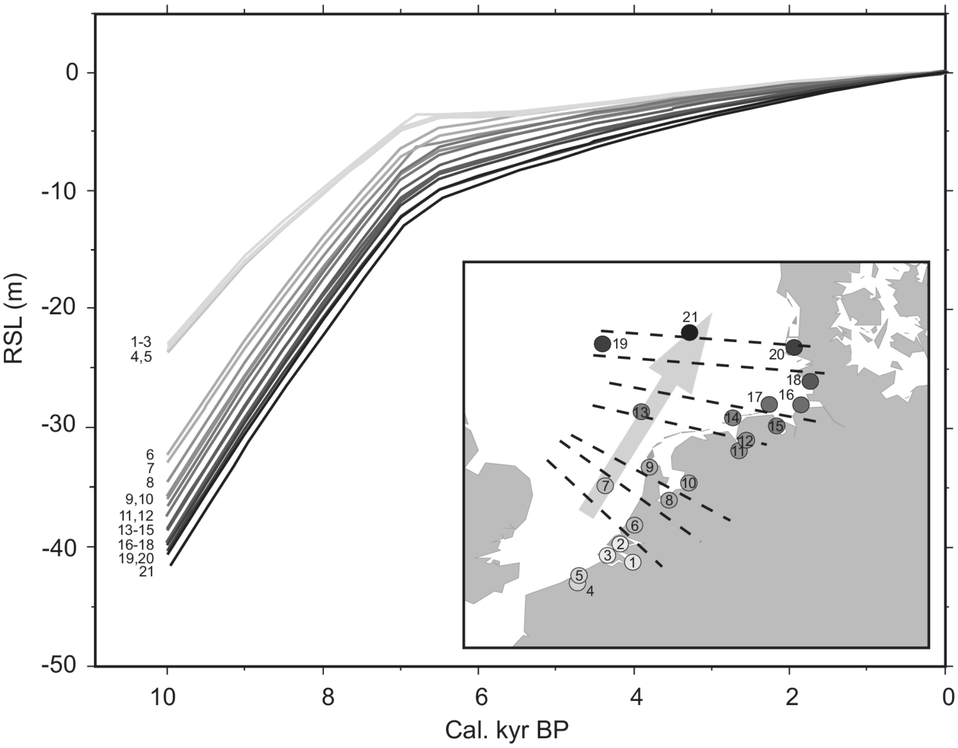

Figure 3.10: Predicted smooth RSL curves based on regional best-fit Earth models for 21 locations in NW Europe, showing a quasi-continuous drop in RSL altitude from the southwest to the northeast of the analysed area. 1 = Berendrechtsluis; 2 = Bouwlust; 3 = Middelburg; 4 = Dijk; 5 = Westende; 6 = Hillegersberg; 7 = Dutch North Sea west; 8 = Almere; 9 = Den Helder; 10 = Schokland; 11 = Winschoten; 12 = Hatzum; 13 = oyster grounds (Dutch North Sea); 14 = Juist; 15 = Wilhelmshaven; 16 = Cuxhaven; 17 = Wangerooge; 18 = Tiebensee; 19 = Dogger Bank; 20 = Föhr; 21 = Weiße Bank.

the constraints involved, in the following section.

In areas such as the Central Netherlands where sample compaction was not considered to be a problem, tectonic activity has been low [Kooi et al., 1998] and tidal ranges were low enough (maximally 0.7 m) to neutralise the uncertainties involved in calculating MSL from limiting data, sea-level index points show an excellent fit to the predicted RSL curve (Fig. 3.11C). However, such a perfect relationship is an exception rather than the general trend of the dataset. For example, many of the Belgian and Zeeland sea-level index points plot considerably below the best-fit (1σ) curve of predicted RSL for the region, but above the curve predicted by the second minimum (described in section 3.6.1, which lies in the 2σ range and most likely contains a small isostatic component (Fig. 3.11A and B). The fact that two very different earth models can show such a good fit with the same dataset is problematic, and has most likely been caused by the scatter in the Zeeland data as well as the good fit of the sea-level data to the general ocean model. The uncertainties carried by the model results hamper the further analysis of observational data, the results being quite anomalous depending on the curve used. When focussing purely on the relatively high position of the best-fit 1σ RSL curve, a change in past tidal range can be postulated. Here, the negative discrepancy between observed and modelled RSL values cannot be explained with tectonic subsidence, as Eemian sea-level highstand sediments are found relatively close to the surface in Belgium [1 - 2 m below present-day MSL, implying a tectonic subsidence rate of only ca. 0.008 m/kyr

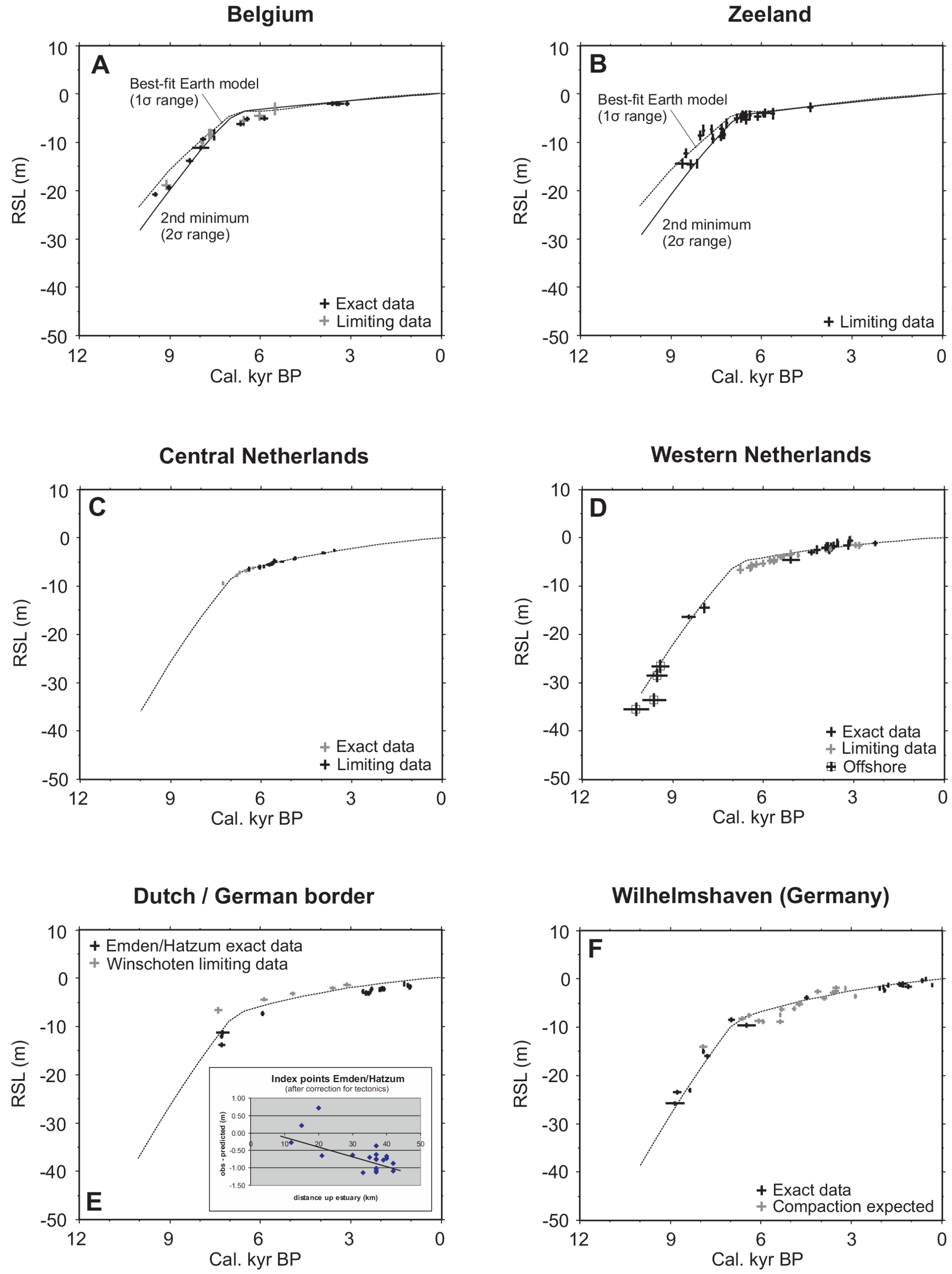

Figure 3.11: Comparisons between observational and predicted RSL data for selected areas within NW Europe. Predicted RSL curves are based on regional best-fit earth models and reflect the situation in one particular location only (i. e. do not indicate small within-region variations in RSL). Discrimination between the use of exact and limiting data has been made. The relationship between the observed-model RSL difference and distance up the Ems estuary (Emden/Hatzum) is shown in the inset of E.

since then: Mostaert and De Moor, 1989], and Kooi et al. [1998] estimate a long-term (Quaternary) tectonic subsidence rate of maximally 0.05 m/kyr for Zeeland. Compaction of peat, when assumed to have occurred at all (Tab. A.1), will only have dropped sample altitude levels by 0.2 to 0.35 m at the most. After correction for these two processes, several of the lower sea-level index points still remain at a depth of around 1 m below the predicted curve, at least between 9 and 6 cal. kyr BP. By ∼3 cal. kyr BP, the index points have drawn near to the predicted curve. This trend could indicate that the sea-level data have been overcorrected to MSL due to the use of present-day high coastal tidal amplitude (1.9 m along the Belgian coastal plain; 1.7 m in Zeeland), suggesting that tidal amplitude was ca. 1 m lower between 9 and 6 cal. kyr BP, and then increased to present-day values by 3 cal. kyr BP. Such a change in tidal amplitude may have been associated with the connection of the North Sea to the English Channel occurring at around 9 cal. kyr BP, and the subsequent swift change of coastline geometry in response to rapid sea-level rise [e. g. Shennan et al., 2000a; Beets and van der Spek, 2000, Fig. 3.12 of this paper]. However, when focussing on the second minimum RSL curve, discrepancies between observed and modelled data are positive between 10 and 7 kyr BP but negative between 7 and 5 kyr BP, which can only be explained by ecological factors such as sea-level independent peat growth and variations in the indicative meaning of the peats leading to an overestimation of MSL, respectively. In reality, changes in tidal range may well have acted simultaneously with these factors. The area has simply been too little affected by GIA to allow a clear discrimination between the two model RSL options.

The limiting data obtained from the Hillegersberg donk of the western Netherlands Rhine-Meuse area also appear to reflect an overestimation to MSL (grey points between 7 and 4 cal. kyr BP on Fig. 3.11D). Sample compaction was not assumed to be a problem for these index points, but variable tectonic activity will have occurred within the structurally complex Rhine valley. Based on long-term Quaternary subsidence rates [Kooi et al., 1998] and the height of Eemian sea-level highstand sediments in Amersfoort which occur at ∼8 m below present-day MSL [Zagwijn, 1983], an average regional tectonic subsidence rate of 0.092 m/kyr can be tentatively assumed for the area. Although greatly simplified, we suggest that rates will not have greatly exceeded this value, as the index points deriving from exact data already lie close to the predicted RSL curve (Fig. 3.11D). After correction for tectonics, the limiting index points of Hillegersberg still lie below the predicted RSL curve, the residuals steadily decreasing from -1.34 m to -0.23 m between 6.8 and 5.4 cal. kyr BP, respectively. Even if we assume that these index points were formed at MSL rather than reflecting its upper limit, corrected residuals remain negative and still decrease from -1 m to -0.1 m between 6.8 and 5.7 cal. kyr BP, respectively. This suggests that peat formed locally *below* MSL at this donk during the given time interval, which is highly unlikely in this humid, river-influenced environment where problems associated with peat growth above contemporaneous MSL due to the river-gradient effect would be much more likely [van de Plassche, 1982]. As depth and age determination for these index points are considered to be absolutely unambiguous [van de Plassche, 1982] and MSL levels are independent of past changes in tidal range, only compaction of the older / deeper samples can explain the observed negative residuals. Indeed, van de Plassche [1982] states that “Whether the data from the river dunes are entirely free of subsidence due to compaction is not absolutely certain. ’Donken’ may be underlain by a layer of sandy clay or loam, as in all probability is the case for the ’donk’ of Hillegersberg (Grondmechanische Dienst Rotterdam)”. However, he assumed that by the time peat growth commenced on the slope of the dune, consolidation of the sandy clay / loam under the weight of the dune would have proceeded to such an extent that the effect of further loading would be negligible. Our data, however, show that sediment compaction was still in process at this donk at 6.8 cal. kyr BP, the effects of compaction gradually decreasing towards 5.7 cal. kyr BP and then becoming negligible after that time. Sea-level index points of the other donks incorporated into the dataset seem to have been much less affected by compaction.

Trends shown by the German sea-level index points are somewhat easier to interpret, as the north-western German coast has been less influenced by variable tectonic activity and all observational data were obtained from exact MHW data. For example, a clearly lower past tidal range is reflected by the sea-level data of Emden/Hatzum (Fig. 3.11E), which derive from the Ems River estuary (close to the Dutch border, see Fig. 3.10) and where tidal ranges at present vary between 2.6 and 3 m. After correction for an average tectonic subsidence rate of 0.053 m/kyr based on Eemian sea-level highstand sedimentary data from the island of Juist [Behre et al., 1979], all observational index points still lie below the predicted RSL curve by, on average, about 0.7 m. As compaction effects were assumed to be negligible by the original authors [see Behre, 2003], this discrepancy can only be explained by an overcorrection to MSL using present-day tidal ranges. Furthermore, when the residuals are plotted against distance up-estuary following Shennan et al. [2000a], we see that the discrepancies increase with increasing distance from the coast (Fig. 3.11E inset). Thus, it appears that tidal dampening occurred up-estuary at least until 1 cal. kyr BP, with reconstructed tidal ranges varying from ca. 1.6 - 2 m in the outer estuary to only about 0.8 - 1 m in the inner estuary. Differences occurring between samples of the same distance may be due to differing bathymetries, local tectonics, consolidation or sea-level independent peat formation. The effects of the latter process are nicely illustrated by the limiting sea-level data from Winschoten (northern Netherlands, close to Emden), which plot almost a metre above predicted RSL even without possible upward corrections for compaction and / or local tectonics (Fig. 3.11E). They have obviously been formed in a groundwater-related setting above contemporaneous MSL and are thus unsuitable for sea-level studies of the region.

As mentioned in earlier sections, one of the disadvantages of the German dataset is that many of the older sea-level data derive from compaction-sensitive intercalated peats which can, strictly speaking, only deliver limiting information. We plotted the sea-level data from the region around Wilhelmshaven, where most of the intercalated peats of the dataset are concentrated, in Fig. 3.11F. The exact data show that the high present-day tidal ranges (3 - 3.7 m) which were used for the conversion to MSL are more or less confirmed for the past 9 cal. kyr BP. However, index points which may have been influenced by (considerable) compaction due to intercalation tend to plot on both sides of the predicted RSL curve, implying the possibility of compaction effects of up to 2.5 m between 6 and 4.9 cal. kyr BP, but a form of negative compaction of up to 1 m between 4.7 and 3.2 cal. kyr BP! As local uplift phenomena are highly unlikely and undocumented for the region, these high observational MSL values despite likely effects of compaction may be a true reflection of the Calais IV transgression and the succeeding regression 2 described by Behre [2003]; possible fluctuations of this nature not being incorporated into RSL models. However, the data do not allow further statements on the effects of compaction on index point altitude at this stage.

As a last example, we show that contrary to all other data, altitude differences between southern North Sea observational and predicted MSL often exceed 1 - 2 m, even reaching a value of 10.17 m at the Dogger Bank (Tab. 3.2). Basal peat compaction was not assumed to have greatly affected the altitudes of the observational data. Furthermore, with the exception of the German near-coastal index points, low present-day tidal amplitudes of maximally 0.8 m were used to calculate MSL from MHW at these sites. Thus, in the unlikely case of an even lower past tidal amplitude, the altitude difference would actually not undergo a substantial change. Indeed, residuals from Wilhelmshaven have also shown that tidal ranges in that area probably remained relatively constant throughout the Holocene (Fig. 3.11F). Negative residual values greater than the range of the index point MSL error band are therefore considered to significantly reflect tectonic subsidence in the southern North Sea (as shown by the horizontal grey bars in Tab. 3.2). Positive residuals imply tectonic uplift but more likely represent peat formation above contemporaneous sea level or an artefact in the model predictions due to the restricted use of only one best-fit Earth model

Table 3.2: Rough predictions of Holocene tectonic and / or compactional subsidence in the North Sea as determined from MSL residuals. Negative residual values greater than the range of the observed MSL error band are considered to significantly reflect subsidence and are indicated by the grey bars in the table. Positive residuals imply tectonic uplift but more likely represent peat formation above contemporaneous sea level or a poor relationship to the applied best-fit earth model. A comparison with average Quaternary sedimentation rates as a simplistic measure of total Quaternary subsidence [deduced from Caston, 1979] suggests an approximate 2 - 4 times higher subsidence rate during the Holocene.

no.	sample location	age (cal. kyr BP)	MSL obs (m NN)	error (+/-) (m)	MSL pred (m NN)	residual (obs-pred) (m)	implied tectonic uplift (Holocene: m/kyr)	av. Quat. thickness (m) (from Caston, 1979)	av. Quat. sed. rate (m/kyr)
5	Dogger Bank 55	9060	-31.56	1.4	-30.45	-1.11	-0.12	800	0.4
1	Dogger Bank	9710	-46.7	1.4	-36.53	-10.17	-1.05	700	0.35
3	Weiße Bank 235	9180	-38.98	1.4	-34.78	-4.2	-0.46	350	0.175
3	Weiße Bank 235	9500	-39.08	1.4	-36.64	-2.44	-0.26	350	0.175
Gauss 1987/5	Weiße Bank	10590	-48.84	1.4	-48.88	0.04	0	280	0.14
4	Northern grounds 172	9410	-38.28	1.4	-35.09	-3.19	-0.34	200	0.1
BSK VC-15	Northern grounds	9490	-34.15	1.4	-34.37	0.22	0.02	100	0.05
BSK VC-21	Northern grounds	9950	-37.36	1.4	-38.72	1.36	0.14	100	0.05
AU04-07-VC	Helgoland	9020	-25.23	1.4	-27.89	2.66	0.29	20	0.01
6	Wangerooge A10	8860	-25.93	0.45	-24.88	-1.05	-0.12	20	0.01
7	Wangerooge A10	8790	-23.6	0.5	-25.91	2.31	0.26	20	0.01
8	Wangerooge A10	8370	-23.16	0.5	-23.17	0.01	0	20	0.01
9	Scharhörn 56/67	8560	-25.9	0.5	-25.56	-0.34	-0.04	20	0.01
10	Scharhörn 58/67	8500	-25.84	0.5	-24.74	-1.1	-0.13	20	0.01
11	Neuwerk 60/67	8150	-22.81	0.5	-22.67	-0.14	-0.02	20	0.01
2	oyster grounds	9710	-43.2	1.4	-37.4	-5.8	-0.60	500	0.25
1	oyster grounds	11300	-46.7	1.4	-51.07	4.37	0.39	750	0.375
2	oyster grounds	10610	-47.7	1.4	-47.19	-0.51	-0.05	1000	0.5
5	west	9410	-26.7	1.4	-27.77	1.07	0.11	400	0.2
6	west	9520	-28.7	1.4	-28.51	-0.19	-0.02	300	0.15
7	west	9610	-33.7	1.4	-32.91	-0.79	-0.08	200	0.1
8	west	10210	-35.7	1.4	-34.37	-1.33	-0.13	150	0.075

for all North Sea sample locations. A comparison between our rough estimations of potential Holocene tectonic subsidence rates and average Quaternary sedimentation rates [calculated from Caston, 1979] as a simplistic measure of total Quaternary subsidence of the North Sea Basin suggests an approximate 2 - 4 times higher subsidence rate during the Holocene (Tab. 3.2). One possible cause could be the uncertainty in determining the base of the Quaternary and / or the exact amount of time constrained by Quaternary sediments in the North Sea [Caston, 1979]. However, another factor which certainly forms part of the tectonic component, especially in regions where the Late Pleistocene / Holocene sedimentary layer is thick, is Holocene compaction of underlying Cenozoic sediments (e.g. Tertiary marine shales) in response to sediment loading [e. g. Kooi et al., 1998]. In many coastal parts of the Netherlands, this factor contributes as much to the present total vertical land movement as do the long-term factors together [Kooi et al., 1998]. Such a form of short-term Holocene subsidence could thus explain at least one order of magnitude when comparing subsidence rates at different time scales. Although we are aware of the fact that one best-fit earth model for the southern North Sea may oversimplify matters, it is promising that precisely this model is capable of reconciling both offshore and coastal data in the total NW-European dataset and thus we assume that these first tentative estimates of short-term tectonic and / or compactional subsidence of the southern North Sea fall within the spectrum of acceptable values until more detailed surveys are carried out.

3.7 Conclusions

The observational and geophysical reassessment of 245 previously published, valid Holocene sea-level index points from the NW European coast reveals a complex pattern of differential crustal movement between Belgium, the Netherlands and north-western Germany which cannot be solely attributed to tectonic activity. It clearly contains a non-linear, glacio- and/or hydro-isostatic subsidence component, which is negligible on the Belgian coastal plain but increases significantly towards the northeast in the direction of the Fennoscandian land mass. North-western Germany, for example, has been subjected to a total isostatic lowering of ca. 7.5 m between 8 and 4.8 cal. kyr BP, after which isostatic subsidence processes can no longer be unambiguously identified using our simple comparative approach. Nevertheless, our analyses show that neither the western Netherlands sea-level curve of van de Plassche [1982], nor the German sea-level curve of Behre [2003] can be viewed as optimally reflecting absolute sea-level rise in north-western Europe (at least not during the early and middle Holocene). Our results confirm former investigations of Kiden et al. [2002] from the Belgian-Netherlands coastal plain and provide new evidence from the German and southern North Sea sectors for the post-glacial collapse of the so-called peripheral forebulge which developed around the Fennoscandian centre of ice loading during the last glacial maximum. However, sea-level index data extending northwards into the Danish sector and north-westwards into the deeper parts of the North Sea are now urgently required in order to better constrain the geographical extent and the temporal progression of (early) forebulge collapse, respectively.

Geodynamic modelling of the Earth's internal structure, using a spherically symmetric, compressible, Maxwell-viscoelastic earth model, a global ice (RSES) and ocean model and the sea-level observational data, reveals that a broad range of Earth parameters fit the Belgian RSL data, the ranges then becoming narrower towards the southern North Sea region. In fact, the Belgian data appear to simply trace the ocean model, confirming the stable behaviour of the Belgian crust during and after the last ice age [Kiden et al., 2002]. Hence, the data are not very sensitive to changes in the Earth's interior structure and additionally too far away from former ice sheets (British Isles and Scandinavia) to allow a better determination of the Earth's structure beneath Belgium with this method. The models which show a best fit with the remaining RSL data predict an average lithosphere thickness of ca. 90 km along the NW-European coast, although thicknesses decrease to values around 80 km beneath the Netherlands and 70 km below north-western Germany. Upper mantle viscosities for all regions except Belgium are well-constrained at ca. 7×10^{20} Pa s, and cover a range between $\eta_{UM} \in [6.5 \times 10^{20}, 10 \times 10^{20}]$ Pa s. Lower mantle viscosities are, however, almost unconstrained, confirming the low resolving power for lower mantle viscosity of RSL data with a small spatial distribution. These results confirm earlier findings of Lambeck et al. [1998a] and Steffen and Kaufmann [2005]. In the model predictions, a general misfit improvement of at least 4% due to correction for compaction was observed, being around 8% for the whole dataset, which is mainly due to a better fit with the ocean model. Using the best-fit earth model for the NW European coast and modern bathymetry, Holocene palaeogeographies which reflect the transgression of the southern North Sea coastline can be reconstructed (Fig. 3.12). The most important events are the opening of the English Channel from the south ($\sim$10 cal. kyr BP), the development of the Dogger Bank as an island ($\sim$9.5 cal. kyr BP), the connection between the English Channel and the transgressive North Sea ($\sim$9 cal. kyr BP), the drowning of Dogger Bank ($\sim$7.5 cal. kyr BP) and the development of a close-to-modern southern North Sea coastline ($\sim$7 cal. kyr BP). The reconstructions compares well with those of Shennan et al. [2000b] for the western North Sea based on data and model results from eastern England, although our data suggest an approximately 0.5 kyr earlier drowning of the majority of the Dutch and German sectors of the southern North Sea at ca. 9 cal. kyr BP. It would be interesting to combine both datasets and recalculate palaeogeographies in future analyses.

The comparison between modelled and observational sea-level data can provide important information on local-scale processes such as temporal changes in tidal range (Belgian coast; Ems estuary), differences in the indicative meaning of limiting peat data in relation to MSL (Zeeland), sediment compaction (Hillegersbergdonk), and/or tectonic subsidence (North Sea). However, additional observational data are required in order to pin down more exact earth models with a smaller variation in parameter range for

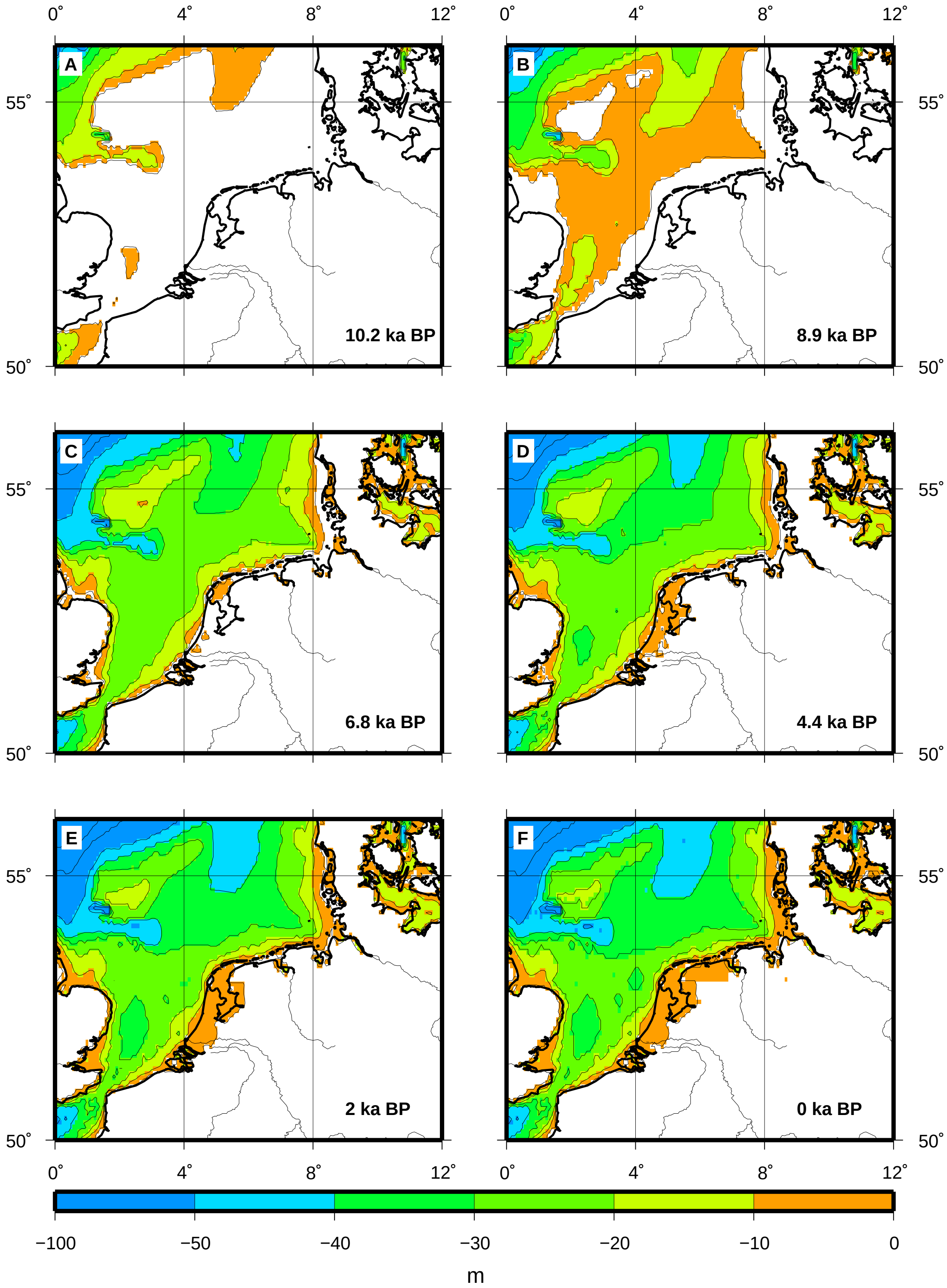

Figure 3.12: Palaeogeographic reconstructions of the southern North Sea. (A) 10.2 cal. kyr BP; (B) 8.9 cal. kyr BP; (C) 6.8 cal. kyr BP; (D) 4.4 cal. kyr BP; (E) 2 cal. kyr BP; (F) 0 cal. kyr BP. Elevation (m) is relative to MSL.

each local area. Conversely, data-model comparisons will benefit greatly from the refinement of existing global ice models and the definition of more focussed regional-scale models. As such, there is still room for analytical improvement for Quaternary field geologists as well as geophysical modellers, the progress of each inevitably being linked to that of the other on a give-and-take principle which will hopefully yield fruitful results in the upcoming years.

Acknowledgements

Many thanks to Kurt Lambeck (Canberra, Australia) for providing the RSES ice model. We also sincerely thank the consulting company Dr. - Ing. V. Patzold for the possibility of joining their North Sea sampling cruise in May 2005, and Manfred Frechen of the Leibniz Institute for Applied Geosciences (GGA) in Hannover for conventional radiocarbon dating of the three BGR North Sea peat index points. Figs. 3.8, 3.9 and 3.12 in this paper have been drawn using the GMT graphics package [Wessel and Smith, 1991, 1998]. The research of H. Steffen and G. Kaufmann was funded by the DFG (research grant KA1723-1,2).

4. Three-dimensional finite-element modeling of the glacial isostatic adjustment in Fennoscandia

Abstract[a]

During the last ice age cycles, large ice sheets have covered North America, Northern Eurasia, Greenland and Antarctica. The Earth's crust and mantle has been depressed by the weight of these ice sheets by several hundreds of meters. At the end of the last ice-age cycle, the ice sheets have vanished around 6000 years ago, and the Earth's surface rebounded. However, due to the time-dependent viscoelastic relaxation of the Earth's mantle, the rebound, also termed glacial isostatic adjustment (GIA), is still observable today. In Fennoscandia, a key region of GIA, numerous observations such as paleo-strandlines, present-day crustal deformations monitored by GPS observations, and present-day changes in the gravity field seen by satellite missions, provide a detailed picture of the past and ongoing deformation.

We model the GIA process in Fennoscandia by means of the finite-element technique. We employ a three-dimensional viscosity structure in the Earth's mantle derived from seismic shear-wave tomography models, and we use thermodynamic considerations to convert the shear-wave perturbations into viscosity variations. We then compare the results based on the three-dimensional Earth's structure with a simpler earth model, where viscosity depends on the vertical direction only. Our results indicate significant differences between three- and one-dimensional modeling:

The vertical crustal velocities reveal differences up to 7 mm/yr, and horizontal crustal velocities are effected even stronger. The typical divergent motions of the latter observed for one-dimensional earth models is no longer present for three-dimensional viscosity models. Instead, a regional velocity field with movements away from the Norwegian coast towards the old Baltic Shield is observed. In a sensitivity analysis we show that the dramatic change in the horizontal flow pattern has its origin deeper in the upper mantle, between 450 and 670 km depth. We also confirm that the observed GIA process in Fennoscandia is not very sensitive to the viscosity structure in the lower mantle. However, a comparison with BIFROST data reveals a best-fit with the simple, one-dimensional model, which requires a revision of our three-dimensional models in a future analysis.

---

[a] Steffen, Kaufmann and Wu (2006a). Three-dimensional finite-element modeling of the glacial isostatic adjustment in Fennoscandia, Earth Planet. Sci. Lett. **250**, 358-375.

4.1 Introduction

During the ice ages, large ice sheets covered North America, Northern Eurasia, Greenland and Antarctica repeatedly with a cyclicity of about 120,000 years. The solid Earth has been significantly deformed by the changing weight of these ice sheets on land and the water load in the oceans, as mantle material can flow on these timescales. While the last remnants of the Late Pleistocene ice sheets vanished around 6000 years ago, the Earth's surface is still readjusting from the last deglaciation event due to the time-dependent viscoelastic relaxation of the Earth's mantle. This process is called glacial isostatic adjustment (GIA).

Records of the crustal motion through observations such as paleo-shorelines (that indicate past sea-levels) and global positioning system (GPS) measurements (that map present-day crustal velocities) provide constraints to GIA modeling. In this paper, we focus on data in Fennoscandia since a large set of different observations, both in space and time, are available.

The observations of the GIA process constrain the material properties of the Earth, especially the mantle viscosity. As mantle viscosity can vary in all three dimensions, the observations are equally sensitive to radial and lateral changes of this parameter. However, the traditional theory of GIA has been developed for a one-dimensional (1D) earth model [Peltier, 1974; Farrell and Clark, 1976; Milne and Mitrovica, 1998], which greatly facilitates the computation. The improvement in computational power in the last decades allows the consideration of more complex two- (2D) and three-dimensional (3D) earth models, including lateral heterogeneities in lithospheric thickness and in mantle viscosity. Some representative examples for 2D and 3D GIA predictions will be discussed below:

The first investigations using 2D earth models were performed by Sabadini et al. [1986], Gasperini and Sabadini [1989], Sabadini and Gasperini [1989], Gasperini and Sabadini [1990] and Gasperini et al. [1991]. These authors used axi-symmetric finite-element (FE) models for a flat Earth and simple ice-load models to analyze the effects of lateral viscosity variations in the asthenosphere on model predictions. As a result, Sabadini et al. [1986] showed that a lithospheric thickness variation only weakly influences the deformation near the center of the former ice sheet. In contrast, the uplift near the edge of the ice load is extremely sensitive to lateral variations in lithospheric thickness and asthenospheric viscosity. Gasperini and Sabadini [1989] found a strong influence of lateral viscosity variations in the upper mantle on crustal deformations induced by the deglaciation. A comparison between radial and 2D viscosity models indicated that purely radial viscosity variations used in previous studies could possibly lead to a misinterpretation of GIA signals. Gasperini and Sabadini [1990] showed for lateral variations in viscosity that average viscosities in the upper and lower mantle depend on the magnitude and pattern of the heterogeneities in each layer. Gasperini et al. [1991] focused on effects of a high-viscosity craton below the lithosphere in Scandinavia. They concluded that close to the center of the former ice load, the stiffer region could be responsible for a reduction of one third in total vertical displacement and of an increase of one fourth in vertical velocity, which could affect the interpretation of relative sea-level (RSL) changes along continental margins and gravity anomalies in the center and along the peripheral regions.

Kaufmann et al. [1997] picked up the 2D modeling and used a 2D FE model with simple axisymmetrical ice-load histories and compared model predictions for both laterally homogeneous and heterogeneous earth models. They found that lateral heterogeneities in the lithosphere and asthenosphere, and also variations in lithospheric thickness, significantly influence the calculated land uplift and thus confirmed former results of Sabadini et al. [1986] and Gasperini and Sabadini [1989]. In addition, they showed that if the geological structure is known, a determination of lateral heterogeneities in lithospheric thickness with a set of laterally homogeneous earth models is possible.

Wu et al. [1998] utilized for the first time 2D *and* 3D FE flat-Earth models, both with simple and realistic deglaciation histories to study the effects of lateral heterogeneities in earth rheology and density on geodetic signatures of the GIA process. The authors demonstrated with a 2D model that the effect of a low density continental root on geodetic data is generally small and that lateral variations in asthenospheric properties affect geodetic quantities more than lateral variations in lithospheric thickness. Using the 3D FE models, they confirmed these results. Furthermore, they found that lateral viscosity variations in the lower mantle have a larger effect on RSL data than heterogeneities only in the upper mantle. Thus, they advocated further studies especially for ice loads with size comparable to the Laurentide Ice Sheet.

Using a spherical spectral-FE 2D earth model, Martinec and Wolf [2005] showed that a model for Fennoscandia with a central 200 km thick lithosphere underneath the Gulf of Bothnia and a peripheral 80 km thick lithosphere underlain by a 100 km thick low-viscosity asthenosphere essentially gives the same response in the inverse relaxation time for the inverse relaxation-time spectrum (IRTS) as a 1D viscosity profile with a 100 km thick lithosphere and no asthenosphere.

More realistic, fully 3D ice and earth models for Fennoscandia were developed by Kaufmann et al. [2000] and Kaufmann and Wu [2002]. Kaufmann et al. [2000] also showed with these models that lateral variations in lithospheric thickness and asthenospheric viscosity do influence GIA predictions of paleo-shorelines and crustal motions. The difference in RSL predictions between radially symmetric models and models with a realistic 3D earth structure can be as large as 10 - 20 m. Also the predicted uplift rate and free-air gravity anomaly differ by 1 - 3 mm/yr and 2 - 4 mGal, respectively. For the first time, Kaufmann and Wu [2002] inverted synthetic RSL data, generated with a 3D earth model for the Fennoscandian region, for the best 1D radial viscosity profile and found that 1D earth models fail to correctly predict the correct values for lithospheric thickness and asthenospheric viscosities.

Several papers based on such flat 3D FE models considered other regions, e.g. the Barents Sea [Kaufmann and Wu, 1998a,b], Antarctica [Kaufmann et al., 2005] and Laurentia [Wu, 2005]. Kaufmann and Wu [1998a] investigated lateral viscosity variations across a continental margin and their influence on observable signatures of the GIA. They concluded that interpretations from laterally homogeneous models can be biased by effects arising from 3D viscosity structures in the Earth's mantle. Kaufmann and Wu [1998b] compared a laterally homogeneous and a laterally heterogeneous earth model and found a strong influence of lateral viscosity changes in the asthenosphere on uplift, present-day velocity and present-day gravity anomaly observations. Kaufmann et al. [2005] calculated the GIA induced crustal velocities and fault instability for a 1D and a 3D viscosity structure beneath Antarctica. The 3D earth model includes a stiff cratonic root underlying East Antarctica. As a result, the cratonic root induces a horizontal motion from East- to West Antarctica. The cratonic root also influences the fault stability offshore. Wu [2005] investigated the effect of lateral variations in lithosphere thickness and mantle viscosity on surface motions in Laurentia and found an influence on horizontal motion as well as on the uplift rate.

Wu [2002] extended the FE method to a 3D self-gravitating spherical earth model, which was coupled to the sea-level equation [Wu and van der Wal, 2003]. Completely introduced by Wu [2004], this method is called Coupled-Laplace Finite-Element Method. Wu and van der Wal [2003] and Wu et al. [2005] used this model approach and confirmed the results of flat 3D FE models. Their investigations found that effects of lateral viscosity variations in the deeper mantle are large.

Zhong et al. [2003] also developed a 3D spherical FE model with a 3D viscosity structure, but without the inclusion of the sea-level equation. In their paper, the authors investigated the role of laterally varying lithosphere thickness. They showed that the effects of the lithospheric structure on the RSL change depend on the locations of the observation sites and on the size of loads.

Latychev et al. [2005b] developed a finite-volume (FV) formulation for 3D spherically symmetric, self-gravitating and elastically compressible earth model, which does not include self-gravity in the oceans. This model has been benchmarked by comparing a suite of predictions based on a spherically symmetric test model with results generated using the normal-mode approach [e.g. Mitrovica et al., 1994]. The first applications of their new FV method considered the effect of of lithospheric thickness variations [Latychev et al., 2005a] and of lateral viscosity variations in the mantle [Latychev et al., 2005b] on predictions of present-day 3D crustal velocities in North America. They found that lateral viscosity variations have a more significant impact on horizontal velocities than on radial velocities.

From the papers discussed above it is evident that a realistic 3D variation in mantle viscosity produces significantly different model predictions than a simpler 1D mantle-viscosity model.

One aim of this paper is to investigate how the thermodynamic properties of the mantle affect the background radial viscosity profile and also the inferred lateral viscosity variations. Another aim is to understand the relative importance between the contribution of the lateral viscosity variations in the various layers in the upper mantle and that from the lower mantle. Our focus will be on the GIA response induced by the melting of the Late Pleistocene Fennoscandian ice-sheet complex, based on realistic 3D viscosity distributions in the Earth's mantle. We employ a flat 3D FE model with compressible, viscoelastic material properties. It has been shown earlier that for GIA predictions in the Scandinavian region the flat-earth approach is adequate [e.g. Wolf, 1984; Amelung and Wolf, 1994; Wu and Johnston, 1998]. The GIA predictions of RSL change and crustal velocities are then compared to observed data of sea-level indicators and the BIFROST project. Our main emphasis is a comparison of a 1D and three 3D viscosity models. The 1D viscosity model is laterally homogeneous model, the 3D viscosity models are based on results of shear-wave tomography. For the 3D structure, different rheological reference models were used. In addition to the model comparison, we employ a sensitivity analysis for different mantle layers to localize regions, which influence the rebound pattern.

4.2 FE-model geometry

The GIA process in Fennoscandia is modeled using the FE method. A changing ice load is applied to the surface of a flat, viscoelastic earth model which has horizontal dimensions of 130,000 km and consists of 10 layers in the vertical direction, stretching from the Earth's surface to the core-mantle boundary at 2886 km depth. The generated mesh of $50 \times 50 \times 10$ hexahedra elements is divided into a central and a peripheral frame (Fig. 4.1). The 3000 km wide central frame, located in the center of the model, is meshed with 30 elements with a horizontal dimension of 100 km. The 10 elements of the 63,500 km wide peripheral frame have variable side lengths, increasing towards the edge. This huge horizontal dimension of the peripheral frame, which is about 10 times the Earth's radius is necessary, because viscoelastic investigations with flat FE models require an infinite horizontal extent, which can be modeled either using infinite boundary elements or, our choice, a surrounding frame with about 5 to 10 times the dimension of the area of interest. Both methods aim in allowing the mantle material to flow due to application of a surface load outside the area of interest. The first two vertical layers, with thickness values of 15 and 55 km, simulate the elastic lithosphere. The depth layers 3 to 6 with a total thickness of 600 km and the layers 7 to 10 with a total thickness of 2216 km represent the upper and lower mantle, respectively. The thickness values are summarized in Tab. 4.1. Rigid boundary conditions

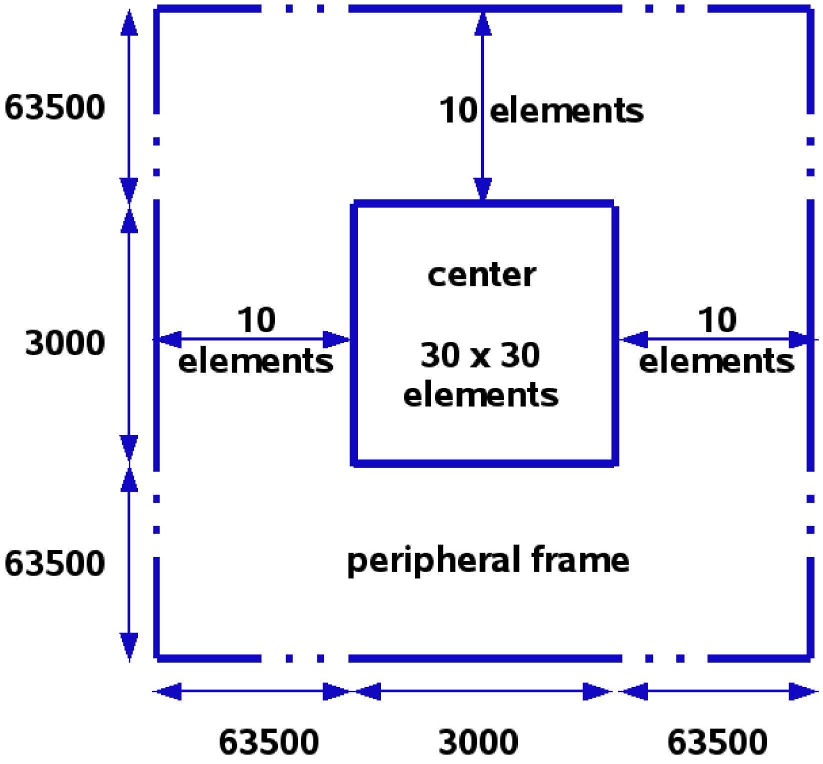

Figure 4.1: Sketch of the FE model geometry. Numbers on the left and bottom indicate the dimension in km.

are applied to the bottom and the sides of the model.

Table 4.1: Model dimensions and parameterization.

layer	thickness in m	depth in km	density in kg/m^3	Young's modulus in GPa	Poisson's ratio	
1	15	15	2653	75.3	0.278	lithosphere
2	55	70	3361	170.4	0.279	
3	176	246	3392	172.1	0.290	upper mantle
4	204	450	3597	213.4	0.300	
5	100	550	3854	267.5	0.297	
6	120	670	3974	305.5	0.295	
7	550	1220	4570	468.9	0.276	lower mantle
8	580	1800	4880	559.6	0.288	
9	520	2320	5156	641.5	0.296	
10	566	2886	5429	725.9	0.307	

4.3 Ice load

The ice model for the Late Pleistocene glacial history in Europe is taken from the FBKS8 ice model of Lambeck et al. [1998a], and applied within the central frame. The ice model FBKS8 simulates the extent and melting history of the Fennoscandian and Barents Sea Ice Sheets from the last glacial maximum (LGM) towards the present day. The extent of these ice sheets for four different epochs is shown in Fig. 4.2. The ice sheets are included in a high spatial and temporal resolution model that is consistent with the majority of the field evidence for ice-margin retreat and with the GIA data. The ice volume at the LGM approximately 22 000 years BP corresponds to 17 m of eustatic sea-level change. All reconstructions subsequent to the LGM are based on glaciological and geomorphological evidence and thus reflect the approximate extent of the Late Pleistocene ice sheets throughout the last glacial cycle. The time dependence of the load is applied as follows: A maximum load, corresponding to the LGM (at 22,000 years BP), is applied from 212,000 to 122,000 years BP. Then the load is instantly removed, and the model is ice free during the penultimate interglacial until 112,000 years BP. Then the load increases linearly, until it reaches its maximum extent at 22,000 years BP, followed by a detailed deglaciation history until the present. This parameterization has been shown to be sufficient to correctly predict changes in surface displacements [Kaufmann et al., 2000; Kaufmann and Wu, 2002]. In addition, we have tested our model adding a complementary ocean load. However, the effect of the ocean load on our present-day observables is one order of magnitude less than the ice-load signal and thus, the ocean load is not included in our load history.

4.4 Earth models

A layered, isotropic, compressible, Maxwell-viscoelastic half-space with a constant gravitational attraction of $g = 9.82$ m s^{-2} is used to model the glacially-induced perturbations of the solid Earth. We solve the Boussinesq problem for a layered, viscoelastic half-space using the commercial finite-element package ABAQUS [Hibbitt et al., 2005], which has been modified to include pre-stress in order to allow the deformed free surface to return to its initial equilibrium via viscous flow [Wu, 1992a,b, 2004]. Thus, the equation that describes the conservation of momentum is given by:

$$\nabla \cdot \sigma - g \nabla (\rho w) = 0, \tag{4.1}$$

where σ is the incremental stress tensor, ρ the density, g the gravitational acceleration, and w is the vertical displacement. The first term in equation (4.1), the divergence of stress, describes the surface force deforming the Earth. The second term arises because the undisturbed Earth is assumed to be in hydrostatic equilibrium, with the forces of self-gravitation balanced by the hydrostatic pre-stress. This pre-stress is being “advected” along with the material when the body deforms either elastically or viscoelastically. Thus, the second term in equation (4.1) represents the gradient of the “advected” pre-stress, $\rho g w$. The presence of this term is required in order to provide the buoyancy force that is needed to satisfy the boundary conditions in the fluid limit, and without this term, there would be no viscous gravitational relaxation. The validity of the finite-element model to predict glacial isostatic adjustment has been shown previously [Wu and Johnston, 1998].

Earth models consist of a layered elastic lithosphere over a layered viscoelastic mantle. Density ρ, shear modulus μ and bulk modulus κ are volume-averaged values derived from PREM [Dziewonski and Anderson, 1981] (see Tab. 4.1 for PREM density and elastic parameters). The density is considered to

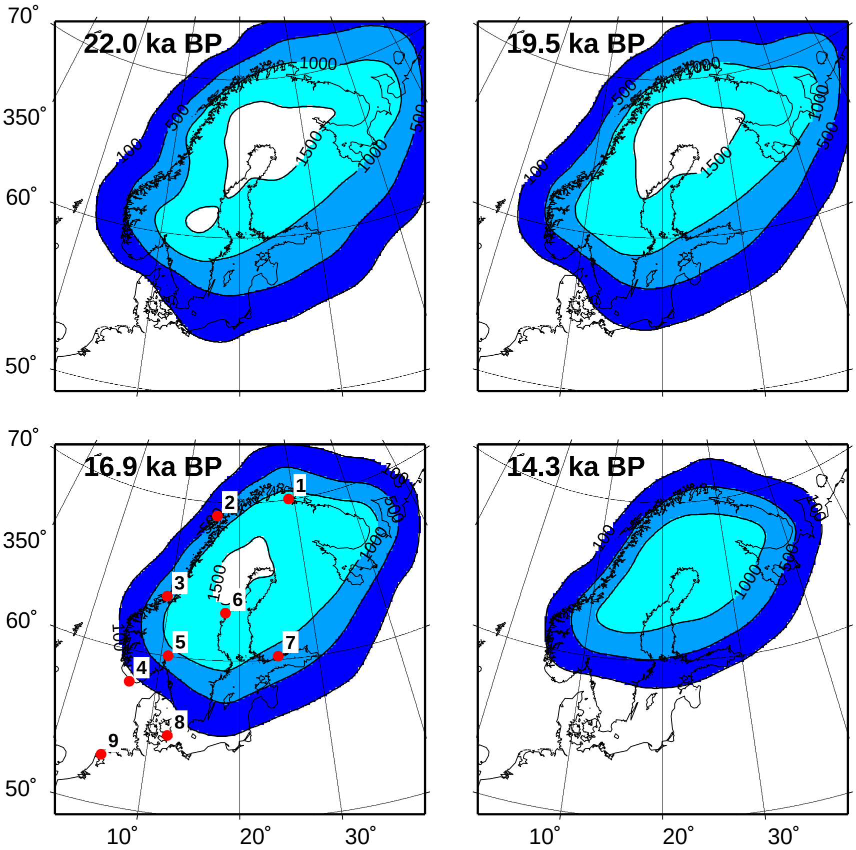

Figure 4.2: Map of ice model FBKS8 over Fennoscandia for four different time epochs. Contours are drawn every 500 m. Red dots mark selected locations with sea-level indicators.

be constant within an element. We compare two sets of earth models, 1D and 3D model sets, which will be discussed in the following sections.

4.4.1 1D viscosity profiles

Models U1L1_V*x*, where U1 refers to a 1D upper mantle, L1 refers to a 1D lower mantle and V*x* the vertical viscosity model number, represent laterally homogeneous reference models. The viscosity $\eta(z)$ varies in the vertical direction only. We define three different vertical viscosity profiles: The first profile, U1L1_V1, is characterized by only two different viscosity values, an upper-mantle viscosity of 4×10^{20} Pa s and a lower-mantle viscosity of 2×10^{22} Pa s (Fig. 4.3). This parameterization has been derived from fitting GIA observations of the Scandinavian region and has been confirmed by several independent studies [e.g. Lambeck et al., 1998a; Wieczerkowski et al., 1999; Milne et al., 2001; Kaufmann and Wu, 2002; Milne et al., 2004; Steffen and Kaufmann, 2005].

In the second profile, U1L1_V2, the radial viscosity has been derived from an Arrhenius-law:

$$\eta(z) = \eta_0 \exp\left(\frac{E(z) + p(z)V(z)}{RT(z)}\right), \tag{4.2}$$

Here, z is depth, η_0 is a scaling parameter, E the activation energy, p the pressure, V the activation

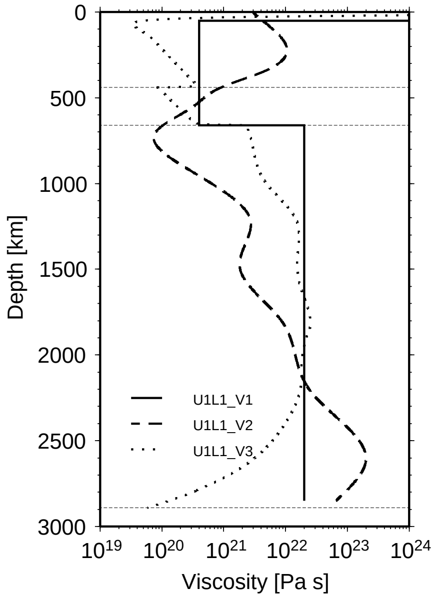

Figure 4.3: Radial viscosity profiles $\eta(z)$ as a function of depth.

volume, R the gas constant, and T the temperature. The parameters used are an activation enthalpy $E+pV$ tabulated in Ivins and Sammis [1995](Fig. 4.4b), and a temperature profile derived from a mantle convection model described in Leitch and Yuen [1989] (Fig. 4.4d). The second viscosity profile is characterized by a relatively high viscosity in the uppermost mantle, a pronounced low-viscosity region ($\simeq 10^{20}$ Pa s) below the 660 km discontinuity, and a high viscosity above 10^{22} Pa s in the lowermost mantle (Fig. 4.3).

The third profile, U1L1_V3, is based on the activation energy and volume for olivine from Karato and Wu [1993] for the upper mantle, and the activation enthalpy for perovskite from Yamazaki and Karato [2001] for the lower mantle (Fig. 4.4b). The temperature profile has been derived by solving the heat conduction problem in the lithosphere and the D”-layer, and an adiabatic gradient in the mantle, including the two phase transitions (Fig. 4.4d). It is characterized by a low viscosity ($< 10^{19}$ Pa s) directly beneath the lithosphere, then generally increasing towards mid-mantle depth to values above 10^{22} Pa s in 200 km depth (Fig. 4.3). At the two phase transitions, viscosity jumps by half an order of magnitude.

In both U1L1_V2 and U1L1_V3 the viscosity scaling parameter η_0 is chosen to satisfy the Haskell constraint of $\bar{\eta}(z) = 10^{21}$ Pa s [Mitrovica, 1996], which is a classic and enduring inference of mantle viscosity. Therefore, the viscosity profile between 100 km and 1400 km depth is shifted, until the volume-averaged viscosity in that depth range is equal that value.

4.4.2 3D viscosity structures

We then define the 3D viscosity model as the product of viscosity variation $\Delta\eta(x,y,z)$ and the vertically-dependent viscosity profile $\eta(z)$:

$$\eta(x,y,z) = \eta(z) \times \Delta\eta(x,y,z), \tag{4.3}$$

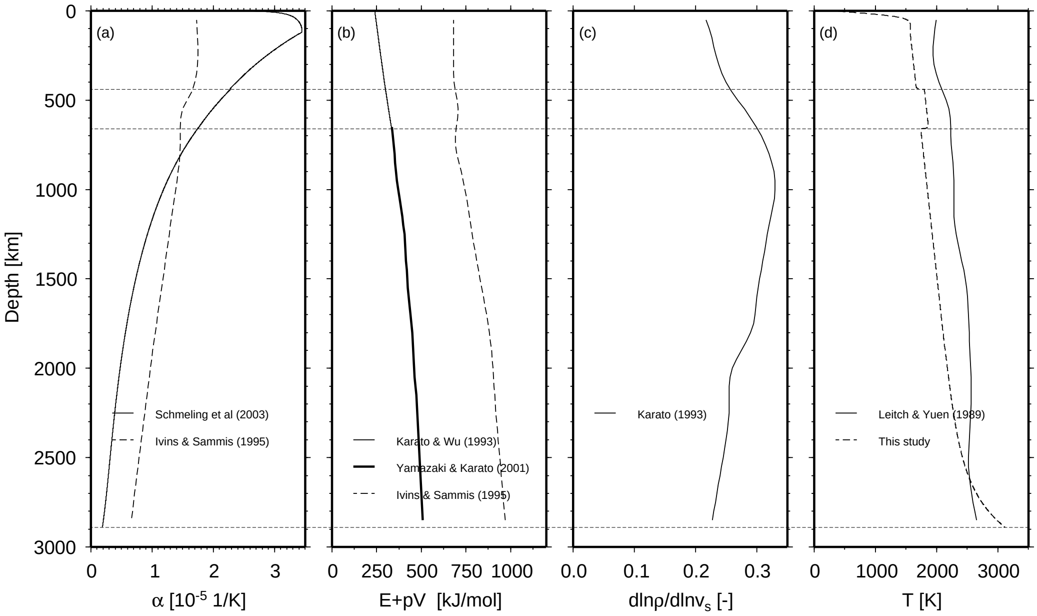

Figure 4.4: (a) Thermal expansivity α as a function of depth. (b) Activation enthalpy $E+pV$ as a function of depth. (c) Density-to-shear-wave velocity conversion $d\ln\rho/d\ln v_s$ as a function of depth. (d) Temperature T as a function of depth.

with x and y the horizontal dimensions. The 3D viscosity variation $\Delta\eta(x,y,z)$ is derived from the shear-wave velocity perturbations in the S20A tomographical model [Ekström and Dziewonski, 1998] by the following scaling relationship [for details see Ivins and Sammis, 1995; Kaufmann et al., 2005]:

$$\Delta\eta(x,y,z) = \exp\left(\frac{E(z)+p(z)V(z)}{R}\frac{1}{\alpha(z)}\frac{1}{T(z)^2}\frac{d\ln\rho}{d\ln v_s}(z)\,d\ln v_s(x,y,z)\right), \tag{4.4}$$

with α the thermal expansivity (see Fig. 4.4a), and $d\ln v_s$ the shear-wave velocity perturbations from S20A. The density-to-velocity conversion, $\frac{d\ln\rho}{d\ln v_s}$, is taken from Karato [1993] (Fig. 4.4c). This equation assumes that the lateral variations in seismic velocities seen in seismic tomography are caused by lateral temperature variation only.

Five different 3D viscosity structures are used in this paper (see Tab. 4.2):

U3L3_V1 is based on the vertical viscosity profile U1L1_V1 with its fixed values for the upper and lower mantle. The thermal parameters needed for the 3D variations (eq. 4.4) are a thermal expansivity and an activation enthalpy tabulated in Ivins and Sammis [1995] (Fig. 4.4a and b), and the temperature profile from Leitch and Yuen [1989]. The resulting viscosity structure, binned into four depth intervals in the upper and lower mantle, respectively, is shown in Fig. 4.5. The most striking feature is the high-viscosity region in the 70 - 250 km depth interval underneath the eastern part of Scandinavia. This high-viscosity region correlates with the cold, stiff Baltic Shield, and results from the strong shear-wave perturbations in the tomographical model. Towards the Mid-Atlantic ridge, viscosities in that depth decrease by several orders of magnitude. In the remaining upper mantle bins, lateral viscosity variations are moderate, mostly confined to a variation of one order of magnitude around the 1D profile. These small lateral variations continue into the lower mantle, only in the lowermost mantle (2300 - 2850 km depth bin) they become larger.

Table 4.2: Used viscosity models for calculation and references for input parameters. Abbreviations: IS = Ivins and Sammis [1995], LY = Leitch and Yuen [1989], KW = Karato and Wu [1993], YK = Yamazaki and Karato [2001], SKW = this study, K = Karato [1993], Sch = Schmeling et al. [2003]

.

		E + pV	T	α	$\frac{d\ln\rho}{d\ln v_s}$
1D	U1L1_V1	-	-		
	U1L1_V2	IS	LY		
	U1L1_V3	KW+YK	SKW		
3D	U3L3_V1	IS	LY	IS	K
	U3L3_V2	IS	LY	IS	K
	U3L3_V3	KW+YK	SKW	Sch	K

In U3L3_V2, the thermal dependencies for the lateral viscosity variation (eq. 4.4) are the same as above, only the 1D viscosity profile U1L1_V2 is different. Hence, the pattern of the 3D viscosity structure is very similar, with the high-viscosity region underneath the lithosphere, and smaller variations through the remaining mantle (Fig. 4.6). However, the absolute viscosity values differ: For example, between 250 - 450 km depth, model U3L3_V2 is about one order of magnitude more viscous than model U3L3_V1, between 550 - 1200 km depth it is one order of magnitude less viscous (see Figs. 4.5 and 4.6).

U3L3_V3, however, is strikingly different (Fig. 4.7). This model is based on the 1D viscosity profile U1L1_V3, while the thermal parameters for the 3D variation are a thermal expansivity taken from Schmeling et al. [2003], which is pressure- and temperature dependent. The temperature-dependence has a pronounced effect, as it can be seen in Fig. 4.4a: In the uppermost mantle, α increases by a factor of two, when compared to the previously used profile. The activation enthalpy is based on the perovskite model of Yamazaki and Karato [2001]. It is around fifty percent smaller than the estimate from Ivins and Sammis [1995] (Fig. 4.4b). The temperature profile is based on the mantle adiabat (Fig. 4.4d), which,

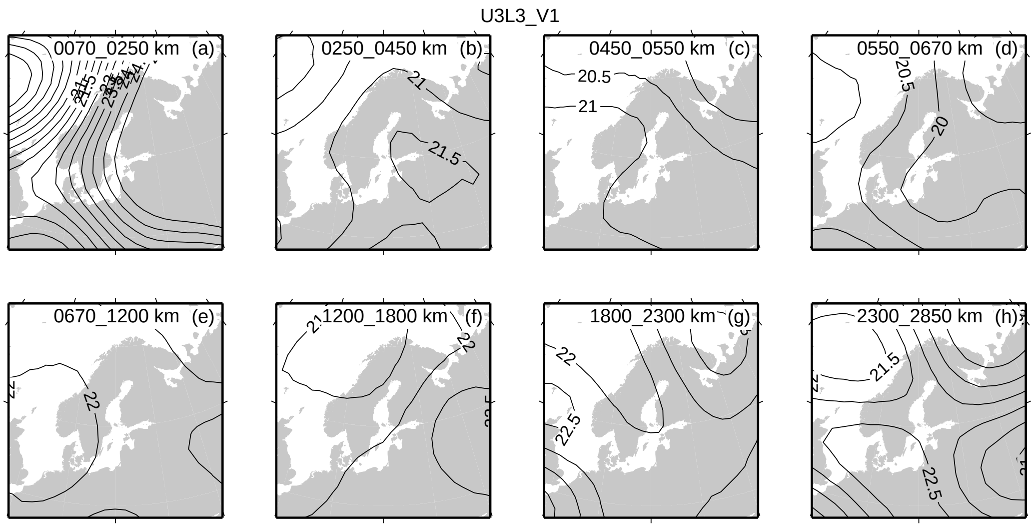

Figure 4.5: Viscosity structure U3L3_V1 for eight depth intervals. Contours show the logarithm of viscosity $log_{10}\eta$.

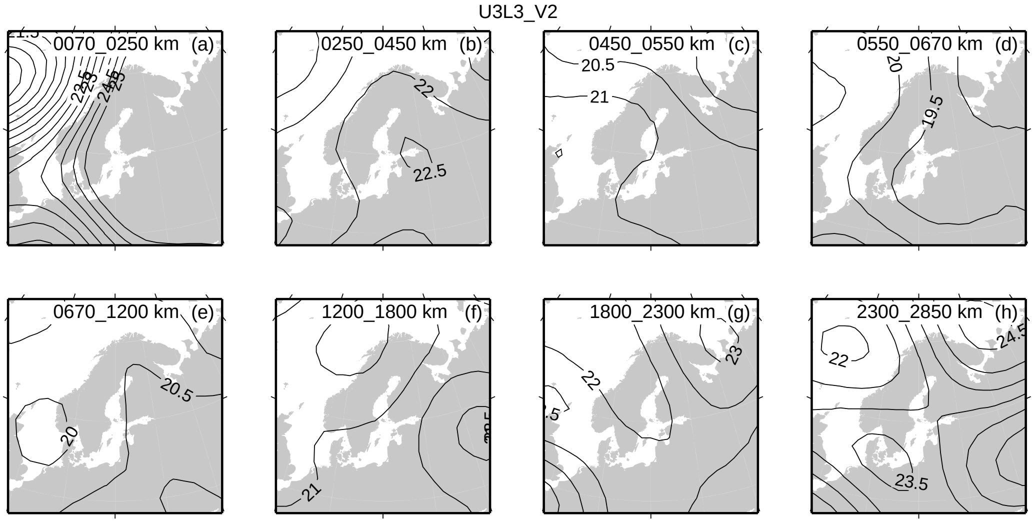

Figure 4.6: Same as Fig.4.5, but for model U3L3_V2.

however, is similar to the temperature inferred from the mantle convection model. As a result, the higher thermal expansivity together with the lower activation enthalpy reduce the effect of lateral viscosity variations in the uppermost mantle, as it can be seen in Fig. 4.7. The cratonic root in the first depth bin is much less pronounced now, and in the remaining upper mantle lateral viscosity variations are less than one order of magnitude. In the lowermost mantle below 1200 km depth, the lateral viscosity variations become larger and are similar to the variations of the two other structures.

The remaining two viscosity structures used are modifications of model U3L3_V1: In U3L1_V1, lateral viscosity variations are only taken into account in the upper mantle, while in U1L3_V1, only the lower mantle has a 3D viscosity structure.

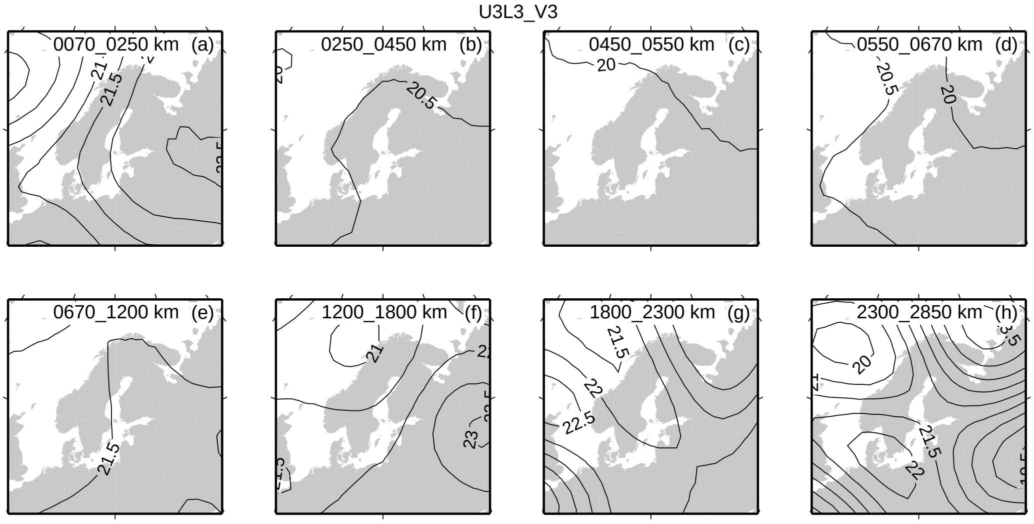

Figure 4.7: Same as Fig.4.5, but for model U3L3_V3.

In section 4.5.3, we also consider lateral heterogeneous models U3*n*L1_V1, which are similar to model U3L1_V1, except that the lateral viscosity variations are restricted to layer $n = 1$, 2, 3 or 4 in the upper mantle, respectively.

4.5 Results

In this section we discuss the modeling results of six different earth models, the five models with 3D viscosity structure mentioned above and the 1D model U1L1_V1 as a simple case for a comparison between 1D and 3D viscosity structures. The 1D models U1L1_V2 and U1L1_V3 are not used for calculation as they only provide the base for the development of the 3D models U3L3_V2 and U3L3_V3, respectively. The model predictions of present-day motions (uplift and horizontal movement) for the Scandinavian region are compared with results of the BIFROST project [Johansson et al., 2002] as well as predicted sea-levels with observed data of sea-level indicators.

4.5.1 1D earth model

We start with the results arising from 1D model U1L1_V1.

Present-day motion. In Fig. 4.8 the predictions of the remaining uplift (left) as well as of the horizontal and vertical movement (right) are illustrated. The contours indicate the vertical uplift rate and the arrows the horizontal velocities. They show a positive uplift rate in the center of the former ice sheet of more than 10 mm/yr with a residual of more than 80 m, which corresponds to a ~11 mGal gravity anomaly. The zero contour of the vertical movement can be traced around 400 km away from the Norwegian coast, through Denmark and Northeastern Germany, Poland, Belarus and Russia. Small subsidence with magnitude much less than 2 mm/yr characterizes the regions beyond. Small horizontal movements are

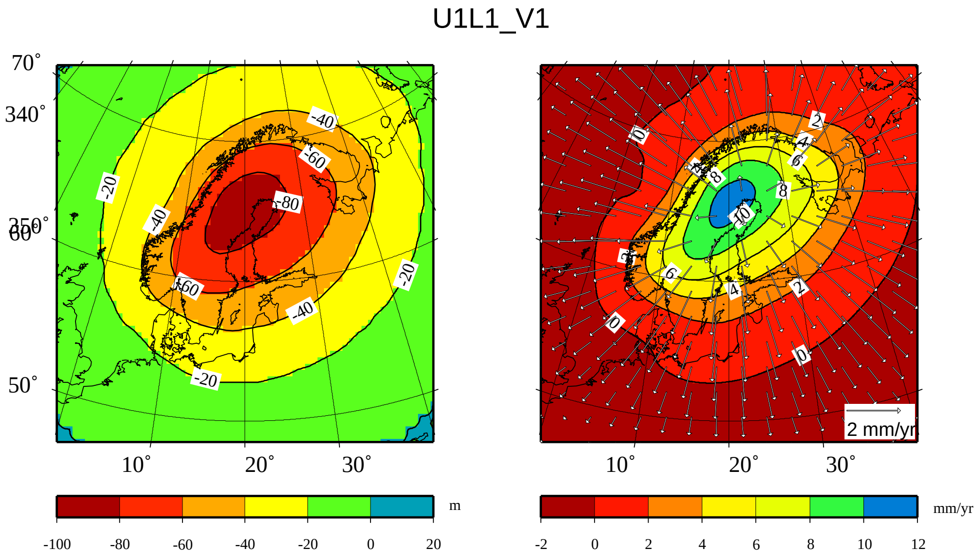

Figure 4.8: Predictions of residual uplift (left, contours) and of horizontal and vertical movement (right, contours and arrows) for the 1D model U1L1_V1.

established in the center and the outer regions of the modeled area. The largest horizontal movements result around 5 mm/yr at the Norwegian coast. The present-day motion indicates a divergent signature from the center of the former ice sheet (NW Golf of Bothnia) towards the outer regions.

Fig. 4.9 shows the observed vertical and horizontal motion in Fennoscandia obtained from the BIFROST campaign [Johansson et al., 2002]. The observations are compared to the predicted motion for the 1D viscosity model U1L1_V1. The center of the predicted uplift lies northwest of the observed uplift center, which is due to the ice sheet model. This is the reason for a difference in the uplift rate of around 2 mm/yr for most of the BIFROST locations situated near the center. Besides this, the maximum uplift rate of more than 10 mm/yr can be reproduced with the 1D model. The horizontal movement shows a divergence from the center, but amplitudes of northwestern BIFROST stations are larger than the calculated. Furthermore, the model indicates large movements by nearly 2 mm/yr to southeast in Southern Sweden and Denmark, which is not observed with BIFROST data.

Sea-level change. In Fig. 4.10, predicted relative land uplift curves for the models based on the viscosity structure V1 are compared to the relative sea-level data (black dots) at nine selected locations of Fennoscandia and northwestern Europe (see Fig. 4.2). The sea-level observations are corrected for a spatially uniform eustatic sea-level change [see Kaufmann and Wolf, 1996, for correction details], and are taken from a database compiled by Tushingham and Peltier [1992], chosen to cover the formerly ice sheet area fairly evenly. They have been converted from the radiocarbon timescale to the U/Th timescale, using the CALIB-4 program [Stuiver and Reimer, 1993; Stuiver et al., 1998]. We are using these data only to indicate the deviation between model predictions, because matching of the observations within their uncertainties by model predictions is achieved much better with a spherical earth model and a realistic load model for the Late Pleistocene ice-ocean mass balance.

The trend of monotonic land uplift indicated at the locations Helsinki, Oslo Fjord, Ångermanland, Varanger Fjord, And Fjord and Bjugn as well as the land subsidence at the locations of Praesto and

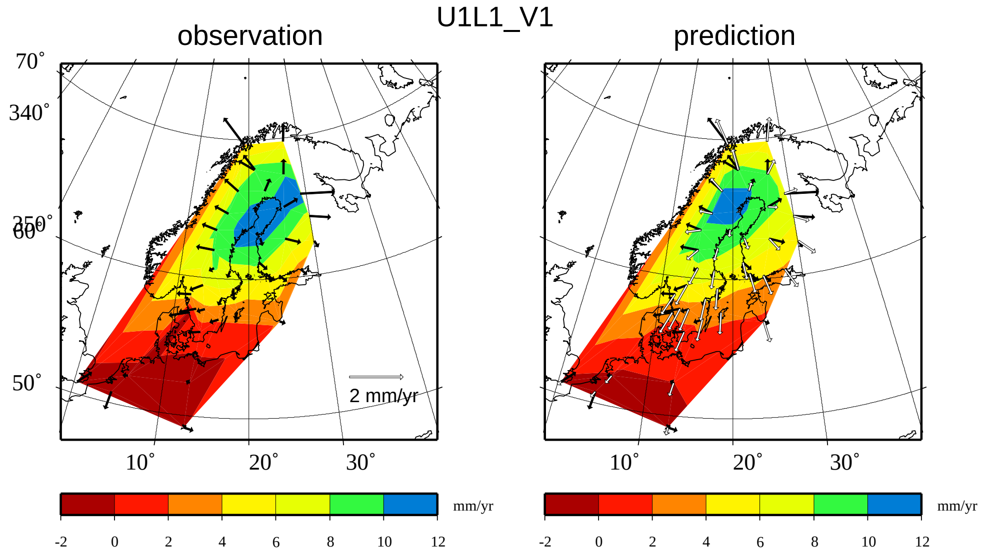

Figure 4.9: BIFROST uplift and horizontal motion data (left) and model prediction from the 1D model U1L1_V1 (right). Contours indicate the vertical motion, the black arrows the horizontal motion derived from BIFROST and white arrows the predicted horizontal motion in mm/yr.

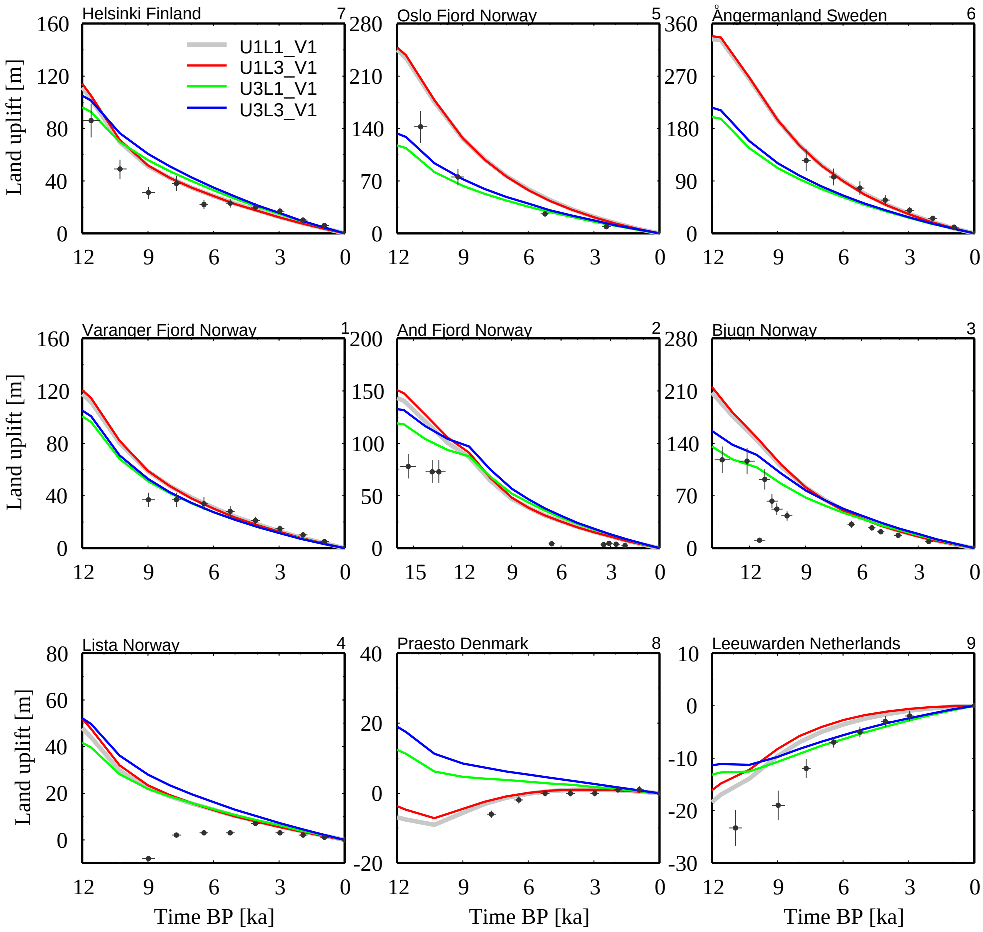

Figure 4.10: RSL observations (black dots with error bars) at selected locations on Fennoscandia compared to the predicted sea-level results from the models U3L3_V1 (blue lines), U3L1_V1 (green lines), U1L3_V1 (red lines) and U1L1_V1 (grey lines). Numbers indicate the locations in Fig. 4.2.

Leeuwarden agree well with the model predictions of U1L1_V1 (grey line). Greater differences can be found at Lista, where uplift instead of subsidence is predicted. The discrepancies between observations and predictions are possibly a consequence of the coarseness of the FE grid of the ice model, and in minor parts due to the not perfectly corrected eustatic sea-level change in the sea-level data. Nevertheless, the good fit in the trend of prediction and observation is also due to the ice model, which was constructed with the help of a 1D earth model to fit the sea level [see Lambeck et al., 1998a, for more information]. This earth model with a lithosphere thickness H_l of 75±10 km, an upper-mantle viscosity η_{um} of 3.6×10^{20} Pa s and a lower-mantle viscosity η_{lm} of 0.8×10^{22} Pa s is comparable to the used one in this work ($H_l = 70$ km, $\eta_{um} = 4 \times 10^{20}$ Pa s, $\eta_{lm} = 2 \times 10^{22}$ Pa s). Hence, our model is able to compute a consistent sea level for a flat earth model.

4.5.2 3D earth models

In this section, we investigate the effects of lateral variations in mantle viscosity on predictions of present-day velocities and RSL change.

Present-day motion. In Fig. 4.11 the predictions of the horizontal (arrows) and vertical velocities (contours) at the BIFROST locations for the six models are plotted. A comparison of the results for the models U1L1_V1 (top left) and U1L3_V1 (middle left) shows a good agreement in land uplift. The agreement at the highest peak is around 98% and is due to the low resolving power of surface motion to the lower-mantle viscosity structure. In contrast, the models U3L3_V1 (top right) and U3L1_V1 (bottom left), which include lateral viscosity variations in the upper mantle, show smaller values for the uplift rate. For both models, at most around 8 mm/yr are predicted, a difference of 2 mm/yr when compared to models U1L1_V1 and U1L3_V1. The horizontal motions are strikingly different for models U1L1_V1 and U3L3_V1 (and also for U3L1_V1). Both predict the divergent movement from the center, but in the northwest of the Scandinavian peninsula a north-directed motion with values at most around 1.2 mm/yr for a 3D upper mantle can be found, in contrast to the west and northwest movements of around 1.2 mm/yr determined with models U1L1_V1 and U1L3_V1. Including a 3D upper mantle, the southern locations of Sweden are characterized by a smaller (around 0.8 mm/yr), more southward directed horizontal motion. The predicted horizontal motions at locations in central Europe are directed towards northwest with at most 0.4 mm/yr. In contrast, for models with a homogeneous upper-mantle viscosity structure a completely different movement is found, which is directed to the southwest with values around 1.6 mm/yr.

The results obtained with background viscosity structures following method V2 and V3 strongly differ from the V1 results. For model U3L3_V2 (middle right), the uplift predicted is at most around 3 mm/yr, less than a third of the observed maximum. The reduced uplift results from the stiffer upper mantle, which is at least one order of magnitude greater than for the V1 model. For horizontal motions velocities mostly around 0.2 mm/yr are predicted, indicating a movement to the northeast in contrast to the divergence obtained with V1 models. In general, model U3L3_V2 cannot explain recent observed movements of Fennoscandia.

For model U3L3_V3 (bottom right), predictions of more than 8 mm/yr for the uplift rate results, but the center of the uplift is situated in the center of the Scandinavian Peninsula, which is 200 km west from the observed uplift center in the Golf of Bothnia. The predicted horizontal movements have a maximum value of 0.7 mm/yr, which are higher than the ones predicted for model U3L3_V2, but still smaller (by around two third) than for the models with viscosity structures following method V1. The horizontal movement indicates a divergence near the uplift center as for model U3L3_V1, but southeastern locations show small values directed towards southwest, induced by the given viscosity structure in the upper two layers. Compared with the observations, the predicted horizontal velocities as well as the vertical uplift rate are too small.

Sea-level change. In Figs. 4.10 and 4.12, a comparison between predicted sea-levels at nine selected locations in Fennoscandia and Central Europe is made. The comparison in Fig. 4.10 indicates on the one hand a similar behavior for viscosity models with a lateral upper-mantle viscosity variation (U3L3_V1, blue lines; U3L1_V1, green) and on the other hand with a fixed 1D upper-mantle viscosity (U1L1_V1, grey; U1L3_V1, red). The predictions for models U1L1_V1 and U1L3_V1 differ at most around 8 m at And Fjord about 16,000 years BP. Larger differencesbetween the two models with heterogeneous upper mantle can mostly be found before 6000 years BP, with a maximum difference of 20 m at Bjugn. Obviously, the two models with heterogeneous upper-mantle viscosities are characterized by greater differences in their predictions than the two models with homogeneous upper-mantle structures, confirming no strong influence of sea-level data by (1) a lateral lower-mantle viscosity variation and (2) the lower mantle itself. Large differences between results of models with homogeneous and heterogeneous upper mantle are also clearly seen, e. g. more than 120 m at Oslo Fjord and Ångermanland. At Bjugn, the dif-

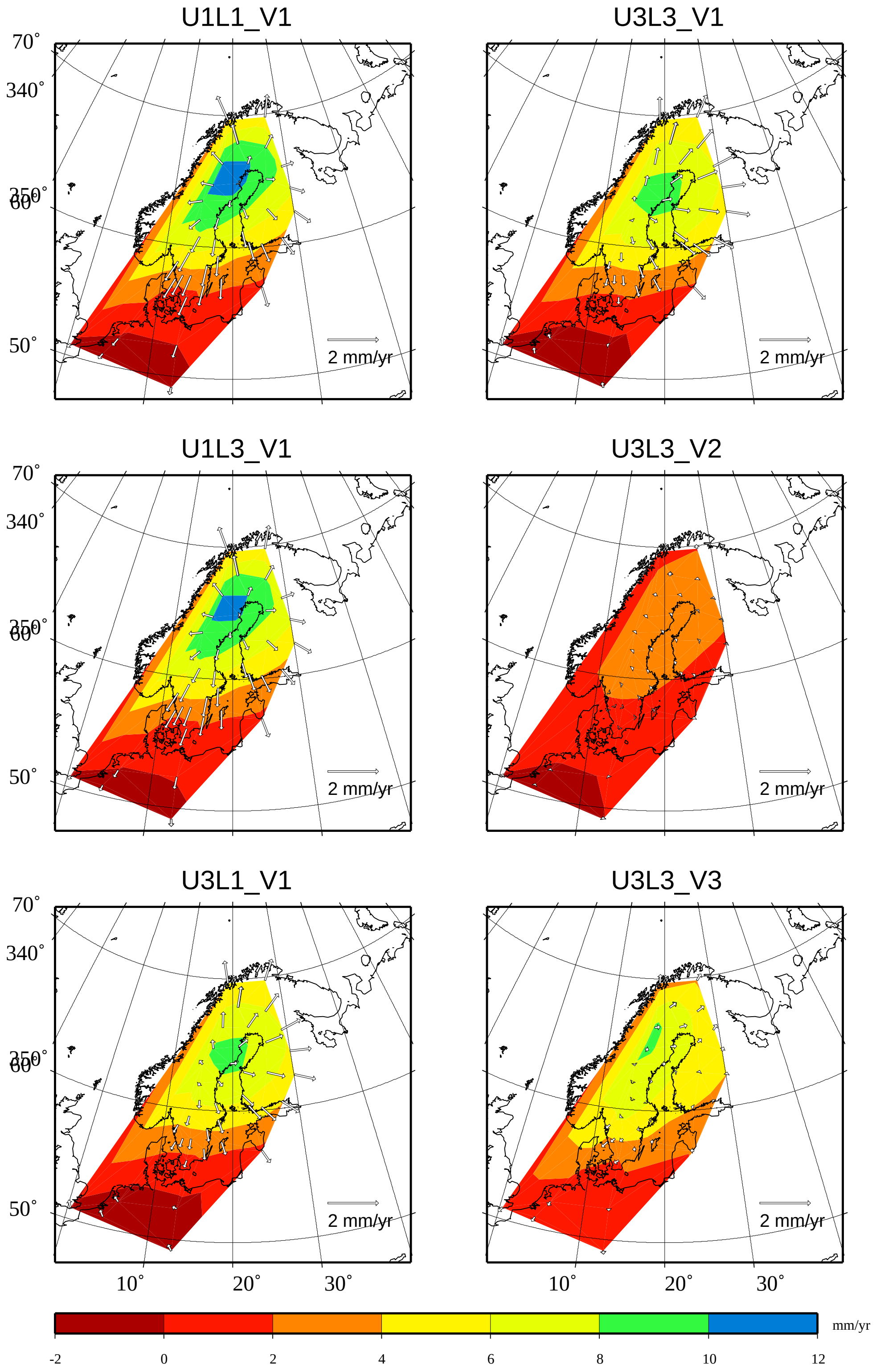

Figure 4.11: Predictions of horizontal and vertical velocities for different earth models. Contours indicate vertical and arrows horizontal velocities (in mm/yr).

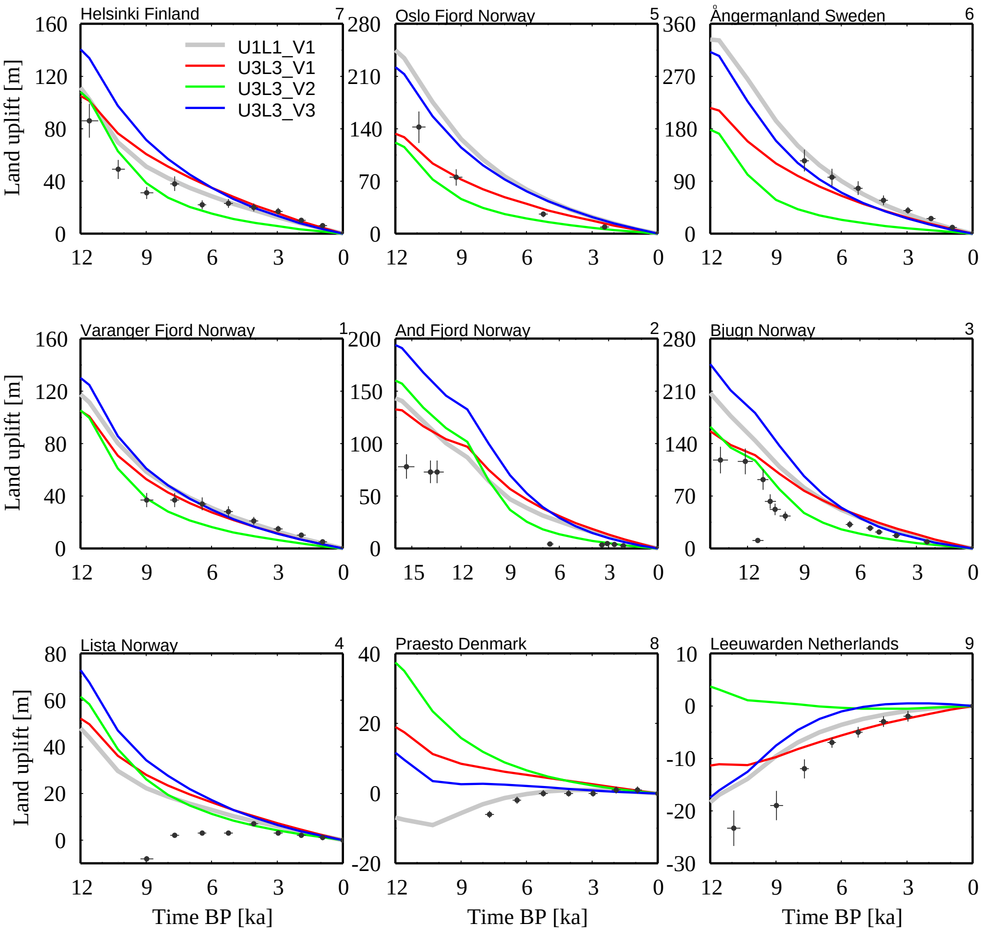

Figure 4.12: RSL observations (black dots with error bars) at selected locations on Fennoscandia compared to the predicted sea-level results from the models U3L3_V1 (red lines), U3L3_V2 (green lines), U3L3_V3 (blue lines) and U1L1_V1 (grey lines). Numbers indicate the locations in Fig. 4.2.

ference is about 80 m, at Helsinki, Varanger Fjord, And Fjord and Praesto, the differences are between 20 m and 30 m. At the locations of Lista and Leeuwarden, the differences are between 8 m and 10 m. Near the position of the former ice sheet, the models with homogeneous upper-mantle viscosity structure show larger land uplift values due to the weaker 1D viscosity. The average 3D viscosity is higher than the 1D (see Fig. 4.5) and therefore, the land uplift is much smaller. Furthermore, at the location Lista none of the models correctly predicts the sea-level observations. As explained earlier, this is due to the limitation of the FE grid in simulating the coast line. In summary, the results of the models U1L1_V1 and U1L3_V1 with a homogeneous upper mantle better fit with the sea-level observations, which is due to the fact that ice model FBKS8 was constructed based on the background earth model and the same RSL data (see section 4.5.1, sea-level change).

In Fig. 4.12 the predicted sea-level curves for the 1D model U1L1_V1 (grey) and the 3D models U3L3_V1 (red), U3L3_V2 (green) and U3L3_V3 (blue) are compared. The predictions of model U3L3_V2 with high background viscosities in the upper mantle differ significantly from the predictions of other models for most of the sites. Compared to the 1D model, differences up to more than 150 m at Ångermanland are found. Comparing U1L1_V1 to the 3D model U3L3_V3 remarkable values of around 130 m are found there. The predictions of model U3L3_V2 are generally closer to that for 3D model U3L3_V1. The stiffer upper mantle of method V2 allows only a small deformation by the former ice sheets, resulting in values less than 200 m for land uplift in Ångermanland 15,000 years BP. For locations beyond the former ice sheet (Lista, Praesto, Leeuwarden) the trend is not traced.

Sea-level predictions of model U3L3_V3 mostly follow the predictions of the 1D model. At Oslo Fjord, Helsinki, Varanger Fjord, Ångermanland and Lista, the differences range between 20 m to 30 m. More than 40 m are determined at Bjugn and And Fjord, less than 20 m at Praesto. A good agreement between the predictions of the models U1L1_V1 and U3L3_V3 is established at Leeuwarden with at most 3 m. The good fit with the predictions of the 1D model is caused by only small variations in upper-mantle viscosity for method V3 and the much less pronounced cratonic root in the first depth bin, which is more in line with a homogeneous upper mantle structure.

4.5.3 Sensitivity of GIA predictions to upper-mantle viscosity structure

From the previous subsection, it is clear that GIA observations in Fennoscandia are not sensitive enough to resolve the viscosity structure of the lower mantle. On the other hand, the effect of lateral viscosity variations in the upper mantle on relative sea levels and present-day velocities is strong, which confirms earlier results of Gasperini and Sabadini [1989], Kaufmann et al. [1997], Kaufmann and Wu [1998b], Kaufmann et al. [2005], and Wu [2005]. Thus, in this subsection we use the subdivision of the upper mantle into the four depth bins depicted in Fig. 4.5 to investigate the sensitivity of GIA predictions depending on the lateral viscosity structure in these individual depth bins.

In Fig. 4.13, model predictions of the vertical (contours) and horizontal (arrows) velocity are shown. The top row depicts our already discussed 1D viscosity model U1L1_V1 (top left) and the 3D viscosity model U3L1_V1 (top right). The model response of the latter one has been shown to be very similar to U3L3_V1. In the middle and bottom rows, models, in which only one of the four upper-mantle depth bins has a 3D viscosity structure, are termed U3*n*L1_V1, with $n = 1, 4$ the depth-bin counter.

In model U31L1_V1 (middle left), the bin between 70 and 250 km depth has a 3D viscosity structure. For this model, the uplift velocities are reduced to a maximum of 8 mm/yr, when compared to the 10 mm/yr for the 1D model U1L1_V1. The reduction is related to the stiffer uppermost mantle. The general pattern of horizontal velocity predictions for U31L1_V1 is similar to the patterns for the 1D model. However, deviations can be found along the Norwegian coast in the west, where the 3D model results in lower horizontal velocities. In general, however, the very high viscosity of model U31L1_V1 in the region of the Baltic Shield with viscosities up to 10^{25} Pa s produces a very thick ($>$ 200 km), almost elastic lithosphere in the eastern parts of Fennoscandia, acting as a plate.

For model U32L1_V1 (middle right), the depth bin between 250 and 450 km has a 3D viscosity structure. Here, the vertical velocities of up to 12 mm/yr are higher, when compared to the 1D model U1L1_V1. Horizontal velocities in the East and Southeast of Fennoscandia are reduced as a result of the high viscosity in the second bin of the 3D model U32L1_V1.

The vertical velocity predictions for 3D model U33L1_V1 (bottom left) are almost similar to the ones for 1D model U1L1_V1. However, when we compare the horizontal velocities of this 3D model to the 1D model, we observe a slight reduction over Central Sweden, where viscosities in the 3D model are higher, and an increase in horizontal velocities over Northeast Finland, where viscosities are lower, when compared to the 1D model.

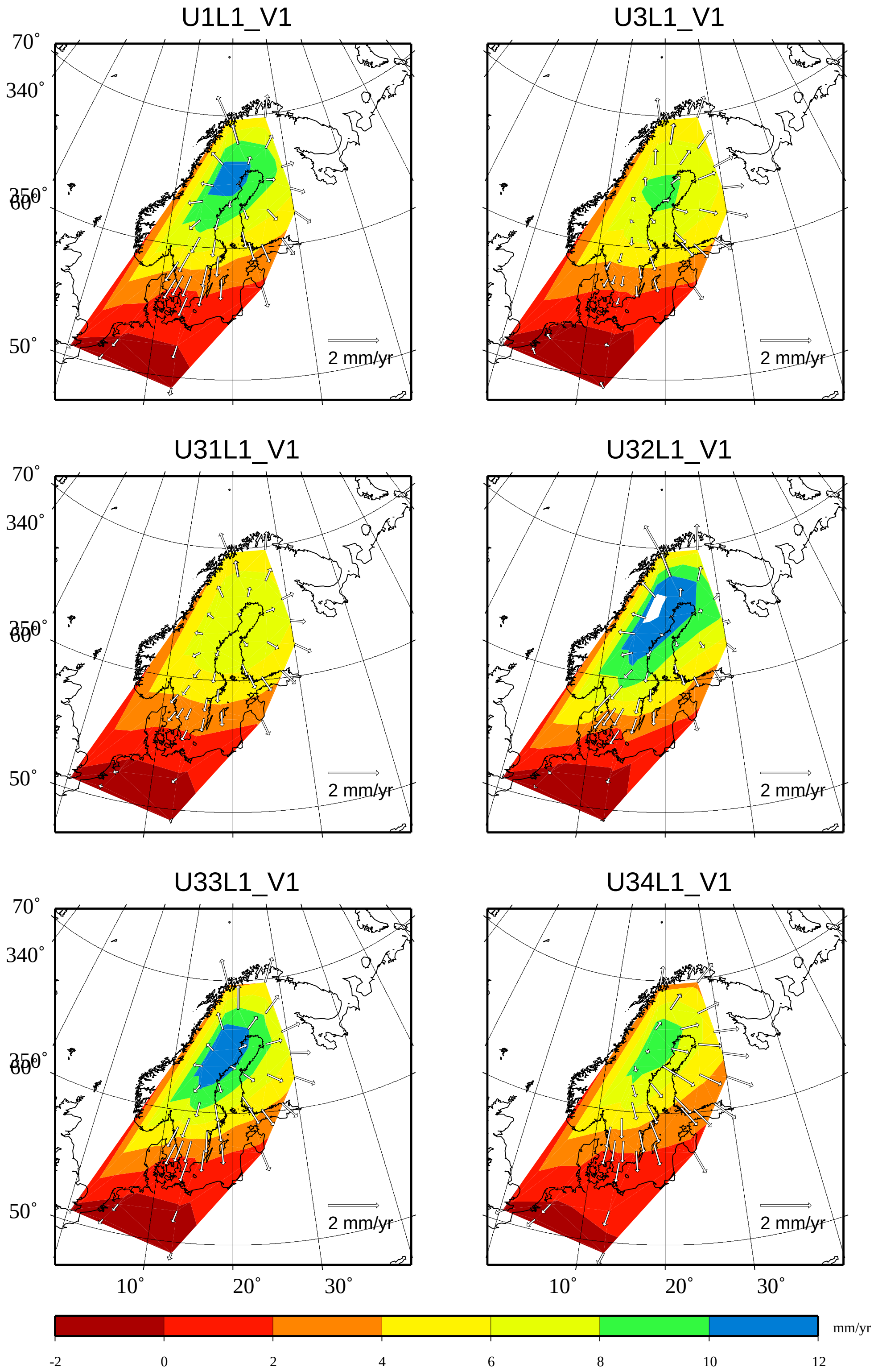

Figure 4.13: Predictions of horizontal and vertical velocities for Earth models with only one 3D layer and models U1L1_V1 and U3L1_V1. Contours indicate vertical and arrows horizontal velocities (in mm/yr).

Finally, a pronounced effect in both vertical and horizontal velocities can be observed for 3D model U34L1_V1 (bottom right). The vertical velocities are reduced by 2 mm/yr due to the weaker viscosity underneath Central Fennoscandia in the bin between 550 and 670 km depth. Even more impressive, the horizontal velocities show a strong asymmetry, with negligible velocities along the Caledonian Mountains between Norway and Sweden, but large eastward-directed velocities for the Baltic Sea and Finland. This eastward drift is a consequence of the viscosity high underneath the Atlantic and the viscosity low underneath the Baltic Shield in the transition zone of the mantle, when compared to the 1D model.

In summary, comparison of the tangential motion of the lateral heterogeneous models shows that the lateral viscosity variations in the transition zone have a strong influence on the tangential motion of model U3L1_V1.

4.6 Conclusions

We have developed a set of 1D and 3D FE flat-earth models with compressible, viscoelastic material properties to study the GIA response induced by an ice-load model simulating the last two cycles of the Late-Pleistocene Fennoscandian ice sheet. The radial dependence of mantle viscosity is based on either results of a formal inverse procedure of the GIA process [Steffen and Kaufmann, 2005], or on an Arrhenius-law. For the 3D models, the lateral viscosity structure has been derived from seismic shear-wave tomography. Model results have been compared to observations of relative sea-level (RSL) changes and crustal velocities (BIFROST data).

We have shown that a consideration of lateral viscosity structure in the Earth's upper mantle significantly influences the crustal velocity predictions, with differences in uplift velocities up to 7 mm/yr. The observed BIFROST crustal velocity data are best fit using a 1D earth model, as for the different 3D earth models deviations between observations and predictions can differ by 2 - 7 mm/yr. The presence of lateral viscosity variations in the upper mantle significantly influences the horizontal velocities, which is the result of a strong horizontal flow component in the 3D earth models. Again, horizontal velocities from the 3D earth model prediction cannot explain the BIFROST data well, the prediction from the 1D earth model scores better. However, we need to stress here that the ice model used has been constructed with a 1D viscoelastic earth model. Thus it is very likely that the better fit of the 1D model prediction is a relict of the ice-model construction. Additionally, our 3D earth models have to be revised, because it is quite unsatisfactory that a less sophisticated 1D model shows better results than a more sophisticated 3D model. For example, chemical variation could be included due to fact that in our models the lateral variations in seismic velocities seen in seismic tomography are caused by lateral temperature variation only. Using another tomography model is also an option. Furthermore, the ice model has to be changed, especially in the central part.

Predictions of RSL curves show significant differences between models with homogeneous and heterogeneous upper mantle of up to more than 150 m. The monotonic land uplift indicated at locations situated within the margins of the former ice sheet is reproduced well by all model predictions. The land subsidence at locations beyond is well modeled (with one exception) by models with homogeneous upper mantle. Models with 3D upper-mantle viscosity structure can only trace the land subsidence at the location of Leeuwarden. Greater differences can be established for the location Lista, where for all models uplift instead of subsidence is predicted. The discrepancies in the values between observations and predictions are possibly a consequence of the coarseness of the FE grid of the ice model. A reason for the differences especially in the regions beyond the former ice sheet is mainly due to the not perfectly corrected eustatic sea-level change in the sea-level data.

In general, only minor dependencies of the lower-mantle viscosity structure to RSL and crustal motion data can be established, confirming the results of Mitrovica [1996] and Steffen and Kaufmann [2005]. Special investigations to the background model V1 show a strong influence of a laterally varied viscosity in the transition zone to the direction and value of the horizontal velocities. The uplift is mainly influenced by the viscosity structure beneath the lithosphere.

The results demonstrate the complexity of the GIA process and the search for a heterogeneous earth model reproducing observed physical quantities such as surface motions and sea-level data.

Acknowledgments

Many thanks to Kurt Lambeck for providing the FBKS8 ice model. We are grateful for numerous comments and suggestions by two anonymous referees. The figures in this paper are drawn using the GMT graphics package [Wessel and Smith, 1991, 1998]. This research was funded by the DFG (research grant KA1723/1-1).

5. Sensitivity of crustal velocities in Fennoscandia to radial and lateral viscosity variations in the mantle

Abstract[a]

We investigate the sensitivity kernels of the present-day velocities in Fennoscandia induced by the retreat of the Late Pleistocene ice sheets with a 3D Finite-element model having compressible, viscoelastic material properties and a realistic ice load history of the Fennoscandian ice sheet. The model is subdivided into blocks of variable size, which results in a large number of kernels to interpret. Thus, we introduce a simple approach to calculate the kernel of a block by averaging the perturbed predictions of all surface nodes of this block to one value for this block.

Our results show that the present-day uplift velocity is mostly sensitive to upper-mantle layers between 220 and 540 km depth, independent of the block size. Velocities in blocks located inside the former ice sheet area are more sensitive to viscosity variations than velocities in blocks located outside the former ice sheet. The largest effects are found for blocks located below the former ice maximum on the surface. The uplift velocity in smaller blocks is more sensitive to viscosity changes than in larger blocks.

For the present-day horizontal velocity, the sensitivity depends on the block size and the location of this block in relation to the former ice sheet. In general, lateral viscosity variations in the transition zone of the mantle have a strong influence on the tangential motion. A comparison of the results of smaller and larger blocks also indicates higher sensitivities for the horizontal velocities of larger blocks.

---

[a] Steffen, Wu and Kaufmann (2006b). Sensitivity of crustal velocities in Fennoscandia to radial and lateral viscosity variations in the mantle, Earth Planet. Sci. Lett., submitted.

5.1 Introduction

The viscosity of the mantle is a very important parameter in the study of geodynamics and the evolution of the Earth. Observations of the glacial isostatic adjustment (GIA) process such as palaeo-shorelines and global positioning system (GPS) measurements can be used to constrain the material properties of the Earth, especially the mantle viscosity. As mantle viscosity can vary in all three dimensions, the observations are equally sensitive to radial and lateral changes of this parameter. This means that if one varies the viscosity in a certain depth or region of the mantle, a measure of the sensitivity of a certain datum can be provided. Wu [2006] has presented such an approach for observations of relative sea levels and crustal velocities in North America using an axisymmetric, laterally heterogeneous, self-gravitating spherical viscoelastic earth model. For an earth model with a laterally variable viscosity he showed that if there is only one perturbed region, its influence is usually strongest for the sites lying directly above. With increasing depth, the width of its influence increases also to neighboring regions, but with decreasing signal level. In contrast, the closer the region lies to the ice load the stronger the signal level. In general, data from any location are most sensitive to viscosity variations in regions below the former ice load, e. g. if there is more than one perturbed region, the influence from the region near or below the ice load dominates the influence. He also found a trade-off between radial and lateral viscosity variations, which complicates the inversion of mantle viscosity. Another interesting result is that regions with viscosity variations lying underneath the ice sheet can influence tangential velocities at sites far away from the former ice sheet. However, these results are obtained with an axisymmetric and simple ice model, which allows the tangential velocity to be calculated only in direction normal to the ice sheet margin. Therefore one of the aims of this paper is to investigate the sensitivity kernel without the assumption of axisymmetry and with a *realistic* ice model.

These so called sensitivity or Frech´et kernels can be very useful for finding the optimal location of sites that are most sensitive to the viscosity variation in a certain region. Since Peltier [1976], a number of works used sensitivity kernels [e. g. Mitrovica and Peltier, 1991, 1993, 1995; Peltier and Jiang, 1996a,b; Peltier, 1998; Milne et al., 2004; Wu, 2006]. For example, Mitrovica and Peltier [1991] investigated the radial dependence of the kernels. Milne et al. [2004] calculated sensitivity kernels of the radial and tangential velocities for 8 BIFROST GPS stations to determine the resolving power of the BIFROST data set. Except for one station (Hässleholm) they found “moderate, but a nonnegligible sensitivity to variations in lower-mantle viscosity (at least in the shallowest portions of this region)”. The sensitivity of the horizontal velocities is largest in the uppermost mantle (sub-lithosphere to 450 km), but nonzero near the base of the mantle at some sites. Furthermore, the sensitivity of the uplift velocity receives large contributions by upper-mantle viscosity changes, but the upper lower-mantle also influences these contributions. In contrast, Steffen et al. [2006a] showed with a flat three-dimensional (3D) earth model that the uplift velocity is not strongly influenced by the lower mantle and the horizontal velocities receive large contributions from 3D viscosity variations in the transition zone of the upper mantle between 450 and 660 km depth. This difference in the results of both papers might be explained by the possibility that the sensitivity seen by the global model of Milne et al. [2004] is actually from GIA contribution from the Laurentide ice sheet [Wu, 2006]. However, the difference in sensitivity for horizontal velocities still needs to be explained. Thus, another aim of this paper is to clarify the different results of Milne et al. [2004] and Steffen et al. [2006a].

It has been shown earlier that for GIA predictions in the Scandinavian region the flat-earth approach is adequate [e.g. Wolf, 1984; Amelung and Wolf, 1994; Wu and Johnston, 1998]. It was successfully used in the last decade [e. g. Wu et al., 1998; Kaufmann and Wu, 1998a,b; Kaufmann et al., 2000; Kaufmann and Wu, 2002; Kaufmann et al., 2005; Wu, 2005; Steffen et al., 2006a], and complements newer results based on 3D spherical earth models [e. g. Wu, 2002; Wu and van der Wal, 2003; Zhong et al., 2003; Wu et al., 2005; Latychev et al., 2005b; Wang and Wu, 2006a,b,c; Spada et al., 2006]. A main result of these papers is that a realistic 3D variation in mantle viscosity produces significantly different model predictions than a simpler 1D mantle-viscosity model. In addition, the investigations by Steffen et al. [2006a] showed that the lower mantle itself as well as a possible 3D viscosity structure of the lower mantle beneath Fennoscandia have no significant influence on the velocities and sea-level observations in that region.

To summarise, this paper will deal with the following: we focus on data in Fennoscandia since a large set of different observations, both in space and time, are available. But, in contrast to the work of Wu [2006] related to the Laurentide ice sheet, who used an axially symmetric earth model with a simple symmetric ice model, (i) we apply a *realistic* ice load history of the Fennoscandian ice sheet - namely the RSES ice model from Kurt Lambeck - on the model surface and (ii) we employ a *flat* 3D FE model with compressible, viscoelastic material properties. We have chosen this model approach as it is simple, efficient in computation time and memory requirements, and, in comparison to spherical investigations, the smaller distribution of regions with viscosity variations might provide more precise information concerning the sensitivity of the Earth's 3D structure. This allows us to explore the sensitivity of different data from different parts of Fennoscandia with a realistic ice history.

Our main emphasis is to show how sensitive BIFROST stations are to special mantle layers and regions and to suggest ideal locations for new GPS stations with higher sensitivity.

5.2 FE-Modelling

5.2.1 Earth models

The GIA process in Fennoscandia is modelled using the finite-element (FE) method. A changing ice load is applied to the surface in a central region of 3000 km $\times$ 3000 km of a flat, viscoelastic earth model which is described in Steffen et al. [2006a]. The horizontal element size is 100 km, which results in 900 element surfaces and 961 nodes. It is a layered, isotropic, compressible, Maxwell-viscoelastic half-space with a constant gravitational attraction of $g = 9.82$ m s^{-2}. We solve the Boussinesq problem for a layered, viscoelastic half-space using the commercial finite-element package ABAQUS, which has been modified to include pre-stress in order to allow the deformed free surface to return to its initial equilibrium via viscous flow [see Wu, 2004, for a summary]. The validity of the finite-element model to predict glacial isostatic adjustment has been shown previously [Wu and Johnston, 1998]. To allow the mantle material to flow due to application of a surface load outside the area of interest, we follow the approach described in Steffen et al. [2006a] and enlarge the model in horizontal direction with a peripheral frame of 60,000 km width.

Generally, our earth models consist of a layered elastic lithosphere over a layered viscoelastic mantle [see Steffen et al., 2006a, for more information]. All models have a uniform 70-km-thick lithosphere. The upper as well as the lower mantle are divided in to 4 layers, respectively. Density ρ, shear modulus μ and bulk modulus κ are volume-averaged values derived from PREM [Dziewonski and Anderson, 1981], and they are considered to be constant within an element. The 1D viscosity profile used for the sensitivity analysis is the viscosity profile V1 from Steffen et al. [2006a], characterised by only two different viscosity values, an upper-mantle viscosity of 4×10^{20} Pa s and a lower-mantle viscosity of 2×10^{22} Pa s. This parameterisation has been derived from fitting GIA observations of the Scandinavian region and has been confirmed by several independent studies [e.g. Lambeck et al., 1998a; Wieczerkowski et al., 1999; Milne et al., 2001; Kaufmann and Wu, 2002; Milne et al., 2004; Steffen and Kaufmann, 2005].

One of the challenges we face in studying the sensitivity kernel for a 3D problem is the very large number of model calculations - each with viscosity perturbation in a certain block in the 3D earth model. To overcome this challenge, we adopted the following strategy: First, we consider a small number of blocks, then we progress with more but smaller blocks. For each case, the models are termed UMi_Bj, where UMi with $i \in [1,4]$ refers to one of the upper-mantle layers and Bj is the block number. Every model represents a laterally homogeneous model except one block of one layer having a half an order of magnitude higher viscosity of 1.26×10^{21} Pa s [as suggested by Wu, 2006]. This approach is used due to the results of Steffen et al. [2006a] only for the upper mantle of the model. They found that the observed GIA process in Fennoscandia (i) is not very sensitive to the viscosity structure in the lower mantle and (ii) to the lower mantle itself. We employ three different models with varying resolution:

1. Coarse model:
   At first, the central frame is subdivided into 4 central blocks of 1000 km × 1000 km, respectively, and a frame of 500 km width (Fig. 5.1a). The viscosity is changed in only one of the blocks and in only one of the four upper-mantle layers. Hence, we have 16 different models (4 layers × 4 blocks). This division allows us to investigate in a simple way the sensitivity kernel of the central Fennoscandian region below the ice sheet and the horizontal size of 1000 km is comparable to the smallest grid of 7.5° (∼ 835 km) of Wu [2006]. In addition, the quite perfect arrangement of the 4 blocks around the uplift centre in the Gulf of Bothnia eases the discussion of the horizontal velocities. Every block consists of 100 elements and has 121 nodes on the surface.

2. Intermediate model:
   Next, we subdivide the whole central area into 9 blocks of 1000 km × 1000 km, respectively (Fig. 5.1b). This division with models of the same block size allows a discussion of the sensitivity

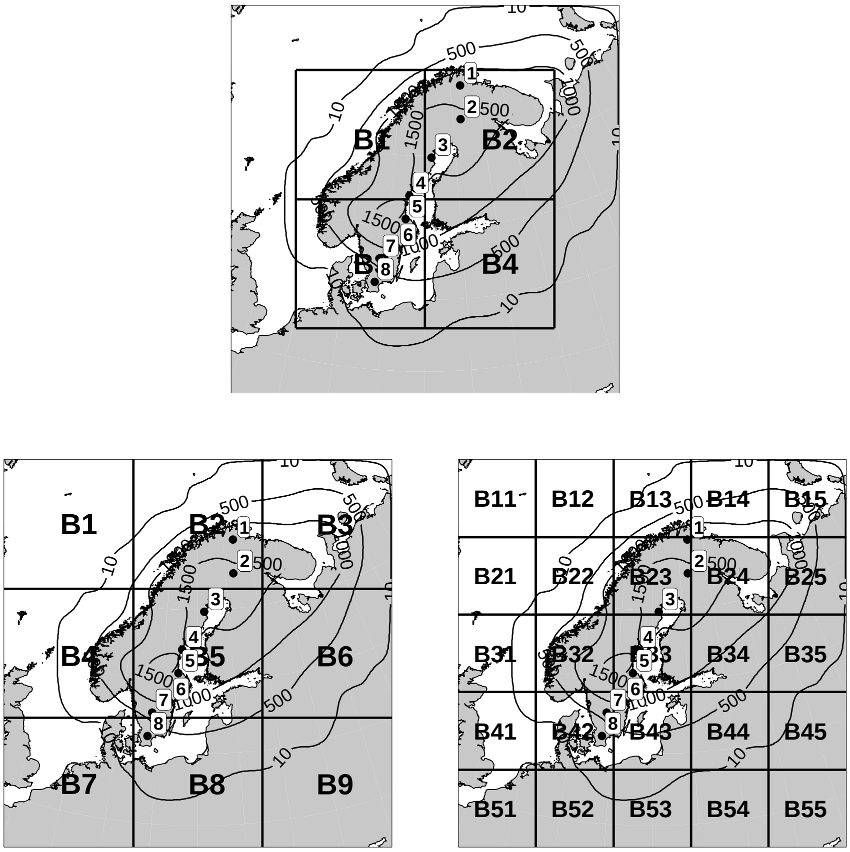

Figure 5.1: Finite-element block structure over Fennoscandia. The ice sheet thickness (in m) at 22,000 years BP is drawn with contours. Dots mark the 8 selected BIFROST locations of Figs. 5.8 - 5.10. From north to south: Kevo (1), Sodankyla (2), Skelletea (3), Sundsvall (4), Martsbo (5), Norrkoping (6), Jonkoping (7) and Hässleholm (8).

kernels of the whole Fennoscandian region. Furthermore, block B5 is located in the central uplift region, which allows a discussion of the velocities' direction in comparison to the position of the former ice load. Changing the viscosity in only one of the blocks and only one of the layers, we have 36 different models for our investigation. Again, every block consists of 100 elements and has 121 nodes on the surface.

3. Fine model:
   Finally, the whole area is subdivided into 25 blocks of 600 km × 600 km, respectively (Fig. 5.1c), resulting in 100 different models. Every block consists of 36 elements and has 49 nodes on the surface. This much finer resolution allows us to discuss results inside the ice-sheet shape and the regions beyond in more detail.

5.2.2 Ice load

The ice model for the Late Pleistocene glacial history in Europe is taken from the FBKS8 ice model of Lambeck et al. [1998a], and applied within the model area. The ice model FBKS8 simulates the extent and melting history of the Fennoscandian and Barents Sea Ice Sheets from the last glacial maximum (LGM) towards the present day. The extent of these ice sheets for four different epochs is shown in

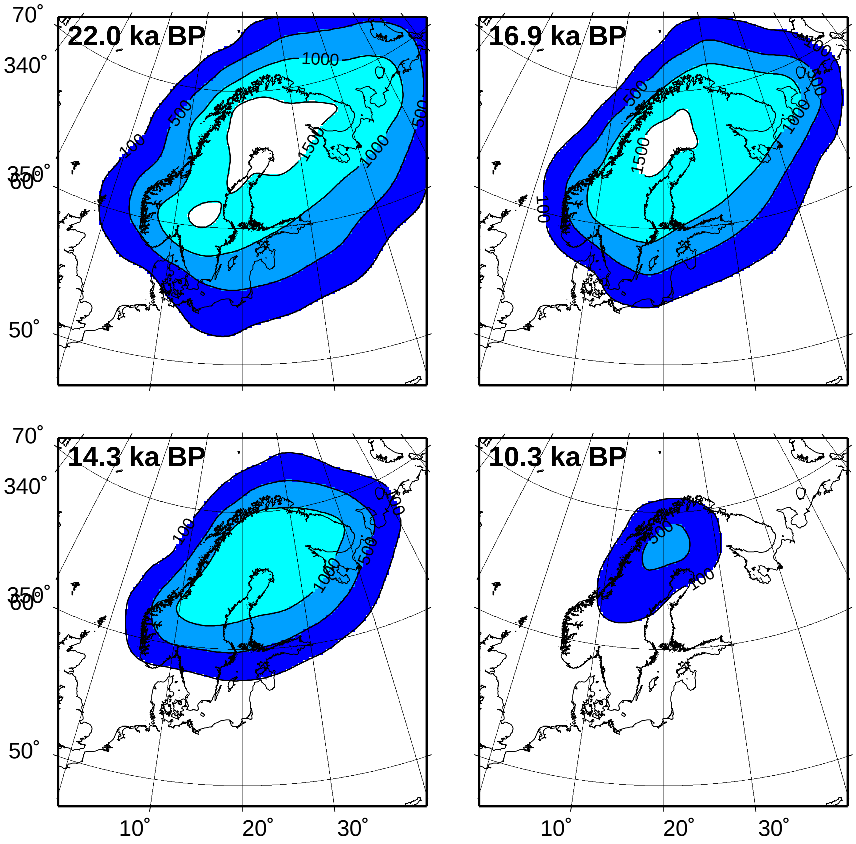

Figure 5.2: Map of ice model FBKS8 over Fennoscandia for four different time epochs. Contours are drawn every 500 m.

Fig. 5.2. The ice sheets are included in a high spatial and temporal resolution model that is consistent with the majority of the field evidence for ice-margin retreat and with the GIA data. The ice volume at the LGM approximately 22,000 years BP corresponds to 17 m of eustatic sea-level change. All reconstructions subsequent to the LGM are based on glaciological and geomorphological evidence and thus reflect the approximate extent of the Late Pleistocene ice sheets throughout the last glacial cycle. The time dependence of the load is applied as follows: A maximum load, corresponding to the LGM (at 22,000 years BP), is applied from 212,000 to 122,000 years BP. Then the load is instantly removed, and the model is ice free during the penultimate interglacial until 112,000 years BP. Then the load increases linearly, until it reaches its maximum extent at 22,000 years BP, followed by a detailed deglaciation history until the present. This parameterisation has been shown to be sufficient to correctly predict changes in surface displacements [Kaufmann et al., 2000; Kaufmann and Wu, 2002; Steffen et al., 2006a]. The ocean-load is not included, as the effects are at least one order of magnitude smaller than the ice-load signal [Steffen et al., 2006a].

5.3 Results

In this section we discuss and compare the modelling results of the different earth models, particularly the influence of certain regions to the BIFROST velocity predictions. The model predictions of present-day motions (uplift and horizontal movement) for the Scandinavian region are used to calculate the sensitivity kernels of a certain region. Furthermore, we discuss how selected stations of the BIFROST project [Johansson et al., 2002] are affected.

The calculation of the sensitivity kernels follows the approach given in Wu [2006], which is based on an expression given by Peltier [1998]. They are defined by:

$$K_{lj}(r) = K_{lj}(r_i) = \frac{\delta p_l}{\delta m_j(r_i)\Delta V_j(r_i)}. \tag{5.1}$$

$K_{lj}(r_i)$ is the sensitivity kernel with l the location of the observation, and j the number of the perturbed region (block number in Fig. 5.1). r_i is the depth of the perturbed region, and thus $K_{lj}(r_i)$ corresponds to a certain model UMi_Bj. In sections 5.3.1 to 5.3.3 of this paper, the location of the observation point l is assumed to be directly above the location of the perturbed viscosity region. In section 5.3.4, we consider the effect of the block with viscosity change on crustal velocities measured in nearby blocks. The differential prediction δp_l (in our case a horizontal velocity or uplift velocity) is defined as

$$\delta p_l = p_l^{3D} - p_l^{1D}, \tag{5.2}$$

with δp_l^{3D} the prediction of a certain perturbed 3D model and δp_l^{1D} the prediction of the 1D model V1 from Steffen et al. [2006a] (Fig. 5.3). ΔV_j is the fractional volume of the block j in depth i:

$$\Delta V_j(r_i) = \frac{V_{ij}}{V_{model}}, \tag{5.3}$$

with V_{ij} the block volume and V_{model} the volume of the entire central area. The viscosity perturbation δm_j of block j in depth i in our modelling is equal to 0.5, the difference of half an order of magnitude between the viscosities. The kernels are calculated for every surface grid point of the FE model and thus, we are able to make a sensitivity analysis for each location in the model area to the different blocks. However, this would produce a huge number of figures to show and interpret making the paper unreadable (Just

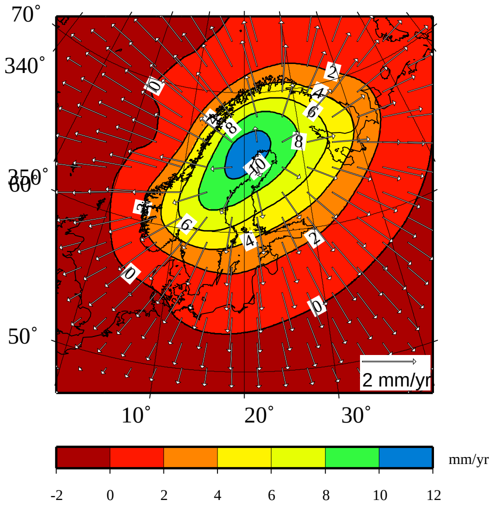

Figure 5.3: Predictions of horizontal (arrows) and vertical movement (contours) for the 1D model V1 from Steffen et al. [2006a].

take the 3 present-day velocity components at the 961 surface nodes with each of the nodes sensitive to a viscosity change in 4 depth ranges *i* of the 25 blocks of the fine model. This would result in 72075 curves when drawn over the depth!). Hence, we introduce following approach: We calculate the kernel of a block UMi_Bj, by averaging the perturbed predictions of all surface nodes of this block to one value for block UMi_Bj. This means for the coarse and intermediate model averaging the values of 121 nodes to one value, and for the fine model averaging the values of 49 nodes to one value. With this approach an overview is given on how a viscosity change in a certain block influences on average the velocities at each surface point of the block area (Figs. 5.4 and 5.5). The effect of a block UMi_Bj_1 at the locations of another block UMi_Bj_2 is calculated by averaging all perturbed predictions of all surface nodes of block UMi_Bj_2 to one value. Here, only selected examples are discussed as the number of curves is still large (Figs. 5.6 and 5.7). Finally, the results for the BIFROST stations discussed in Milne et al. [2004] are presented (Figs. 5.8 and 5.9). All these figures show the sensitivity kernels of the present-day velocities (in WE and NS–direction, and the uplift) over the depth as normalised Earth radius. They are interpreted as the sensitivity of one block or one BIFROST station to viscosity changes (i) in one of the 4 upper-mantle layers below that block area or station, or (ii) in one of the 4 upper-mantle layers next to that block area or station.

5.3.1 Coarse model (1000 km × 1000 km block models, central area)

Fig. 5.4 shows the sensitivity kernels of the velocities for 4 different 1000 km × 1000 km blocks of the coarse model. The present-day uplift velocity is most sensitive to the second and third layer, with a kernel amplitude of around 0.6 mm/yr in block B2. Except for B4, the first layer is also more sensitive than the fourth one. Furthermore, viscosity changes in blocks B1-B3 result in an additional uplift, while block B4 induces an additional subsidence component, when compared to the 1D viscosity model.

For the present-day horizontal velocity in WE–direction, we generally find a smaller kernel amplitude of around 0.1 mm/yr, and an increase in sensitivity to deeper parts of the upper mantle and/or only small variations in the first 3 layers. The blocks B1 and B3 west of the model centre show an additional

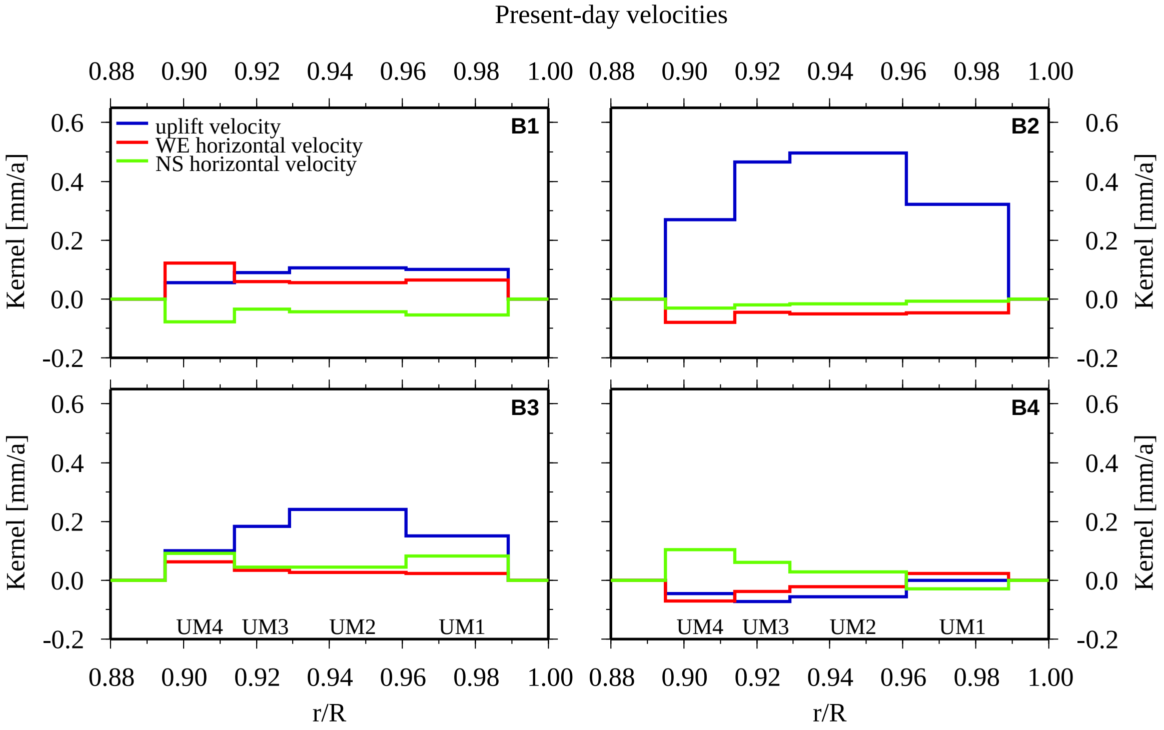

Figure 5.4: Sensitivity kernels of the present-day velocities plotted as a function of the normalised Earth radius for the coarse model.

movement to east, while the additional movement in blocks B2 and B4 east of the model centre is directed to west, except for the first upper-mantle layer in B4. Since the horizontal movement due to the uplift is generally directed outward, these differences in the horizontal velocity between the 1D model and the perturbed 3D model indicates that a higher viscosity in the perturbed region results in a decrease of the horizontal radially outward motion. For B1-B3, the sensitivity of the lowest part of the upper mantle is around twice that of the other parts. These blocks lie within the former ice sheet. In contrast to this, the sensitivity for B4, where most parts are located outside the former ice sheet, is small and directed eastward in the first layer. Also, the sensitivity changes sign but increases in magnitude at the deeper part of the upper mantle. For B1, which is located in the northwestern part of the former ice sheet and in the region with the highest amount of ice, the largest sensitivity with around 0.13 mm/yr is obtained.

The sensitivity of the present-day velocity in NS–direction, with a kernel amplitude of around 0.1 mm/yr, shows again the highest sensitivity at the bottom of the upper mantle, except for the first upper-mantle layer beneath B3. Here, compared to the sensitivity in the fourth layer the sensitivity is relatively higher. Besides this, an additional northward directed motion is found for blocks B3 and B4, which are located in the south of the model, and the additional southward motion for the two blocks B1 and B2, that are located in the northern part. This confirms again the decrease of the horizontal velocities due to the higher viscosity of the perturbed region. In summary, comparison of the tangential motion of our four models with the results of the 1D model shows that a lateral viscosity variation in the transition zone has a strong influence on the tangential motion.

The results of this section have many similarities with the next two sections. Thus, we first state and summarise the common findings in the next sections and then discuss differences.

5.3.2 Intermediate model (1000 km × 1000 km block models, whole area)

In Fig. 5.5 the sensitivity of the present-day uplift velocity can be seen for the nine blocks with a maximum kernel amplitude of around 0.6 mm/yr at most. Generally, the kernels are positive within the ice margin and negative outside. As expected, the largest effects are found for B5, the block above which the former ice maximum was located. The uplift velocity is most sensitive to the second and third upper-mantle layer. The effect from the fourth layer reaches only around 60% of the second layer and is smaller than the one of the sub-lithospheric layer. The sensitivity of variations in other blocks is smaller with the smallest sensitivities for B4 and B6.

The sensitivity kernels of the present-day horizontal velocity in WE–direction shows kernel amplitudes of around 0.2 mm/yr. The first diagram row encompasses the northern model parts. As for the coarse

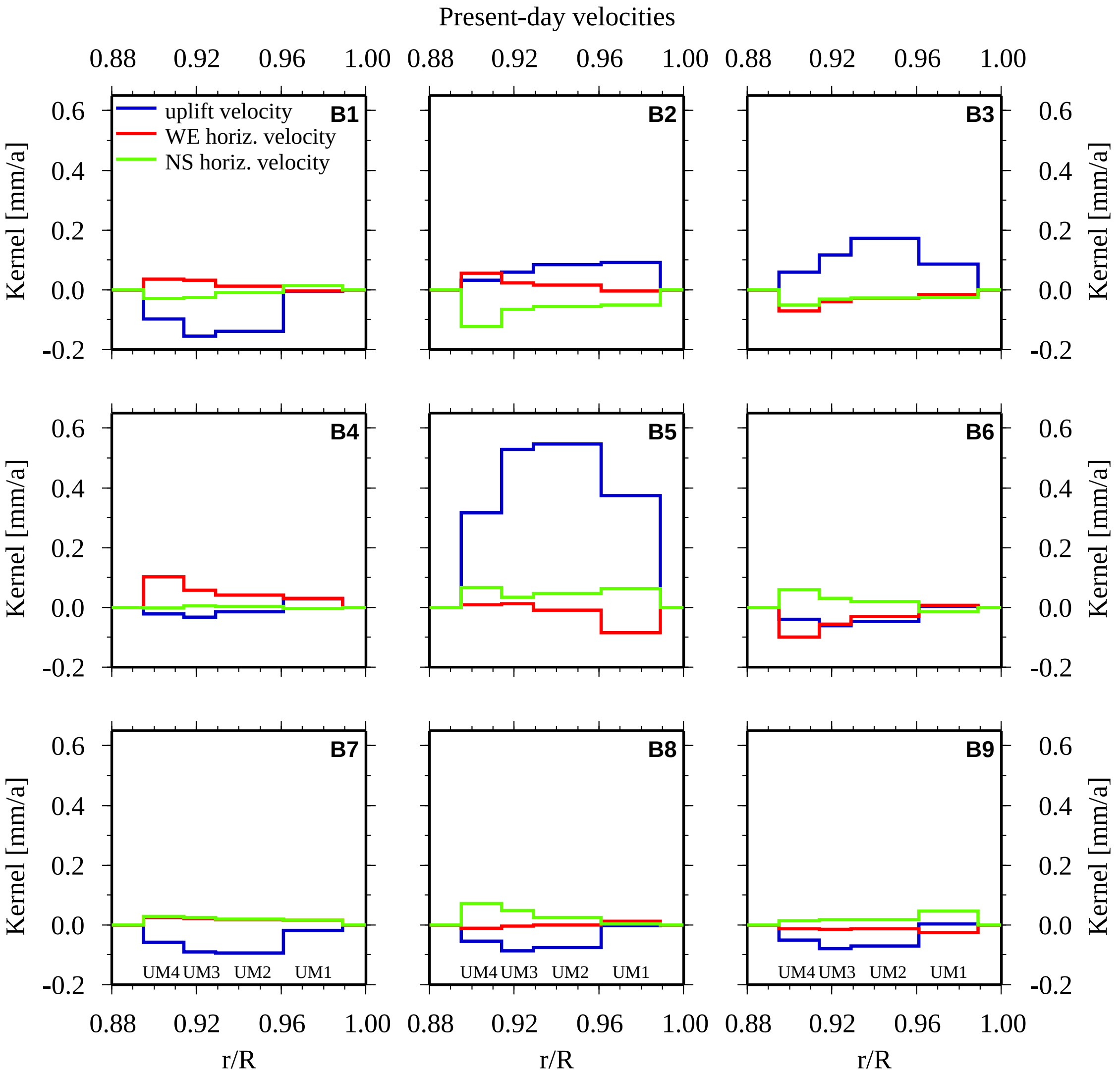

Figure 5.5: Sensitivity kernels of the present-day velocities plotted as a function of the normalised Earth radius for the intermediate model..

model (section 5.3.1), we also find that the higher viscosity reduces the outward directed horizontal motion from the centre of rebound. For B1 the kernel has nearly the same sensitivity in the transition zone (third and fourth layer), while for the first layer it is negligible. For B2 we observe an eastward trend, which indicates a decrease of the uplift-induced westward movement due to the higher viscosity in the perturbed region. The ice sheet was located on top of B2 and also B3, east of B2. The surface was depressed mainly in those two regions of the northern parts, which after the disappearance of the ice mass now induces westward directed velocities on B2 and eastward directed velocities on B3. The second diagram row summarises the results of central model blocks B4 to B6. For B4 and B6 comparable results to B1 and B3 can be established, except that B4 has larger kernels than B1 due to the thicker ice load on top of B4's surface. The most impressive behaviour is found for B5. Here, the WE–velocity is most sensitive to the first upper-mantle layer. This is a consequence of the ice load, which was largest on B5's surface among all other blocks (see Fig. 5.1) and acts directly in the uppermost mantle parts and hence, for the WE–velocity in the first layer. The last diagram row highlights the sensitivity for B7 to B9. As there is only a small surface load we find only small sensitivities. For B7 and B8 the sensitivity in the fourth layer is still the largest. For B9 the first layer is the most sensitive, which is the block with the smallest surface load of all 9 blocks.

Fig. 5.5 also summarises the sensitivity of the present-day horizontal velocity in NS–direction for the nine blocks. For the northern blocks of the model, we can confirm the highest sensitivity of the fourth layer to NS–velocity and the southward movement due to the viscosity contrast between the underlying block and the rest of the blocks in a specific layer. The second diagram row focuses on the central model area. Interestingly, B4 is nearly insensitive to the NS–velocity, as here horizontal velocities are mainly in the western direction. For B5 a high sensitivity can be found in all layers, with maxima in the first and fourth layer. This is, as already mentioned in the discussion of the WE–velocity, a consequence of the large ice load on the surface of this block. B6 is again most sensitive to the lowest part of the upper mantle, indicating a northward motion, which is due to the ice load on B3 to the north. The sensitivity of B7 and B8 is highest in the fourth layer, but for B7 smaller than for B8. In contrast to this, B9 shows the highest sensitivity in the first layer. The movement to north for the last three blocks is due to the viscosity contrast.

5.3.3 Fine model (600 km $\times$ 600 km block models)

We do not show here the results of the fine model, as they are comparable to the former results. A rough comparison of the results of smaller and bigger blocks indicates higher sensitivities for the horizontal velocities of bigger blocks. In contrast, the uplift velocity of smaller blocks has a higher sensitivity than that of the bigger blocks. Thus, we clearly see a dependence of the sensitivity kernels on the size of a block. This means if we scale down the block size, the sensitivity to uplift velocity would increase and the horizontal velocity would decrease. In addition, both grids show that blocks within the former ice sheet are more sensitive than blocks beyond. The biggest values are obtained for blocks in the former ice sheet centre with the maximum ice height.

5.3.4 Sensitivity of blocks in selected distances

The results shown in the previous sections focus on the sensitivity of a disturbed block on the averaged crustal motion directly above the block itself. In this section we investigate the influence of viscosity changes in a selected block to the locations on surrounding blocks. However, we only focus on the present-day horizontal velocities, because the effect on the uplift velocity of a neighbouring block of a perturbed block is negligible. Hence, we do not show any figure for this case.

Fig. 5.6 summarises the sensitivity kernels of three blocks of the coarse model (Fig. 5.1a) to the neighbouring blocks for the present-day horizontal velocities. We observe again the biggest sensitivities in the first and the fourth upper-mantle layer, but a discussion of the effects is quite complicated. Generally, the horizontal velocities in each block are mainly influenced by viscosity changes in blocks 2 and 3, which have the thickest ice. For example, Fig. 5.6d and h show that both velocities at B4 are most sensitive to viscosity changes in the third and fourth layer of B3, and also to the first and second layer of B2. The velocities at B3 are mainly influenced by B2, while velocities at B2 are most sensitive to B3 in NS–direction and to B1 in WE–direction. At B1 the NS–velocity shows the biggest sensitivity to B3. For the WE–velocity contributions by all other blocks are observed.

Fig. 5.7 shows the sensitivity kernels for the intermediate model, in one case for block B5 to the 8 other blocks (Fig. 5.7a, b, e and f), and in the other case each of these 8 blocks to B5 for the present-day horizontal velocities (Fig. 5.7c, d, g and h). Fig. 5.7a and b highlights a strong influence of viscosity changes in the first layers of B5 on the present-day WE velocity at the other surrounding blocks, which tends to decrease with deeper upper-mantle layers. The same behaviour is observed for block B5 on blocks B1 to B9 for the NS–velocity (Fig. 5.7e and f). The influence of block B5 on B3 and B4 is small on the NS–velocity, while the influence on the NS–velocity at B2 shows maxima in the first and fourth layer. The influence of viscosity changes in the 8 other blocks on WE–velocity at B5 (Fig. 5.7c and d) is twofold: on the one hand, the sensitivity due to changes in B1, B2 and B7 to B9 is low and / or decreases towards the deeper parts of the lower upper mantle, on the other hand, changes in each upper-mantle layer of B3, B4 and B6 show a nearly constant influence on WE–velocity at B5. Interestingly, these are three blocks with a thick ice cover. Furthermore, B4 and B6 are situated west and east of B5, respectively, in the same direction as the discussed velocity component. Fig. 5.7g and h reveals comparable effects. Here, B2, B8 and B3 show a constant influence, while the sensitivity for NS-velocity generally decreases with deeper depth as in WE-velocity. Again, B2 and B8 are located in the direction of the resulting velocity component, north and south of B5.

The comparison, in view of the grid size, indicates similar behaviour between the intermediate model and the fine model. Two main results arise: (i) the influence of a perturbed block on the uplift velocity of a neighbouring block is negligible (not shown), and (ii) the influence of one block on the horizontal velocity on another block is strongest if the direction of the horizontal velocity is along the same direction between the two blocks. In the case of a block located right next to the perturbed block, the other component is much less affected. Additionally, the amplitude of the sensitivity kernel decreases as the distance between the two blocks increases.

5.3.5 Effects on BIFROST stations

Figs. 5.8 and 5.9 show the sensitivity kernels of the present-day velocities for 8 selected BIFROST stations due to viscosity changes directly below the block. These 8 stations are the same as those taken by Milne et al. [2004], oriented along a North-South-profile. The locations can be found in Fig. 5.1.

Coarse model:
Fig. 5.8 focuses on the results for the coarse model. The sensitivity in the uplift velocity generally increases for the central BIFROST locations, with the lowest sensitivity found for the stations Hässleholm and Kevo in the far south and north. Looking at the sensitivity to the upper-mantle layers, the maximum is resolved for the second and third layer. At Sundsvall, Skelletea and Sodankyla the sensitivity in the

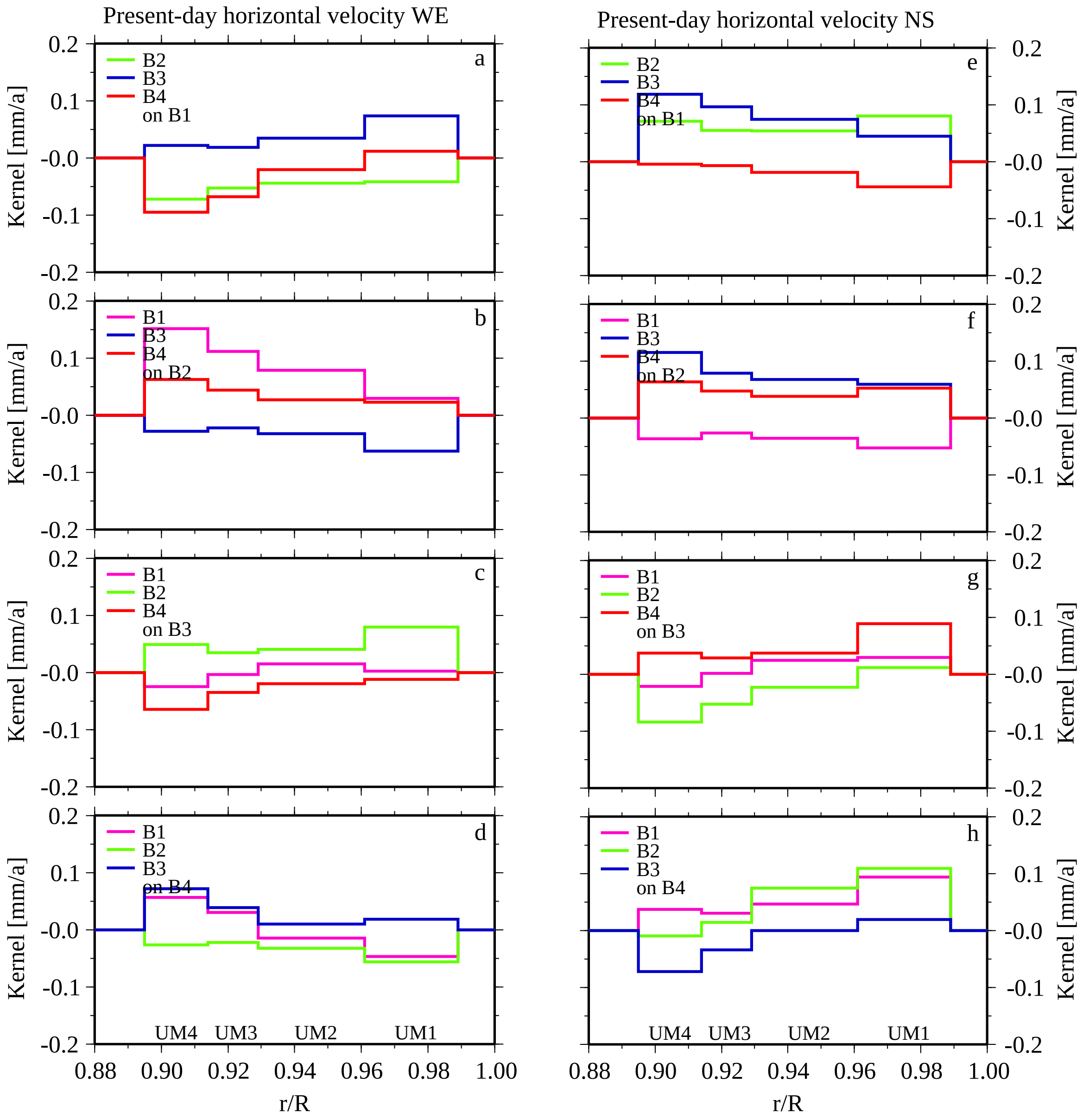

Figure 5.6: a - d) Sensitivity kernels for the coarse model of three out of four blocks on the fourth one for the present-day horizontal velocity in WE–direction plotted as a function of the normalised Earth radius. e - h) Same as a and b, but for the present-day horizontal velocity in NS–direction.

third layer is slightly larger than in the second layer. The first layer is, except for the three central stations Martsbo, Sundsvall and Skelletea, more sensitive than the fourth layer. The sensitivity of the horizontal velocities is different, when compared to the results averaged for one block (Figs. 5.4 - 5.7), as the general tendency to increase in the deeper upper mantle is only partially observed (WE–horizontal velocity at Hässleholm, Jonkoping, Sodankyla and Kevo). Instead, the second and third upper-mantle layer often dominate the sensitivity. In exception, the NS–horizontal velocity at Hässleholm, Jonkoping and Norrkoping is characterised being most sensitive to the first and fourth layer with slightly higher values in the fourth layer. At Martsbo, this component shows a nearly constant sensitivity to all layers.

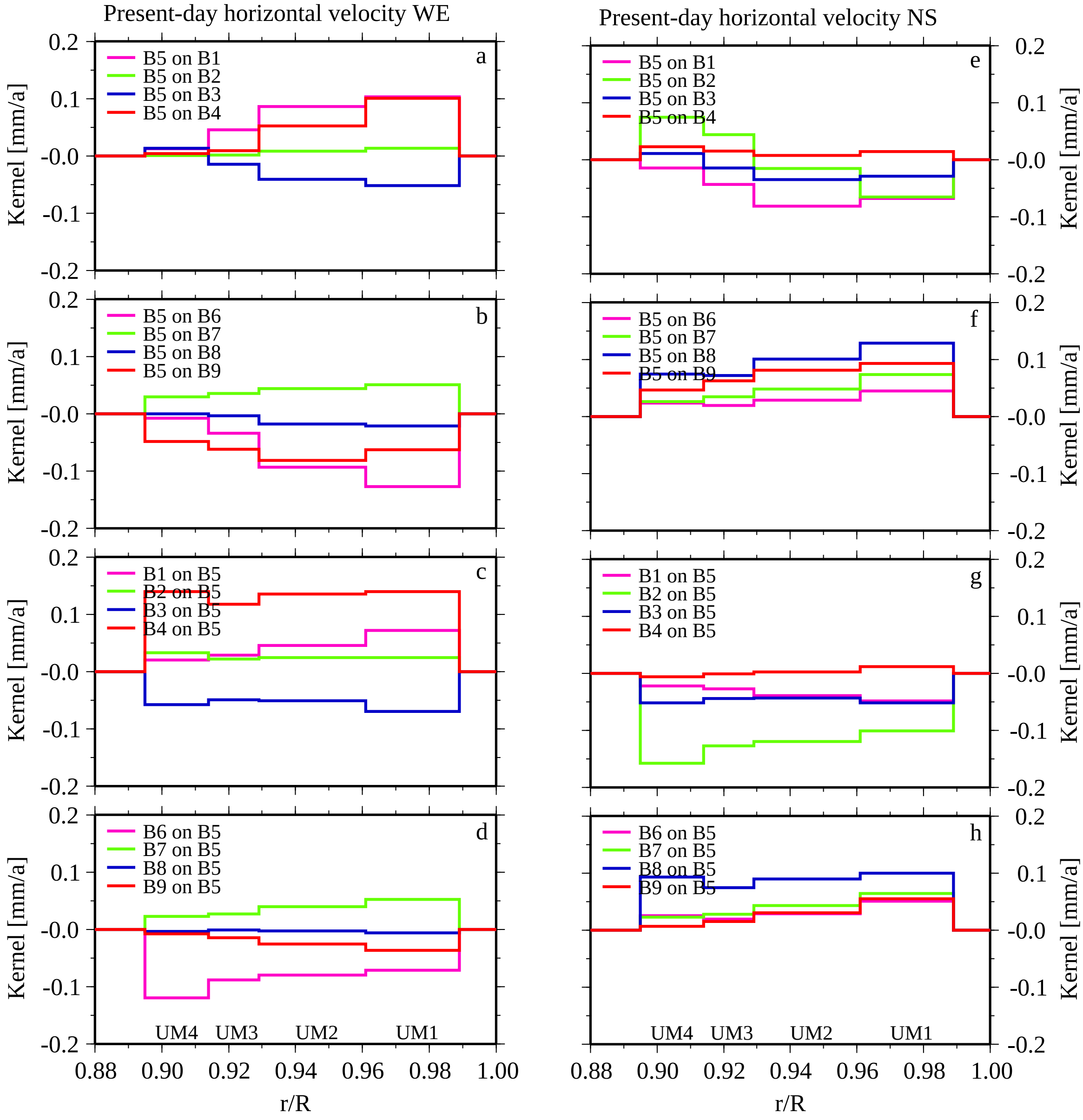

Figure 5.7: a and b) Sensitivity kernels of the central block B5 of the intermediate model on the eight other blocks for the present-day horizontal velocity in WE–direction plotted as a function of the normalised Earth radius. c and d) Sensitivity kernels of the eight outer blocks of the intermediate model on block B5 for the present-day horizontal velocity in WE–direction plotted as a function of the normalised Earth radius. e and f) Same as a and b, but for the present-day horizontal velocity in NS–direction. g and h) Same as c and d, but for the present-day horizontal velocity in NS–direction.

Intermediate model:

Fig. 5.9 is the same as Fig. 5.8, but for the intermediate model. As for the coarse model, the uplift velocity (i) is most sensitive in the second and third layer and (ii) reaches its largest values at the central BIFROST stations. At Sundsvall and Skelletea the third layer is the most sensitive. Furthermore, at these two stations the fourth layer is more sensitive than the first layer. Interestingly, those stations are located

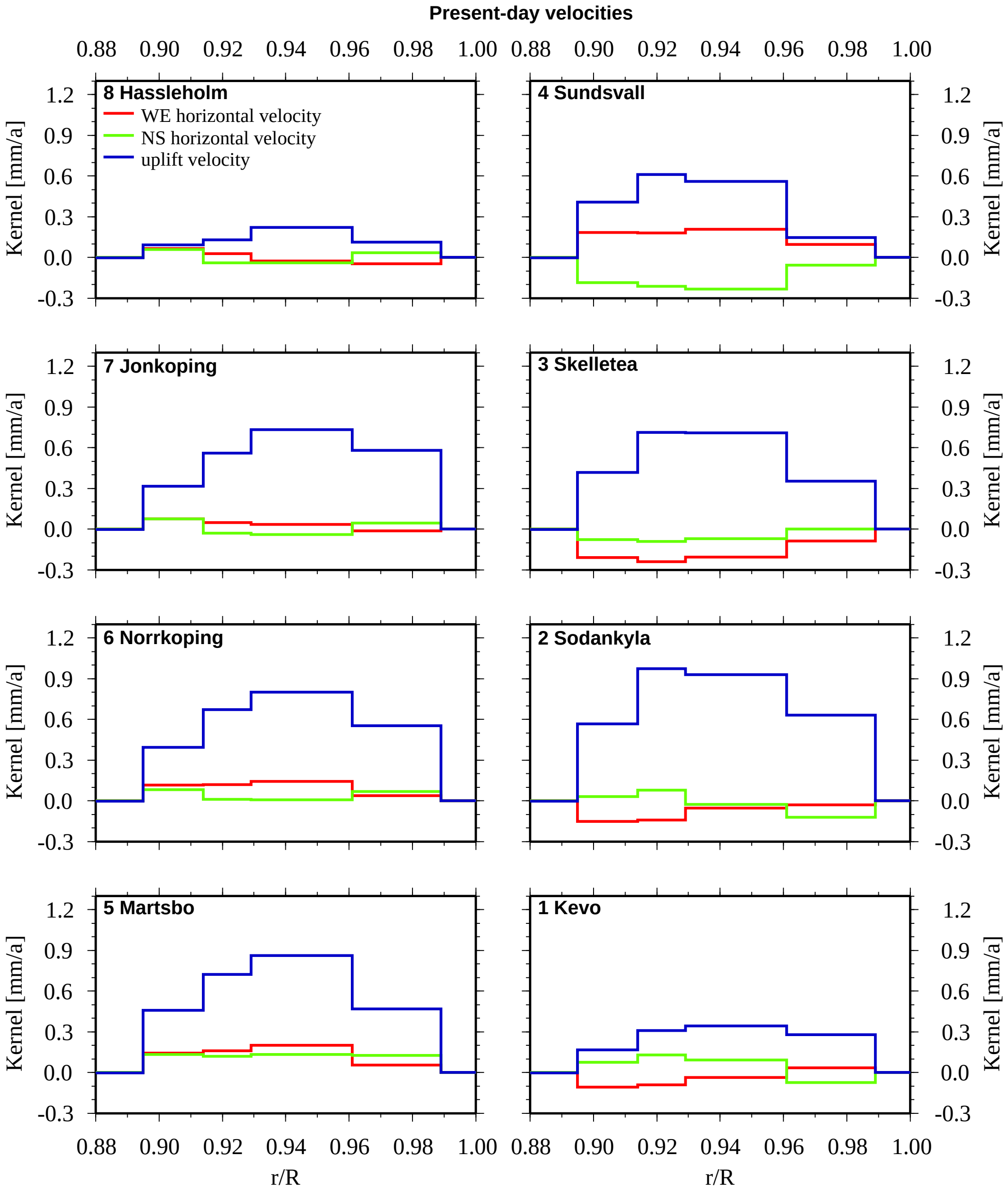

Figure 5.8: Sensitivity kernels of the present-day velocities of 8 BIFROST stations for the coarse model plotted as a function of the normalised Earth radius.

in the centre of the former ice sheet and are also the ones where Milne et al. [2004] found the largest sensitivities. The station of Jonkoping seems to be insensitive to variations in the fourth upper-mantle layer. The horizontal velocities are influenced differently. For example, at Hässleholm the sensitivity is low, but with a maximum in the fourth layer. At Sodankyla, the WE–velocity is most sensitive from the second to the fourth layer, but negligible in the first layer, while the sensitivity of the NS–velocity remains quite constant in all layers. At Jonkoping, Norrkoping and Martsbo a decrease in sensitivity to deeper parts is observed, while at Kevo an increasing trend results.

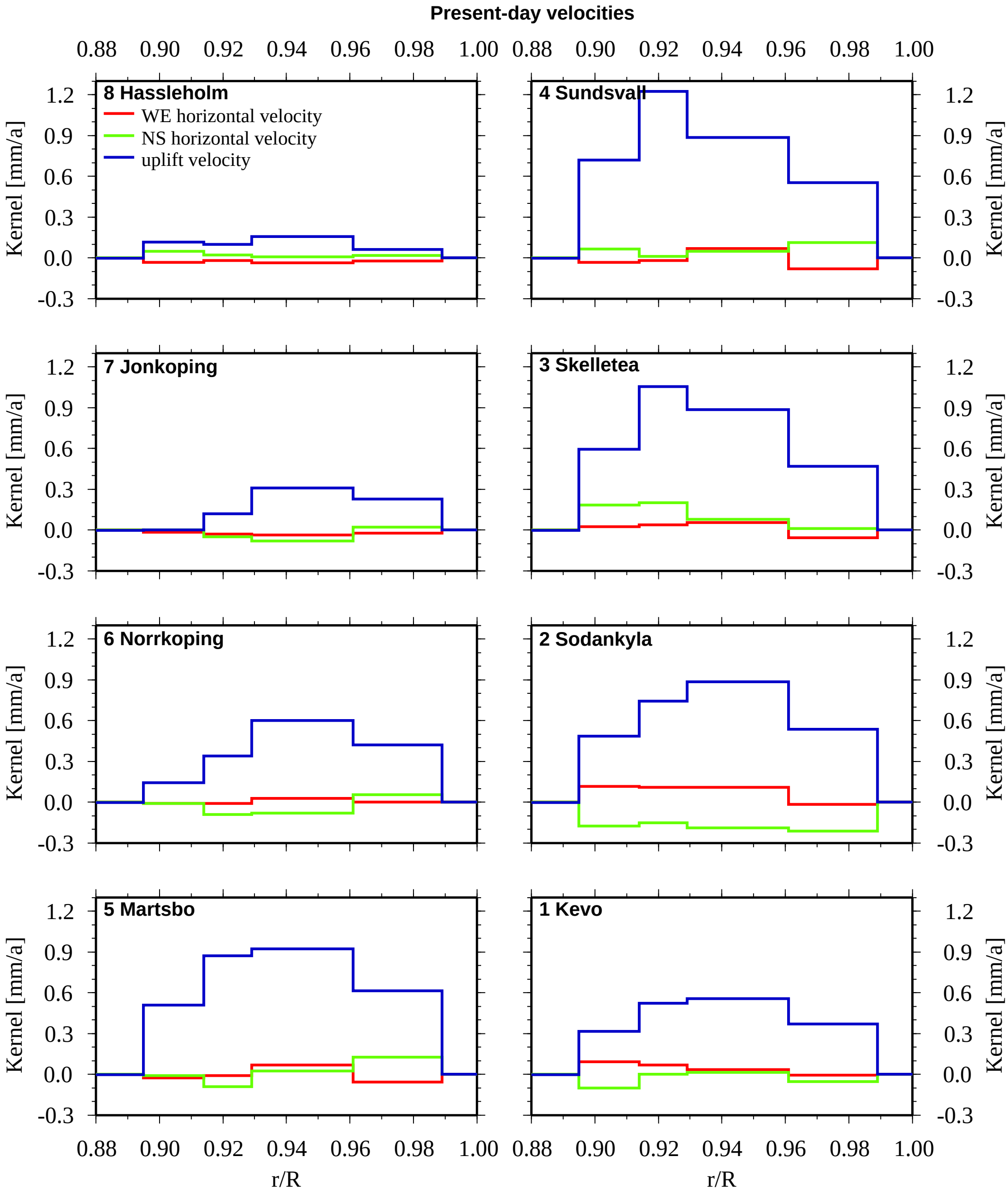

Figure 5.9: Sensitivity kernels of the present-day velocities of 8 BIFROST stations for the intermediate model plotted as a function of the normalised Earth radius.

In agreement with the results of Milne et al. [2004] and independent of the block size, the uplift velocity obtained with the different block grids also shows the largest sensitivity values at the stations of Sundsvall and Skelletea, followed by Martsbo and Sodankyla, then Norrkoping, Jonkoping and Kevo, and finally the smallest values are found at Hässleholm. In contrast, the difference between the third and fourth layer is greater than between a (simply resolved by averaging the respective layers) third and fourth layer of Milne et al. [2004]. For the horizontal velocities a different behaviour is established, which we think is mainly due to the model geometry and thus due to the “simple” lateral heterogeneity of our 3D model. Our results do not show the decrease in sensitivity of horizontal velocities to deeper upper-mantle parts (except for the NS–velocity at Skelletea and Sodankyla) as observed by Milne et al. [2004]. They are more affected by the location of a station on a block in relation to the location of the block in the model, the distance of the station to the block border and the ice sheet geometry, which finally confirms the results of Wu [2006]. This effect can be seen with a closer look at the results. If we take for example the station of Hässleholm, it is located on the 4 block model in the centre of B3. The uplift velocity is small compared to other stations due to the smaller ice load. The direction of the horizontal velocities in each layer differs due to the location in the centre. This becomes clearer when looking at Hässleholm and its location on the 9 block model. Here, Hässleholm is situated in the northwestern corner of B8. The uplift velocity is, as expected, still small, but the horizontal velocities clearly show a movement to west for the WE–component and north for the NS–component. These analyses can be done for each of the 8 BIFROST stations and their position on the different block models. The results confirm the behaviour discussed above.

Fine model:
Fig. 5.10 shows the sensitivity kernels for the BIFROST stations of Norrkoping, Sundsvall and Kevo and the perturbed blocks B13 to B53 of the fine model (see Fig. 5.1c). Thus, this figure summarises on a block profile from north to south the influence of a viscosity change on the present-day velocities of the three stations. The station of Norrkoping is located in the northwestern part of block B43. Hence, the largest effects on this site in Fig. 9 are due to this block. Remarkable effects are also found for the uplift velocity for a perturbed block B33. This is due to the location of Norrkoping on block B43 next to block B33, which in addition is located in the centre of the Fennoscandian ice sheet. Again, the largest effects are found in the second layer. The sensitivity of the horizontal velocity is smaller but not negligible. The contributions of the other blocks (B13, B23 and B53) are small and they decrease more as the region of viscosity change gets further away. As shown here, the amplitude of the uplift velocity decreases much faster than that for the horizontal velocities. The station Sundsvall is located near the middle of block B33, which is reflected by the amplitude of the kernels. The uplift velocity is largest at B33 and strongly decreases as the viscosity change moves farther away. Interestingly, the largest amplitude in the uplift kernel in B23 and B43 is found in the fourth layer, while the sensitivity in the second layer is very small. The horizontal velocities show a different behaviour. The amplitude of the NS-velocity kernel first increases in the nearby blocks B23 and B43, then it decreases with increasing distance, while the WE-velocity steadily decreases. This behaviour is due to the location of the perturbed block and the direction of the component. The opposite is observed for a WE block profile (not shown). The results for Kevo have many similarities with the one for Norrkoping, as Kevo is located quite near the block border to B13. As expected, due to its close proximity, the influence of the neighbouring block B13 on uplift velocity is comparable to that for B23. The exception is in the fourth layer where the amplitude due to viscosity change in B13 is larger by a factor of 10.

These results can be summarised as follows: (i) for a selected station, the sensitivity of the uplift velocity is largest for the block where the station is located and may include the neighboring block, if the station is located close to its border, (ii) the sensitivity of the uplift velocity strongly decreases as the viscosity change moves farther away, (iii) the sensitivity for the horizontal velocity component is largest at the neighbouring block if that block is situated in the direction of this component, (iv) the sensitivity of the horizontal velocities increases at the neighbouring block but decreases as one moves further away, (v) the amplitude of the uplift velocity decreases much faster with distance than that for the horizontal velocities.

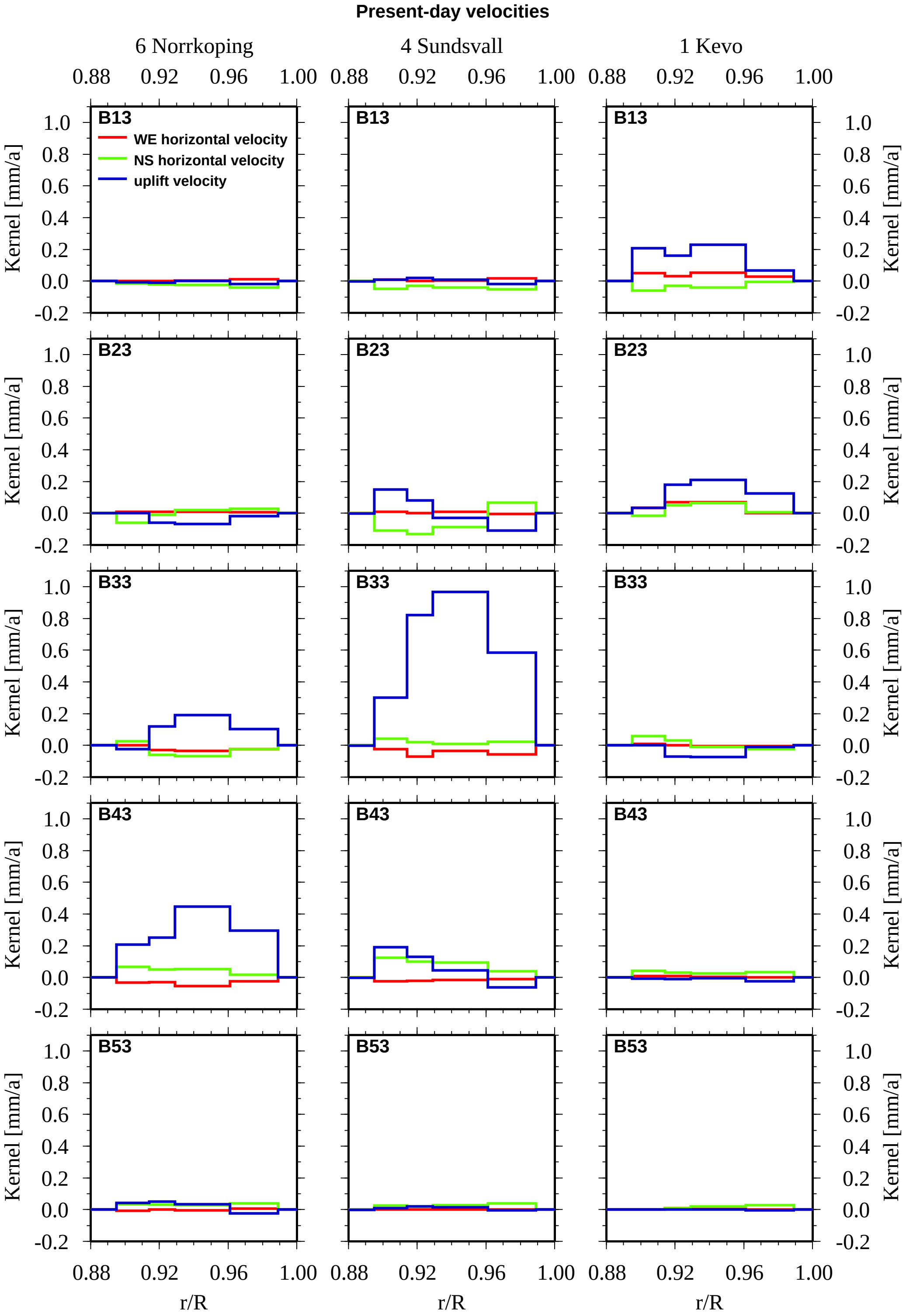

Figure 5.10: Sensitivity kernels of the present-day velocities at 3 BIFROST stations and 5 selected 600 km × 600 km blocks plotted as a function of the normalised Earth radius.

5.4 Conclusions

We have investigated the sensitivity kernels of the present-day velocities in Fennoscandia with a 3D FE model with compressible, viscoelastic material properties and a realistic ice-load history of the Fennoscandian ice sheet, which allowed us to explore the sensitivity of different data from different parts of Fennoscandia. Therefore, we have subdivided the model into different blocks and have changed the viscosity in a certain block by half an order of magnitude as suggested by Wu [2006]. The different subdivisions yielded in a huge number of kernels to interpret and thus we have introduced an approach to calculate the kernel of a block by averaging the perturbed predictions of all surface nodes of this block to one value for this block.

Our results show that the present-day uplift velocity is most sensitive to the second and third layer of the upper mantle independent of the block size and the sensitivity for the second layer is generally higher than that in the third one. This is in agreement with the findings from Steffen et al. [2006a], who observed in their simple sensitivity analysis high contributions to uplift velocity from those two layers. The first layer is also more sensitive than the fourth one. Furthermore, viscosity changes in blocks within the former ice sheet produce larger effects than blocks with mainly parts outside the former ice sheet. The largest effects are found for blocks located below the former ice maximum. The effect of a viscosity change in neighbouring blocks to one block on the uplift rate is negligible. The uplift velocity of smaller blocks is more sensitive than the one of bigger blocks. For the smaller blocks is also observed, that the sensitivity in the surrounding blocks of the maximum sensitivity decreases up to the minimum for blocks far away of the shape of former ice sheet. Thus, we see a clear influence of the block size on our results.

For the present-day horizontal velocity and bigger blocks, we generally found an increase in sensitivity to deeper parts of the upper mantle and/or only small variations in the first 3 layers. In contrast, the first upper-mantle layer is most sensitive for the smaller blocks. The smallest influence is obtained for the second layer. Deeper into upper mantle, the sensitivity increases. For all block sizes we establish the directed movement of the kernels out of the perturbed block induced by the higher viscosity in that block. For blocks within the former ice sheet, the sensitivity in the lowest part of the upper mantle is around twice as much as the sensitivity of the other parts. In contrast, the sensitivity at the block below the former ice sheet maximum is most sensitive to the first layer. The sensitivity for blocks with most parts located outside the former ice sheet is small. In summary, comparison of the horizontal motion of the perturbed models with the results of the 1D model shows that a lateral viscosity variation in the transition zone has a strong influence on the horizontal velocities. A comparison of the results of smaller and larger blocks also indicates higher sensitivities for the horizontal velocities of larger blocks.

The sensitivity of a selected block to the surrounding blocks is for the horizontal velocities large in the first and the fourth upper-mantle layer. It is mainly influenced by viscosity changes in blocks with ice load on the surface. The strongest influence results from blocks which are located in the direction of the discussed horizontal component. For the smaller blocks, different results are obtained, which makes it quite complicated to analyse. The uplift velocity is less influenced at all blocks.

The sensitivity kernels of the present-day velocities for 8 selected BIFROST stations represent in the uplift velocity generally an increase in sensitivity for the central BIFROST locations. The lowest sensitivity is found for the stations in the far north and south. The maximum is resolved for the second and third layer and the first layer is generally more sensitive than the fourth layer. This confirms the results for the blocks except for a few sites near the load centre. The sensitivity of the horizontal velocities is not comparable with the results for the blocks, as the second and third upper-mantle layer also can dominate the sensitivity. This is in agreement with the results of Milne et al. [2004]. In contrast, the difference between the third and fourth layer is greater. The horizontal velocities are more affected by the location of a station on a block in relation to the location of the block in the model, the distance of the station to the block border and the ice sheet geometry, which confirms the results of Wu [2006].

In view of the ideal location of GPS stations in Fennoscandia to determine the viscosity structure beneath we would like to point out:
(i) Steffen et al. [2006a] showed that GPS data from Fennoscandia include less information of the lower-mantle viscosity, and thus it is not possible to resolve a sufficient heterogeneous structure. Nevertheless, a detailed picture of the upper-mantle viscosity can be obtained with a net of stations located in the shape of the former ice sheet.
(ii) The stations far outside the former ice sheet shape contribute to the determination of lateral viscosity contrasts in the upper mantle beneath Fennoscandia. As this is dependent on the size of a perturbed region and the location of this region to the GPS station, further investigations have to be made with a preliminary, but reliable viscosity structure of Fennoscandia.

Acknowledgements

Many thanks to Kurt Lambeck for providing the FBKS8 ice model. The figures in this paper are drawn using the GMT graphics package Wessel and Smith [1991, 1998]. This research was funded by the DFG (research grant KA1723-1).

6. Numerical modelling of deformation changes induced by lake-level fluctuations of the Hohenwarte reservoir, Thuringia, Germany

Abstract[a]

The Hohenwarte reservoir in southeast Thuringia (Germany) is a medium-sized artificial reservoir, holding on average 180 Mill. m^3 of water. It was constructed between 1936 - 43 and is operational since then. The water load impounded induces stress and deformations of the underlying crust and upper mantle.

The Geodynamic Observatory Moxa is located around 4 km to the north. The observatory is equipped with seismometers and sensitive tilt– and strainmeters, accurate to the nrad and nstrain range.

We explore the deformation effects caused by the water load of the Hohenwarte reservoir, both on a short-term seasonal time scale and a long-term decadal time scale. The seasonal effect, mainly induced by elastic deformation, results in tilt and strain deformation in the 4 μrad and 1 μstrain ranges, respectively. Long-term decadal variations, however, are unlikely to be significant, if a realistic viscoelastic structure of the underlying upper mantle is used.

---

[a] Steffen and Kaufmann (2006a). Numerical modelling of deformation changes induced by lake-level fluctuations of the Hohenwarte reservoir, Thuringia, Germany, J. Geodyn. 41(4), 411 - 421; Steffen and Kaufmann (2006b). Influence of the Hohenwarte reservoir on tilt and strain observations at Moxa. Bull. d'Inf. Mar. Terr. 142, 11399 - 11406.

6.1 Introduction

Artificial reservoirs hold back water behind a concrete or earthen dam. They are important for flood protection, for providing drinking water and for the generation of electricity. Furthermore, many jobs can be provided around a reservoir, especially in the tourism business. From a scientific view, the filling of reservoirs with water induces a load on the Earth's surface, deforming the crust and mantle and producing tilt and strain deformations. In addition, reservoir-induced deformations due to accumulation of large water masses behind a dam are potentially seismogenic [e. g. Rothe, 1968; Simpson, 1976; Withers, 1977; Bell et al., 1978; Li and Han, 1987].

The deformation of the Earth's surface by reservoirs has been studied extensively in the literature. Some examples are discussed below:

Lambert et al. [1986] observed an anomalous relative vertical uplift of 4 cm and relative changes in gravity of 14 μgal after the filling of La Grande-2 reservoir, Quebec, Canada. The gravity change is thought to be the result of lateral transport of water in a high-permeability formerly undersaturated zone, hydraulically coupled to the reservoir. The possible elastic expansion of cracks and fractures in this zone or unexpectedly high rates of regional tilting cause the anomalous uplift.

Kaufmann & Amelung [2000] investigated the reservoir-induced deformation in vicinity of Lake Mead, Nevada, USA, to constrain the rheological properties of the continental crust and of the uppermost mantle. The reservoir has a total volume of 35.5 km^3 and encompasses an area of 635 km^2. The subsidence pattern clearly showed relaxation of the underlying basement due to the water load of the lake.

Wang [2000] calculated the water load-induced surface vertical displacements and level plane changes in the front reservoir area of the Three-Gorges Reservoir, China, during the filling period and discussed the height changes. The results are thought to bound the water load-induced responses. For the expected water level of 175 m, a maximum depression of 48.3 mm was derived.

A first stage of subsidence monitoring for Salto Caxias power dam in Brazil was summarised by Santos et al. [2001]. Here, a monitoring network to determine the subsidence of the surrounding area to be flooded was implemented before closing of the dam. By stage 1 the network design, installation and first field campaign is meant, so no results are derived yet.

Yan et al. [2004] reported that the Jiangya dam, China, and the rock masses on both valley sides were uplifted to various degrees during the filling of the reservoir, with a measured maximum uplift of 32.6 and 19.08 mm, respectively. To understand the uplift mechanism, a 3D numerical analysis was carried out. The authors concluded that the rise of an artesian head of a confined hot aquifer as a result of the reservoir inundation is the principal factor contributing to the uplift.

The Hohenwarte reservoir in the southeast of Thuringia is the 3rd largest reservoir in Germany with a volume of 182 Mill. m^3, covering an area of 7.3 km^2. In 4 km distance to the reservoir, the Geodynamic Observatory Moxa is situated. The data of seismometers and strainmeters are successfully used for studies of the Earth's interior structure and properties. With the used types of instruments it is possible to observe tilt changes in the range of 10^{-9} rad and displacement changes of 10^{-9} strain. We explore the possibility that registrations of the seismometers and strainmeters are influenced by deformation changes induced by lake-level fluctuations of the Hohenwarte reservoir. We therefore use the Finite Element (FE) method to calculate the deformations in vicinity of the Hohenwarte reservoir.

6.2 Saale Kaskaden

In the southeast of Thuringia, the river Saale crosses the Thuringian Slate Mountains between Blankenberg and Saalfeld (Fig. 6.1). The drop in elevation on a length of 80 km is about 170 m. Till the 1920's the Saale was running through small and deep valleys. Due to the small, incised valley, the spring snowmelt often resulted in floods. Three large flood catastrophes, in November 1890, February 1909 and January 1918, were the reason for planning several artificial dams, the Saale Kaskaden (Fig. 6.1). They should catch the water of the Saale and its tributary Wisenta in several reservoirs. The first reservoir was the Wisenta reservoir, dammed by a 60 m long barrage and finished in 1920. Later on, between 1933 to 1934 this barrage was replaced by a concrete dam. The two largest reservoirs, the Bleiloch reservoir and the Hohenwarte reservoir were built between 1926 to 1932 and between 1936 to 1943, respectively. In 37 years a new landscape along the Saale was formed. All reservoirs with their dimensions are summarised in Tab. 6.1.

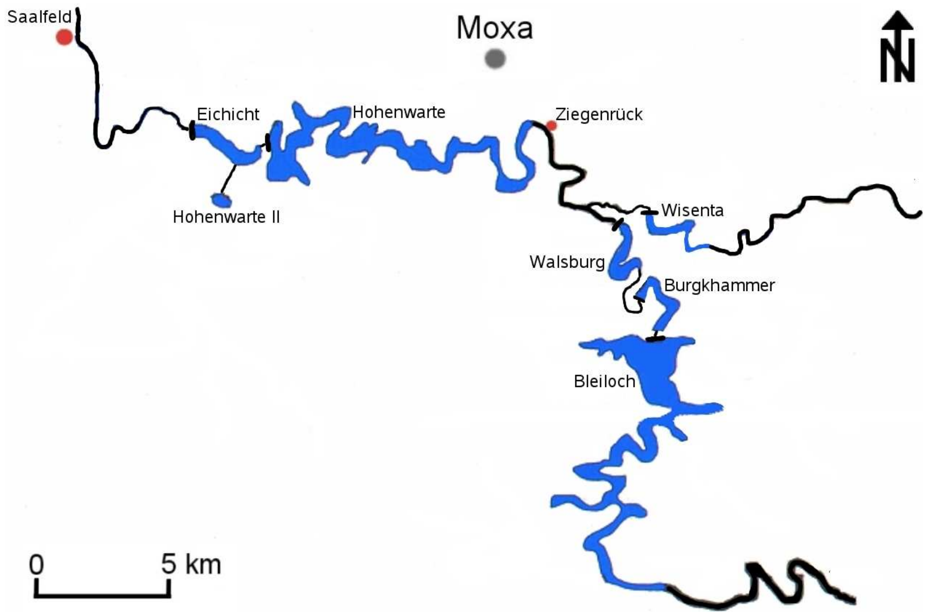

Figure 6.1: Overview of the Saale Kaskaden with the seven reservoirs and the artificial dams (black bars) between Blankenberg and Saalfeld.

The Hohenwarte reservoir is the 3rd largest reservoir in Germany. The lake encompasses an area of 7.3 km^2, and the total volume is 182 Mill. m^3. The dam was built between 1936 and 1943, and put into operation in 1941. The balance reservoir is the 4.3 km long Eichicht reservoir in the west. The task of the Hohenwarte reservoir is generation of electricity, flood protection and increasing the base flow of the rivers Elbe and Saale in the summer months.

6.3 Geodynamic Observatory Moxa

The Geodynamic Observatory Moxa, a station of the German Regional Seismic Network (GRSN), is located about 30 km south of Jena (Thuringia, Germany) at the border of the Thuringian Slate Mountains

Table 6.1: Reservoir dimensions of the Saale Kaskaden.

name	construction	volume in 10^6 m^3	length in km	area in km^2	concrete dam l [m] x h [m]
Wisenta	1933 - 1934	1.04	2.4	0.28	148 x 16
Bleiloch	1926 - 1932	215.00	28.0	9.20	205 x 65
Burgkhammer	1930 - 1932	5.64	6.5	0.84	122 x 22
Walsburg	1938 - 1939	2.54	5.0	0.50	118 x 16
Hohenwarte	1936 - 1943	182.00	27.0	7.30	412 x 75
Eichicht	1942 - 1945	5.21	4.3	0.71	215 x 20
Hohenwarte II	1956 - 1963	3.28	-	0.22	man-made basin

(Fig. 6.1) and is maintained by the Institute of Geosciences of the Friedrich–Schiller University Jena. It is embedded on the east hill flank of the remote Silberleite valley. The seismometers and two quartz tube strainmeters are installed in a gallery between 20 and 50 m deep in a hill. The covering with rock and gravel is about 35 m. The strainmeters have a length of 26 m with one instrument installed in EW– and NS–direction, respectively. The rock in the observatory area is dominated by metapelite. The distance from the observatory to the Hohenwarte reservoir is about 4 km. For further information, a detailed description of the observatory can be found in Teupser [1975] and Jahr et al. [2001].

6.4 Model description

6.4.1 Geometry

We model the water impounded in the Hohenwarte reservoir as surface load on a flat, viscoelastic earth by means of the FE method. We employ the modelling software ABAQUS [Hibbitt et al., 2005].

The earth model is a cube with 100 km side length and consists of 13 layers in vertical direction, simulating the crust and the upper mantle. Looking on the surface, the generated mesh of 100 × 100 × 13 hexahedra elements is divided into a centre and a peripheral frame. The 20 km × 20 km large centre, between 40 and 60 km in each horizontal direction, is meshed with 80 × 80 elements with a horizontal side length of 250 m. The remaining 10 element rows of the 40 km wide peripheral frame have a variable side length from short side lengths near the centre to long side lengths for the outer elements. With 25 m, the elements in the first layer have the smallest thickness in vertical direction. The second layer has a thickness of 225 m, layers 3 to 5 a thickness of 250 m. The other thickness values for layers 6 to 13 are summarised in Tab. 6.2. The material parameters for the crust and the upper mantle are taken from PREM [Dziewonski and Anderson, 1981, Tab. 6.2]. The depth of the Mohorovičić discontinuity at the Hohenwarte reservoir location is, after Dèzes & Ziegler [2001], around 29±1 km. To simplify the geometry of the model, the transition between crust and upper mantle is set to 25 km. A linear, elastic

Table 6.2: Model dimensions and parameterisation.

layer	thickness in m	depth in km	density in kg/m^3	Young's modulus in GPa	Poisson's ratio	
1	25	0.025	2600	67.9	0.282	crust
2	225	0.25	2600	67.9	0.282	
3	250	0.5	2600	67.9	0.282	
4	250	0.75	2600	67.9	0.282	
5	250	1	2600	67.9	0.282	
6	1000	2	2600	67.9	0.282	
7	8000	10	2600	67.9	0.282	
8	15000	25	2913	111.6	0.263	
9	15000	40	3380	173.3	0.280	upper mantle
10	15000	55	3378	172.8	0.280	
11	15000	70	3377	172.3	0.280	
12	15000	85	3375	169.5	0.283	
13	15000	100	3373	165.9	0.287	

rheology is used for the crust and for model 1 also for the upper mantle (Fig. 6.2). Thus, model 1 simulates a purely elastic Earth. A viscoelastic rheology for the upper mantle is used for two calculations: in model 2, the viscosity for the upper mantle is set to 5×10^{20} Pa s, and in model 3 to 10^{19} Pa s between 25 and 40 km and 5×10^{20} Pa s below. Thus, models 2 and 3 allow the relaxation of stress in the upper mantle. The viscosity of 5×10^{20} Pa s for the upper mantle in model 2 is taken as an average of upper-mantle viscosities beneath Europe resolved by different investigations in the last years [see Steffen and Kaufmann, 2005, for a summary]. The viscosity of 10^{19} Pa s for the uppermost mantle in model 3 is to be thought as an extreme example for the viscoelastic modelling and is probably not consistent with the actual viscosity below the Thuringian Slate Mountains. The buoyancy force, which is necessary for a viscoelastic investigation, is included after the approach introduced by Wu [2004].

6.4.2 Boundary conditions

The movement of the nodes in both models is constrained as follows:

(i) the nodes at the model bottom must not move in vertical direction (no slip);

(ii) the nodes at the vertical model boundaries must not move in horizontal direction perpendicular to the model sides (no slip).

These boundary conditions simulate the surrounding unmodelled Earth. It is assumed that the deformation signal of pressure changes at the earth surface decays with depth and over large horizontal distances. To ensure that the boundary conditions as well as the model size have no effect on the modelling results, we have carried out tests with different resolution, and found the used grid as appropriate for the model.

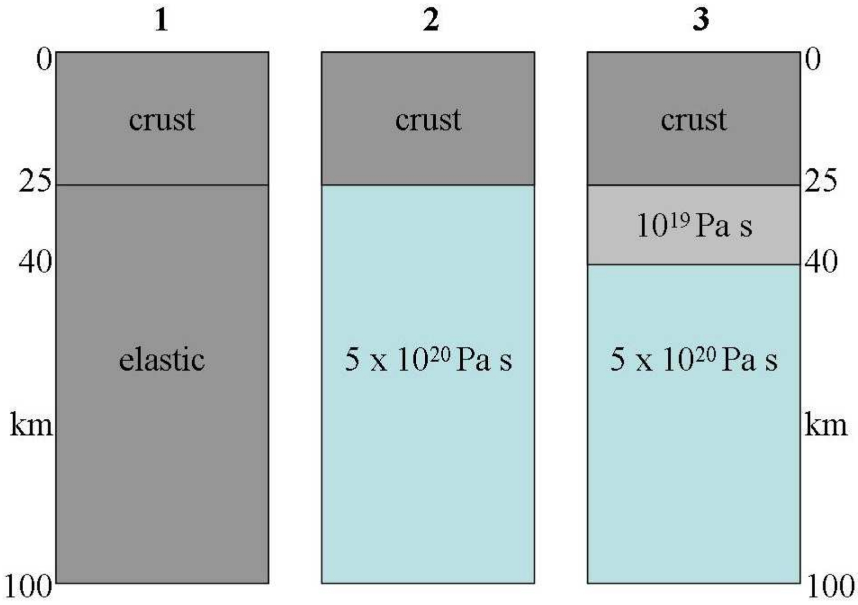

Figure 6.2: Structure of the three earth models.

6.4.3 Water load

The full water load of 182 Mill. m^3 is applied uniformly over the shape of the reservoir (Fig. 6.3), approximated by 135 element surfaces (250 m × 250 m), which correspond to a reservoir area of 8.44 km^2. The load is generated by dividing the water volume of the reservoir by this area multiplied with a water density of 1000 kg/m^3 and a gravity of 9.81 m/s^2. The full load of the Hohenwarte reservoir is 215,820 Pa corresponding to a constant water column of 22 m. The Eichicht reservoir has a full load of 58,860 Pa, a water column of 6 m.

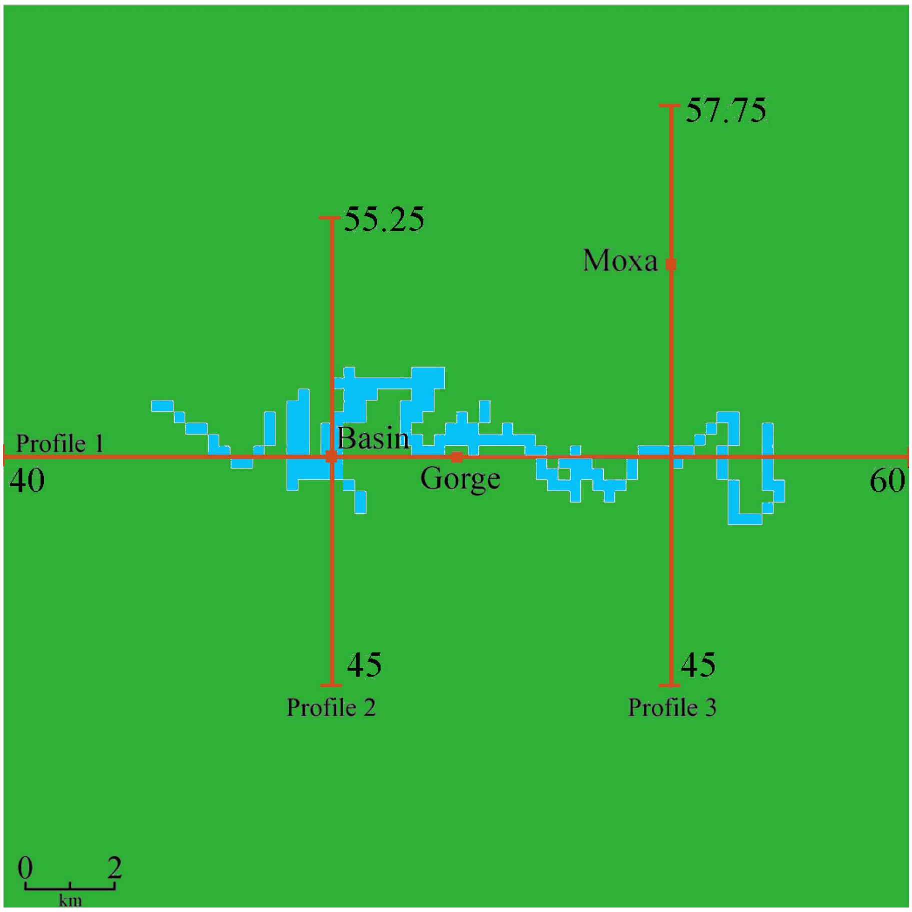

Figure 6.3: Top view of the model centre (20 km × 20 km) with the shape of the reservoir (white) and the profiles for the deformations. The location of the Geodynamic Observatory Moxa and the locations Basin and Gorge are marked. Numbers indicate locations in km relative to the entire grid of 100×100 km used.

The load initially increases linearly over 2 years, after the dam was closed. Then, pressure changes simulating the seasons follow (Fig. 6.4). The filling starts at 0% of water volume in the year 1941 and ends after 2 years with a maximum water volume of 100%. In the next 6 months, the reservoir volume is reduced to 70% (summer) and after another 6 months increased again to 100% (winter). This cycle is repeated once. Thereafter the load is kept constant at 100% till the year 2011. With this approximation, we are able to study seasonal changes and we save computation time.

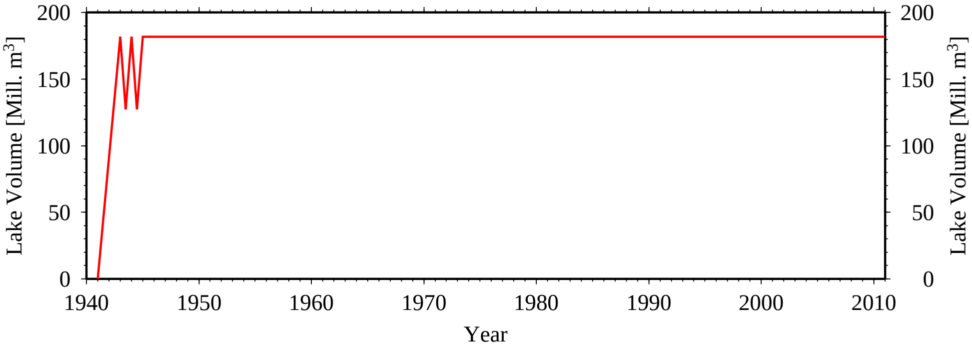

Figure 6.4: Lake volume as function of time.

6.5 Results

The deformation of the model by the time-dependent water load is calculated, and vertical deformations, strains and tilts are shown along three profiles (Fig. 6.3). Profile 1 starts west of the Eichicht reservoir and runs in EW–direction over the whole distance of the central frame. Profile 2 and 3 are directed perpendicular to Profile 1 from north to south. The location of Moxa observatory is at 54.25 km on Profile 3. The strain is obtained by calculating the difference of the horizontal displacements between two nodes and normalising this difference to the element length. The tilt is calculated as the angle resulting from the node displacement in EW– and NS–direction relative to the displacement of the next node vertically below (vertical tilt). This definition was successfully used for FE modellings by Fischer [2002], Kroner et al. [2005], and Steffen et al. [2006c]. In addition three points (Fig. 6.3) are selected to compare the vertical deformation on top of the model between the location in the greatest basin (Basin), in the centre of the model (Gorge) and at Moxa observatory (Moxa).

6.5.1 Short-term seasonal variations

Tilt: Fig. 6.5 shows the tilt in the NS– and EW–component for the elastic model (model 1) at different load times. To compare the results, the tilts at different times of an annual cycle are taken when the reservoir is filled-up (winter) and 70%-filled (summer). The tilt changes on each profile reflect the location of the reservoir and which reservoir border is tangent to the profile. The NS–component in Profile 1 shows for the southern border between 48 and 52 km a tilt northward and for the northern between 52 and 54 km a tilt southward. The tilt in the EW–component in Profile 1 traces the meanders of the old river valley. The tilts of Profile 2 are dominated by the load of the dam basin between 49 and 50.5 km. In Profile 3 the tilt only shows eye-catching changes when the reservoir is crossed at 50 km. The amplitude on all profiles is affected by the load sum in the vicinity of each point and is in winter at most 4.5 μrad eastward in the EW–component behind the dam. Between winter and summer significant differences in the amplitude of the tilts are found, especially at the location of the reservoir. Here, the tilt difference between winter and summer is at most 30% of the full load in winter and therefore a result of the elastic behaviour. Changes in the direction of the tilt are not observed.

The tilt changes of the viscoelastic models are not shown as there are only small differences in the tilts resulting from an elastic and a viscoelastic rheology. For example, the difference at the Basin and Gorge location is in the EW–component at most 0.2 nrad, in the NS–component at most 1 nrad. At Moxa

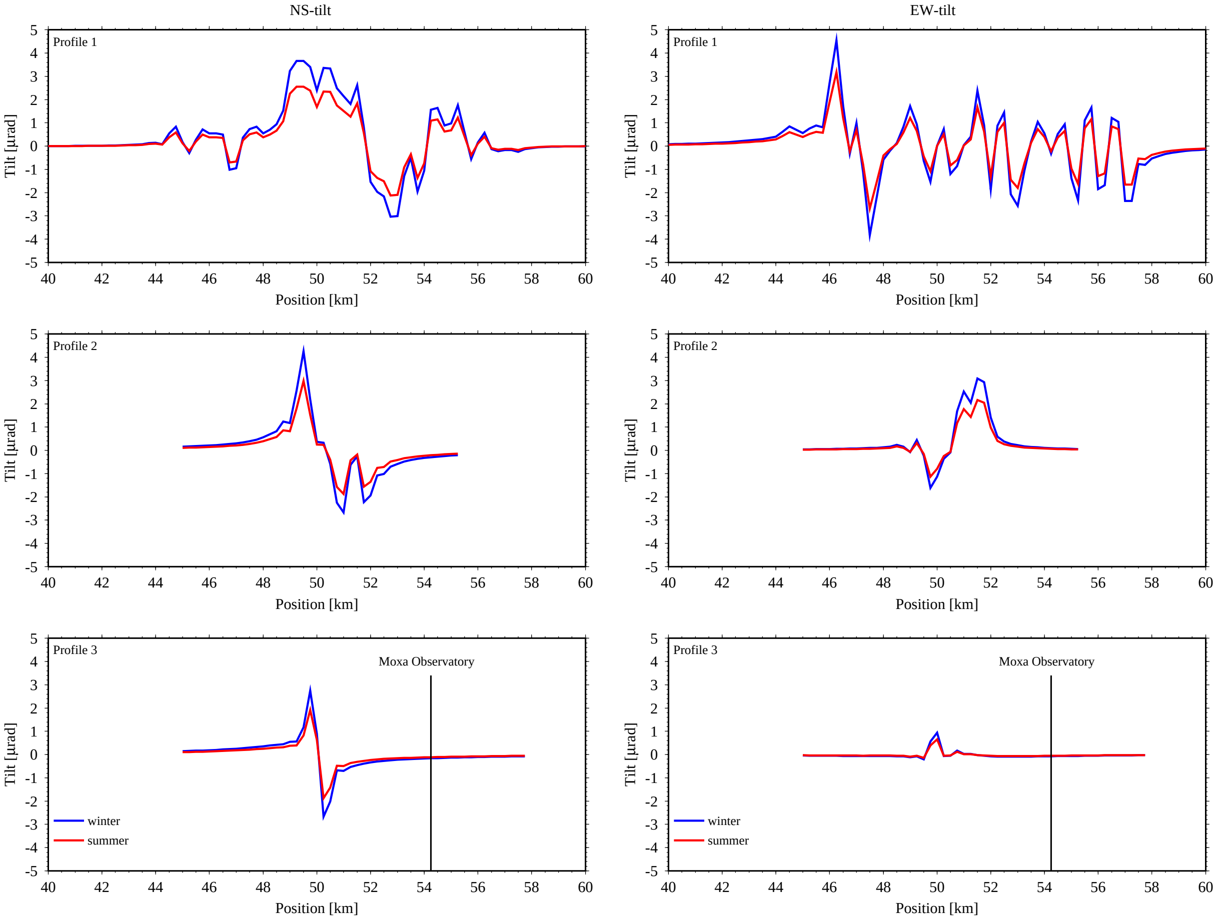

Figure 6.5: Tilt in the NS– component (left) and EW–component (right) obtained for the elastic model at different load times. Tilt northward and eastward positive.

location no difference is observed. The tilt differences are insignificant to the viscoelastic behaviour of the upper mantle for short-time load changes as they are too small for visible effects in tiltmeter registrations at Moxa. A comparison of the tilts in both components at Moxa location between different upper-mantle viscosities in the first mantle layer of 10^{19} Pa s (model 3) and 5 x 10^{20} Pa s (model 2) indicates 0.4 nrad larger effects for model 3.

Strain: Fig. 6.6 shows the strain in the NS– and EW–component for the elastic model at different load times, (1) when the reservoir is filled up (winter) and (2) 70%-filled (summer). The maximum amplitude is found in winter along Profiles 1 and 3 with around 1 μstrain compression. The strain changes reflect the location of the reservoir in compression. Profiles 2 and 3 demonstrate this behaviour clearly when the reservoir is crossed around 50 km. The extension observed in the EW–component of Profile 1 results between two meander valleys of the former river valley and is explained as compensation of the compression induced by the load in each valley. The amplitude is larger the more the valley distance increases and the less load is applied in vicinity of this point. As for the tilts, between winter and summer significant differences in the amplitude of the strains are found. At the location of the reservoir, the difference between winter and summer is at most 30% of the full load in winter and again a result of the elastic behaviour. No changes in the direction of the strain are detected.

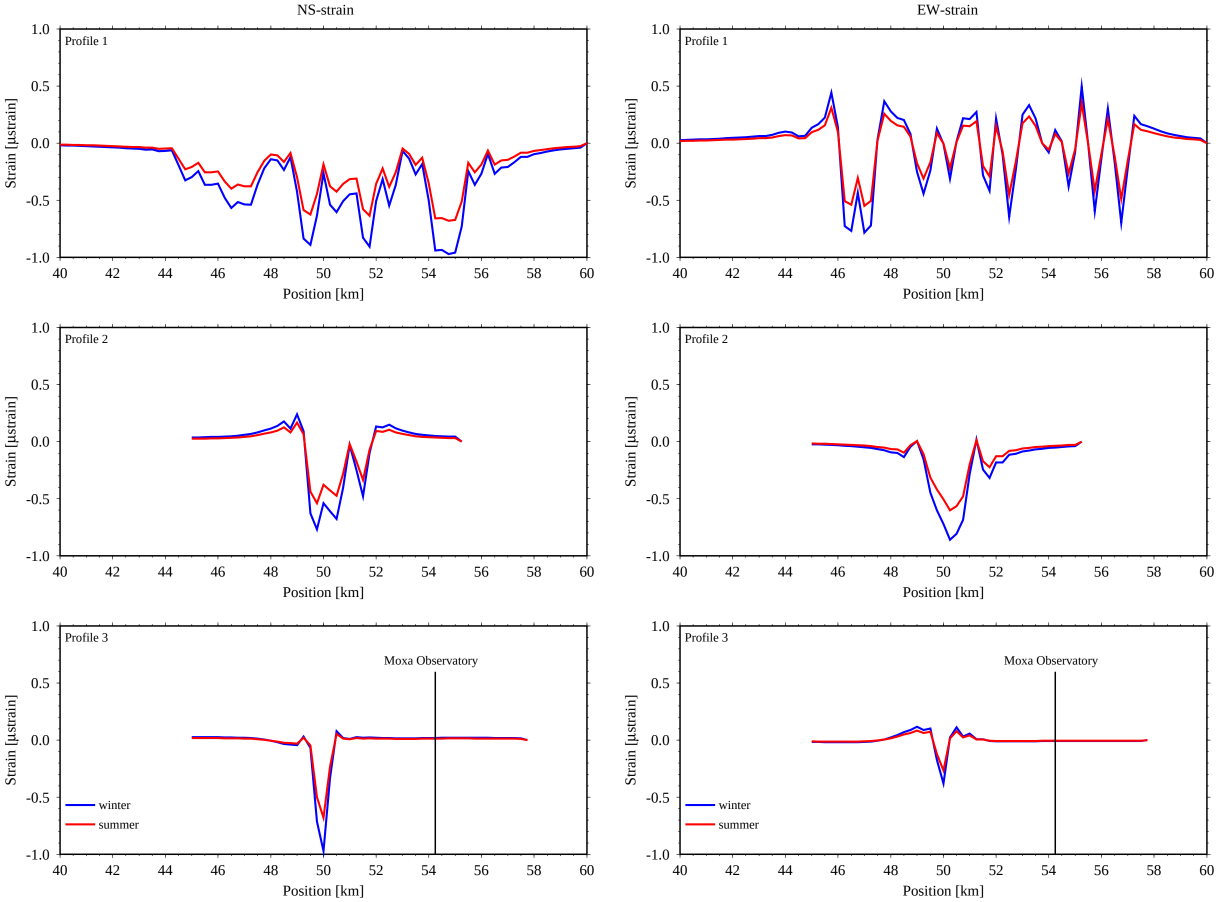

Figure 6.6: Strain in the NS–component (left) and the EW–component (right) obtained for the elastic model at different load times. Extension positive.

Again the strains resulting from a viscoelastic rheology are not shown, as the differences are to small to be seen. Existing, but small differences in the strains between an elastic and a viscoelastic rheology are found for both components at the location of the Basin and Moxa. At both locations this difference is at most 0.15 nstrain for both components when the reservoir is filled-up. For a 70%-filled reservoir in summer this effect is nearly doubled. The strains are as well as the tilts nearly independent of the viscoelastic behaviour of the upper mantle and the past load time. At the location of Moxa observatory, strain differences in the EW–component up to 0.2 nstrain between model 2 and 3 are found. At the Basin location 0.3 nstrain result.

Tilt and strain at Moxa: Fig. 6.7 shows for the location of the Moxa observatory the tilt and the strain in the NS– and EW–component for the elastic model in winter (filled-up) and summer (70%–filled). The maximum tilt in the EW–component is around 75 nrad westward and in the NS–component around 160 nrad southward. The maximum strain results for the EW–component in compression around 10 nstrain and for the NS–component in extension around 20 nstrain. The figure shows clearly the difference of 30% between winter and summer, which is at most 48 nrad in tilt and 6 nstrain in strain and should be observable with the sensitive instruments at Moxa [see Kroner et al., 2005, for a description]. In the tilt and the tilt direction to the source of pressure, which is applied around 50 km, a tendency to smaller effects is found. For the NS–component of the strain, which here results in extension, the curves

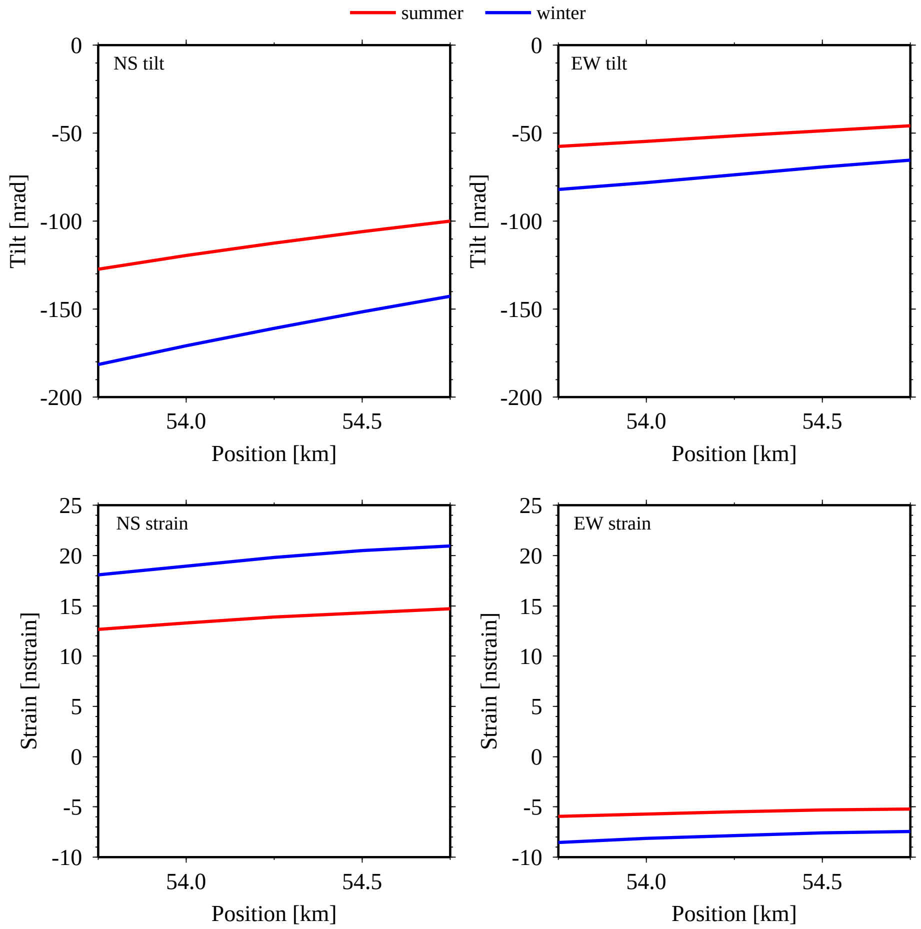

Figure 6.7: Tilts and strains in both components obtained for the elastic model at different load times at the location of Moxa observatory (54.25 km). Tilt eastward, northward positive. Extension positive.

diverge, which is explained as compensation for the compression at the location of the reservoir (see Fig. 6.6). As there are no significant differences in the strains and no differences in the tilts between an elastic and a viscoelastic rheology (see sections above), the curves for the viscoelastic models are not included.

6.5.2 Long-term seasonal variations

Vertical deformation: Fig. 6.8 shows the vertical deformation on the surface for all models at the three locations Basin, Gorge and Moxa for the load cycle. As expected, the greatest deformations are found near the dam (Basin) and the smallest in distance to the reservoir at the location of the observatory (Moxa). The curves reflect the location and the distance to the reservoir. The dominating elastic part (filled-up reservoir) at Moxa is about 0.85 mm, at the Gorge location 3.2 mm, and at the Basin location 5.1 mm. There is a clear difference between the results of the elastic model 1 and the viscoelastic model 3 after a long time period. The loading period of the Hohenwarte reservoir is sufficient for long-term deformation changes related to a viscosity of 10^{19} Pa s between 25 and 40 km depth, when a long time is taken into account. After 70 years, the viscoelastic part is responsible for 0.25 mm of vertical

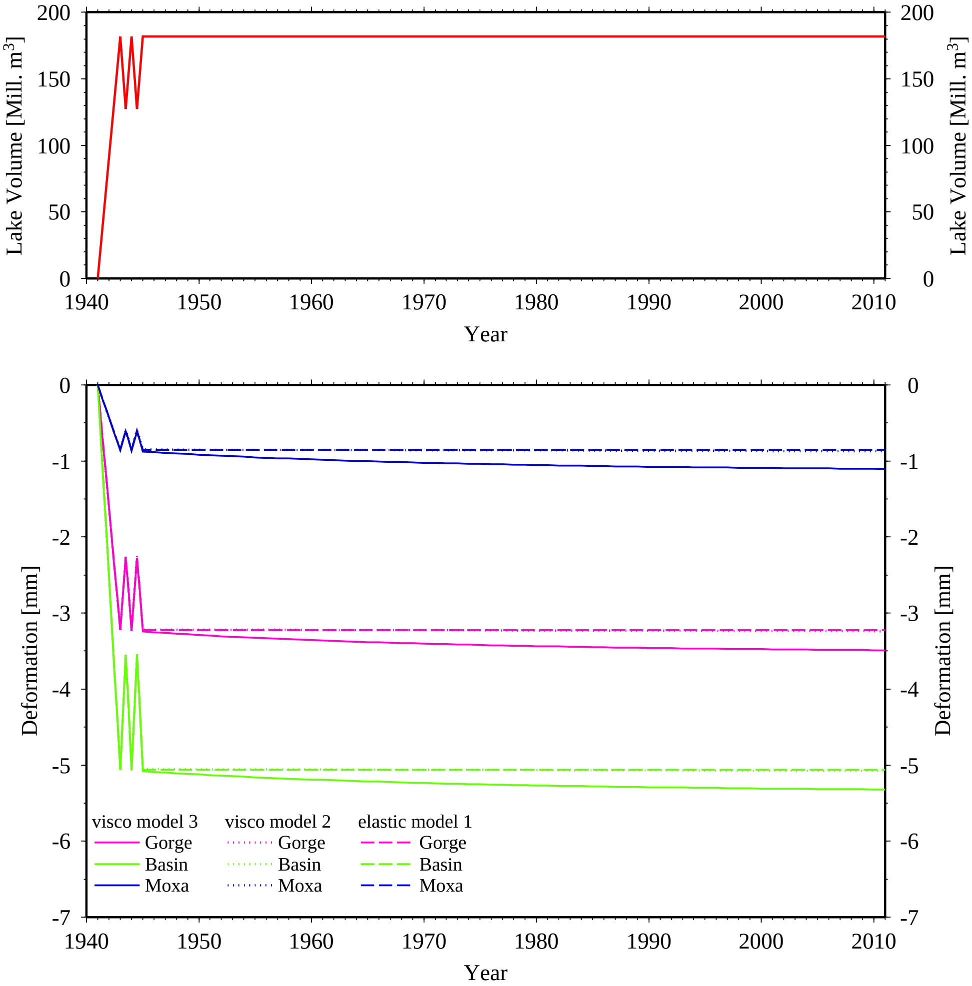

Figure 6.8: Top: Lake volume as a function of time. Bottom: Vertical deformation over 70 years obtained for all models at the three selected points Basin, Gorge and Moxa.

deformation. A comparison of the viscoelastic model 2 and the elastic model 1 shows nearly identical results. At Moxa the difference is about 5 μm after 4 years and about 17 μm after 70 years.

We have also investigated the effect of the Bleiloch reservoir, situated 10 km southeast of the observatory (Fig. 6.1). At the location of Moxa, an additional vertical deformation of 0.17 mm is induced, which, however, is spatially uniform at this location. Thus, the elastic deformation at Moxa will be around 20% larger, when the Bleiloch reservoir is also considered, but there is no significant effect in tilt and strain at the Moxa location. The remaining reservoirs have also no significant effect at the Moxa location, neither in tilt, strain or vertical deformation.

Differences in the vertical deformation induced by short-term load changes are mainly caused by the elastic crust. The viscoelastic part for viscoelastic model 3 is only around 6.2 μm, which corresponds to 2.4% of the deformation difference of 0.25 mm in 6 months. Regarding model 2, the viscoelastic part is in the range of 1 - 2 μm. Therefore, the short-term load change of the Hohenwarte-reservoir is not sensitive enough to observable vertical deformation induced by a upper mantle with a viscosity of 5×10^{20} Pa s or for the fictitious case of a upper mantle with a low-viscosity layer of 10^{19} Pa s.

Tilt and strain: The changes in the tilts and strains induced only by the viscoelastic relaxation are too small to be observed in registrations at Moxa observatory. Here, the viscoelastic part is for the strains around 2% of the elastic part of at most 20 nstrain, which is not observable in a time range of around 70 years. The tilts are not influenced.

6.6 Conclusions

Artificial reservoirs such as the Hohenwarte reservoir in Thuringia, Germany, induce additional loads on the Earth's surface. The resulting effects in tilt and strain deformations can be observed with sensitive instruments. In a distance of 4 km to the reservoir, where the Geodynamic Observatory Moxa is located, the influence of lake-level changes on the registrations is significant. It can be shown that the influence of lake-level fluctuations up to 30% to tilt and strain registrations at the observatory for all three different models is larger than the resolution of the instruments. At the location of Moxa differences of at most 48 nrad for the tilts and 6 nstrain for the strains are established. The vertical deformation is more affected by load changes. For the viscoelastic case the viscoelastic part is small compared to the elastic part and only observable over a long time period. For short-time lake-level fluctuations, the viscoelastic influence is less than 3%. All changes induced by lake-level fluctuations in the tilt, strain and vertical deformation should be observable at the Geodynamic Observatory Moxa independent of the model structure.

Acknowledgements

We are grateful for numerous comments and suggestions by Patrick Wu and an anonymous referee. This research was funded by the DFG (research grant KA1723/1-1).

7. Discussion

This thesis focused on the viscosity structure of Northern and Central Europe. It was investigated with different modelling techniques, on the one hand 1D investigations with the pseudo-spectral method, on the other hand 1D and 3D investigations with the FE method. The load applied was either an ice-load model (RSES from Kurt Lambeck) or a water-load model (Hohenwarte reservoir). The results of the modelling obtained with the ice load were compared to RSL data and GPS data from the BIFROST campaign [Johansson et al., 2002]. The investigation concerning the Hohenwarte reservoir has predicted tilt and strain data, which up to now have not been compared to observed data from seismometers and strainmeters in the nearby Moxa observatory.

7.1 Results of the forward modellings

Chapters 2 and 3 employed a forward modelling strategy, on the one hand with RSL data from Scandinavia, the Barents Sea, and NW Europe, which cover the last deglaciation interval (21,400 years BP to present), as well as radial crustal velocities from the BIFROST project, and on the other hand with recently compiled RSL data from the NW European coast including the regions Belgium, the Netherlands, NW Germany, and the southern North Sea, which cover a time period from 11,500 years BP to present. The first investigation was used to infer the radial viscosity variation of the Earth's mantle underneath Scandinavia and NW Europe, and to possibly detect a low-viscosity zone underneath those regions, which was proposed in the literature. The second investigation focused on the comparison of modelling results to the sea-level curves of the RSL data.

The analysis in chapters 2 was twofold, first using the pseudo-spectral method to calculate the optimum values for lithospheric thickness and bulk upper- and lower-mantle viscosities for different subregions of the RSL data, and then using the Neighbourhood Algorithm, a global inverse procedure developed by Sambridge [1999a,b], to search for a low-viscosity asthenosphere.

The results in the former case show that differences arise for the thickness of the lithosphere, with thicker values underneath Scandinavia ($H_l \sim 120$ km), and thinner values underneath the British Isles and the Barents Sea ($H_l \sim$60-70 km). This agrees with the thickening of the crust and the lithosphere from the North Atlantic Mid-Ocean Ridge towards the Baltic Shield. While the values for bulk upper-mantle viscosities are similar for all three regional subsets with $\eta_{UM} \sim 4 \times 10^{20}$ Pa s, the lower-mantle viscosity is poorly constrained ($\eta_{LM} > 10^{22}$ Pa s), which indicates an insensitivity of these RSL data to the lower mantle.

The results from the NA inversion only indicate a low-viscosity zone underneath the subregion of the Barents Sea. Here, in a depth interval of 120 - 200 km, this zone is characterised by viscosities around 10^{19}-10^{20} Pa s. Then the lower part of the upper mantle (transition zone) becomes more viscous, with viscosities up to 10^{22} Pa s. However, underneath the subregion of Scandinavia no evidence for a low-viscosity zone was found from the inversion of RSL data, while underneath NW Europe no clear indication for such a zone is possible, as too much earth models reproduce these RSL data. Interestingly, the NA inversion of the BIFROST uplift data favours a thin low-viscosity layer between 160 - 200 km depth, which confirms an earlier inference by Milne et al. [2004], but which is actually not resolved by the data. In agreement with the pseudo-spectral method, the NA results also reveal that the thickness of the rheological lithosphere increases from 60 - 70 km underneath NW Europe and the Barents Sea towards values exceeding 120 km underneath Scandinavia.

The results of chapter 3 show that a broad range of Earth parameters can predict the Belgian RSL data, the ranges then becoming narrower towards the southern North Sea region. In fact, the Belgian data appear to simply trace the eustatic sea-level rise, confirming the stable behaviour of the Belgian crust (London-Brabant massif) during and after the last ice age [Kiden et al., 2002]. Hence, the data are not very sensitive to changes in the Earth's interior structure, and they are too far away from former ice sheets (British Isles and Scandinavia) to allow a better determination of the Earth's structure beneath Belgium with this method. In contrast, a narrow range of Earth parameters define the southern North Sea region, reflecting the greater influence of the GIA. The difference between the behaviour of the Belgian and the southern North Sea data is based on the time and depth range of the data. The North Sea data are deeper (up to -50 m) and older (up to 11,500 years BP) samples than the Belgian data (up to -20 m and up to 9500 years BP). The models which show a best fit with the RSL data from the other regions predict an average lithospheric thickness of ca. 90 km along the NW-European coast, although thicknesses decrease to values around 80 km beneath the Netherlands and 70 km below NW Germany. The upper-mantle viscosities for all regions except Belgium are well constrained at ca. $7\times\ 10^{20}$ Pa s, and cover a range between $\eta_{UM} \in [6.5\times10^{20}, 10\times10^{20}]$ Pa s. The lower-mantle viscosities are, however, almost unconstrained, confirming the low resolving power for the lower-mantle viscosity of RSL data with a small spatial distribution. These results confirm earlier findings for RSL data of Lambeck et al. [1998a] and Steffen and Kaufmann [2005, chapter 2]. Furthermore, the modelling results confirm visual comparisons of sea-level curves, e. g. they reveal a non-linear, glacio- and/or hydro-isostatic subsidence component, which is negligible on the Belgian coastal plain but increases significantly to a value of ca. 7.5 m (since 8000 years BP) along the NW German coast. This subsidence is at least in part related to the post-glacial collapse of the so-called peripheral forebulge, which developed around the Fennoscandian ice-load centre during the last glacial maximum. Nevertheless, the analyses show that neither the western Netherlands sea-level curve of van de Plassche [1982], nor the German sea-level curve of Behre [2003] can be viewed as optimally reflecting absolute sea-level rise in NW Europe (at least not during the early and middle Holocene). The results of chapter 3 confirm former investigations of Kiden et al. [2002] from the Belgian-Netherlands coastal plain and provide new evidence from the German and southern North Sea sectors for the post-glacial collapse of the peripheral forebulge.

7.2 Results of the FE modellings

Chapters 4 to 6 used the FE technique either with an ice load (4 and 5) or with a water load (6) for investigations of the Earth's structure in Northern and Central Europe. The results of the ice load were compared with the crustal velocities from the BIFROST project, while for the results of the water load no comparison was made, as it was a test of the sensitivity of the reservoir load to the mantle. In chapter 4, a 3D viscosity structure, derived from seismic shear-wave tomography models, was employed in the Earth's mantle to compare 1D and 3D models and also to investigate how the thermodynamic properties of the mantle affect the viscosity variations. In chapter 5, a sensitivity analysis of the BIFROST GPS data to the upper mantle was performed with a model subdivided into blocks of variable size. As the subdivisions yielded a huge number of sensitivity kernels to interpret, a new approach was introduced to calculate the kernel of a block by averaging the perturbed predictions of all surface nodes of this block to one value for this block.

The results of chapter 4 indicate significant differences between 3D and 1D modelling. The observed BIFROST crustal velocity data are best fit using a 1D earth model, as for the different 3D earth models observations and predictions can differ by 2-7 mm/yr. The horizontal crustal velocities are affected even stronger. The typical divergent motions of the 1D earth models is no longer dominating for 3D viscosity models. Instead, a regional velocity field with movements away from the Norwegian coast towards the old Baltic Shield is observed. The presence of lateral viscosity variations in the upper mantle with a strong horizontal flow component significantly influences the horizontal velocities. Again, horizontal velocities from the 3D earth model prediction cannot explain the BIFROST data well, the prediction from the 1D earth model scores better. The results of a sensitivity analysis show that the dramatic change in the horizontal flow pattern has its origin deeper in the upper mantle, between 450 and 670 km depth. The uplift is mainly influenced by the viscosity structure beneath the lithosphere. In general, only minor dependencies of the lower-mantle viscosity structure to RSL and crustal motion data can be established, confirming the results of Mitrovica [1996] and Steffen and Kaufmann [2005].

In chapter 5, the results show that the present-day uplift velocity is mostly sensitive to viscosity variations in upper-mantle layers between 220 and 540 km depth, independent of the block size. Viscosity changes in the blocks within the former ice sheet produce larger effects than the blocks with mainly parts outside the former ice sheet. The largest effects are found for the blocks located below the former ice maximum on the surface. The effect of a viscosity change in the neighbouring blocks to one block on the uplift rate is negligible. There is a clear influence of the block size on the results. The uplift velocity is more sensitive to the viscosity changes in smaller blocks than in larger blocks. A comparison of the results of smaller and larger blocks also indicates higher sensitivities for the horizontal velocities of the larger blocks, and the sensitivity depends on the location of this block in relation to the former ice sheet. For all block sizes, we establish the directed movement of the kernels out of the perturbed block induced by the higher viscosity in that block. In general, lateral viscosity variations in the transition zone of the mantle have a strong influence on the tangential motion. The sensitivity for the blocks with most parts located outside the former ice sheet is small. Concerning the sensitivity of a selected block to the surrounding blocks, the influence is large in the first and the fourth upper-mantle layer, and is mainly influenced by viscosity changes in the blocks with an ice load on the surface. The strongest influence results from the blocks which are located in the direction of the discussed horizontal component.

In view of the BIFROST stations, former results can be confirmed: For the uplift velocity, the sensitivity generally increases for the central BIFROST locations, and the lowest sensitivity is found for the stations in the far north and south. The maximum is resolved for the second and third upper-mantle layer. In contrast to the former results of the blocks, the horizontal velocities are mostly sensitive to viscosity changes in the second and third upper-mantle layer. This is in agreement with the investigations of Milne et al. [2004]. Furthermore, the difference between the third and the fourth upper-mantle layer is larger. Another fact is that the horizontal velocities are more affected by (i) the location of a station on a block in relation to the location of the block in the model, (ii) the distance of the station to the block border and (iii) the ice-sheet geometry, which confirms the results of Wu [2006].

Finally, in chapter 6 the FE method is used with a water load instead of an ice load. Two main questions were addressed: (i) is the water load of the Hohenwarte reservoir sensitive enough to mantle viscosity, and (ii) can the induced deformation effects be measured at the nearby Geodynamic Observatory Moxa? The deformation effects were explored both on a short-term seasonal time scale and a long-term decadal time scale. The questions can be answered simply: ”no” for the first question, ”yes” for the second. The vertical deformation is more affected by load changes than the tilt and the strain. For the viscoelastic case, the viscoelastic part is small compared to the elastic part and only observable over a long time period, if an irrealistic viscoelastic structure of the underlying upper mantle is used. For short-time lake-level fluctuations, the viscoelastic influence is less than 3%. Concerning tilt and strain, the seasonal effect is mainly induced by elastic deformation. They result at the location of the reservoir in the μrad and μstrain ranges, respectively. As for the vertical deformation, long-term decadal variations are only significant, if an irrealistic viscoelastic upper-mantle structure is included in the analysed model. In a distance of 4 km to the reservoir, where the observatory is located, the influence of seasonal lake-level fluctuations on tilt and strain is larger than the resolution of the used instruments. Here, differences of at most 48 nrad for the tilts and 6 nstrain for the strains are established, which should be observable at the Geodynamic Observatory Moxa independent of the model structure.

7.3 General conclusions

As already discussed above, the results of chapter 6 cannot be used for conclusions concerning the lithospheric thickness and / or the upper mantle. Thus, the conclusions focus on results from chapters 2 to 5. The results demonstrate the complexity of the GIA process and the search for a heterogeneous earth model reproducing observed physical quantities such as crustal motions and RSL data.

7.3.1 Lithospheric thickness

The lithospheric thickness increases from 60 - 70 km underneath NW Europe towards ca. 90 km underneath the North Sea area and finally to values exceeding 120 km underneath Scandinavia. From the Barents Sea the lithosphere increases from 60 - 70 km to 120 km underneath Scandinavia. A splitting of Scandinavian RSL data into a peripheral and a central part results in lithospheric thicknesses increasing from 100 km in the peripheral region to 160 km in the centre. It additionally improves the correlation of the thickening of the crust and lithosphere from the North Atlantic Mid-Ocean Ridge towards the Baltic Shield both from North to South and West to East. The used 3D viscosity structures in the FE modelling based on the shear-wave velocity perturbations from the S20A tomographical model [Ekström and Dziewonski, 1998] support these results.

The Belgian crust (London-Brabant massif) was fairly stable during and after the last ice age and is not influenced by GIA. The southern North Sea region including the Netherlands and NW Germany was more influenced by GIA in form of the collapsing peripheral forebulge than Belgium. Scandinavia, the Barents Sea and the British Isles clearly show an influence by the uplift of the crust.

7.3.2 Upper-mantle viscosity

The upper-mantle viscosity is determined to values around $(3 - 6) \times 10^{20}$ Pa s underneath Scandinavia, the Barents Sea and the British Isles by comparison with the RSL data. In the southern North Sea area, values around $(6.5 - 10) \times 10^{20}$ Pa s are found. The GPS data from BIFROST also support the value of 7×10^{20} Pa s, but for the Fennoscandian uplift region. This is a discrepancy between the results of the Scandinavian RSL data and the GPS data. In the FE modelling, the upper-mantle viscosity of $\eta_{um} = 4 \times 10^{20}$ Pa s is the background viscosity for the 1D and 3D viscosity structure of V1, which results fit best with the observations. Independent of the lithospheric thickness, the 3D upper-mantle structure of V1 underneath the investigated areas indicates higher viscosities of around 10^{21} Pa s in the first two upper-mantle layers. The transition zone is characterised by lower viscosities in the range of $(1 - 10) \times 10^{20}$ Pa s. Due to the less good fit of the observations, the 3D viscosity structures of V2 and V3 are not discussed.

A low-viscosity zone is found underneath the Barents Sea, with viscosities between 10^{19} - 10^{20} Pa s in a depth interval of 120 - 200 km. No such low-viscosity zone is found underneath Scandinavia, and no clear indication for such a zone underneath NW Europe. The viscosity structure in the FE modelling does not include the Barents Sea region. Here, only in the northwestern North Sea / Atlantic Ocean a low-viscosity zone is indicated, which is reasonable as the lithospheric thickness in this region is decreasing towards the North Atlantic Mid-Ocean Ridge to values less than the used one of 70 km.

7.3.3 Lower-mantle viscosity

All RSL data are insensitive to the lower-mantle viscosity underneath Northern and Central Europe, even in view of the Scandinavian RSL data, which provide a large time and depth range. From the results of chapter 2 only the BIFROST GPS data seem to provide enough information, as the 1σ-range is quite small compared to the RSL results. The FE modellings clearly show in a sensitivity analysis that the GPS data are nearly insensitive to the lower mantle, independent of its structure. This difference in the results of the methods can be explained with results from a sensitivity analysis recently published by Wu [2006]. He showed with an ice sheet with size of the Laurentide Ice Sheet that in the far field between 45° and 70° from the former ice-sheet centre, the present-day uplift velocity is most sensitive to viscosity variations in the upper lower-mantle (670 km to 1330 km depth). As the BIFROST GPS stations are located in this distance to the Laurentide Ice Sheet and this ice sheet is included in the inverse modelling of chapter 2, the best earth model fitting the GPS data indicates the value ($\eta_{lm} = 10^{22}$ Pa s) of the lower-mantle viscosity underneath North America! In the FE modelling the Laurentide Ice Sheet is not included and thus the GPS data are also insensitive to the lower mantle.

7.3.4 On the used ice model

The best fit with the present-day velocities from BIFROST is observed with the predictions of the 1D FE model. This is due to the ice model, which was constructed with the help of a 1D earth model to fit the sea level [see Lambeck et al., 1998a]. This earth model with a lithospheric thickness H_l of 75 ± 10 km, an upper-mantle viscosity η_{um} of 3.6×10^{20} Pa s and a lower-mantle viscosity η_{lm} of 0.8×10^{22} Pa s is comparable to the used one in chapter 4 ($H_l = 70$ km, $\eta_{um} = 4 \times 10^{20}$ Pa s, $\eta_{lm} = 2 \times 10^{22}$ Pa s). Nevertheless, the ice model has to be changed, especially in the central part, as the observed uplift maximum is located more in the East in the Gulf of Bothnia.

7.3.5 On the database

In this thesis, more than 1500 RSL data and the crustal velocities of 44 BIFROST stations have been used to determine the mantle viscosity beneath Northern and Central Europe. Nevertheless, more data, RSL data as well as GPS observations, are required in order to determine more exactly earth models with a smaller variation in the parameter range of lithospheric thickness and mantle viscosities for each region.

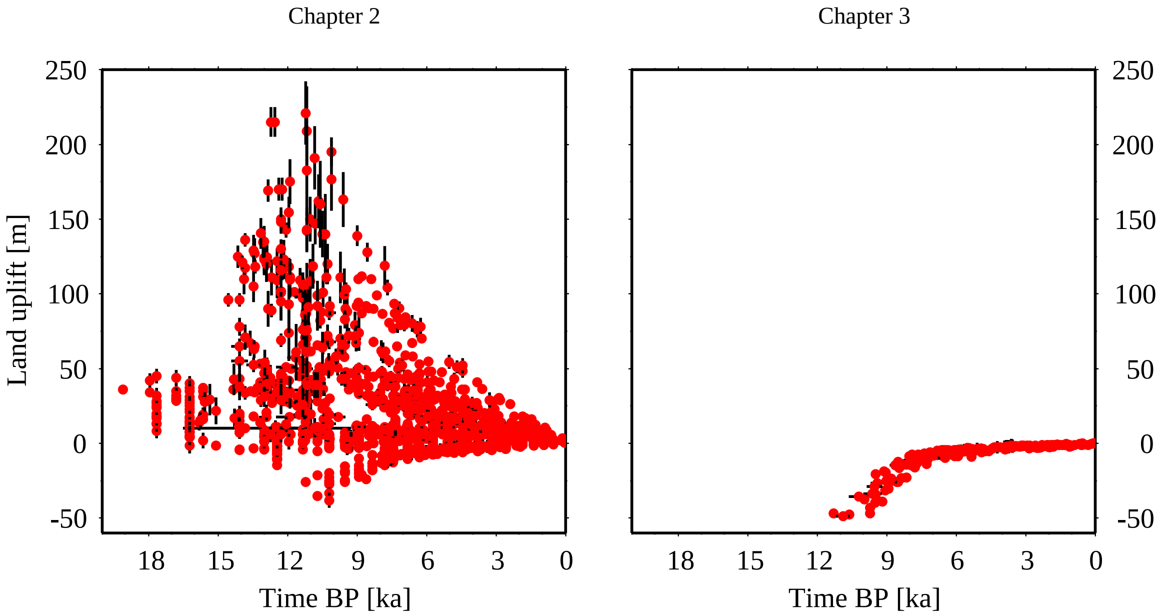

Figure 7.1: Comparison over time and depth range of the RSL data (red dots with black error bars) used in chapters 2 (1320 samples) and 3 (240 samples).

In chapter 2, 1320 North and Central European samples were used, covering 19,000 years and 300 m of uplift, eustatic and tectonic component. In chapter 3, a database with 240 samples is used for the investigation to the North Sea, covering 11,500 years and 50 m of subsidence and eustatic component (Fig. 7.1). This database includes much less rebound information than the Scandinavian database, resulting in the large white area from 0 to 250 m over the whole time on the right side in Fig. 7.1. Unfortunately, in the North Sea area no uplift data can be expected. The region is too far away from the former ice sheet, and thus the white area cannot be filled with sample dots. Nevertheless, more data can be obtained from 9000 years ago and before, and also deeper values of more than 50 m depth. With more older and deeper RSL data from the North Sea as well as data from the Danish sector one can better constrain the geographical extent and the temporal progression of the forebulge collapse, respectively. The question of the stable behaviour of the Belgian crust needs further investigation with new data, and also the difference in the upper-mantle viscosity between the North Sea region and the regions of Scandinavia, Barents Sea and the British Isles. In addition, the comparison between modelled and observational sea-level data can provide important information on local-scale processes such as sediment compaction, and/or tectonic subsidence, e. g. in the North Sea.

The best location of GPS stations in Fennoscandia is within the shape of the former ice sheet. Here, new stations could be installed to determine a more detailed picture of the lithospheric thickness and the upper-mantle viscosity, as the results show that the present-day uplift velocity is most sensitive to the depth interval from 246 - 550 km of the upper mantle. Also new stations far outside the former ice-sheet shape can contribute to future investigations in highlighting the lateral viscosity contrasts in the upper mantle beneath Fennoscandia. The sensitivity analysis in chapter 5 indicates with results depending on the block size, that the size of an area with constant viscosity in the upper mantle directly influences the signal at the GPS station.

7.3.6 Possible model improvements

The differences between the predicted and observed present-day velocities of the 3D FE models forces a revision of the 3D models in a future analysis, because it is quite unsatisfactory that a less sophisticated 1D model shows better results than a more sophisticated 3D model. This revision might include chemical variation due to fact that in the used models the lateral variations in seismic velocities seen in seismic tomography are caused by lateral temperature variation only. Using another tomography model, e. g. one of those introduced by Ritsema et al. [1999]; Zhao [2001] or Zhou et al. [2006], is another option, in addition in combination with a global crustal model [e. g. from Bassin et al., 2000].

References

Amelung, F., and Wolf, D. (1994). Viscoelastic perturbations of the Earth: significance of the incremental gravitational force in models of glacial isostasy. *Geophys. J. Int.* **117 (3)**, 864-879.

Austin, R. M. (1991). Modelling Holocene tides on the NW European continental shelf. *Terra Nova* **3**, 276-288.

Bassin, C., Laske, G., and Masters, G. (2000). The current limits of resolution for surface wave tomography in North America. *EOS* **F897**, 81.

Beets, D. J., and van der Spek, A. J. F. (2000). The Holocene evolution of the barrier and the back-barrier basins of Belgium and the Netherlands as a function of late Weichselian morphology, relative sea-level rise and sediment supply. *Netherlands Journal of Geosciences* **79**(1), 3-16.

Behre, K.-E. (2003). Eine neue Meeresspiegelkurve für die südliche Nordsee: Transgressionen und Regressionen in den letzten 10.000 Jahren. *Probleme der Küstenforschung im südlichen Nordseegebiet* **28**, 9-63.

Behre, K.-E., Menke, B., and Streif, H. (1979). The Quaternary geological development of the German part of the North Sea. In: E. Oele, R. T. E. Schüttenhelm, A. J. Wiggers, editors, *The Quaternary history of the North Sea.*, 85-113, Acta Universitatis Upsaliensis, Symposia Universitatis Upsaliensis Annum Quingentesimum Celebrantis 2, Uppsala.

Bell, M. L., and Nur, A. (1978). Strength changes due to reservoir-induced pore pressure and stresses and application to Lake Oroville. *J. Geophys. Res.* **83**, 4469-4483.

Bennema, J. (1954). Holocene movements of land and sea-level in the coastal area of the Netherlands. *Geologie en Mijnbouw*, Nieuwe Serie **16**, 254-264.

Berger, A. L. (1978). Long-term variations of daily insolation and Quaternary climatic changes. *J. Atmos. Sci.* **35**, 2362-2367.

Calcagnile, G. (1982). The lithosphere-asthenosphere system in Fennoscandia. *Tectonophys.* **90**, 19-35.

Caston, V.N.D. (1979). A new isopachyte map of the Quaternary of the North Sea. In: E. Oele, R. T. E. Schüttenhelm, A. J. Wiggers, editors, *The Quaternary history of the North Sea.*, 23-28, Acta Universitatis Upsaliensis, Symposia Universitatis Upsaliensis Annum Quingentesimum Celebrantis 2, Uppsala.

Cathles, L. M. (1975). *The Viscosity of the Earth's Mantle.* Princeton Univ. Press, Princeton.

Chappell, J., and Shackleton, N. J. (1986). Oxygen isotopes and sealevel. *Nature* **324**, 137-140.

Denton, G. H., and Hughes, T. J. (1981). *The Last Great Ice Sheets.* John Wiley and Sons, New York.

Denys, L., and Baeteman, C. (1995). Holocene evolution of relative sea level and local mean high water spring tides in Belgium - a first assessment. *Marine Geology* **124**, 1-19.

Dèzes, P., and Ziegler, P. A. (2001). European Map of the Mohorovicic discontinuity. 2nd EUCOR-URGENT Workshop (Upper Rhine Graben Evolution and Neotectonics), Mt. St. Odile, France.

Dziewonski, A. M., and Anderson, D. L. (1981). Preliminary reference Earth model. *Phys. Earth Planet. Inter.* **25**, 297-356.

Ekman, M. (1991). A concise history of postglacial land uplift research (from its beginning to 1950). *Terra Nova* **3**, 358-365.

Ekström, G., and Dziewonski, A. M. (1998). The unique anisotropy of the Pacific upper mantle. *Nature* **394**, 168-172.

Ervynck, A., Baeteman, C., Demiddele, H., Hollevoet, Y., Pieters, M., Schelvis, J., Tys, D., van Strydonck, M., and Verhaeghe, F. (1999). Human occupation because of a regression, or the cause of a transgression? A critical review of the interaction between geological events and human occupation in the Belgian coastal plain during the first millennium AD. *Probleme der Küstenforschung im südlichen Nordseegebiet* **26**, 97-121.

Fairbanks, R. G. (1989). A 17,000-year glacio-eustatic sea level record; influence of glacial melting rates on the Younger Dryas event and deep-ocean circulation. *Nature* **342**, 637-642.

Fairbridge, R. W. (1961). Eustatic changes in sea level. *Physics and Chemistry of the Earth* **4**, 100-185.

Farrell, W. E., and Clark, J. A. (1976). On postglacial sea level. *Geophys. J. R. astr. Soc.* **46**, 647-667.

Fischer, K. D. (2002). Sources and transfer mechanism of seismic noise: Preliminary results from FEM models. *Bull. d'Inf. Marees Terr.* **137**, 10881-10886.

Fjeldskaar, W. (1994). Viscosity and thickness of the asthenosphere detected from the Fennoscandian uplift. *Earth Planet. Sci. Lett.* **126**, 399-410.

Fjeldskaar, W. (1997). Flexural rigidity of Fennoscandian inferred from the postglacial uplift. *Tectonics* **16(4)**, 596-608.

Fleming, K., Johnston, P., Zwartz, D., Yokoyama, Y., Lambeck, K., and Chappell, J. (1998). Refining the eustatic sea-level curve since the Last Glacial Maximum using far- and intermediate-field sites. *Earth Planet. Sci. Let.* **163**, 327-342.

Fleming, K., Martinec, Z., and Wolf, D. (2003). A reinterpretation of the Fennoscandian relaxation-time spectrum for a viscoelastic lithosphere. In: I. N. E. Tziavos, editor, *Gravity and Geoid 2002, 3rd Meeting of the International Gravity and Geoid Commission,* 432-438, Ziti Pub., Thessaloniki.

Forte, A. M., and Mitrovica, J. X. (1996). New inferences of mantle viscosity from joint inversion of long-wavelength mantle convection and post-glacial rebound data. *Geophys. Res. Lett.* **23 (10)**, 1147-1150.

Gasperini, P., and Sabadini, R. (1989). Lateral heterogeneities in mantle viscosity and post-glacial rebound. *Geophys. J.* **98**, 413-428.

Gasperini, P., and Sabadini, R. (1990). Finite element modeling of lateral viscosity heterogeneities and post-glacial rebound. *Tectonophys.* **179**, 141-149.

Gasperini, P., Sabadini, R., and Yuen, D. A. (1991). Deep continental roots: the effects of lateral variations of viscosity on post-glacial rebound. In: R. Sabadini, K. Lambeck, E. Boschi, editors, *Glacial Isostasy, Sea-Level and Mantle Rheology,* 21-32. Kluwer Acad. Pub., Dordrecht.

Goes, S., and Govers, R. (2000). Shallow mantle temperatures under Europe from *p* and *s* wave tomography. *J. Geophys. Res.* **105 (B5)**, 11153-11169.

Gripp, K. (1964). Erdgeschichte in Schleswig-Holstein. Neumünster.

Hays, J., Imbrie, J., and Shackleton, N. (1976). Variations in the Earth's Orbit: Pacemaker of the Ice Ages. *Science* **194**, 1121-1132.

Haskell, N. A. (1935). The motion of a viscous fluid under a surface load. *Physics* **7**, 56-61.

Hibbitt, D., Karlsson, B., and Sorensen, P. (2005). Getting Started with ABAQUS - Version (6.5-2). Hibbitt, Karlsson & Sorensen, Inc.

Ivins, E. R., and Sammis, C. G. (1995). On lateral viscosity contrast in the mantle and the rheology of low frequency geodynamics. *Geophys. J. Int.* **123**, 305-322.

Jahr, Th., Jentzsch, G., and Kroner, C. (2001). The Geodynamic Observatory Moxa/Germany: Instrumentation and Purposes. *J. Geod. Soc. Japan* **47(1)**, 34-39.

Jelgersma, S. (1961). Holocene Sea Level changes in the Netherlands. Van Aelst, Maastricht, 101 pp.

Jelgersma, S., Oele, E., and Wiggers, A. J. (1979). Depositional history and coastal developement in The Netherlands and the adjacent North Sea since the Eemian. In: E. Oele, R. T. E. Schüttenhelm, A. J. Wiggers, editors, *The Quaternary history of the North Sea.*, 115-142, Acta Universitatis Upsaliensis, Symposia Universitatis Upsaliensis Annum Quingentesimum Celebrantis 2, Uppsala.

Johansson, J. M., Davis, J. L., Scherneck, H.-G., Milne, G. A., Vermeer, M., Mitrovica, J. X., Bennett, R. A., Jonsson, B., Elgered, G., Elósegui, P., Koivula, H., Poutanen, M., Rönnäng, B. O., and Shapiro, I. I. (2002). Continuous GPS measurements of postglacial adjustment in Fennoscandia 1. Geodetic results. *J. Geophys. Res.* **107**, doi: 10.1029/2001JB000400.

Johnston, P., and Lambeck, K. (1999). Postglacial rebound and sea level contributions to changes in the geoid and the Earth's rotation axis. *Geophys. J. Int.* **136 (3)**, 537-558.

Karato, S. (1993). Importance of anelasticity in the interpretation of seismic tomography. *Geophys. Res. Lett.* **20 (15)**, 1623-1626.

Karato, S., and Wu, P. (1993). Rheology of the upper mantle: a synthesis. *Science* **260**, 771-778.

Kaufmann, G. (2004). Program package ICEAGE, Version 2004. Manuscript, Institut für Geophysik der Universität Göttingen, 40 pp.

Kaufmann, G., and Wolf, D. (1996). Deglacial land emergence and lateral upper-mantle heterogeneity in the Svalbard Archipelago – II. Extended results for high-resolution load models. *Geophys. J. Int.* **127 (1)**, 125-140.

Kaufmann, G., and Wu, P. (1998a). Upper mantle lateral viscosity variations and postglacial rebound: application to the Barents Sea. In: P. Wu, editor, *Dynamics of the Ice Age Earth: A Modern Perspective*, 583-602, Trans Tech Pub., Zürich, Switzerland.

Kaufmann, G., and Wu, P. (1998b). Lateral asthenospheric viscosity variations and postglacial rebound: a case study for the Barents Sea. *Geophys. Res. Lett.* **25 (11)**, 1963-1966.

Kaufmann, G., and Amelung, F. (2000). Reservoir-induced deformation and continental rheology in vicinity of Lake Mead, Nevada. *J. Geophys. Res.* **105(B7)**, 16341-16358.

Kaufmann, G., and Lambeck, K. (2000). Mantle dynamics, postglacial rebound and the radial viscosity profile. *Phys. Earth Planet. Int.* **121 (3-4)**, 303-327.

Kaufmann, G., and Lambeck, K. (2002). Glacial isostatic adjustment and the radial viscosity profile from inverse modeling. *J. Geophys. Res.* **107 (B11)**, ETG5-1-ETG5-15.

Kaufmann, G., and Wu, P. (2002). Glacial isostatic adjustment in Fennoscandia with a three-dimensional viscosity structure as an inverse problem. *Earth Planet. Sci. Lett.* **197 (1-2)**, 1-10.

Kaufmann, G., Wu, P., and Wolf, D. (1997). Some effects of lateral heterogeneities in the upper mantle on postglacial land uplift close to continental margins. *Geophys. J. Int.* **128**, 175-187.

Kaufmann, G., Wu, P., and Li, G. (2000). Glacial isostatic adjustment in Fennoscandia for a laterally heterogeneous Earth. *Geophys. J. Int.* **143 (1)**, 262-273.

Kaufmann, G., Wu, P., and Ivins, E. R. (2005). Lateral viscosity variations beneath Antarctica and their implications on regional rebound motions and seismotectonics. *J. Geodyn.* **39 (2)**, 165-181.

Kiden, P. (1995). Holocene relative sea-level change and crustal movement in the southwestern Netherlands. *Marine Geology* **124**, 21-41.

Kiden, P., Denys, L., and Johnston, P. (2002). Late Quaternary sea-level change and isostatic and tectonic land movements along the Belgian-Dutch North Sea coast: geological data and model results. *J. Quat. Sci.* **17**, 535-546.

Klemann, V., and Wolf, D. (2005). The eustatic reduction of shoreline diagrams: implications for the inference of relaxation-rate spectra and the viscosity stratification below Fennoscandia. *Geophys. J. Int.* **162 (1)**, 249-256.

Kooi, H., Johnston, P., Lambeck, K., Smither, C., and Molendijk, R. (1998). Geological causes of recent (100 yr) vertical land movement in the Netherlands. *Tectonophysics* **299**, 297-316.

Kroner, C., Jahr, T., Kuhlmann, S., and Fischer, K. D. (2005). Pressure-induced noise on horizontal seismometer and strainmeter records evaluated by finite element modeling. *Geophys. J. Int.* **161**, 167 - 179, doi:10.1111/j.1365-246X.2005.02576.x.

Kudraß, H.-R., and cruise participants (2004). Cruise Report: North Sea BGR04-AUR / Leg 2. Internal report, 93 pp.

Lambeck, K. (1993a). Glacial rebound of the British Isles – I. Preliminary model results. *Geophys. J. Int.* **115**, 941-959.

Lambeck, K. (1993b). Glacial rebound of the British Isles – II. A high-resolution, high-precision model. *Geophys. J. Int.* **115**, 960-990.

Lambeck, K. (1995). Late Devensian and Holocene shorelines of the British Isles and North Sea from models of glacio-hydroisostatic rebound. *Jour. Geol. Soc. London* **152**, 437-448.

Lambeck, K., Johnston, P., Smither, C., and Nakada, M. (1996). Glacial rebound of the British Isles: III. Constraints on mantle viscosity. *Geophys. J. Int.* **125**, 340-354.

Lambeck, K., Smither, C., and Johnston, P. (1998a). Sea-level change, glacial rebound and mantle viscosity for northern Europe. *Geophys. J. Int.* **134**, 102-144.

Lambeck, K., Smither, C., and Ekman, M. (1998b). Tests of glacial rebound models for Fennoscandia based on instrumented sea- and lake-level records. *Geophys. J. Int.* **135**, 375-387.

Lambert, A., Liard, J. O., and Mainville, A. (1986). Vertical movement and gravity change near the La Grande-2 reservoirs, Quebec. *J. Geophys. Res.* vol. **91(B9)**, 9150-9160.

Lange, W., and Menke, B. (1967). Beiträge zur frühpostglazialen erd- und vegetationsgeschichtlichen Entwicklung im Eidergebiet, insbesondere zur Flußgeschichte und zur Genese des sogenannten Basistorfes. *Meyniana* **17**, 29-44.

Latychev, K., Mitrovica, J. X., Tamisiea, M. E., Tromp, J., and Moucha, R. (2005a). Influence of lithospheric thickness variations on 3-D velocities due to glacial isostatic adjustment. *Geophys. Res. Lett.* **32**, doi: 10.1029/2004GL21454.

Latychev, K., Mitrovica, J. X., Tromp, J., Tamisiea, M. E., Komatisch, D., and Christara, C. C. (2005b). Glacial isostatic adjustment on 3-D Earth models: a finite-volume formulation. *Geophys. J. Int.* **161**, 421-444, doi: 10.1111/j.1365-246X.2005.02536.x.

Leitch, A. M., and Yuen, D. A. (1989). Internal heating and thermal constraints on the mantle. *Geophys. Res. Lett.* **16**, 1407-1410.

Li, A. R., and Han, X. G. (1987). Composite factors for reservoir-induced earthquakes in the Three Gorges area. In: *Impacts of the Three Gorges Project on Ecosystem and Environments and Possible Countermeasures* (in Chinese), 553-563, Science Press, Beijing.

Li, X. D., and Romanowicz, B. (1996). Global mantle shear velocity model developed using nonlinear asymptotic coupling theory. *J. Geophys. Res.* **101 (B10)**, 22245-22272.

Louwe Kooijmans, L. P. (1974). The Rhine/Meuse delta; four studies on its prehistoric occupation and Holocene geology. PhD thesis, University of Leiden, 421 pp.

Ludwig, G., Müller, H., and Streif, H. (1979). Neuere Daten zum holozänen Meeresspiegelanstieg im Bereich der Deutschen Bucht. *Geologisches Jahrbuch* **D32** Hannover, 3-22.

Makaske, B., van Smeerdijk, D. G., Peeters, H., Mulder, J. R., and Spek, T. (2003). Relative water-level rise in the Flevo lagoon (The Netherlands), 5300-2300 cal. yr BC: an evaluation of new and existing basal peat time-depth data. *Netherlands J. Geosci.* **82**, 115-131.

Martinec, Z. (2005). Spectral-finite element approach to three-dimensional viscoelastic relaxation in a spherical earth. *Geophys. J. Int.* **142**, 117-142.

Martinec, Z., and Wolf, D. (2005). Inverting the Fennoscandian relaxation-time spectrum in terms of an axisymmetric viscosity distribution with a lithospheric root. *J. Geodyn.* **39**, 143-163.

McConnell, R. K. (1968). Viscosity of the mantle from relaxation time spectra of isostatic adjustment. *J. Geophys. Res.* **73 (22)**, 7089-7105.

Menke, B. (1996). Palynologische Untersuchung des Vibrokerns "Gauss 1987/5" aus der südlichen Nordsee. In: H. Streif, editor, *Deutsche Beiträge zur Quartärforschung in der südlichen Nordsee. Geologisches Jahrbuch* **A146**, 177-182, Hannover.

Milne, G. A., and Mitrovica, J. X. (1998). Postglacial sea-level change on a rotating Earth. *Geophys. J. Int.* **133**, 1-19.

Milne, G. A., Davies, J. L., Mitrovica, J. X., Scherneck, H.-G., Johansson, J. M., Vermeer, M., and Koivula, H. (2001). Space-geodetic constraints on glacial isostatic adjustment in Fennoscandia. *Science* **291**, 2381-2385.

Milne, G. A., Mitrovica, J. X., Scherneck, H.-G., Davis, J. L., Johansson, J. M., Koivula, H., and Vermeer, M. (2004). Continuous GPS measurements of postglacial adjustment in Fennoscandia: 2. Modeling results. *J. Geophys. Res.* **109 (B2)**, doi: 10.1029/2003JB002619.

Mitrovica, J. X. (1996). Haskell [1935] revisited. *J. Geophys. Res.* **101 (B1)**, 555-569.

Mitrovica, J. X., and Forte, A. M. (1997). Radial profile of mantle viscosity: results from a joint inversion of convection and postglacial rebound observables. *J. Geophys. Res.* **102 (B2)**, 2751-2769.

Mitrovica, J. X., and Milne, G. A. (1998). Glaciation-induced perturbations in the Earth's rotation: a new appraisal. *J. Geophys. Res.* **103**, 985-1005.

Mitrovica, J. X., and Peltier, W. R. (1991). A complete formalism for the inversion of post glacial rebound data: Resolving power analysis. *Geophys. J. Int.* **104**, 267-288.

Mitrovica, J. X., and Peltier, W. R. (1993). The inference of mantle viscosity from an inversion of the fennoscandian relaxation spectrum. *Geophys. J. Int.* **114**, 45-62.

Mitrovica, J. X., and Peltier, W. R. (1995). Constraints on mnatle viscosity based upon the inversion of post-glacial uplift data from the Hudson Bay region. *Geophys. J. Int.* **122**, 353-376.

Mitrovica, J. X., Davis, J. L., and Shapiro, I. I. (1994). A spectral formalism for computing three-dimensional deformations due to surface loads 1. Theory. *J. Geophys. Res.* **99 (B4)**, 7057-7073.

Mörner, N.-A. (1984). Planetary, solar, atmospheric, hydrospheric and endogene processes as origin of climatic changes on the Earth. In: N.-A. Mörner, W. Karlén, editors, *Climatic Changes on a yearly to millennial Basis*, 637-651, Reidel Publ. Co.

Mostaert, F., and De Moor, G. (1989). Eemian and Holocene sedimentary sequences on the Belgian coast and their meaning for sea level reconstruction. In: J.P. Henriet, G. De Moor, editors, *The Quaternary and Tertiary Geology of the Southern Bight, North Sea*, 137-148, Ministry of Economic Affairs, Belgian Geological Survey, Brussels.

Munk, W. H., and MacDonald, G. J. F. (1960). *The Rotation of the Earth: A Geophysical Discussion.* Cambridge Univ. Press, London.

Nakada, M., and Lambeck, K. (1988). The melting history of the late Pleistocene Antarctic ice sheet. *Nature* **333**, 36-40.

Panza, G. F., Mueller, S., and Calcagnile, G. (1980). The gross features of the lithosphere-asthenosphere system in Europe from seismic surface waves and body waves. *Pure appl. Geophys.* **118**, 1209-1213.

Peltier, W. R. (1974). The impulse response of a Maxwell Earth. *Rev. Geophys. Space Sci.* **12 (4)**, 649-669.

Peltier, W. R. (1976). Glacial isostatic adjustment – II. The inverse problem. *Geophys. J. R. astr. Soc.* **46**, 669-706.

Peltier, W. R. (1998). The inverse problem for mantle viscosity. *Inverse Problems* **14 (3)**, 441-478.

Peltier, W. R., and Andrews, J. T. (1976). Glacial-isostatic adjustment – I. The forward problem. *Geophys. J. R. astr. Soc.* **46**, 605-646.

Peltier, W. R., and Jiang, X. (1996a). Glacial isostatic adjustment and earth rotation: refined constraints on the viscosity of the deepest mantle. *J. Geophys. Res.* **101**, 3269-3290.

Peltier, W. R., and Jiang, X. (1996b). Mantle viscosity from the simultaneous inversion of multiple data sets pertaining to postglacial rebound. *Geophys. Res. Lett.* **23**, 503-506.

Ritsema, J., van Heijst, H., and Woodhouse, J. (1999). Complex shear wave velocity structure imaged beneath Africa and Iceland. *Science* **286**, 1925-1928.

Roeleveld, W. (1974). The Holocene evolution of the Groningen Marine-Clay District. *Berichten van de Rijksdienst voor het Oudheidkundig Bodemonderzoek* **24** (supplement), S'Gravenhage.

Roeleveld, W., and Gotjé, W. (1993). Holocene waterspiegelontwikkeling in de Noordoostpolder in relatie tot zeespiegelbeweging en kustontwikkeling. In: *De Holocene laagveenontwikkeling in de randzone van de Nederlandse kustvlakte (Noordoostpolder)*, 76-86, PhD thesis, Vrije Universiteit Amsterdam.

Roep, T. B., and Beets, D. J. (1988). Sea-level rise and paleotidal levels from sedimentary structures in the coastal barrier in the western Netherlands since 5600 B.P. *Geologie en Mijnbouw* **67**, 53-60.

Romanowicz, B. (1998). Attenuation tomography of the Earth's mantle: A review of current status. *Pure appl. Geophys.* **153**, 257-272.

Rothe, J. R. (1968). Fill a lake, start an earthquake. *New scientist* **39**, 75-78.

Sabadini, R., and Gasperini, P. (1989). Glacial isostasy and the interplay between upper and lower mantle lateral viscosity heterogeneities. *Geophys. Res. Lett.* **16 (5)**, 429-432.

Sabadini, R., Yuen, D. A., and Portney, M. (1986). The effects of upper mantle lateral heterogeneities on postglacial rebound. *Geophys. Res. Lett.* **13 (4)**, 337-340.

Sambridge, M. (1998). Exploring multidimensional landscapes without a map. *Inverse Problems* **14 (3)**, 427-440.

Sambridge, M. (1999a). Geophysical inversion with a neighbourhood algorithm I: Searching the parameter space. *Geophys. J. Int.* **138**, 479-494.

Sambridge, M. (1999b). Geophysical inversion with a neighbourhood algorithm II: Appraising the emsemble. *Geophys. J. Int.* **138**, 727-746.

Sambridge, M. (2001). Finding acceptable models in nonlinear inverse problems using a neighbourhood algorithm. *Inverse Problems* **17**, 387-403.

Santos, M. C., Gamael, C., Blake, B., Faggion, P., Krueger, C. P., Ferreira, L. D. D., Soares, M., and Szostak-Chrzanowski, A. (2001). Stage 1 of subsidence monitoring of the area surrounding Salto Caxias power dam, in Brazil. *Proc. 10th FIG Int. Symp. on Deformation Measurements*, Orange, California, USA, 19.-22.03.01, 89-97.

Schellmann, G., and Radtke, U. (2004). The Marine Quaternary of Barbados. *Kölner Geographische Arbeiten* **81**, 137 pp.

Schmeling, H., Marquart, G., and Ruedas, T. (2003). Pressure- and temperature-dependent thermal expansivity and the effect on mantle convection and surface observables. *Geophys. J. Int.* **154 (1)**, 224-229.

Shennan, I., Lambeck, K., Horton, B., Innes, J., Lloyd, J., McArthur, J., and Rutherford, M. (2000a). Holocene isostasy and relative sea-level changes on the east coast of England. In: I. Shennan, J. Andrews, editors, *Holocene Land-Ocean Interaction and Environmental Change around the North Sea.*, 275-298, Geological Society, London, Special Publications 166.

Shennan, I., Lambeck, K., Flather, R., Horton, B., McArthur, J., Innes, J., Lloyd, J., Rutherford, M., and Wingfield, R. (2000b). Modelling western North Sea palaeogeographies and tidal ranges during the Holocene. In: I. Shennan, J. Andrews, editors, *Holocene Land-Ocean Interaction and Environmental Change around the North Sea.*, 299-319, Geological Society, London, Special Publications 166.

Simpson, D. W. (1976). Seismicity changes asociated with reservoir loading. *Engineering Geology* **10**, 123-150.

Spada, G., Antonioli, A., Cianetti, S., and Giunchi, C. (2006). Glacial isostatic adjustment and relative sea-level changes: the role of lithospheric and upper-mantle heterogeneities in a 3-D spherical Earth. *Geophys. J. Int.* **165**, 692-792.

Steffen, H., and Kaufmann, G. (2005). Glacial isostatic adjustment of Scandinavia and northwestern Europe and the radial viscosity structure of the Earth's mantle. *Geophys. J. Int.* **163/2**, 801-812.

Steffen, H., and Kaufmann, G. (2006a). Numerical modelling of deformation changes induced by lake-level fluctuations of the Hohenwarte reservoir, Thuringia, Germany. *J. Geodyn.* **41(4)**, 411-421.

Steffen, H., and Kaufmann, G. (2006b). Influence of the Hohenwarte reservoir on tilt and strain observations at Moxa. *Bull. d'Inf. Marees Terr.* **142**, 11399-11406.

Steffen, H., Kaufmann, G., and Wu, P. (2006a). Three-dimensional finite-element modelling of the glacial isostatic adjustment in Fennoscandia. *Earth Planet. Sci. Lett.* **250**, 358-375, doi: 10.1016/j.epsl.2006.08.003.

Steffen, H., Wu, P., and Kaufmann, G. (2006b). Sensitivity of crustal velocities in Fennoscandia to radial and lateral viscosity variations in the mantle. *Earth Planet. Sci. Lett.*, submitted.

Steffen, H., Kuhlmann, S., Jahr, T., and Kroner, C. (2006c). Numerical Modelling of the Barometric Pressure-Induced Noise in Horizontal Components for the Observatories Moxa and Schiltach. *J. Geodyn.* **41(1-3)**, 242-252.

Streif, H. (1972). The results of stratigraphical and facial investigations in the coastal Holocene of Woltzeten/Ostfriesland, Germany. *Geologiska Föringen i Stockholm Förhandlingar* **94**, 281-299.

Streif, H., Uffenorde, H., and Vinken, R. (1983). Untersuchungen zum pleistozänen und holozänen Transgressionsgeschehen im Bereich der südlichen Nordsee. Unpublished Internal Report, Niedersächsisches Landesamt für Bodenforschung, Hannover, 102 pp.

Stuiver, M., and Reimer, P. (1993). Extended ^{14}C database and revised CALIB radiocarbon calibration program. *Radiocarbon* **35**, 15-230.

Stuiver, M., Reimer, P., and Braziunas, T. F. (1998). High-precision radiocarbon age calibration for terrestrial and marine samples. *Radiocarbon* **40**, 1127-1151.

Su, W., and Dziewonski, A. M. (1991). Predominance of long-wavelength heterogeneity in the mantle. *Nature* **352**, 121-126.

Tarantola, A., and Valette, B. (1982). Generalized nonlinear inverse problems solved using the least squares criterion. *Rev. Geophys. Space Phys.* **20(2)**, 219-232.

Teupser, Ch. (1975). The seismological station of Moxa. *Veröff. Zentralinst. Physik d. Erde* **31**, 577-584.

Töppe, A. (1992). Zur Analyse des Meeresspiegelanstiegs aus langjährigen Wasserstandaufzeichnungen an der deutschen Nordseeküste. *Mitt. Leichtweiß-Institut f. Wasserbau der TU Braunschweig* **120**, 1-132.

Töppe, A. (1995). Beschleunigter Meeresspiegelanstieg an der deutschen Nordseeküste? *Jahrbuch Hafenbautechnische Gesellschaft* **49**, 200-209.

Tushingham, A. M., and Peltier, W. R. (1991). Ice-3G: a new global model of late Pleistocene deglaciation based upon geophysical predictions of post-glacial relative sea level change. *J. Geophys. Res.* **96**, 4497-4523.

Tushingham, A. M., and Peltier, W. R. (1992). Validation of the Ice-3G model of Würm-Wisconsin deglaciation using a global data base of relative sea level histories. *J. Geophys. Res.* **97**, 3285-3304.

van Bemmelen, R. W., and Berlage, H. P. (1935). Versuch einer mathematischen Behandlung geotektonischer Bewegungen unter besonderer Berücksichtigung der Undationstheorie. *Gerlands Beitr. Geophys.* **42**, 19-55.

van de Plassche, O. (1982). Sea-level change and water-level movements in the Netherlands during the Holocene. *Mededelingen rijks geologische dienst* **36-1**, 93 pp.

van de Plassche, O., Bohncke, S. J. P., Makaske, B., and van der Plicht, J. (2005). Water-level changes in the Flevo area, central Netherlands (5300-1500 BC): impications for relative mean sea-level rise in the Western Netherlands. *Quat. Int.* **133-134**, 77-93.

Vink, A., Steffen, H., Reinhardt, L., and Kaufmann, G. (2006). Holocene relative sea-level change, isostatic subsidence and the radial viscosity structure of the mantle of north-western Europe (Belgium, the Netherlands, Germany, southern North Sea). *Quat. Sci. Rev.,* submitted.

Wang, H. S. (2000). Surface vertical displacements and level plane changes in the front reservoir area caused by filling the Three Gorges Reservoir. *J. Geophys. Res.* vol. **105(B6)**, 13211-13220.

Wang, H. S., and Wu, P. (2006a). Effects of lateral variations in lithospheric thickness and mantle viscosity on glacially induced surface motion on a spherical self-gravitating Maxwell earth. *Earth Planet. Sci. Lett.* **244** (3-4), 576-589.

Wang, H. S., and Wu, P. (2006b). Effects of lateral variations in lithospheric thickness and mantle viscosity on glacially induced relative sea levels and long wavelength gravity field in a spherical, self-gravitating Maxwell Earth. *Earth Planet. Sci. Lett.* **249**, 368-383.

Wang, H. S., and Wu, P. (2006c). Role of background viscosity in the investigation of postglacial induced crustal motion in a laterally heterogeneous mantle. *J. Geodyn.* **42**, 85-94.

Wessel, P., and Smith, W. H. F. (1991). Free software helps map and display data. *EOS* **72**, 441-446.

Wessel, P., and Smith, W. H. F. (1998). New, improved version of generic mapping tools released. *EOS* **79**, 579.

Wieczerkowski, K., Mitrovica, J. X., and Wolf, D. (1999). A revised relaxation-time spectrum for Fennoscandia. *Geophys. J. Int.* **139**, 69-86.

Williams, M., Dunkerley, D., DeDekker, P., Kershaw, P. & Chappell, J. (1998). Quaternary Environments. Arnold, 329 pp.

Withers, R. J. (1977). Seismicity and stress determination at man-made lakes. Ph.D. thesis, Univ. of Alberta, Edmonton.

Wolf, D. (1984). The relaxation of spherical and flat Maxwell Earth models and effects due to the presence of the lithosphere. *J. Geophys.* **56**, 24-33.

Wolf, D. (1987). An upper bound on lithosphere thickness from glacio-isostatic adjustment in Fennoscandia. *J. Geophys.* **61**, 141-149.

Wu, P. (1992a). Deformation of an incompressible viscoelastic flat Earth with power-law creep: a finite element approach. *Geophys. J. Int.* **108**, 35-51.

Wu, P. (1992b). Viscoelastic versus viscous deformation and the advection of pre-stress. *Geophys. J. Int.* **108**, 136-142.

Wu, P. (2002). Mode coupling in a viscoelastic self-gravitating spherical earth induced by axisymmetric loads and lateral viscosity variations. *Earth Planet. Sci. Lett.* **202**, 49-60.

Wu, P. (2004). Using commercial Finite element packages for the study of earth deformations, sea levels and the state of stress. *Geophys. J. Int.* **158/2**, 401-408.

Wu, P. (2005). Effects of lateral variations in lithospheric thickness and mantle viscosity on glacially induced surface motion in Laurentia. *Earth Planet. Sci. Lett.* **235**, 549-563.

Wu, P. (2006). Sensitivity of relative sea levels and crustal velocities in Laurentide to radial and lateral viscosity variations in the mantle. *Geophys. J. Int.* **165**, 401-413.

Wu, P., and Johnston, P. (1998). Validity of using flat-earth finite element models in the study of postglacial rebound. In: P. Wu, editor, *Dynamics of the Ice Age Earth: A Modern Perspective*, 191-202, Trans Tech Pub., Zürich, Switzerland.

Wu, P., and van der Wal, W. (2003). Postglacial sealevels on a spherical, self-gravitating viscoelastic earth: Effects of lateral viscosity variations in the upper mantle on the inference of viscosity contrasts in the lower mantle. *Earth Planet. Sci. Lett.* **211**, 57-68.

Wu, P., Ni, Z., and Kaufmann, G. (1998). Postglacial rebound with lateral heterogeneities: from 2D to 3D modeling. In: P. Wu, editor, *Dynamics of the Ice Age Earth: A Modern Perspective*, 557-582, Trans Tech Pub., Zürich, Switzerland.

Wu, P., Wang, H. S., and Schotman, H. (2005). Postglacial induced surface motions, sea levels and geoid rates on a spherical, self-gravitating laterally heterogeneous earth. *J. Geodyn.* **39 (2)**, 127-142.

Yamazaki, D., and Karato, S.-i. (2001). Some mineral physics constraints on the rheology and geothermal structure of the Earth's lower mantle. *Am. Miner.* **86**, 385-391.

Yan, F., Xinbin, T., and Li, G. (2004). The uplift mechanism of the rock masses around the Jiangya dam after reservoir inundation, China. *Engineering Geology* **76**, 141-154.

Yokoyama, Y., Lambeck, K., De Dekker, P., Johnston, P. & Keith Fifield, L. (2000) Timing of the Last Glacial Maximum from observed sea-level minima. *Nature* **406**, 713-716.

Zagwijn, W. H. (1983). Sea-level changes in The Netherlands during the Eemian. *Geologie en Mijnbouw* **62**, 437-450.

Zhao, D. (2001). Seismic structure and origin of hotspots and mantle plumes. *Earth Planet. Sci. Lett.* **192**, 251-265.

Zhong, S., Paulson, A., and Wahr, J. (2003). Three-dimensional finite-element modelling of Earth's viscoelastic response: effects of lateral variations in lithospheric thickness. *Geophys. J. Int.* **155**, 679-695.

Zhou, Y., Nolet, G., Dahlen, F. A., and Laske, G. (2006). Global upper-mantle structure from finite-frequency surface-wave tomography. *J. Geophys. Res. – Solid Earth* **111**(B4), B04304.

Zonneveld, I. S. (1960). De Brabantse Biesbosch. PhD thesis, University of Wageningen, 210 pp.

A. Appendix

Table A.1: **–on the next 4 pages–** Locations, ages, depths, nature and sources of reliable sea-level index points from the Belgian coastal plain, the south-western Netherlands (Zeeland), the western and northern Netherlands, the central Netherlands, north-western Germany and the southern North Sea. [1] index numbers refer to those as listed in the original publications (see references). [2] BP = before 1950 (historical / archaeological dates have been adapted accordingly). [3] all depths have been converted to German NN using Dutch NAP = NN; Belgian TAW = NAP - 2.33 m.)

index no. [1]	country / region	site location	coordinates		lab no.	14C age	1σ calibrated age	sample depth	sample depth	altitude error	dated material	stratigraphic	compaction	reference
			Lat. N	Long. E		(yrs BP)	(cal. yrs BP) [2]	max. (m NN) [3]	min. (m NN)	(m)	(thickness of peat layer in m)	position in peat	expected	
1	Belgium	Schoudervliet	51.0916°	2.7042°	IRPA 681	8440 ± 130	9277 - 9546	-19	-18.97	± 0.1	reed peat (0.33)	top	yes	Denys and Baeteman, 1995
3	Belgium	Oostkerke	51.0444°	2.7250°	IRPA 734	8170 ± 90	9012 - 9263	-17.96	-17.92	± 0.1	amorphous peat	base		Denys and Baeteman, 1995
4	Belgium	Woestijne	51.0611°	2.7306°	IRPA 616	8120 ± 100	8981 - 9267	-17.58	-17.5	± 0.1	peaty, clayey sand (0.27)	top	yes	Denys and Baeteman, 1995
6	Belgium	Veurne	51.0667°	2.6556°	Utc 2625	7490 ± 130	8173 - 8404	-11.97	-11.95	± 0.1	clayey peat (0.05)	top		Denys and Baeteman, 1995
9	Belgium	Avekapelle	51.0778°	2.7570°	Hv 8797	7170 ± 275	7715 - 8198	-9.38	-9.28	± 0.1	sandy amorphous peat (0.38)	top	yes	Denys and Baeteman, 1995
11	Belgium	Orthodoxe Kerk	51.0556°	2.7922°	IRPA 534	7110 ± 90	7829 - 8009	-7.5	-7.46	± 0.07	amorphous peat (0.09)	top		Denys and Baeteman, 1995
12	Belgium	Dijk	51.0197°	2.8028°	IRPA 542	6870 ± 70	7615 - 7756	-7.43	-7.4	± 0.1	peaty clay	base		Denys and Baeteman, 1995
13	Belgium	Westende 4	51.1647°	2.7797°	IRPA 615	6780 ± 80	7569 - 7681	-7.52	-7.47	± 0.1	sandy peat	base		Denys and Baeteman, 1995
15	Belgium	Dijk	51.0197°	2.8028°	IRPA 541	6680 ± 80	7474 - 7611	-7.26	-7.23	± 0.1	peaty clay (0.2)	top	yes	Denys and Baeteman, 1995
16	Belgium	Spoorweg 1	51.0736°	2.8000°	IRPA 927	6665 ± 60	7479 - 7585	-6.05	-6	± 0.1	clayey peat (0.13)	top		Denys and Baeteman, 1995
19	Belgium	B407, Steenkerke	51.0700°	2.6928°	ANTW 136	5830 ± 115	6492 - 6751	-4.58	-4.08	± 0.1	peat (0.1)	middle		Denys and Baeteman, 1995
20	Belgium	Noordhoek	51.1847°	2.8889°	IRPA 729	5770 ± 100	6466 - 6666	-4.7	-4.63	± 0.1	peat	base		Denys and Baeteman, 1995
23	Belgium	Spermalie 2	51.1306°	2.8542°	IRPA 519	5650 ± 70	6313 - 6496	-3.42	-3.37	± 0.1	clayey reed peat (0.22)	top	yes	Denys and Baeteman, 1995
25	Belgium	B71, Lampernisse	51.0311°	2.7639°	ANTW 251	5310 ± 190	5903 - 6296	-3.58	-3.48	± 0.1	peat	base		Denys and Baeteman, 1995
27	Belgium	B71, Lampernisse	51.0311°	2.7639°	ANTW 250	5100 ± 140	5660 - 5947	-3.28	-3.18	± 0.1	peat (0.3)	top	yes	Denys and Baeteman, 1995
30	Belgium	B990, Lo-Reninge	50.9750°	2.7847°	Utc 2636	4720 ± 100	5324 - 5583	-2.19	-2.16	± 0.3	peat	base		Denys and Baeteman, 1995
33	Belgium	Leffinge 2	51.1444°	2.8703°	IRPA 337	3340 ± 185	3378 - 3828	-0.16	-0.1	± 0.1	fen peat (0.4)	top	yes	Denys and Baeteman, 1995
34	Belgium	Leffinge 2	51.1444°	2.8703°	IRPA 338	3225 ± 160	3259 - 3640	-0.16	-0.1	± 0.1	wood (0.4)	top	yes	Denys and Baeteman, 1995
36	Belgium	Leffinge 2	51.1444°	2.8703°	IRPA 283	3140 ± 165	3159 - 3554	-0.16	-0.1	± 0.1	fen peat (0.4)	top	yes	Denys and Baeteman, 1995
37	Belgium	Leffinge 2	51.1444°	2.8703°	Hv 8800	2960 ± 50	3060 - 3210	-0.16	-0.1	± 0.1	fen peat (0.4)	top	yes	Denys and Baeteman, 1995
A	Belgium	Drie Grachten	50.9611°	2.8250°	IRPA 520	7030 ± 80	7757 - 7972	-9.18	-9.08	± 0.1	clayey peat	base	yes	Denys and Baeteman, 1995
1	Zeeland	Bouwlust	51.6572°	3.9711°	GrN 2283	7850 ± 100	8537 - 8777	-13.65	-13.58	± 0.12	peat	base		Jelgersma, 1961; in Kiden, 1995
2	Zeeland	Stavenisse	51.5842°	4.0211°	GrN 16282	7730 ± 40	8430 - 8540	-11.48	-11.46	± 0.1	*Phragmites* peat	base		Vos, 1992; in Kiden, 1995
3	Zeeland	Anna Jacobapolder	51.6369°	4.1194°	GrN 16938	7510 ± 150	8164 - 8427	-13.73	-13.7	± 0.11	organic soil			Vos, 1992; in Kiden, 1995
4	Zeeland	Anna Jacobapolder	51.6369°	4.1194°	GrN 16937	7290 ± 50	8029 - 8165	-13.63	-13.6	± 0.11	wood peat	base		Vos, 1992; in Kiden, 1995
5	Zeeland	Veere	51.5517°	3.6572°	GrN 1580	7210 ± 90	7939 - 8153	-7.76	-7.73	± 0.11	peat	base		Jelgersma, 1961; in Kiden, 1995
6	Zeeland	Gapinge	51.5431°	3.6347°	GrN 20276	7070 ± 50	7837 - 7941	-6.75	-6.7	± 0.3	sandy peat	base		RGD; in Kiden, 1995
7	Zeeland	Middelburg	51.5031°	3.5914°	GrN 1626	6800 ± 85	7571 - 7697	-6.52	-6.49	± 0.11	peat	base		Jelgersma, 1961; in Kiden, 1995
8	Zeeland	Scherpenisse	51.5514°	4.1089°	GrN 16946	6730 ± 50	7512 - 7656	-8.45	-8.43	± 0.1	sandy peat	base		Vos, 1992; in Kiden, 1995
9	Zeeland	Waarde	51.4272°	4.0717°	GrN 1112	6370 ± 85	7245 - 7419	-6.4	-6.38	± 0.1	peat/organic soil	base		Jelgersma, 1961; in Kiden, 1995
10	Zeeland	Kreekrak	51.4300°	4.2292°	GrN 16942	6330 ± 70	7205 - 7323	-7.62	-7.6	± 0.1	sandy organic soil			Vos, 1992; in Kiden, 1995
11	Zeeland	Kreekrak	51.4300°	4.2292°	GrN 16941	6290 ± 45	7161 - 7266	-7.56	-7.54	± 0.1	*Phragmites* peat	base		Vos, 1992; in Kiden, 1995
12	Zeeland	Perkpolder	51.3972°	4.0050°	GrN 1045	6240 ± 70	7027 - 7248	-5.25	-5.2	± 0.11	peat	base		Jelgersma, 1961; in Kiden, 1995
13	Zeeland	Berendrechtsluis	51.3500°	4.2667°	IRPA 769	6000 ± 75	6731 - 6909	-4.24	-4.2	± 0.11	wood peat	base		Kiden, 1989; in Kiden, 1995
15	Zeeland	Ellewoutsdijk	51.3903°	3.8069°	GrN 1571	5820 ± 70	6535 - 6721	-4.09	-4.05	± 0.11	peat	base		Jelgersma, 1961; in Kiden, 1995
16	Zeeland	Oude Stoof 4-2	51.3436°	3.9883°	GrN 1120	5790 ± 70	6499 - 6663	-3.55	-3.5	± 0.11	*Phragmites* peat	base		RGD; in Kiden, 1995
17	Zeeland	Oude Stoof 3-1	51.3511°	3.9733°	GrN 1042	5770 ± 100	6466 - 6666	-3.8	-3.77	± 0.11	*Phragmites* peat	base		Jelgersma, 1961; in Kiden, 1995
18	Zeeland	Ritthem	51.4536°	3.6267°	GrN 405	5720 ± 120	6403 - 6643	-4.44	-4.4	± 0.11	peat	base		Jelgersma, 1961; in Kiden, 1995
19	Zeeland	Oude Stoof 4-3	51.3436°	3.9883°	GrN 1129	5695 ± 55	6407 - 6546	-3.55	-3.5	± 0.11	*Phragmites* peat	base		RGD; in Kiden, 1995
20	Zeeland	Zeesluis Hingene-Wintham	51.1169°	4.3042°	IRPA 710	5550 ± 75	6282 - 6408	-3.58	-3.53	± 0.11	wood peat	base		Kiden, 1989; in Kiden, 1995
21	Zeeland	Oude Stoof 3-2	51.3511°	3.9733°	GrN 1121	5340 ± 80	5994 - 6198	-3.8	-3.77	± 0.11	*Phragmites* peat	base		RGD; in Kiden, 1995
22	Zeeland	Zeesluis Hingene-Wintham	51.1169°	4.3042°	IRPA 741	5110 ± 70	5749 - 5924	-2.78	-2.73	± 0.11	wood peat (0.8)	middle	yes	Kiden, 1989; in Kiden, 1995
23	Zeeland	Groede	51.3775°	3.5094°	GrN 187	5100 ± 180	5642 - 5995	-3.15	-3.13	± 0.1	peat	base		Jelgersma, 1961; in Kiden, 1995
27	Zeeland	Oosterweel	51.2431°	4.3861°	IRPA 713	3890 ± 65	4237 - 4415	-2.01	-1.96	± 0.11	wood peat	base		Kiden, 1989; in Kiden, 1995
29	Belgium	Zeebrugge	51.3172°	3.2125°	Lv 855	4880 ± 65	5583 - 5707	-3.18	-3.08	± 0.2	wood (alder)	base		Denys and Baeteman, 1995
76	Zeeland	Willemstad	51.67°	4.25°	GrN 4922	6400 ± 85	7264 - 7419	-8		± 0.1	wooden statue in peat	base		Louwe Kooijmans, 1976; in van de Plassche, 1982
144	Dutch west coast	Hillegersberg donk			GrN 7848	5685 ± 35	6410 - 6494	-6.13	-6.1	± 0.13	fen peat	base		van de Plassche, 1982
145	Dutch west coast	Hillegersberg donk			GrN 7846	5560 ± 40	6304 - 6398	-5.94	-5.9	± 0.14	fen peat	base		van de Plassche, 1982
147	Dutch west coast	Hillegersberg donk			GrN 7844	5440 ± 35	6200 - 6286	-5.75	-5.71	± 0.14	fen peat	base		van de Plassche, 1982
149	Dutch west coast	Hillegersberg donk			GrN 7842	5490 ± 80	6198 - 6397	-5.44	-5.42	± 0.12	fen peat	base		van de Plassche, 1982
150	Dutch west coast	Hillegersberg donk			GrN 7841	5275 ± 45	5946 - 6169	-5.27	-5.23	± 0.14	fen peat	base		van de Plassche, 1982
151	Dutch west coast	Hillegersberg donk			GrN 7840	5070 ± 40	5750 - 5891	-4.84	-4.8	± 0.14	fen peat	base		van de Plassche, 1982
152	Dutch west coast	Hillegersberg donk			GrN 7838	4925 ± 40	5602 - 5706	-4.47	-4.43	± 0.14	fen peat	base		van de Plassche, 1982
153	Dutch west coast	Hillegersberg donk			GrN 7835	4655 ± 55	5313 - 5465	-4	-3.98	± 0.12	fen peat	base		van de Plassche, 1982
154	Dutch west coast	Hillegersberg donk			GrN 7834	4500 ± 60	5048 - 5290	-3.71	-3.69	± 0.12	fen peat	base		van de Plassche, 1982
155	Dutch west coast	Hillegersberg donk			GrN 7833	4525 ± 40	5065 - 5300	-3.36	-3.32	± 0.14	fen peat	base		van de Plassche, 1982
6	Dutch west coast	Loosduinen				2275 ± 75	2154 - 2349	-0.75		± 0.2	inhabited peat surface	top		Bennema, 1954; in van de Plassche, 1982
166	Dutch west coast	Rijksweg donk			GrN 8912	5955 ± 45	6725 - 6852	-6.54	-6.5	± 0.14	wood peat	base		van de Plassche, 1982
167	Dutch west coast	Rijksweg donk			GrN 8434	3820 ± 90	4089 - 4353	-2.62	-2.6	± 0.12	wood peat	base		van de Plassche, 1982
168	Dutch west coast	Rijksweg donk			GrN 8433	3510 ± 90	3685 - 3893	-2.38	-2.35	± 0.13	wood peat	base		van de Plassche, 1982
169	Dutch west coast	Rijksweg donk			GrN 8432	3530 ± 80	3692 - 3898	-2.01	-1.98	± 0.13	wood peat	base		van de Plassche, 1982
170	Dutch west coast	Rijksweg donk			GrN 8431	3455 ± 35	3641 - 3822	-1.8	-1.78	± 0.12	wood peat	base		van de Plassche, 1982
171	Dutch west coast	Rijksweg donk			GrN 8799	2985 ± 30	3079 - 3211	-1.5		± 0.1	oak root			van de Plassche, 1982
172	Dutch west coast	Rijksweg donk			GrN 8798	2700 ± 45	2761 - 2845	-1.5		± 0.1	alder roots			van de Plassche, 1982

index no. [1]	country / region	site location	coordinates		lab no.	14C age	1σ calibrated age	sample depth	sample depth	altitude error	dated material	stratigraphic	compaction	reference
			Lat. N	Long. E		(yrs BP)	(cal. yrs BP) [2]	max. (m NN) [3]	min. (m NN)	(m)	(thickness of peat layer in m)	position in peat	expected	
28	Dutch west coast	donk of Brandwijk 2			GrN 192	2830 ± 135	2782 - 3079	-1.15	-1.11	± 0.14	fen-wood peat	base		Jelgersma, 1961; in van de Plassche, 1982
29	Dutch west coast	donk of Brandwijk 4			GrN 191	4590 ± 150	5046 - 5469	-3.31	-3.29	± 0.12	fen-wood peat	base		Jelgersma, 1961; in van de Plassche, 1982
37	Dutch west coast	donk of Barendrecht VII			GrN 1146	4270 ± 55	4726 - 4872	-3.24	-3.19	± 0.15	fen-wood peat	base		Jelgersma, 1961; in van de Plassche, 1982
38	Dutch west coast	donk of Barendrecht X			GrN 1147	3900 ± 70	4236 - 4419	-2.67	-2.63	± 0.14	fen-wood peat	base		Jelgersma, 1961; in van de Plassche, 1982
39	Dutch west coast	donk of Barendrecht XII			GrN 1148	3480 ± 50	3690 - 3828	-1.97	-1.92	± 0.15	fen-wood peat	base		Jelgersma, 1961; in van de Plassche, 1982
174	Dutch west coast	M1 Maaldrift			GrN 8414	2955 ± 50	3026 - 3209	-0.62	-0.6	± 0.05	wood peat, sandy			van de Plassche, 1982
175	Dutch west coast	M2 Maaldrift			GrN 8415	2985 ± 35	3078 - 3212	-0.94	-0.91	± 0.06	wood peat, sandy			van de Plassche, 1982
177	Dutch west coast	M4 Maaldrift			GrN 8417	3315 ± 25	3476 - 3570	-1.27	-1.24	± 0.06	fen-wood peat, non-clayey			van de Plassche, 1982
178	Dutch west coast	M5 Maaldrift			GrN 8418	3565 ± 40	3776 - 3909	-1.6	-1.58	± 0.05	clayey wood peat			van de Plassche, 1982
180	Dutch west coast	M7 Maaldrift			GrN 8420	3615 ± 40	3865 - 3979	-1.99	-1.96	± 0.06	*Phragmites* peat	base		van de Plassche, 1982
182	Dutch west coast	M12 Maaldrift			GrN 8910	3515 ± 55	3696 - 3840	-1.48	-1.46	± 0.05	fen-wood peat			van de Plassche, 1982
188	Dutch west coast	W1 Wassenaar			GrN 8909	3495 ± 55	3692 - 3831	-1.65	-1.63	± 0.05	sedge peat			van de Plassche, 1982
190	Dutch west coast	R3 Rijksdorp			GrN 8907	3325 ± 30	3478 - 3628	-0.91	-0.89	± 0.05	sedge peat			van de Plassche, 1982
2	Dutch west coast	Velsen			GrN 75	7140 ± 200	7786 - 8163	-14.25		± 0.7	wood in basal peat	top	yes	Bennema, 1954; in van de Plassche, 1982
3	Dutch west coast	Haarlemmermeer polder				4500 ± 200	4864 - 5327	-4.15		± 0.3	sea-clay on sand			Bennema, 1954; in van de Plassche, 1982
22	Dutch west coast	Koegras II			GrN 476	4925 ± 90	5587 - 5749	-4.72	-4.7	± 0.2	fen peat	base		Jelgersma, 1961; in van de Plassche, 1982
26	Dutch west coast	Velsen			GrN 161	7745 ± 200	8356 - 8778	-16.1		± 0.1	*Alnus* roots			Jelgersma, 1961; in van de Plassche, 1982
66	Dutch west coast	St. Maartensvlotbrug			GrN 1633	6080 ± 60	6803 - 7006	-7.22	-7.17	± 0.1	fen peat	base		Jelgersma, 1961; in van de Plassche, 1982
118	Dutch west coast	Zwaagdijk			GrN 8098	6980 ± 40	7743 - 7842	-12.6	-12.58	± 0.1	fen peat	base		Jelgersma, 1979; in van de Plassche, 1982
5	Dutch North Sea	west	52.50°	3.80°	Pollen A	8400 ± 300	9000 - 9771	-26		± 1	peat	base		Jelgersma, 1961; in Kiden et al., 2002
6	Dutch North Sea	west	52.50°	3.50°	Pollen D	8500 ± 300	9127 - 9892	-28		± 1	peat	base		Jelgersma, 1961; in Kiden et al., 2002
7	Dutch North Sea	west	52.50°	3.25°	Pollen C	8700 ± 300	9472 - 10180	-33		± 1	peat	base		Jelgersma, 1961; in Kiden et al., 2002
8	Dutch North Sea	west	52.50°	2.92°	Pollen B	9000 ± 300	9691 - 10430	-35		± 1	peat	base		Jelgersma, 1961; in Kiden et al., 2002
14	Dutch north coast	Farmsum B1			GrN 621	6460 ± 145	7249 - 7492	-6.2	-6.17	± 0.1	fen-wood peat	base		Jelgersma, 1961; in van de Plassche, 1982
16	Dutch north coast	Winschoten 518			GrN 1091	5050 ± 80	5725 - 5902	-4.23	-4.19	± 0.1	fen peat	base		Jelgersma, 1961; in van de Plassche, 1982
17	Dutch north coast	Winschoten 515			GrN 1088	4350 ± 75	4834 - 5036	-3.03	-2.98	± 0.1	fen peat	base		Jelgersma, 1961; in van de Plassche, 1982
18	Dutch north coast	Winschoten 513b			GrN 1090	3350 ± 60	3477 - 3638	-1.92	-1.87	± 0.1	fen peat	base		Jelgersma, 1961; in van de Plassche, 1982
19	Dutch north coast	Winschoten 512			GrN 1089	2950 ± 70	2995 - 3210	-0.94	-0.9	± 0.1	fen peat	base		Jelgersma, 1961; in van de Plassche, 1982
100	Dutch north coast	Ezinge				2500 ± 75	2486 - 2734	-0.6		± 0.25	inhabited salt-marsh surface		yes	Louwe Kooijmans, 1976; in van de Plassche, 1982
121	Dutch north coast	Engwierumer Polder V			GrN 7641	5800 ± 40	6548 - 6662	-7.05	-7.01	± 0.18	fen peat	base		Griede, 1978; in van de Plassche, 1982
122	Dutch north coast	Stiens VI			GrN 7644	4760 ± 30	5471 - 5583	-4.31	-4.26	± 0.15	peat	base		Griede, 1978; in van de Plassche, 1982
Alm12	Dutch central area	Almere	52.32°	5.28°	UtC 9100	5490 ± 45	6202 - 6311	-6.09		± 0.1	peat	base		Makaske et al., 2003
Alm 13	Dutch central area	Almere	52.32°	5.28°	UtC 9101	5719 ± 43	6444 - 6553	-6.72		± 0.1	peat	base		Makaske et al., 2003
Alm 14	Dutch central area	Almere	52.32°	5.28°	UtC 9102	5861 ± 43	6637 - 6732	-7.08		± 0.1	peat	base		Makaske et al., 2003
Alm 15	Dutch central area	Almere	52.32°	5.28°	UtC 9103	5980 ± 46	6744 - 6866	-7.56		± 0.1	peat	base		Makaske et al., 2003
Alm 23/25/26	Dutch central area	Almere	52.35°	5.22°	UtC 9109, 9111, 9112 av.	6334 ± 30	7246 - 7309	-9.34		± 0.1	peat	base		Makaske et al., 2003
Alm 27/28	Dutch central area	Almere	52.35°	5.22°	UtC 9113, 9114 av.	6330 ± 35	7240 - 7310	-9.19		± 0.1	peat	base		Makaske et al., 2003
77	Dutch central area	Swifterbant	52.55°	5.65°	GrN 5067	5610 ± 60	6310 - 6441	-6.2		± 0.25	fen peat	base		Louwe Kooijmans, 1976; in van de Plassche, 1982
78	Dutch central area	Swifterbant	52.55°	5.65°	GrN 7043	5300 ± 50	5992 - 6171	-5.35		± 0.25	tidal creek levee		yes	Louwe Kooijmans, 1976; in van de Plassche, 1982
8	Dutch central area	Schokland	52.62°	5.78°	GrN 15130	4720 ± 90	5325 - 5581	-4.68	-4.66	± 0.12	*Juncus* peat			Roeleveld and Gotjé, 1993
12	Dutch central area	Schokland	52.62°	5.78°	GrN 16367	4320 ± 60	4832 - 4966	-4	-3.97	± 0.12	sedge with birch peat	base		Roeleveld and Gotjé, 1993
13	Dutch central area	Schokland	52.62°	5.78°	GrN 16373	4350 ± 45	4855 - 4966	-4.13	-4.1	± 0.14	dry sedge with birch peat	base		Roeleveld and Gotjé, 1993
14	Dutch central area	Schokland	52.62°	5.78°	GrN 16366	4790 ± 70	5466 - 5599	-4.42	-4.39	± 0.2	dry sedge with birch peat	base		Roeleveld and Gotjé, 1993
15	Dutch central area	Schokland	52.62°	5.78°	GrN 16370	4880 ± 60	5584 - 5661	-4.81	-4.78	± 0.15	sedge with birch peat	base		Roeleveld and Gotjé, 1993
16	Dutch central area	Schokland	52.62°	5.78°	GrN 16369	4920 ± 60	5597 - 5709	-4.93	-4.91	± 0.15	sedge peat	base		Roeleveld and Gotjé, 1993
17	Dutch central area	Schokland	52.62°	5.78°	GrN 16368	4990 ± 60	5647 - 5863	-5.19	-5.16	± 0.15	sedge peat	base		Roeleveld and Gotjé, 1993
18	Dutch central area	Schokland	52.62°	5.78°	GrN 16372	5000 ± 60	5655 - 5884	-5.38	-5.35	± 0.15	very wet sedge peat	base		Roeleveld and Gotjé, 1993
19	Dutch central area	Schokland	52.62°	5.78°	GrN 16371	5160 ± 40	5891 - 5987	-5.73	-5.7	± 0.15	sedge with birch peat	base		Roeleveld and Gotjé, 1993
B2 22/23	Dutch central area	Schokland	52.62°	5.78°	GrA 16219, 16225 av.	3365 ± 40	3553 - 3685	-2.37	-2.35	± 0.1	*Phragmites* peat	base		van de Plassche et al., 2005
A3 24/25	Dutch central area	Schokland	52.62°	5.78°	GrA 16216, 16217 av.	3655 ± 40	3905 - 4075	-2.86	-2.85	± 0.1	sedge-carr peat	base		van de Plassche et al., 2005
C4 28	Dutch central area	Schokland	52.62°	5.78°	GrA 12714	4340 ± 50	4847 - 4966	-3.89	-3.87	± 0.1	birch-carr peat	base		van de Plassche et al., 2005
D1 32	Dutch central area	Schokland	52.62°	5.78°	GrA 12718	4570 ± 50	5067 - 5441	-4.68	-4.67	± 0.1	sedge-carr peat	base		van de Plassche et al., 2005
5	German Coast	Marne B35	53.94°	8.98°	Hv 6189	8000 ± 60	8928 - 9007	-29		± 0.1	limnic vs. tidal sediments			Menke, 1976; Behre et al., 1979; in Behre 2003
6	German Coast	Wangerooge A10	53.87°	7.91°	Hv 8602	7960 ± 205	8540 - 9032	-24.23		± 0.5	base tidal flat with *Phragmites* roots			Ludwig et al., 1979; in Behre 2003
7	German Coast	Wangerooge A10	53.87°	7.91°	Hv 8601	7980 ± 60	8768 - 8998	-23.6		± 0.5	base tidal flat with *Phragmites* roots			Ludwig et al., 1979; in Behre 2003
8	German Coast	Wangerooge A10	53.87°	7.91°	Hv 8600	7540 ± 80	8210 - 8406	-23.16		± 0.5	base tidal flat with *Phragmites* roots			Ludwig et al., 1979; in Behre 2003
9	German Coast	Scharhörn 56/67	53.95°	8.41°	Hv 2575	7790 ± 90	8420 - 8646	-24.4		± 0.1	base tidal flat			Linke, 1982; in Behre 2003
10	German Coast	Scharhörn 58/67	53.95°	8.46°	Hv 2143	7720 ± 65	8417 - 8541	-24.34		± 0.1	*Phragmites* peat (0.17)	top		Linke, 1982; in Behre 2003
11	German Coast	Neuwerk 60/67	53.94°	8.48°	Hv 2242	7280 ± 230	7928 - 8339	-21.31		± 0.1	roots from brackish plants			Linke, 1982; in Behre 2003
12	German Coast	GK Hooksiel G57	53.67°	8.05°	Hv 11607	6975 ± 110	7690 - 7925	-14.32		± 0.1	*Phragmites* peat (0.15)	top		Streif, 1985; in Behre 2003
13	German Coast	Land Würden II/I	53.51°	8.53°	Hv 7195	7110 ± 65	7841 - 7975	-13.28		± 0.1	peat	base		Preuss, 1979; in Behre 2003
14	German Coast	GK Wilhelmshaven G738	53.56°	8.05°	Hv 8928	7070 ± 150	7728 - 7982	-12.37		± 0.1	fen peat (0.21)	top	yes	Streif, 1981; in Behre 2003
15	German Coast	GK Emden-West G320	53.42°	7.19°	Hv 6306	6345 ± 120	7177 - 7420	-12.4		± 0.1	wood on clastic Holocene			Barckhausen, 1984; in Behre 2003
16	German Coast	Land Würsten I/4	53.67°	8.54°	Hv 7133	6855 ± 90	7610 - 7754	-11.5		± 0.1	*Phragmites* peat (0.5)	top	yes	Preuss, 1979; in Behre 2003

index no.[1]	country / region	site location	coordinates		lab no.	14C age	1σ calibrated age	sample depth	sample depth	altitude error	dated material	stratigraphic	compaction	reference
			Lat. N	Long. E		(yrs BP)	(cal. yrs BP)[2]	max. (m NN)[3]	min. (m NN)	(m)	(thickness of peat layer in m)	position in peat	expected	
17	German Coast	GK Emden-West G103	53.39°	7.04°	Hv 6321	6385 ± 75	7252 - 7417	-10.66		± 0.1	wood on clastic Holocene			Barckhausen, 1984; in Behre 2003
18	German Coast	GK Emden-West G81	53.41°	7.16°	Hv 4755	6320 ± 195	7003 - 7425	-9.92		± 0.1	wood on clastic Holocene			Barckhausen, 1984; in Behre 2003
19	German Coast	GK Wilhelmshaven G479	53.51°	8.02°	Hv 8944	5685 ± 310	6171 - 6807	-7.92		± 0.1	wood on clastic Holocene			Streif, 1981; in Behre 2003
20	German Coast	GK Wilhelmshaven G743	53.51°	8.02°	Hv 8936	6105 ± 80	6859 - 7028	-6.73		± 0.1	fen peat	base		Streif, 1981; in Behre 2003
21	German Coast	GK Wilhelmshaven G743	53.51°	8.02°	Hv 8935	5765 ± 115	6443 - 6669	-6.55		± 0.1	*Phragmites* peat (0.23)	top	yes	Streif, 1981; in Behre 2003
22	German Coast	GK Hooksiel G24	53.62°	8.02°	Hv 9944	5575 ± 105	6280 - 6485	-5.92		± 0.1	*Phragmites* peat	top	yes	Streif, 1985; in Behre 2003
23	German Coast	GK Wilhelmshaven G749	53.51°	8.02°	Hv 8943	5300 ± 90	5947 - 6176	-7.05		± 0.1	*Phragmites* peat (0.46)	top	yes	Streif, 1981; in Behre 2003
24	German Coast	Wilhelmshaven Kanalweg	53.53°	8.09°	Pollen	5150 ± 50	5764 - 5986	-7.1		± 0.1	*Phragmites* peat	top	yes	Behre et al., 1975; in Behre 2003
25	German Coast	GK Emden G170	53.37°	7.30°	Hv 10453	5155 ± 55	5762 - 5987	-5.94		± 0.1	wood on clastic Holocene			Barckhausen, 1984; in Behre 2003
26	German Coast	GK Hooksiel G19	53.59°	7.99°	Hv 9940	4655 ± 75	5305 - 5471	-7.18		± 0.1	peat (0.65)	top	yes	Streif, 1985; in Behre 2003
27	German Coast	Land Wursten III/7	53.79°	8.55°	Hv 7434	4715 ± 85	5324 - 5579	-5.97		± 0.1	swimming peat on lagunal sediments	base	yes	Preuss, 1979; in Behre 2003
28	German Coast	GK Hooksiel G26	53.59°	8.05°	Hv 9946	4710 ± 50	5326 - 5575	-5.74		± 0.1	*Phragmites* peat	top	yes	Streif, 1985; in Behre 2003
29	German Coast	Föhr, F 3/1	54.76°	8.49°	Kl 1050,01	4680 ± 100	5310 - 5579	-5.13		± 0.1	basal peat (1.0)	top	yes	Hoffmann,1980; in Behre 2003
30	German Coast	GK Wilhelmshaven G743	53.51°	8.02°	Hv 8934	4570 ± 90	5049 - 5447	-4.65		± 0.1	swimming *Phragmites* peat	base	yes	Streif, 1981; in Behre 2003
31	German Coast	GK Wilhelmshaven G743	53.51°	8.02°	Hv 8933	4340 ± 70	4833 - 4977	-4.43		± 0.1	swimming *Phragmites* peat (0.26)	top	yes	Streif, 1981; in Behre 2003
32	German Coast	Föhr, F 2/1	54.75°	8.45°	Kl 1049,02	4120 ± 75	4528 - 4813	-3.93		± 0.1	basal peat (1.5)	top	yes	Hoffmann,1980; in Behre 2003
33	German Coast	GK Hooksiel G24	53.62°	8.02°	Hv 9943	4175 ± 65	4617 - 4828	-3.6		± 0.1	swimming *Phragmites* peat	top	yes	Streif, 1985; in Behre 2003
34	German Coast	Sehestedter Moor binnendeichs	53.46°	8.30°	Hv 8019	4160 ± 45	4616 - 4822	-3.2		± 0.1	fen peat on brackish clay	base	yes	Streif, 1984; in Behre 2003
35	German Coast	GK Wilhelmshaven G744	53.51°	8.02°	Hv 8937	4035 ± 85	4411 - 4805	-2.22		± 0.1	upper fen peat on clayey sands	base		Streif, 1981; in Behre 2003
36	German Coast	GK Wilhelmshaven G749	53.53°	8.07°	Hv 8941	3775 ± 75	3989 - 4253	-0.92		± 0.1	upper peat on brackish clay	base	yes	Streif, 1981; in Behre 2003
37	German Coast	GK Wilhelmshaven G743	53.51°	8.02°	Hv 8932	3585 ± 70	3825 - 3980	-2.32		± 0.1	upper peat on brackish clay	base	yes	Streif, 1981; in Behre 2003
38	German Coast	GK Hooksiel G44	53.61°	8.02°	Hv 10674	3375 ± 85	3476 - 3693	-1.19		± 0.1	upper peat on clayey sand	middle	yes	Streif, 1985; in Behre 2003
39	German Coast	Wilhelmshaven Kanalweg	53.53°	8.09°	Hv 6904	3255 ± 100	3378 - 3584	-0.74		± 0.1	upper peat on brackish clay	base	yes	Behre et al., 1975; in Behre 2003
40	German Coast	GK Hooksiel G19	53.59°	7.99°	Hv 9939	3250 ± 80	3384 - 3554	-0.18		± 0.1	fen peat on brackish clay (0.08)		yes	Streif, 1985; in Behre 2003
41	German Coast	Feddersen wierde Untergrund	53.69°	8.52°	Pollen		3150 - 3350	-0.65		± 0.1	upper peat	base		Körber-Grohne, 1967; in Behre 2003
42	German Coast	Sehestedter Moor außendeichs	53.46°	8.30°	Kl 4159,09	2980 ± 25	3079 - 3209	-0.22		± 0.1	upper peat on brackish clay	base	yes	Behre and Kučan, 1999; in Behre 2003
43	German Coast	Rodenkirchen	53.40°	8.44°	archeology + 14C		2800-2900	-1.8		± 0.1	lower settlement layer on shore bank		yes	Strahl, 2002; in Behre 2003
44	German Coast	Esing-Haferacker/Eiderstedt	54.30°	8.68°	Hv 6753	2630 ± 60	2712 - 2792	-0.9		± 0.1	Peat layer in beach bank			Menke, 1988; in Behre 2003
45	German Coast	Jemgum I VEZ	53.27°	7.39°	archeology		2550-2650	-1.36		± 0.1	lower settlement layer on shore bank			Haarnagel, 1957; in Behre 2003
46	German Coast	Hatzum-Boomborg SS 1 A	53.31°	7.35°	archeology + 14C		2450-2550	-1.7		± 0.1	lower settlement layer on shore bank			Haarnagel, 1969; in Behre 2003
47	German Coast	Jemgumkloster VEZ	53.25°	7.40°	archeology		2450-2550	-1.66		± 0.1	lower settlement layer on shore bank			Brandt, 1980; in Behre 2003
48	German Coast	Hatzum-Boomborg	53.31°	7.35°	GrN 4669	2445 ± 35	2360 - 2706	-1.7		± 0.1	House pillar of settlement 1 A			Haarnagel, 1969; in Behre 2003
49	German Coast	Rheiderland	53.31°	7.35°	Hv 2051	2330 ± 50	2207 - 2433	-1.2		± 0.1	Birch stubs on bank			Behre, 1970; in Behre 2003
50	German Coast	Hatzum-Boomborg	53.31°	7.35°	GrN 4668	2340 ± 30	2335 - 2355	-1.2		± 0.1	House pillar of settlement 2			Haarnagel, 1969; in Behre 2003
51	German Coast	Hatzum-Boomborg SS 5	53.31°	7.35°	archeology		2250-2350	-0.8		± 0.1	Base of settlement layer 5 (on bank)			Haarnagel, 1969; in Behre 2003
52	German Coast	Westdorf	53.68°	7.31°	archeology		1850-1950	-1		± 0.1	Base settlement plain			Haarnagel, 1980; in Behre 2003
53	German Coast	Jemgumkloster SS 3	53.25°	7.40°	archeology		2020-2080	-1		± 0.1	Base of settlement layer 3 on D I b sediments			Brandt, 1980; in Behre 2003
54	German Coast	Barward SS 1	53.65°	8.53°	archeology		1950-2000	-0.75		± 0.1	Base of settlement layer on bank			Brandt, 1980; in Behre 2003
55	German Coast	Feddersen Wierde SS 1 a	53.69°	8.52°	archeology		1950-2050	-0.7		± 0.1	Base settlement plain 1 a on bank			Haarnagel, 1979; in Behre 2003
56	German Coast	Bentumersiel SS 1	53.27°	7.39°	archeology		1950-2000	-0.8		± 0.1	Base of settlement layer on bank			Brandt, 1980; in Behre 2003
57	German Coast	Eppingawehr	53.29°	7.39°	archeology		1850-1950	-0.8		± 0.1	Base of settlement layer on bank			Brandt, 1980; in Behre 2003
58	German Coast	Förriesdorf/Zissenhausen	53.58°	7.86°	archeology		1850-1950	-0.65		± 0.1	Base of settlement layer			Brandt, 1980; in Behre 2003
59	German Coast	Seeverns	53.56°	8.28°	archeology		1850-1950	-0.6		± 0.1	Base of settlement layer			Brandt, 1980; in Behre 2003
60	German Coast	Hodorf SS 1	53.88°	9.43°	archeology		1750-1850	-0.8		± 0.1	Base of settlement layer 1			Brandt, 1980; in Behre 2003
61	German Coast	Hatzum-Boomborg RKZ	53.31°	7.35°	archeology		1920-1980	-0.7		± 0.1	footbridge in tidal gully			Haarnagel, 1980; in Behre 2003
62	German Coast	Feddersen Wierde SS 1 c	53.69°	8.52°	archeology		1905-1925	-0.3		± 0.1	Base of settlement layer 1 c (plain)			Haarnagel, 1979; in Behre 2003
63	German Coast	Lüdingworth Osterende	53.82°	8.86°	archeology		1850-1950	-0.35		± 0.1	Base of settlement layer			Brandt, 1980; in Behre 2003
64	German Coast	Tholendorf/Eiderstedt	54.30°	8.68°	Hv 3371	1925 ± 65	1816 - 1949	-0.3		± 0.1	Peat horizon in beach bank			Menke, 1988; in Behre 2003
65	German Coast	Ostermoor	53.93°	9.17°	archeology		1850-1900	-0.3		± 0.1	Base of settlement layer		yes	Bantelmann, 1960; in Behre 2003
66	German Coast	Feddersen Wierde SS 1 c	53.69°	8.52°	archeology		1905-1925	-0.25		± 0.1	footbridge			Haarnagel, 1979; in Behre 2003
67	German Coast	Einswarden, Flachsiedlung	53.54°	8.53°	archeology		2000-2080	-0.2		± 0.1	Base of settlement layer on bank			Brandt, 1980; in Behre 2003
68	German Coast	Ritsch	53.74°	9.40°	archeology		1900-2000	-0.2		± 0.1	Base of settlement layer			Brandt, 1980; in Behre 2003
69	German Coast	Tiebensee (Dithmarschen)	54.23°	8.99°	archeology		1850-1950	0		± 0.1	Base of settlement layer of living space 1			Meier, 2001a; in Behre 2003
70	German Coast	Borkum BO 1 b	53.60°	6.68°	Hv 22942	2090 ± 115	1923 - 2157	-0.11		± 0.1	*Hydrobia ulvae*			Freund and Streif, 2000; in Behre 2003
71	German Coast	Barnkrug	53.72°	9.42°	archeology		1900-2000	-0.15		± 0.1	Base of settlement layer			Brandt, 1980; in Behre 2003
72	German Coast	Feddersen Wierde SS 2	53.69°	8.52°	archeology		1825-1875	-0.15		± 0.1	Lowermost house of settlement layer 2			Haarnagel, 1979; in Behre 2003
73	German Coast	Juist	53.68°	6.90°	Hv 13131	1965 ± 130	1768 - 2062	0.08		± 0.1	"Groden" surface			Streif, 1986; in Behre 2003
74	German Coast	Süderbusenwurth/Dithmarschen	54.05°	9.01°	archeology		1800-1804	0.5		± 0.1	House of the lowermost settlement layer			Meier, 2001b; in Behre 2003
75	German Coast	Borkum BO 2	53.62°	6.80°	Hv 22943	2120 ± 115	1987 - 2304	-0.1		± 0.1	*Cerastoderme edule*			Freund and Streif, 2000; in Behre 2003
76	German Coast	Tofting	54.35°	8.94°	archeology		1800-1850	0.45		± 0.1	Base of lower settlement layer on bank			Bantelmann et al., 1984; in Behre 2003
77	German Coast	Feddersen Wierde SS 3	53.69°	8.52°	archeology		1775-1825	0.35		± 0.1	lowermost house of settlement layer 3			Haarnagel, 1979; in Behre 2003
78	German Coast	Langwarden	53.62°	8.31°	archeology		1725-1775	0.4		± 0.1	Base of settlement layer on bank			Brandt, 1980; in Behre 2003
79	German Coast	Feddersen Wierde SS 4	53.69°	8.52°	archeology		1725-1775	0.5		± 0.1	lowermost house on settlement layer 4			Haarnagel, 1979; in Behre 2003
80	German Coast	Feddersen Wierde SS 5	53.69°	8.52°	archeology		1725-1775	0.65		± 0.1	lowermost house on settlement layer 5			Haarnagel, 1979; in Behre 2003
81	German Coast	Feddersen Wierde SS 6	53.69°	8.52°	archeology		1625-1675	0.8		± 0.1	lowermost house on settlement layer 6			Haarnagel, 1979; in Behre 2003
82	German Coast	Feddersen Wierde SS 7	53.69°	8.52°	archeology		1575-1625	0.4		± 0.1	lowermost house on settlement layer 7			Haarnagel, 1979; in Behre 2003

index no. [1]	country / region	site location	coordinates		lab no.	14C age	1σ calibrated age	sample depth	sample depth	altitude error	dated material	stratigraphic	compaction	reference
			Lat. N	Long. E		(yrs BP)	(cal. yrs BP) [2]	max. (m NN) [3]	min. (m NN)	(m)	(thickness of peat layer in m)	position in peat	expected	
83	German Coast	Feddersen Wierde SS 8	53.69°	8.52°	archeology		1522-1575	0.4		± 0.1	lowermost house on settlement layer 8			Haarnagel, 1979; in Behre 2003
84	German Coast	Wangerooge	53.80°	7.87°	Hv 9257	1540 ± 75	1385 - 1516	0.1		± 0.1	*Scrobicularia* in living position in upper tidal flat			Hanisch, 1980; in Behre 2003
85	German Coast	Wangerooge	53.80°	7.87°	Hv 300	1450 ± 180	1174 - 1542	0.2		± 0.1	*Scrobicularia* in living position in upper tidal flat			Sindowski, 1969a; in Behre 2003
86	German Coast	Wellinghusen SS 1	54.15°	8.96°	archeology		1250-1270	1		± 0.1	plain of settlement layer 1			Meier, 2001a; in Behre 2003
87	German Coast	Elisenhof	54.30°	8.92°	archeology		1150-1250	0.6		± 0.1	bridge over tidal gully			Bantelmann, 1966; in Behre 2003
88	German Coast	Elisenhof	54.30°	8.92°	archeology		1150-1250	0.6		± 0.1	plough land			Bantelmann, 1966; in Behre 2003
89	German Coast	Elisenhof	54.30°	8.92°	archeology		1200-1250	0.6		± 0.1	surface of bank and base of "Wurt"			Bantelmann, 1975; in Behre 2003
90	German Coast	Groothusen	53.45°	7.07°	archeology		1200-1250	0.2		± 0.1	Base of settlement layer II			Reinhardt, 1965; in Behre 2003
91	German Coast	Niens SS 1	53.61°	8.33°	archeology		1250-1300	0.5		± 0.1	Base of settlement layer 1 on bank			Brandt, 1991; in Behre 2003
92	German Coast	Oldorf	53.67°	7.91°	archeology		1320-1330	0.4		± 0.1	Base of "wurt" on bank			Schmid, 1994; in Behre 2003
93	German Coast	Juist	53.68°	6.90°	Hv 13130	1185 ± 125	972 - 1233	-0.02		± 0.1	"Groden" surface			Streif, 1986; in Behre 2003
94	German Coast	Neuwarfen	53.66°	7.93°	Hv 20509	1205 ± 115	993 - 1240	0.05		± 0.1	Field as basis of "wurt"			Ey, 1995; in Behre 2003
95	German Coast	Hatzum-Burg/Rheiderland	53.33°	7.34°	archeology		1050-1150	-0.1		± 0.1	Base of settlement layer on bank			Brandt, 1980; in Behre 2003
96	German Coast	Alte Boomborg/Rheiderland	53.31°	7.35°	archeology		975-1075	-0.35		± 0.1	Base of settlement layer on bank			Brandt, 1980; in Behre 2003
97	German Coast	Klunderborg/Rheiderland	53.33°	7.30°	archeology		1000-1100	-0.5		± 0.1	Base of settlement layer on bank			Brandt, 1980; in Behre 2003
98	German Coast	Pellworm	54.51°	8.63°	archeology		1050-1150	-0.5		± 0.1	Base of settlement on plain			Higelke et al., 1984; in Behre 2003
99	German Coast	Juist P 7 b	53.68°	6.90°	Hv 22575	920 ± 95	759 - 925	0.2		± 0.1	Groden			Freund and Streif, unpubl. data; in Behre 2003
100	German Coast	Juist P 6 a	53.68°	6.90°	Hv 22570	650 ± 135	522 - 706	-0.05		± 0.1	Groden			Freund and Streif, unpubl. data; in Behre 2003
101	German Coast	Juist P 6 b	53.68°	6.90°	Hv 22568	670 ± 140	531 - 731	0.1		± 0.1	Groden			Freund and Streif, unpubl. data; in Behre 2003
102	German Coast	Juist	53.68°	6.90°	Hv 22569	630 ± 100	546 - 662	0.4		± 0.1	brackish water reed			Freund and Streif, 2000; in Behre 2003
103	German Coast	Borkum BO 1 a	53.60°	6.68°	Hv 22941	660 ± 60	560 - 664	0.27		± 0.1	bones of *Gavia stellata* in tidal flat			Freund and Streif, 2000; in Behre 2003
104	German Coast	Juist P 8	53.68°	6.90°	Hv 22576	410 ± 115	316 - 528	0.54		± 0.1	Groden			Freund and Streif, unpubl. data; in Behre 2003
105	German Coast	Juist P 7 a	53.68°	6.90°	Hv 22572	440 ± 90	324 - 544	0.59		± 0.1	Groden			Freund and Streif, unpubl. data; in Behre 2003
106	German Coast	Juist P 3 b	53.68°	6.90°	Hv 22563	515 ± 90	488 - 645	0.79		± 0.1	Groden			Freund and Streif, unpubl. data; in Behre 2003
107	German Coast	Juist P 3 a	53.68°	6.90°	Hv 22561	570 ± 155	458 - 688	0.94		± 0.1	Groden surface			Freund and Streif, unpubl. data; in Behre 2003
108	German Coast	Juist P 2	53.68°	6.90°	Hv 22559	615 ± 75	551 - 650	0.99		± 0.1	Groden surface			Freund and Streif, unpubl. data; in Behre 2003
109	German Coast	Juist P 1	53.68°	6.90°	Hv 22554	555 ± 70	519 - 643	0.99		± 0.1	Groden surface			Freund and Streif, unpubl. data; in Behre 2003
110	German Coast	Langeoog	53.75°	7.47°	Hv 1998	690 ± 110	550 - 709	0.86		± 0.1	vegetation horizon			Barckhausen, 1969; in Behre 2003
111	German Coast	Wangerooge	53.80°	7.87°	Hv 12303	545 ± 80	513 - 645	1.15		± 0.1	roots from groden horizon			Streif, 1986; in Behre 2003
112	German Coast	Sande	53.48°	8.05°	history		306	0.4		± 0.1	"Maifeld" during dike construction			Schütte, 1939; in Behre 2003
113	German Coast	Cuxhaven	53.87°	8.71°	hydrology		166	1.04		± 0.1	Gauge measurement			Rohde, 1975; in Behre, 2003
114	German Coast	Cuxhaven	53.87°	8.71°	hydrology		98	1.25		± 0.1	Gauge measurement			Rohde, 1975; in Behre, 2003
115	German Coast	Cuxhaven	53.87°	8.71°	hydrology		50	1.3		± 0.1	Gauge measurement			Rohde, 1975; in Behre, 2003
116	German Coast	Cuxhaven	53.87°	8.71°	hydrology		0	1.37		± 0.1	Gauge measurement			Rohde, 1975; in Behre, 2003
5	English North Sea	Dogger Bank 55/+02/213VE	55.00°	2.92°	AA22662	8140 ± 55	9011-9236	-30.86		± 1	silty peat (0.04)	top		Shennan et al., 2000
1	German North Sea	Dogger Bank	54.7683°	3.4617°	Pollen	8750 ± 300	9474 - 10223	-46		± 1	fen peat (0.5)	middle	yes	Behre and Menke, 1969; in Behre 2003
3	German North Sea	Weiße Bank 235	54.9433°	5.7500°	Hv 7095	8190 ± 140	9007 - 9399	-38.28		± 1	fen peat (0.13)	top		Ludwig et al., 1979; in Behre 2003
3	German North Sea	Weiße Bank 235	54.9433°	5.7500°	Hv 7094	8485 ± 125	9295 - 9560	-38.38		± 1	fen peat	base		Ludwig et al., 1979
245	German North Sea	Weiße Bank	54.6967°	6.1917°	Pollen	9000 ± 200	9887 - 10289	-45.75		± 1	fen peat (0.05)	top		Streif et al., 1983 (internal report)
240	German North Sea	Weiße Bank	54.8050°	5.9867°	Pollen	9300 ± 300	10188 - 11073	-42.5		± 1	peat (0.03)	middle		Streif et al., 1983 (internal report); Ludwig et al., 1979
234	German North Sea	Weiße Bank	54.9567°	5.7083°	Pollen	9000 ± 200	9887 - 10289	-42.9		± 1	peat (0.08)	middle		Streif et al., 1983 (internal report); Ludwig et al., 1979
Gauss 1987/5	German North Sea	Weiße Bank	55.0773°	5.8282°	Hv 15375	9165 ± 230	10146 - 10642	-48.14	-48.1	± 1	fen peat	base		Menke, 1996
4	German North Sea	Northern grounds 172	55.3233°	6.5167°	Pollen	8400 ± 200	9125 - 9550	-37.58		± 1	peat (0.03)	middle		Ludwig et al., 1979; in Behre 2003
BSK VC-15	German North Sea	Northern grounds	54.9030°	6.8769°	Hv 25340	8520 ± 100	9430 - 9600	-33.46		± 1	fen peat	base		unpublished new data
BSK VC-21	German North Sea	Northern grounds	54.9133°	6.9513°	Hv 25342	8865 ± 65	9890 - 10150	-36.66		± 1	fen peat (~0.4)	top	yes	unpublished new data
AU04-07-VC	German North Sea	Helgoland	54.2829°	8.0699°	Hv 25321	8065 ± 80	8780 - 9090	-24.53	-24.48	± 1	fen peat (0.1)	top		unpublished new data
H 15/2V	German North Sea	Elbe palaeovalley	54.1696°	6.9830°	Hv 10336	8975 ± 90	9920 - 10219	-38.45		± 1	fen peat (0.03)	top		Streif et al., 1983 (internal report)
H 18/3V	German North Sea	Elbe palaeovalley	54.11°	6.92°	Hv 11603	8535 ± 150	9398 - 9714	-36.5		± 1	fen peat (~0.1)	middle		Streif et al., 1983 (internal report)
280	German North Sea	Elbe palaeovalley	54.1183°	7.2133°	Pollen	9000 ± 200	9887 - 10289	-38.05		± 1	fen peat (0.1)	middle		Streif et al., 1983 (internal report); Ludwig et al., 1979
6	German Coast	Wangerooge A10	53.87°	7.91°	Hv 8602	7960 ± 205	8540 - 9032	-24.23		± 0.5	base tidal flat with *Phragmites* roots			Ludwig et al., 1979; in Behre 2003
7	German Coast	Wangerooge A10	53.87°	7.91°	Hv 8601	7980 ± 60	8768 - 8998	-23.6		± 0.5	base tidal flat with *Phragmites* roots			Ludwig et al., 1979; in Behre 2003
8	German Coast	Wangerooge A10	53.87°	7.91°	Hv 8600	7540 ± 80	8210 - 8406	-23.16		± 0.5	base tidal flat with *Phragmites* roots			Ludwig et al., 1979; in Behre 2003
9	German Coast	Scharhörn 56/67	53.95°	8.41°	Hv 2575	7790 ± 90	8420 - 8646	-24.4		± 0.1	base tidal flat			Linke, 1982; in Behre 2003
10	German Coast	Scharhörn 58/67	53.95°	8.46°	Hv 2143	7720 ± 65	8417 - 8541	-24.34		± 0.1	*Phragmites* peat (0.17)	top		Linke, 1982; in Behre 2003
11	German Coast	Neuwerk 60/67	53.94°	8.48°	Hv 2242	7280 ± 230	7928 - 8339	-21.31		± 0.1	roots from brackish plants			Linke, 1982; in Behre 2003
2	Dutch North Sea	oyster grounds	53.74°	4.50°	Hv 12092	8750 ± 110	9557 - 9893	-42.5		± 1	*Phragmites* peat (0.1)	middle		Behre et al., 1984; in Behre 2003
1	Dutch North Sea	oyster grounds	54.00°	4.40°	GrN 5758	9935 ± 55	11228 - 11546	-46		± 1	peat	base		Jelgersma et al., 1979; in Kiden et al., 2002
2	Dutch North Sea	oyster grounds	54.00°	4.70°	GrN 5759	9445 ± 80	10557 - 11057	-47		± 1	peat	base		Jelgersma et al., 1979; in Kiden et al., 2002
5	Dutch North Sea	west	52.50°	3.80°	Pollen A	8400 ± 300	9000 - 9771	-26		± 1	peat	base		Jelgersma, 1961; in Kiden et al., 2002
6	Dutch North Sea	west	52.50°	3.50°	Pollen D	8500 ± 300	9127 - 9892	-28		± 1	peat	base		Jelgersma, 1961; in Kiden et al., 2002
7	Dutch North Sea	west	52.50°	3.25°	Pollen C	8700 ± 300	9472 - 10180	-33		± 1	peat	base		Jelgersma, 1961; in Kiden et al., 2002
8	Dutch North Sea	west	52.50°	2.92°	Pollen B	9000 ± 300	9691 - 10430	-35		± 1	peat	base		Jelgersma, 1961; in Kiden et al., 2002

Acknowledgements

I would like to sincerely thank Prof. Dr. Georg Kaufmann, my supervisor, for providing me this interesting work. His generous supervision made me feel comfortable in pursuing the subject, and during the three years of my work, he had always time for discussion and answering my countless questions.

Prof. Dr. Patrick Wu from the University of Calgary deserves special thanks: He invited me to Calgary and broadened my mind about GIA. During my stay in Calgary, he had always time for very special scientific discussions.

Furthermore, I would like to thank Prof. Dr. Serge Shapiro for serving as co-referee.

Dr. Annemiek Vink from the BGR Hannover is thanked for the co-operation and for the work up of the numerous old and new sea-level data.

I am especially thankful to Dr. Douchko Romanov and Wouter van der Wal for carefully reading the manuscript.

I would like to thank the colleagues of the Institute of Geophysics from the Georg August University in Göttingen for the joyful time. Along with all others I thank specially Wilfried Steinhoff, Dr. Martin Leven, Rainer Hennings, Manfred Herden, Erika Eggert-Heise, Ellen Hage, Simon Schmitz, Dr. Tomi Haramina, Dr. Ole Hanekop, Stefan Bernhard, Cornelius Warner, Oliver Haase, and Dennis Rippe, and very special thanks go to Ulrich Einecke, the “Administrator”.

I am very thankful to Natalya Nicholson, Amber Kelter and Wouter van der Wal for their hospitality during my stay in Calgary and all my other “Calgarian” friends for making the time unforgettable.

I would also like to thank my friends and colleagues, who accompanied my life and work in the last three years. Along with all others I want to mention Marco Naujoks, Prof. Dr. Corinna Kroner, PD Dr. Thomas Jahr, Dr. Walter Zürn and Dr. Kasper Fischer.

The financial support from the DFG (research grant KA1723/1-1,2) is gratefully acknowledged. The Berliner-Ungewitter-Stiftung is thanked for funding my trip to the 15th International Earth Tide Symposium in Ottawa 2004.

My girlfriend Martina supported me whenever I needed her, I thank you with all my heart.

My final words are dedicated to my parents and grandparents. Their encouragement, support and good wishes made me what I am today.